Spacecraft Flight in the Atmosphere

Josep Virgili Llop

September 2014
School of Engineering, Cranfield University
Supervisor: Dr. Peter C.E. Roberts
Ph.D. Thesis

Abstract

Spacecraft that orbit in Low Earth Orbit travel through a tenuous atmosphere and hence experience aerodynamic forces that can become quite significant, specially at low altitudes. The presence of these forces can become a major design driver for missions that fly at very low altitudes. Unfortunately, spacecraft aerodynamics are not well understood.

In this dissertation, a CubeSat mission is proposed which will study rarefied-gas aerodynamics, with the objective of determining the effect of surface composition, surface finishing and flow incidence angle on the drag and lift coefficients with an error of less than 5% using a novel method. The CubeSat, has been named ΔDsat, because this study, will be performed using differential measurements of drag and lift coefficients in order to eliminate any measurement bias. ΔDsat carries 4 deployable fins that can rotate independently and expose different surface types to the flow at different incident angles.

In addition, in the dissertation four methods to exploit the aerodynamic forces for the missions advantage are proposed and described in detail. The first one is aerostability, which by shaping the spacecraft appropriately, the resulting aerodynamic torques stabilise the attitude spacecraft with respect to the flow. The second method uses aerodynamic drag and lift to change de inclination of a decaying spacecraft in order to maintain the Sun-synchronous aspect of an orbit whilst decaying. The required lift to drag ratio is in the order of 1.0-1.6, which is not currently achievable (it is theoretically possible), but it could be achieved if drag compensating propulsion is used (thus becoming a fuel saving strategy). The third method controls the atmospheric re-entry interface (the location of the burn-up) by modulating the drag, hence controlling the decay profile. When applied to ΔDsat an error of less than 200 km 3σ on the re-entry location is achieved. Finally, aerostable spacecraft can be used to perform in-situ measurements of the atmospheric winds, by observing their attitude evolution. The aerostable ΔDsat CubeSat would be capable of determining the cross-track winds with an error of less 4 m/s 3σ.

Acknowledgments

This research journey would not have been possible without the guidance of Dr. Peter Roberts. His enthusiasm and cheerfulness have showed me how research is really like, and I also have learned many great things from him.

The support from Sandra has smoothed the bumps in the journey and has made it very enjoyable. Thanks for keeping me happy every day.

Finally, my family has helped me stay, one more time, on track to accomplish my goals.

Contents

Executive Summary

Although it is a common assumption to believe that spacecraft orbit above the atmosphere in an absolute vacuum, this conception is far from reality. The Earth's atmosphere extends upwards several hundreds kilometres and the distance where the Earth's atmosphere stops having a noticeable effect is loosely defined. Therefore, all spacecraft that orbit in a Low Earth Orbit are travelling through the Earth's atmosphere. The atmospheric density decreases exponentially with the altitude and hence, at the altitude at which spacecraft orbit, the atmospheric density is very small and the gas cannot longer be considered as a continuum but needs to considered as a rarefied-gas.

Spacecraft travelling through this tenuous atmosphere experience aerodynamic forces and torques that can become quite significant, especially at low altitudes. The presence of these forces, can become a major design driver for missions that fly at very low altitudes < 450 km, in what is known as a Very Low Earth Orbit. Unfortunately, spacecraft aerodynamics are not well understood and hence, the estimation of these aerodynamic forces, is not very accurate and, more importantly, there are no guidelines as to how these forces can be minimised.

To have a better understanding of spacecraft aerodynamics more on-orbit experiments, that investigate the influence of surface materials and incidence angle on the surface aerodynamic properties are required. In this dissertation, a novel CubeSat mission is proposed, which will study rarefied-gas aerodynamics with the objective of determining the effect of surface composition, surface finish and flow incidence angle on the drag and lift coefficients with an error of less than 5% using a novel method. This CubeSat, has been named ΔDsat because this study will be performed using differential measurements of drag and lift coefficients in order to eliminate any measurement bias. ΔDsat carries 4 deployable fins that can rotate independently and expose different surface types to the flow at different incident angles. The CubeSat is designed to be part of the QB50 constellation, which has the objective to study the thermosphere.

Being part of QB50, gives the opportunity to ΔDsat to fly an ion and neutral mass spectrometer, which takes in-situ measurements of the atmospheric density and composition and hence, the aerodynamic study results will be linked to the direct measurements of the atmosphere.

In addition to proposing a mission to study rarefied-gas aerodynamics, this dissertation explores how aerodynamic forces can be exploited in novel ways, using ΔDsat as a case study. Four novel methods are proposed and described in detail. The first one is aerostability, which requires the spacecraft to be shaped appropriately, so that the resulting aerodynamic torques will stabilise the spacecraft at a certain attitude with respect to the flow.

The second, uses aerodynamic drag and lift to change the inclination of a decaying spacecraft in order to maintain the Sun-synchronous aspect of an orbit whilst it decays. The required lift to drag ratio is in the order of 1.0-1.6, which is not currently achievable with currently characterised surfaces (although it is theoretically possible), though it could be achieved if drag-compensating propulsion is used, in order to lower the drag to lift ratio to a manageable magnitude (thus becoming a fuel saving strategy).

The third method controls the atmospheric re-entry interface (where the aerodynamic heating starts to be significant and where the trajectory does not resemble an orbit any more) by modulating the drag and hence controlling the decay. This method could be applied to drag-sails de-orbiting big spacecraft, that would partially survive re-entry, and make them re-entry over unpopulated areas. If this method is applied to ΔDsat, it only needs to start modulating its drag at an altitude of 250 km to achieve global coverage (in terms of potential re-entry interface points) and would re-enter within 200 km of its target re-entry location.

Finally, aerostable spacecraft can be used to perform in-situ measurements of the atmospheric winds by observing the spacecraft attitude evolution. The ΔDsat CubeSat is highly aerostable and would be capable of determining the cross-track winds with an error of less 4 m/s 3σ, with a spatial resolution of 250 - 500 km, depending on the operational altitude.

Part I

Background

Chapter 1

Introduction

It is a common assumption to believe that spacecraft orbiting the Earth travel above the atmosphere through a perfect vacuum. This common assumption does not acknowledge that the Earth's atmosphere extends several hundred kilometres above the Earth's surface. Therefore, the spacecraft that are orbiting in what is known as the Low Earth Orbit (LEO) range (mean altitude $<$ 2000 km), are travelling through the Earth's atmosphere.

The interaction of the atmosphere with spacecraft produces multiple and diverse effects, including: aerodynamic forces, surface degradation due to the interaction with atomic oxygen (sometimes producing airglow due to light emitting byproducts of the chemical reaction) and spacecraft charging (Larson and Wertz, 2005; Fortescue and Stark, 1995).

The research presented in this dissertation has mainly focused on the influence of the atmosphere on spacecraft flight dynamics. The research has therefore focused on the aerodynamic forces and torques that alter the spacecraft dynamics. As the atmospheric density decreases exponentially as the altitude increases, and as the aerodynamic forces are proportional to the atmospheric density, it could be assumed that these forces are irrelevant at orbital altitudes. This is a fair assumption at altitudes above $\sim$600 km. Below these altitudes, the aerodynamic forces start to have a noticeable effect, and bellow $\sim$450 km, the aerodynamic forces can entirely dominate the spacecraft flight dynamics (after the gravity pull of the Earth). It is therefore, at these very low altitudes, that understanding and taking into account these aerodynamic forces becomes really important.

It can be argued that not many spacecraft are orbiting at these very low altitudes. This is mainly due to the added difficulties derived from the increased aerodynamic forces, so studying spacecraft flight in an atmosphere could be deemed as not very important. This Very Low Earth Orbit (VLEO) range, as this very low altitude orbit range is branded, can provide significant benefits when compared to traditional high altitude orbits, specially for Earth Observation missions, and could be the orbit of choice, for Earth Observation (EO) missions, in the mid to long term. There is therefore, a growing interest in these type of orbits to make Earth Observation missions more cost-effective and competitive.

The research presented here has been focused on three different aspects of the spacecraft flight into the atmosphere:

- Identify the benefits of VLEO, identify mission architectures that can exploit the identified benefits, and identify their mission design drivers.

- Propose experiments to study spacecraft aerodynamics (as they are a design driver for VLEO missions).

- Propose and analyse novel methods to exploit the aerodynamic to benefit the mission.

In the research presented here, the main benefits of VLEO have been identified. For Earth Observation missions, flying closer to the observation target is what brings most of the benefits (increased resolution on optical payloads, increased radiometric performance, increased geospatial accuracy and increased surveillance footprint). There are also the general benefits of VLEO, which are inherent to the the orbit low altitude: increased payload mass from the launcher (lower orbit altitude) and reduced debris flux (drag clears debris faster from these orbits).

Using a traditional systems engineering approach, three different missions that exploit the identified benefits of VLEO have been studied at Cranfield University. This work has been done primarily by MSc students with the input and collaboration of the author and the supervisor of this research. The author, has then been focused on the bigger picture that these case studies portray. These VLEO missions highlight that drag is a major design driver, mainly affecting the configuration (slender shapes are preferred), the operations (attitude changes of slender spacecraft cause lots of problems, such as increased drag and undesired aerodynamic torques) and drag-compensating propulsion is required (if a standard lifetime of $\sim$5 years needs to be maintained). Unfortunately, spacecraft aerodynamics are not well understood and hence, having big uncertainties in one of the main mission design drivers, lets to poorly optimised spacecraft systems (more margins are required), making the systems less cost-effective.

To have a better understanding of spacecraft aerodynamics, more on-orbit experiments that investigate the effect of surface materials and incidence angle on the surface aerodynamic properties are required. In particular, little is known regarding the effect of the surface material, surface finish and incidence angle in the aerodynamic properties of spacecraft surfaces. In the past, some experiments have been conducted but either they combine several effects (such as surface material and surface finish), or they ignore that the aerodynamic properties are a function of several parameters, or they have not been conducted in a relevant environment. Hence, their results do not shed much light on the relationship between aerodynamic coefficients, surface material and flow incidence angle (Moe and Bowman, 2005; Moe and Moe, 2010; Mostaza Prieto et al., 2014).

In this dissertation, a CubeSat mission is proposed which will study rarefied-gas aerodynamics, with the objective of determining the influence of surface composition, surface finishing (roughness) and flow incidence angle on the drag and lift coefficients with an error of less than 5% using a novel method. The CubeSat has been named ΔDsat because this study will be performed using differential measurements of drag coefficients in order to eliminate any measurement bias. ΔDsat carries 4 deployable fins that can rotate independently (Steerable Fins) and expose different surface types to the flow at different incident angles. The CubeSat is designed to be part of the QB50

constellation, which has the objective to study the thermosphere. Being part of QB50 gives the opportunity to ΔDsat to fly an Ion and Neutral Mass Spectrometer (INMS), which will be taking in-situ measurements of the atmospheric density and composition and hence, the aerodynamic study results will be linked to the direct measurements of the atmosphere.

The novel method used by ΔDsat consists of exposing two of these fins to the flow (exposing one surface type at a particular incidence angle) and let the spacecraft fly for a certain period of time (around 1 orbit). During this time, the trajectory of the spacecraft is monitored using the measurements from an on-board GPS. Then, by observing the spacecraft trajectory, the amount of drag that the CubeSat has experienced can be extracted (using orbit determination techniques). Next, by using the in-situ density measurements provided by the mass spectrometer, the drag coefficient can be extracted from the observed drag. Finally, this process is repeated again but exposing another surface type at a different incidence angle. The results are then compared to eliminate biases in the measurement (mainly bias in the atmospheric density measurements and in the CubeSat body drag) and then, conclusions can be drawn about the different aerodynamic properties of different surfaces at different incidence angles.

In addition to proposing a mission to study rarefied-gas aerodynamics, in this dissertation, the use of aerodynamic forces to benefit the mission, has also been explored. Four novel methods are proposed and described in detail. The first one is aerostability, which requires the spacecraft to be shaped appropriately so that the resulting aerodynamic torques stabilises the spacecraft in a certain attitude with respect to the flow. This technique is implementation ready and has been included into the ΔDsat design.

The second method, uses aerodynamic drag and lift to change the inclination of a decaying orbit in order to maintain the Sun-synchronous aspect of an orbit whilst it decays. The required lift to drag ratio is in the order of 1.0-1.6 which is not currently achievable with currently characterised surfaces (although it is theoretically possible), but it could be achieved if drag-compensating propulsion is used in order to lower the drag to lift ratio to a manageable magnitude.

The third method, controls the atmospheric re-entry interface (the location of the burn-up or the start of significant heating) by modulating the drag and hence, by controlling the decay. This method could be applied to drag-sails de-orbiting big spacecraft, which would partially survive re-entry, and make them re-entry over unpopulated areas (risk reduction). If this method is applied to ΔDsat, the CubeSat would only need to start modulating its drag at an altitude of 250 km to achieve global coverage, and would re-enter within 200 km of its target re-entry location.

Finally, aerostable spacecraft can be used to perform in-situ measurements of the atmospheric winds by observing their attitude evolution. The ΔDsat CubeSat is highly aerostable and would be capable of determining the cross-track winds with an error of less 4 m/s 3σ, with a spatial resolution of 250 - 500 km depending on the operating altitude.

The research presented in this dissertation has been done with the goal to further increase the interest on VLEO missions (by identifying its benefits and proposing new mission concepts) and also, to make them more attractive (by studying rarefied-gas aerodynamics and methods to exploit the aerodynamic forces and torques to the advantage of the mission). The expected long-term impact of this research is to achieve

more capable, cost-effective and competitive Earth Observation missions.

It is also interesting to note at this point, that the research presented in this dissertation has only been focused on Earth orbiting spacecraft (and hence to the Earth's atmosphere). However, the methods presented here could as well be applied to other planets with only minor adjustments, although it is not clear if this effort is worth it at this point, as no application of VLEO flight in other planets has been envisioned.

1.1 Objectives

The formal objectives that have been covered in this dissertation are:

- Investigate the potential benefits of Very Low Earth Orbit (VLEO) missions and identify the mission design drivers.
- Propose a novel method to study rarefied-gas aerodynamics.
- Propose methods to use the aerodynamic forces for orbit or attitude control.

The original thesis objectives were intentionally loosely defined and therefore have been evolving, as studying one of the areas opened up other interesting research areas. The final objectives, shown above, are the result of pursuing the research areas that the author identified and felt that they were interesting, of scientific merit, and that were appealing to both, the author and the supervisor.

1.2 Structure of this Dissertation

This thesis is structured into three main parts, with several chapters in each of them. The first part (this one) provides the required background information on the atmosphere and spacecraft aerodynamics, so important when dealing with the flight dynamics effects of flying through the atmosphere. Each of these topics is structured around a chapter. Also, in this first part, a discussion on the VLEO benefits, drawbacks and the different mission concepts studied is included. This chapter is included in the first part as the contents are a mix of literature review, summary of the missions concepts develop by MSc students and ideas/conclusions from the author. This chapter hence can be considered an outcome of the research conducted although is drawn from a combination of efforts from different people and from different sources.

The second part is devoted to the ΔDsat mission. This part includes the original objective of the CubeSat mission to study rarefied-gas aerodynamics, with details of the novel method. It then describes its other mission objectives (aerostability, and in-situ measurement of the thermosphere wind). Although these other mission objectives are more aligned with the objective of exploiting the aerodynamic forces to the advantage of the mission, these methods are included in the ΔDsat part, because their study, has not yet been completely generalised (only studied using the ΔDsat case as a reference). This part also includes background information on the QB50 mission and the CubeSat design itself. This provides context for the science objectives and methods, and provides an insight into all the work that has gone on the CubeSat design. Each of these different

topics (science objectives and CubeSat information) is presented in their own chapter. A conclusions and future work chapter is finally included at the end of this second part.

The third part deals with the aerodynamic attitude and orbit control techniques that have been generalised. In this part, three different methods are detailed, each of them in their own chapter. First, different aerostable CubeSats designs are proposed, and their properties analysed. This is then used to define the design space for aerostable CubeSats, to explore the effects of the different parameters and to determine the drivers and the limitations of this attitude control method. In the second chapter of this final part, a method to maintain the Sun-synchronous inclination of an orbit whilst the spacecraft is decaying using lift (to adjust the inclination) is presented. Then, a chapter is devoted to a method that has been developed to target the re-entry point of a spacecraft controlling by controlling its decay rate. The decay rate is controlled by changing the drag that the spacecraft is generating (this case was first envisioned for ΔDsat). Finally, a chapter containing the conclusions and recommended future work for the aerodynamic attitude and orbit control concludes this final part.

It has to be noted at this point, that specific conclusions have been included in each of the different chapters, with more general conclusions and recommended future work brought together in a dedicated chapter at the end of each part.

Finally, the publications derived from this research are presented. In summary, the method to study rarefied-gas aerodynamics with ΔDsat (Virgili and Roberts, 2013) and the inclination of correction using aerodynamic forces to maintain a Sun-synchronous inclination whilst decaying (Virgili et al., 2014) have been published in peer review journals (the targeted re-entry paper has been submitted) and the rest of the work has been presented at international conferences .

Chapter 2

The Atmosphere

A very important element when studying spacecraft flight in the atmosphere is the atmosphere itself. In fact, the presence of an atmosphere is what makes this field interesting and challenging. As mentioned before, the scope of this study only covers Earth bound satellites and hence, the Earth's atmosphere has been the only one considered. In this chapter, a brief description of the relevant properties of the Earth's atmosphere will be provided. A more comprehensive description of the Earth's atmosphere can be found in Saha, 2008 and Ghosh, 2002.

The Earth's atmosphere can be broadly divided into two distinct layers (ISO 14222, 2013; Ghosh, 2002; Saha, 2008):

- The homosphere, which is the surface based layer where the air turbulence ensures that the gases are well mixed, ensuring a quite constant composition of this layer with respect to altitude and horizontal location (longitude and latitude). This layer extends from the ground level up to ∼100 km. The homosphere is, in its turn, comprised of the troposphere, stratosphere, mesosphere and the lowest part of the thermosphere.

- The heterosphere, where the composition of the atmosphere is dominated by the molecular weight of the species and hence, it changes with the altitude and horizontal location. This layer, in its turn, is comprised by the mid and high thermosphere (125 km to 400-600 km depending on solar and geomagnetic activity) and the exosphere (from 400-600 km and extending into space).

The boundaries between the troposphere, stratosphere, mesosphere, thermosphere and exosphere are defined by the sharp changes in the temperature profile, as can be seen in Fig. 2.1. This study is only concerned with orbiting spacecraft (re-entry and launch are excluded) and hence the heterosphere is the only region of interest as orbits below 125 km in altitude are far too impractical (the aerodynamic drag would be enormous and spacecraft would either decay in a matter of a few hours or would need very powerful propulsion and lots of fuel to maintain its altitude).

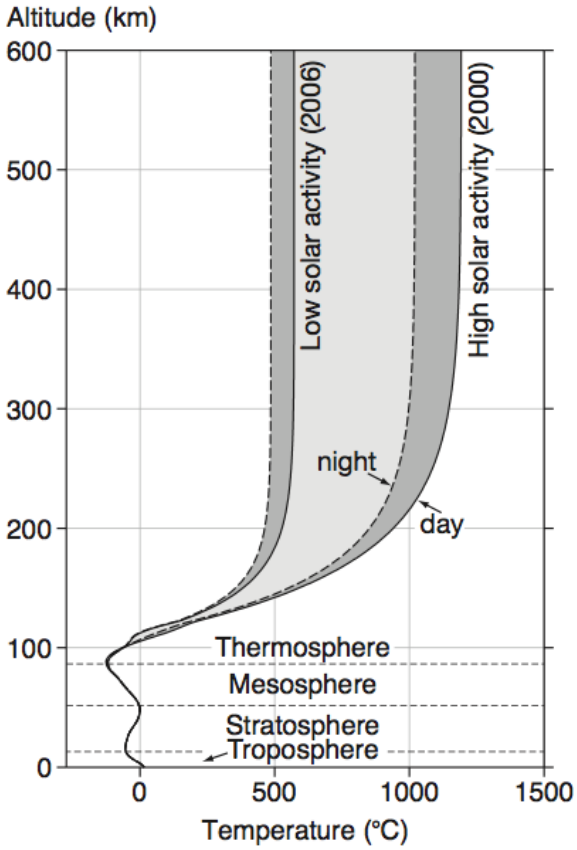

Figure 2.1: Temperature profile of the atmosphere for different solar activities and at different local solar times. Extracted from Doornbos, 2011.

2.1 The Heterosphere

As mentioned before, the heterosphere is the region of the atmosphere where the composition changes with the altitude and location. This is because the mean free path of the gas particles (the distance that each particle travels before colliding with another one) is far greater than the scale of the motions that cause the mixing. This causes the molecules to diffuse, due to their different molecular weights, and hence, causes the composition to change with the altitude and horizontal location.

The heterosphere has two distinct layers (ISO 14222, 2013; Ghosh, 2002; Saha, 2008):

- Thermosphere. In this layer, the temperature increases with altitude due to the atomic oxygen absorbing solar extreme ultraviolet (EUV) radiation. The thermosphere extends from approximately 90 km up to 400-600 km (depending on the solar and magnetic activity).

- Exosphere. In this layer, the temperature is quasi-constant (known as the exospheric temperature) with respect to altitude. Gas particles in this layer may reach the escape velocity (5000 K for Hydrogen) making this region a near-vacuum.

The main effects of the heterosphere on flying spacecraft are the following (Larson and Wertz, 2005):

- Aerodynamic forces. The gas particles colliding with the spacecraft surfaces exchange momentum and generate aerodynamic forces. The generated forces are mainly drag and drag makes the spacecraft lose orbital energy causing orbital decay. Figure 2.2 shows an example of a typical orbital decay due to aerodynamic drag .

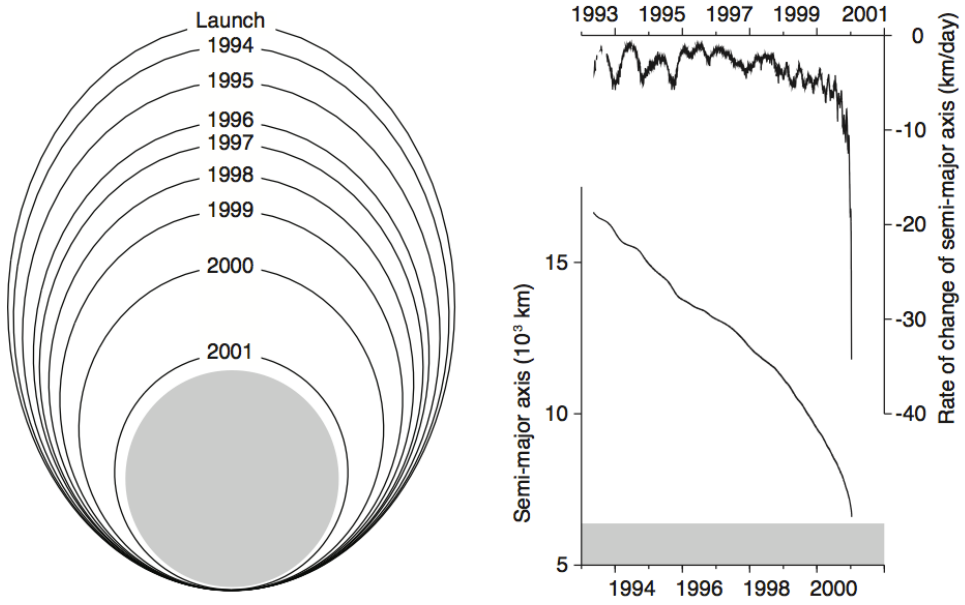

Figure 2.2: Decay of a Payload Assist Module for Delta rocket launches (object 22659) orbit, from its launch in May 13 1993 until its re-entry. Data derived from Two-Line Elements. Figure extracted from Doornbos, 2011.

- Surface corrosion. The gas particles can chemically react with the spacecraft surface when they collide with them. In particular, atomic oxygen, which is the major constituent from ∼200 km to ∼600 km, is very reactive, and can react with the surface materials resulting in degraded sensor performance (for example optics). It is interesting to note that some of the byproducts of these reactions can be radiatively active and create effects such as the Shuttle glow (Viereck et al., 1991).

- Spacecraft charging. Some of the gas particles are electrically charged and get absorbed. Then, the spacecraft can become charged by accumulating an electric potential with respect to the gas (plasma). Differential charging between different spacecraft components can produce electrostatic arcs and potentially damage spacecraft components.

As the density of the atmosphere decreases exponentially with the altitude, as shown in Fig. 2.3, these effects become more significant the lower the spacecraft operates. This

study is focused on those operational altitudes where the effects of the atmosphere have a very important role, therefore the exosphere can be excluded as the extremely thin atmosphere at those altitudes has little effect on spaceflight (charging may still be still an issue at higher altitudes in the long term).

The thermosphere is then the area of interest. In its upper limit (∼600 km) it has a negligible effect on spaceflight, but on its lower altitudes, the density is so great, that orbiting at those altitudes can prove to be extremely difficult. Note that the energy lost is proportional to the density and hence at 250 km the spacecraft losses approximately a thousand times more energy per orbit than at 600 km.

2.2 The Thermosphere

The easiest way to quickly understand how the thermosphere behaves is to look at how the most important properties change with altitude (vertical structure) and location (horizontal structure). Arguably, for flight dynamics, the most important property is the density (which drives the aerodynamic forces). Figures 2.3 and 2.4 show how this property changes with the altitude and with the horizontal location. As it can be clearly seen in these figures, the thermosphere density is very variable with respect to altitude, solar activity and location (night and day variation with a density bulge in the illuminated side of the Earth). Note that this variability is more pronounced at higher altitudes.

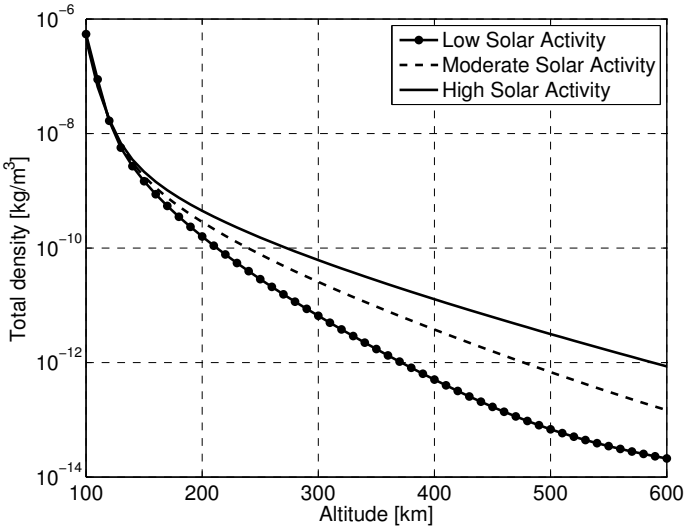

Figure 2.3: Variation of the thermosphere bulk density with the altitude for different solar activities. Estimated above Cranfield at mid-day according to the NRLMSISE-00 model (Picone et al., 2002) using the standard solar indices from ISO 14222.

Another well known fact about the atmosphere is that it co-rotates along with the Earth (Challinor, 1968; King-Hele, 1987). Hence, a spacecraft orbiting the Earth will see the atmosphere moving with the Earth. In addition to this bulk movement, there is wind in the thermosphere. This wind again is highly variable with the altitude and with solar and magnetic activity (specially above the poles). Figure 2.5 shows

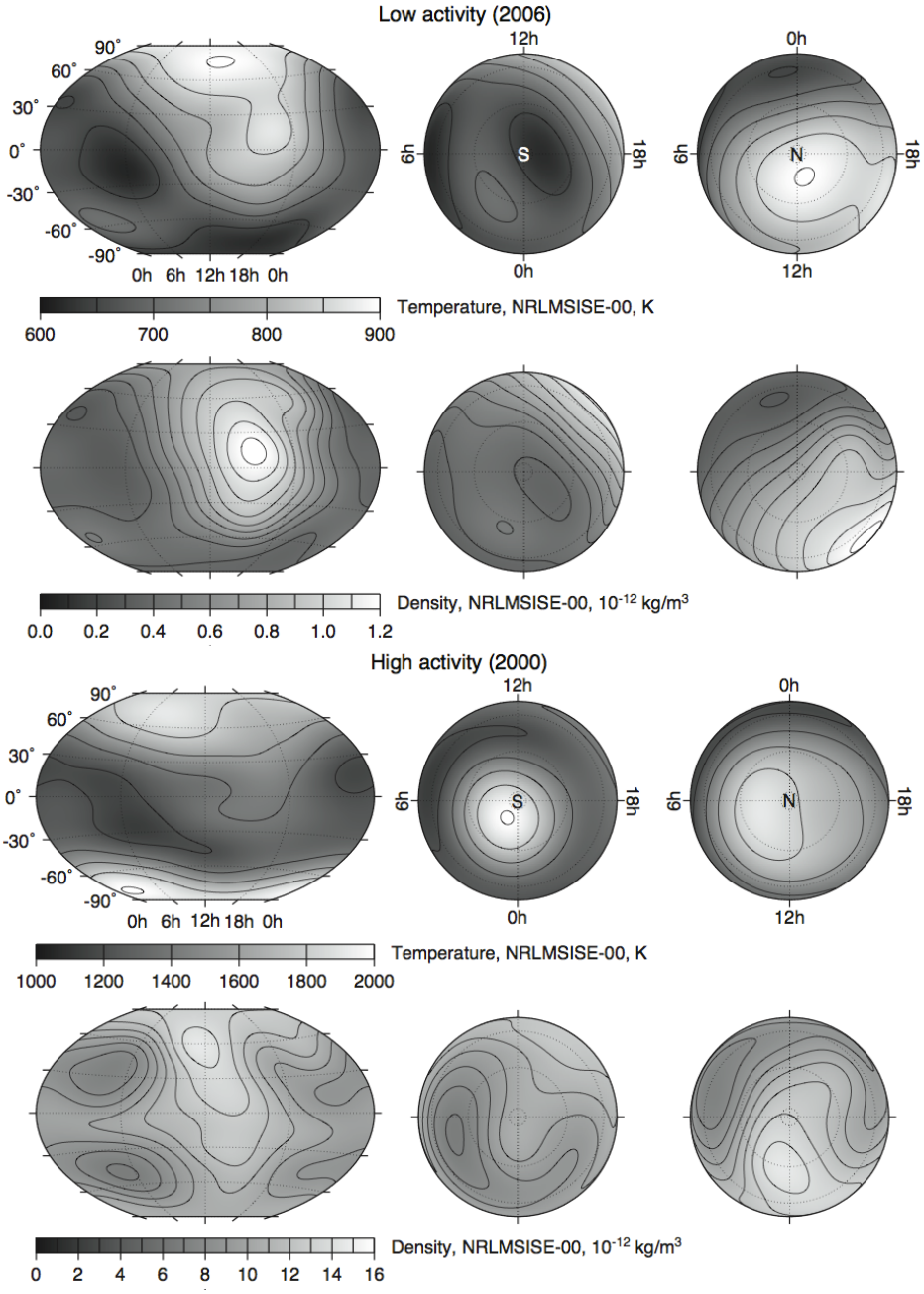

Figure 2.4: Variation of the thermosphere bulk density with the location. Estimated using the NRLMSISE-00 model (Picone et al., 2002) and using high and low solar activity indices from ISO 14222 (2013). Extracted from Doornbos, 2011.

an example distribution of this wind. Note that the wind magnitude is not negligible when compared to typical orbital velocity. The wind is generally against the Earth's co-rotation and it increases its intensity with altitude (hence the atmosphere at high altitudes co-rotates less) and also latitude (high intensity winds can be observed in the poles which transport material from the higher density, higher pressure illuminated side of the Earth, towards its dark side that has lower density and pressure).

Another interesting aspect of the thermosphere is its composition. The raw compos-

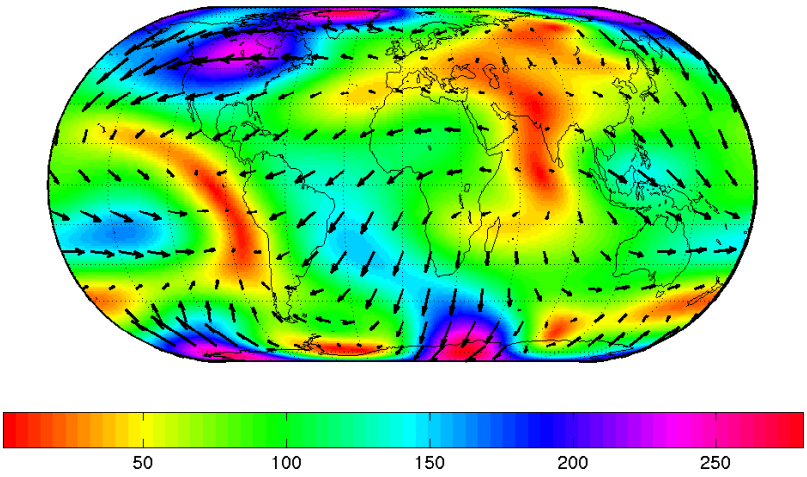

Figure 2.5: Wind pattern (including direction and magnitude) according to the HWM93 (Hedin et al., 1996) model at 450 km with moderate solar activity (ISO 14222, 2013) and during northern hemisphere summer solstice.

ition of the thermosphere is shown in Fig. 2.6a, with Fig. 2.6b showing the composition percentages of the dominant species.

It is interesting to point out that the dominant species is atomic oxygen. This species is quite reactive with the other materials and hence it could potentially damage spacecraft surfaces if atomic oxygen resistant materials are not selected. Also, as well as with the other properties of the thermosphere, the percentage of atomic oxygen in the thermosphere is quite variable with the solar activity. As atomic oxygen absorbs EUV radiation, during an increase of the solar activity, the atomic oxygen heats up and migrates toward higher altitudes. Figure 2.7 shows how the percentage of atomic oxygen changes with different solar activity levels.

Finally, the temperature also plays a significant role determining the interaction of the thermosphere with the spacecraft. Figure 2.8 shows how the temperature of the thermosphere changes with respect to the altitude and the solar conditions. Note how the temperature varies significantly with the altitude and the solar activity and how it stabilises at high altitudes (reaching the exospheric temperature which is only dependant on the solar activity).

It is also interesting to point out that the temperature is quite high and hence the thermal velocity of the gas particles is also quite high. The velocity of this random motion follows the Maxwell–Boltzmann particle velocity distribution (Bird, 1994). The most probable velocity of this distribution (used as a measure of this random thermal motion) can be computed using Eq. 2.1, where $k_B = 1.3806503 \cdot 10^{-23} \frac{m^2 kg^2}{s^2 K}$ is the Boltzmann constant, T the gas particle temperature and m_g the mass of the gas particle. Figure 2.9 shows this most probable velocity using a mean particle mass. Note that this thermal velocity is not negligible compared to typical orbital velocities. In general this thermal velocity is higher at high solar activity due to the increased temperatures, except at high altitudes, where high solar activity makes the heavier atomic oxygen migrate at higher altitudes (increasing the mean mass compared with the normally present lighter helium) and hence increase the mean mass of the gas

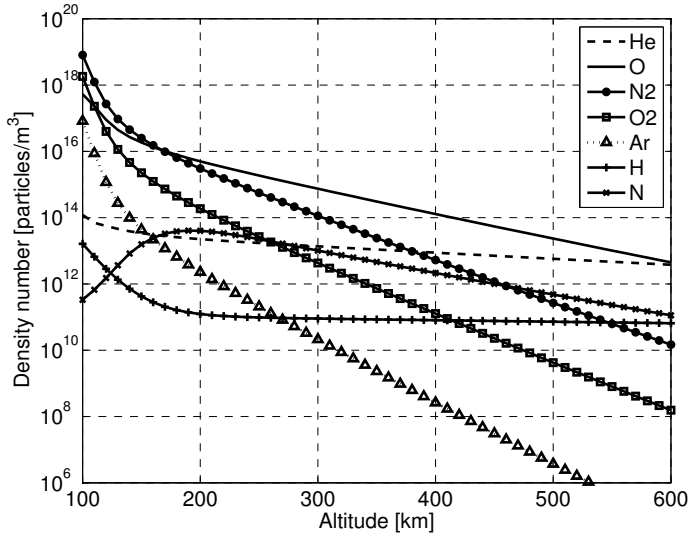

(a)

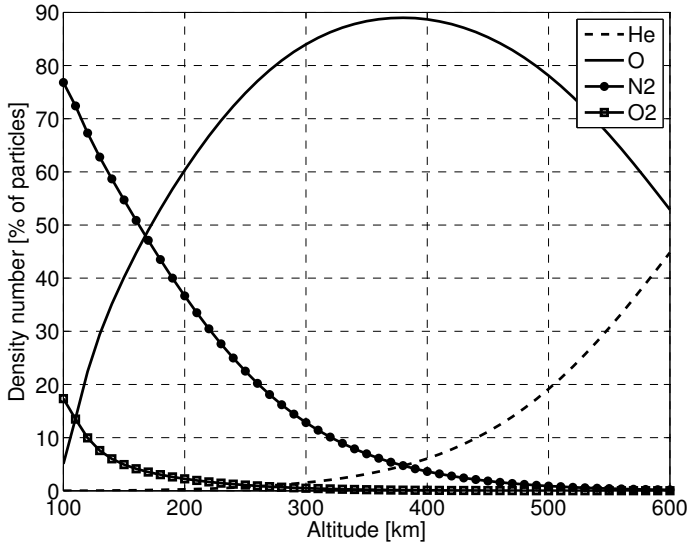

(b)

Figure 2.6: Composition of the atmosphere in a) with the composition percentages of the dominant species in b). Composition estimated above Cranfield at mid-day according to the NRLMSISE-00 model (Picone et al., 2002) using moderate solar activity solar indices from ISO 14222.

particles.

$$v_{thermal} = \sqrt{\frac{2k_B T}{m_g}} \tag{2.1}$$

This section just highlights how variable and complex the thermosphere is. Changing the location, altitude, and solar or magnetic activity produce significant changes in the different thermosphere parameters. Sometimes, the underlying mechanisms that make such changes to occur are complex and difficult to understand at first. Having a

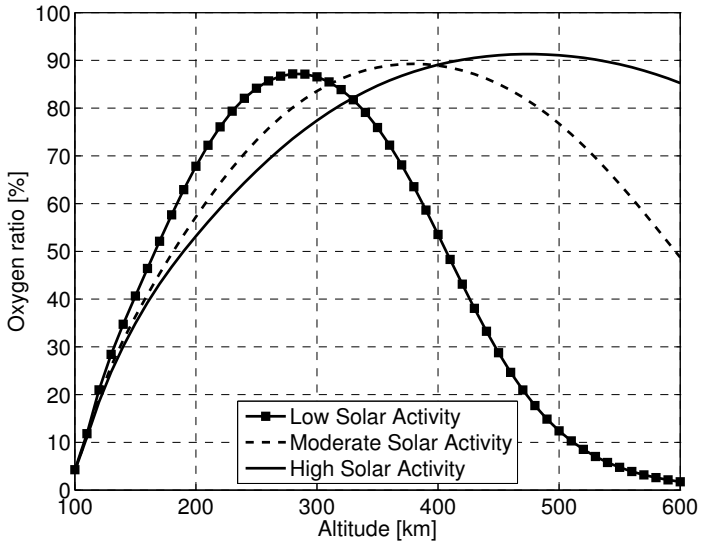

Figure 2.7: Variation of the atomic oxygen composition with the altitude for different solar activities. Estimated above Cranfield at mid-day according to the NRLMSISE-00 model (Picone et al., 2002) using the standard solar indices from ISO 14222.

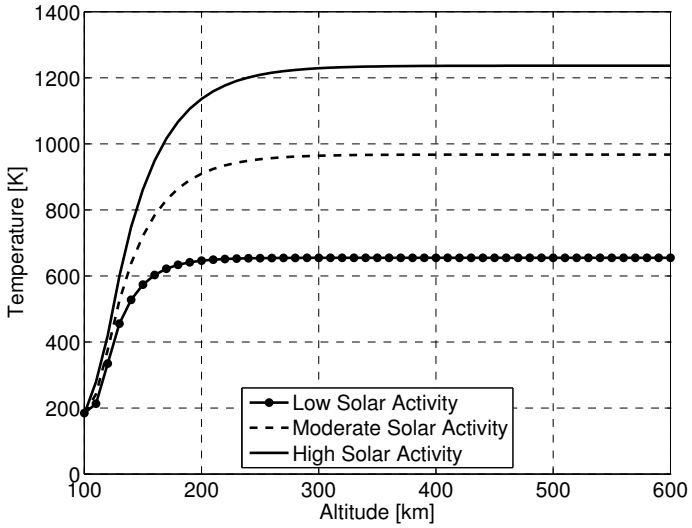

Figure 2.8: Variation of the thermosphere bulk temperature with the altitude for different solar activities. Estimated above Cranfield at mid-day according to the NRLMSISE-00 model (Picone et al., 2002) using the standard solar indices from ISO 14222.

good knowledge of the atmosphere is critical when exploring VLEO mission concepts. The aerodynamic forces can change significantly depending on which atmosphere conditions are considered, hence the mission designer must be able to anticipate which are the worst case scenarios, and confidently explain, the changes in the observed/predicted drag when different atmospheric conditions are analysed (as these may have impacts on the spacecraft design).

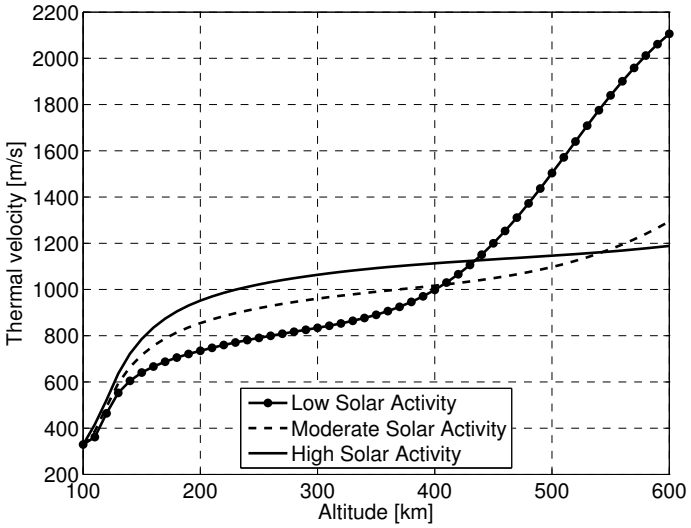

Figure 2.9: Most probable thermal velocity of the gas particles. Estimated above Cranfield at mid-day according to the NRLMSISE-00 model (Picone et al., 2002) using the standard solar indices from ISO 14222.

2.3 Sources of Variability in the Thermosphere

As seen in the previous section the thermosphere is highly variable and the sources of variability are quite diverse, with all of them producing changes in different time and length scales.

Diurnal and Seasonal Variations

Uneven heating of the atmosphere causes a day-to-night variation (atomic oxygen absorbs EUV radiation). This manifests itself in an expansion of the atmosphere in the daytime side, therefore, increasing the density of the illuminated side of the Earth. This variation is also seasonal, as the Earth-Sun geometry changes across the year. It can change the density up to a factor of 5 at 500 km (Doornbos, 2011). Uneven heating of the species also represents changes in the composition.

Solar Activity Variation

Changing solar activity can also produce significant changes in the atmospheric conditions. The 11-year solar cycle produces significant changes in the extreme ultraviolet (EUV) radiation levels of the Sun. During solar minima the radiation is kept at low levels and fairly constant. During solar maximum the radiations levels increase and also its variability. Between solar minimum and solar maximum, the density can increase by a factor of 50 at 500 km (Doornbos, 2011). Apart of the solar cycle, the 27-day Sun's rotation also changes the radiation input that the atmosphere receives and hence, it also has an impact in its properties. These effects are usually captured using several radiation indices (like the $F_{10.7}$ among others) that act as proxies for the solar activity.

Geomagnetic Activity Variation

The geomagnetic activity can also deposit large amounts of energy into the atmosphere and hence alter its properties. The so called geomagnetic storms are triggered by solar events such as solar flares or coronal mass ejections. These events are usually short lived but can dominate the diurnal variation. These effects are usually correlated with the geomagnetic activity index a_p.

Semi-Annual Variation

This variation is not well understood and a possible explanation relating it to the uneven heating of the hemispheres on the solstices was proposed by Fuller-Rowell (1998). It can cause differences of up to 30% in density (Paetzold and Zschörner, 1961).

2.4 Solar Cycle

Most of the variability of the thermosphere comes from the solar activity variation, which is driven by the solar cycle. A comprehensive description of the dynamics that produce the solar cycle is out of the scope of this study, but a brief description of it is included here. More detailed information about the influence that Sun has on the atmosphere and on the space weather in general, is available at Hanslmeier, 2007.

The energy output of the Sun in the peak wavelengths of the visible spectrum is quite constant. The thermosphere absorbs the EUV and X-ray wavelengths, which are highly variable, thus driving the variability of the thermosphere. High energy outputs at these wavelengths are caused by local density peaks in the magnetic field of the Sun. When this occurs, sunspots often form on these areas. The presence of sunspots on the Sun follows a 11 year cycle. During solar minima, there are fewer sunspots and the energy output is hence lower, but also quite stable. During solar maxima, the energy output is higher, but also more unstable (due to the rapid changes of the Sun magnetic field and the 27 days solar rotation).

The activity of the Sun is difficult to measure directly and proxies are used in order to measure it more easily. The most common proxy is the daily observed flux at 2800 MHz (10.7 cm wavelength) in solar flux units ($10^{-22} W/m^2/Hz$) commonly known as the $F_{10.7}$ index. The higher the $F_{10.7}$ index, the higher the energy output from the Sun. The correlation between the $F_{10.7}$ index and the atmospheric density is quite clear, as can be seen in Fig. 2.10.

The $F_{10.7}$ and other solar indices are measured daily at several locations around the globe, with NOAA being one of the most reliable source of these indices. These, and other space weather data products, are freely available form the NOAA's website http://www.swpc.noaa.gov/. Figure 2.11 shows the statistics of the $F_{10.7}$ index during the last 2 solar cycles and confirms that during the solar maxima the solar activity is more unstable.

Forecasting solar activity is extremely difficult and is an area of active research, hence caution has to be used when making predictions of atmospheric conditions that rely on the knowledge of future solar activity. The uncertainty in future solar activity

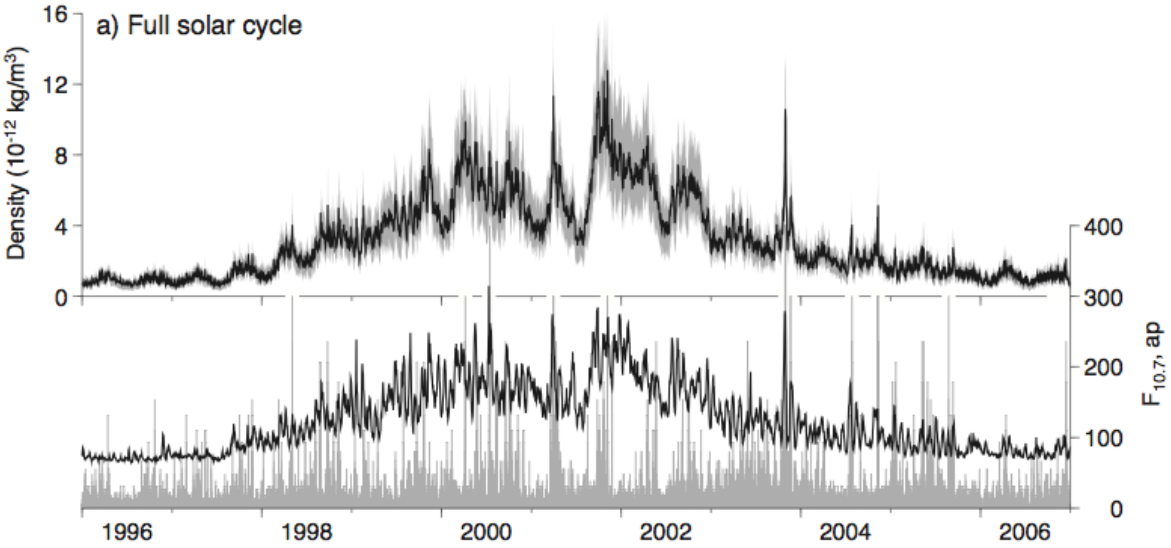

Figure 2.10: Atmospheric density (top part, black is a smoothed mean), and $F_{10.7}$ (black) and a_p (grey) indices (bottom part) for the last solar cycle (23rd). Density modelled over Delft at 400 km. Extracted from Doornbos, 2011.

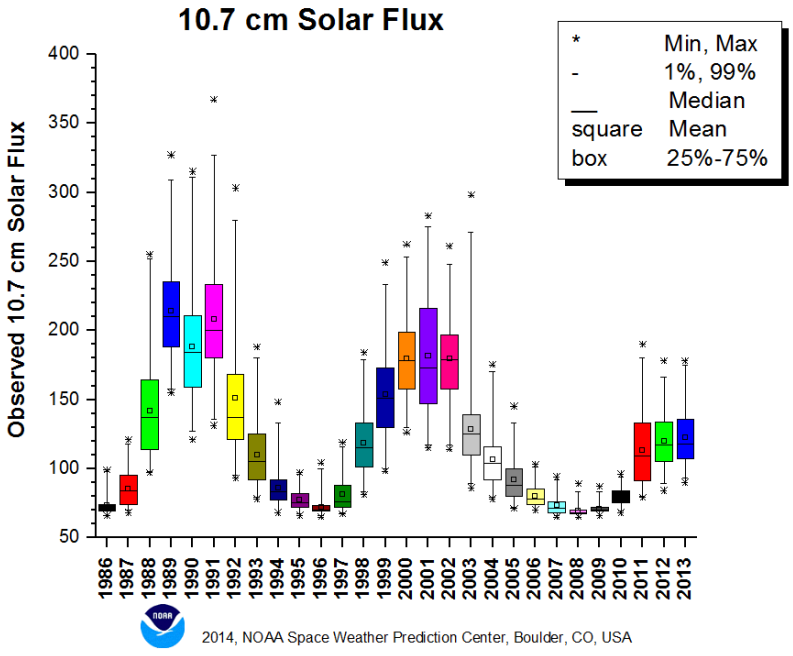

Figure 2.11: Statistics of the $F_{10.7}$ index during the last 2 solar cycles. Graph available from http://www.swpc.noaa.gov/forecast_verification/F10.html.

is, in fact, one of the major sources of uncertainty when forecasting the conditions of the thermosphere.

2.5 Modelling the Thermosphere

It is important when doing quantitative analysis to have a realistic model of the atmosphere. Modelling the Earth's atmosphere is complex and is an area of active research. There are multiple models available, all of them with their advantages and their shortfalls. Fortunately, there is an ISO standard (ISO 14222, 2013) that provides guidance on which one to use for different applications without requiring an extensive knowledge of the models origins and limitations. The Committee on Space Research (COSPAR) also produces recommendations on which models to use (COSPAR, 2013).

There are mainly 3 different families of atmospheric models (although these are not the only ones):

- Jacchia's models. The observation of the orbital decay of the first spacecraft in the late 1950s and early 1960s were used to produce the first atmospheric models in the 1960s and early 1970s. These include the ones by Harris and Priester, 1962 and Jacchia, 1971. COSPAR adopted the Jacchia-71 model as their International Reference Atmosphere in 1972, known as CIRA-72 (Jacchia, 1972). These models have been improved by the US Air Force Space Command over time to include new algorithms that take into account more complex phenomena and have resulted in the recent Jacchia-Bowman 2006 (JB2006) and Jacchia-Bowman 2008 (JB2008) (Bowman and Tobiska, 2008), which are state of the art atmospheric models. The JB2008 has been adopted as a COSPAR International Reference Atmosphere and a software implementation of the model can be found in http://sol.spacenvironment.net/∼jb2008/code.html.

- DTM models. These models also use observations of the dynamics of decaying spacecraft. The first one was published by Barlier in 1978. They have been also updated with the inclusion of new data as it became available, with the most recent updates being the DTM2009, DTM2012 and DTM2013 (Bruinsma, 2013). The DTM2012 and DTM2013 models software implementations can be downloaded from http://www.atmop.eu/index.php/downloads.

- MSIS models. Alan Hedin in 1977 (Hedin et al., 1977a and 1977b) created a new family of models solely based on mass spectrometer and incoherent radar observations. Note that no satellite decay observations were initially used in this approach, hence, giving this model independent measurements of densities and atmospheric composition. The MSIS models development was continued by the US Naval Research Laboratory (NRL) with the most up to date model being the NRLMSISE-00 model (Picone et al., 2002). The later models include a broader range of data sources, including satellite decay observations. In addition to these density and composition models, the Horizontal Wind Models were also develop using the same techniques, with the latest editions being the HWM93 (Hedin et al., 1996) and the HWM07 and DHWM07 (for Disturbed geomagnetic conditions) (Drob et al., 2008).

For this study the following models have been used:

2.5.1 Density and Composition Models

For modelling the density and composition of the atmosphere the NRLMSISE-00 model has been used (Picone et al., 2002). This model relies on the following set of input parameters to output a prediction of the atmospheric species composition, temperature and total density:

- Altitude, latitude and longitude.
- Time of the year and apparent solar time.
- Solar activity $F_{10.7}$ index.
- Geomagnetic activity a_p index.

This model is currently the de-facto standard on the industry (ECSS Secretariat, 2008), but new more accurate models are appearing. Among them there is the JB2008 (Bowman and Tobiska, 2008) that uses more recent data (is specially relevant the inclusion of the CHAMP and GRACE accelerometer density measurements) and also takes into account a wider set of solar activity indices (2 more solar indices). A different approach has been used in the HASDM (Bowman and Storz, 2003), where a traditional atmospheric model is corrected dynamically by observing the real time decay of a large number of calibration spacecraft (or objects). This model is best suited to support operational missions as it uses real-time decay information to produce real-time corrections on atmospheric models.

The NRLMSISE-00 was selected because it does not require too many solar and geomagnetic indices, because it has been the industry standard for a long time (being replaced by the JB2008 now) and because it is already available in MATLAB.

More recent models could have produced more accurate estimates of the density and composition, but they required quite a few more solar and geomagnetic activity indices. For this type of study, that it does not try to use the density results to any operational mission, and where the solar and geomagnetic activity indices are coarsely set, the use of more complex models do not seem to bring any accuracy benefit and it would only slow down the calculations.

2.5.2 Wind Models

To generate the wind, the HWM93 Hedin et al. (1996) model has been used. This model provides the zonal and meridional winds of the upper atmosphere. The inputs of the model are:

- Altitude, latitude and longitude.
- Time of the year and apparent solar time.
- Solar activity $F_{10.7}$ index.
- Geomagnetic activity ia_p index.

This model was updated in the HWM07 Drob et al. (2008), but the accuracy of that last one is dubious (Private conversation with Ethan S Miller, PhD Senior Staff Scientist, Space Department / Geospace and Earth Science Group Johns Hopkins University Applied Physics Laboratory), and hence the HWM93 was selected.

2.5.3 Reference Scenarios of Solar and Geomagnetic Activity

To facilitate the modelling and the comparison of results, this 4 standard (ISO 14222, 2013) solar activity scenarios have been used (note how these indices coarsely match the observations of the past 2 solar cycles shown in Fig. 2.11):

- Low activity. $F_{10.7} = F_{10.7\,avg} = 65$, $S_{10.7} = S_{10.7\,avg} = 60$, $M_{10.7} = M_{10.7\,avg} = 60$, $Y_{10.7} = Y_{10.7\,avg} = 60$, $a_p = 0$, $Dst = -15$.
- Moderate activity. $F_{10.7} = F_{10.7\,avg} = 140$, $S_{10.7} = S_{10.7\,avg} = 125$, $M_{10.7} = M_{10.7\,avg} = 125$, $Y_{10.7} = Y_{10.7\,avg} = 125$, $a_p = 15$, $Dst = -15$.
- Long term high activity[1]. $F_{10.7} = F_{10.7\,avg} = 250$, $S_{10.7} = S_{10.7\,avg} = 220$, $M_{10.7} = M_{10.7\,avg} = 220$, $Y_{10.7} = Y_{10.7\,avg} = 220$, $a_p = 45$, $Dst = -100$.
- Short term high activity. $F_{10.7} = 300$, $F = 250$, $S_{10.7} = 235$, $S_{10.7\,avg} = 220$, $M_{10.7} = 240$, $M_{10.7\,avg} = 220$, $Y_{10.7} = Y_{10.7\,avg} = 220$, $a_p = 240$, $Dst = -300$.

Where:

$F_{10.7}$,$S_{10.7}$,$M_{10.7}$,$Y_{10.7}$ designates the F10.7, S10.7 M10.7 and Y10.7 solar index and are given in units of solar flux, 10^{-22} W/m^2. The avg subindex indicates the 81 day average of the index centred on the current day.

a_p designates the daily planetary geomagnetic index and is given in nT.

Dst designates the hourly disturbance storm time ring current index and is given in nT.

[1]These are the levels used when high activity is mentioned across this dissertation.

Chapter 3

Rarefied-Gas Aerodynamics

A spacecraft flying through the atmosphere will experience aerodynamic forces. These aerodynamic forces are what makes flight dynamics in an atmosphere different. To compute these aerodynamic forces the generic Eq. 3.1 can be used.

$$\overrightarrow{F} = \frac{1}{2}\rho \left\| \overrightarrow{V} \right\|^2 \hat{v} A_{ref} \overrightarrow{C_f} \tag{3.1}$$

where ρ is the atmospheric density, $\overrightarrow{V}$ is the relative velocity of the spacecraft with respect to the flow, $\hat{v} = \frac{\overrightarrow{V}}{\|\overrightarrow{V}\|}$ being the velocity unitary vector, A_{ref} is an arbitrary reference area and $\overrightarrow{C_f}$ are the force coefficients (in the 3 directions). Also, the aerodynamic torques can also be expressed using the generic Eq. 3.2, where l_{ref} is an arbitrary length and $\overrightarrow{C_T}$ are the torque coefficients (in the 3 directions).

$$\overrightarrow{T} = \frac{1}{2}\rho \left\| \overrightarrow{V} \right\|^2 \hat{v} A_{ref} l_{ref} \overrightarrow{C_T} \tag{3.2}$$

Special cases of the force equation use, instead of generic force coefficients, the drag C_D (anti velocity) and lift C_L (normal to velocity) coefficients which leads to the well known Eqs. 3.3 and 3.4, which compute the drag and the lift of a body.

$$D = \frac{1}{2}\rho V^2 A_{ref} C_D \tag{3.3}$$

$$L = \frac{1}{2}\rho V^2 A_{ref} C_L \tag{3.4}$$

As a remainder, drag is the force that acts against the direction of the velocity, and lift, is the force that acts perpendicular to the velocity. Also note, that the vector notation has been dropped in Eqs. 3.3 and 3.4 because these equations now output scalar magnitudes (with the directions inherently defined by the lift and drag coefficients). Lift is usually defined as a vertical force pointing upwards (due to the aircraft heritage of these equations), but in spacecraft aerodynamics lift has no preferable direction (could be sideways as in the method presented in chapter14).

The torque Eq. 3.2 can also be written in a scalar form if the torques in the three different directions are separated into different equations, but their formulation is not as popular as the drag and lift equations.

The term $\frac{1}{2}\rho \left\| \overrightarrow{V} \right\|^2$ represents the dynamic pressure, which is only a function of the environment bulk properties and it is usually represented by q. Then, the $A_{ref}\overrightarrow{C_f}$ terms take into account the geometry of the spacecraft, its orientation with respect to the flow and also other flow properties, as the flow regime, gas and surface composition, gas temperature and other surface parameters. Hence, the equation to compute the forces have some terms directly relating to the environment bulk properties, and some others, relating to the spacecraft geometry and flow regime (exactly the same as aircraft aerodynamics). Separating the terms is useful to identify the origin of the forces and to help compare different scenarios (with different atmospheric environments and different spacecraft geometries).

Spacecraft aerodynamics substantially differ from aircraft aerodynamics because in spaceflight, the flow regime is different, and this changes the mechanisms which create the aerodynamic forces. This difference in flow regime is mainly due to the low density of the thermosphere, compared with the densities encountered by aircraft. The gas in the thermosphere is no longer a continuum but needs to be considered as a rarefied-gas (Bird, 1994).

Another parameter that is often used to describe the aerodynamic properties of a spacecraft is the ballistic coefficient $\beta = \frac{C_d A_{ref}}{m}$, where m is the mass of the spacecraft. This coefficient is independent of the atmospheric environment (at least to first order, as no density and velocity is directly involved, but the drag coefficient is dependant on the flow regime and other flow properties) and also contains the mass of the spacecraft, which can then be used to introduce the acceleration due to aerodynamic forces $a_d = q\beta$. The ballistic coefficient is, in general, a much more compact description (although simplistic) of the spacecraft aerodynamic properties. The force coefficients do not include the reference area or the mass of the spacecraft so they only portray the effect of the geometry (and flow regime) where as the ballistic coefficient includes the size of the spacecraft (through A_{ref}) and its mass (so it is more complete when comparing different spacecraft).

3.1 Flow Regime

Another important aspect to bear in mind is the flow regime that spacecraft is subject to. As the density is so small (compared to aircraft standards) the gas can no longer be considered as a continuum but need to be considered as a rarefied-gas, and hence, the flow can be defined as a free molecular flow. The Knudsen number (K_n) is usually used to define the different flow regimes. The Knudsen number is defined in Eq. 3.5 (Bird, 1994).

$$K_n = \frac{\lambda}{l_{ref}} \tag{3.5}$$

where λ is the mean free path of the gas and l_{ref} is a reference length of the spacecraft. The mean free path is the average distance traveled by a gas particle before colliding with another, and it can be approximated by the kinetic theory of gases using Eq. 3.6 (Bird, 1994).

$$\lambda = \frac{k_B T}{\sqrt{2}\pi d_{avg}^2 p} \tag{3.6}$$

where k_B is the Boltzmann constant, T is the gas temperature, d_{avg} is the average diameter of the gas particles and p is the gas pressure. Figure 3.1 shows the evolution of K_n assuming that the gas is molecular nitrogen N_2 with $d = 4.11 \times 10^{-10}\, m$. The diameter of the N_2 molecule is generally used when computing the mean free path in the atmosphere (although atomic oxygen is the dominant species), but as these results are used to compute the Knudsen number and roughly define the different flow regimes, no significant error is introduced.

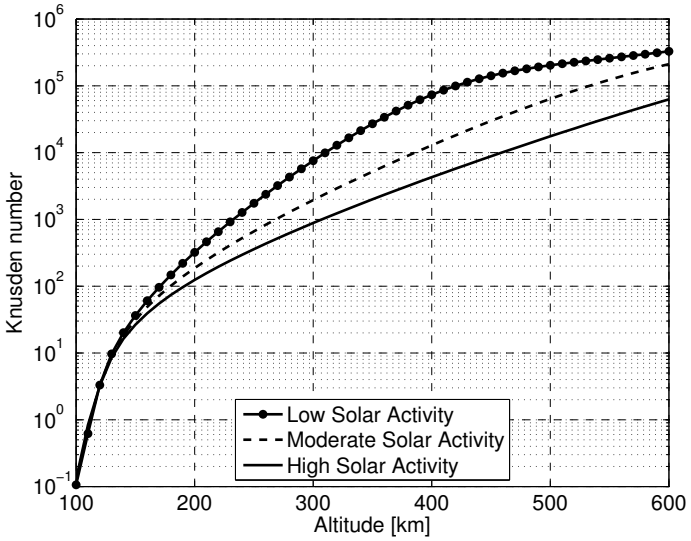

Figure 3.1: Knudsen number for $L = 1$ m and assuming N_2 with $d = 4.11 \times 10^{-10}\, m$.

Different flow regimes can be identified using the Knudsen number (Table 3.1). These flow regimes limit the applicability of certain theories (Figure 3.2). At the range of Knudsen numbers that spacecraft encounters during flight in the thermosphere, the spacecraft will be in free molecular flow in the upper part and in transitional flow in the lower (with a moderate size spacecraft), potentially achieving continuum flow for big spacecraft $>$ 1m at extremely low altitudes $\sim$100 km. Hence, in the lower part of the thermosphere, the Boltzmann equations will need to be applied, and in the upper, a free molecular, collision-less flow could be assumed (simplifying the analysis).

Knudsen number	Flow regime
$Kn > 10$	Free molecular
$0.01 < Kn < 10$	Transitional
$Kn < 0.01$	Continuum

Table 3.1: Flow regimes depending on the Knudsen number.

Note though, that to achieve transitional flow, the orbit altitude needs to be extremely low $<$ 200 km and hence, in the vast majority of the scenarios, the spacecraft will be flying in a free molecular flow. Therefore, free molecular flow will be assumed unless otherwise stated.

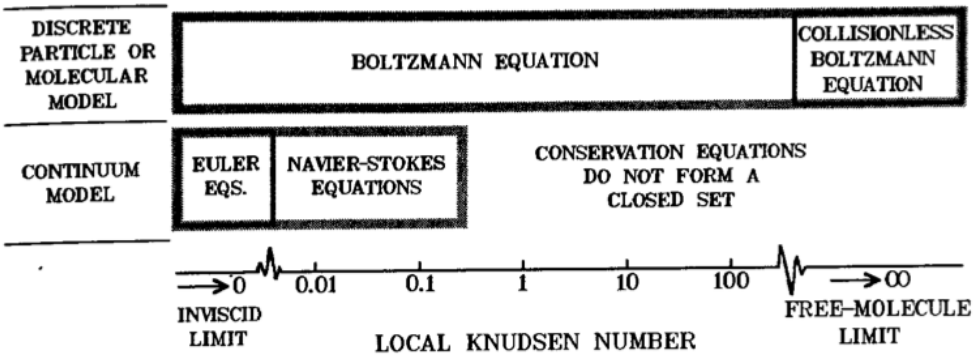

Figure 3.2: Applicability limits of different theories depending on the Knudsen number. Extracted from Bird, 1994.

3.2 Free Molecular Flow

In a free molecular flow the Knudsen number K_n is much greater than one. Therefore, the mean free path of a gas particle is much greater than a representative spacecraft dimension. From this, it can be assumed that the interactions between gas particles (collisions) are very rare, and hence they can be ignored when analysing the interaction of the spacecraft with the flow. When this condition is met, the flow is considered to be a free molecular flow (Bird, 1994), and then the aerodynamic forces are completely dominated by the gas-surface interactions (GSI). The GSI are the interactions of the gas particles when they collide with the spacecraft surfaces.

It is also interesting to note, that due to the high temperature of the gas in the thermosphere, and the high Knudsen number, the flow does have a bulk velocity but each particle has also its own thermal velocity. The combination of these two velocities makes the final velocity of each gas particle. This is shown in Fig. 3.3. More information on how to compute this thermal velocity and some representative values are provided in section 2.2.

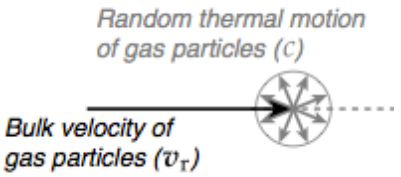

Figure 3.3: The bulk and thermal velocity make the final velocity of each gas particle. Extracted from Doornbos, 2011.

The thermal velocity of the gas particles is quite high (∼1 km/s at 350 km as seen in Fig. 2.9) and hence the gas particles will not be nicely collimated. This has significant implications in spacecraft aerodynamics. Areas of the spacecraft that could appear to be shadowed from the flow, will not be. Particles with high thermal velocities not aligned with the bulk velocity can collide with surfaces that could, at first, appear to be shadowed. Note also, that the velocity computed in Fig. 2.9 is only the most probable

velocity (in a random direction) and hence, there will be gas particles with thermal velocities that exceed this most probable one. The effect of this thermal velocity can be summarised as that all (or nearly all) of the spacecraft surfaces will receive impacts from gas particles.

When a gas particle collides with a spacecraft surface, it can be either adsorbed and then potentially re-emitted or it can be directly reflected (specularly or diffusely) as shown in Fig. 3.4. During the contact with the surface an exchange of energy and linear momentum between the gas particle and the surface can occur. Also, when adsorbed chemical reactions can also occur. Determining what happens when a gas particles collides with the spacecraft surface is what the GSI models determine. Note that when a gas particle is reflected or reemitted it can then collide with other surfaces (or other gas particles if the local density is high enough).

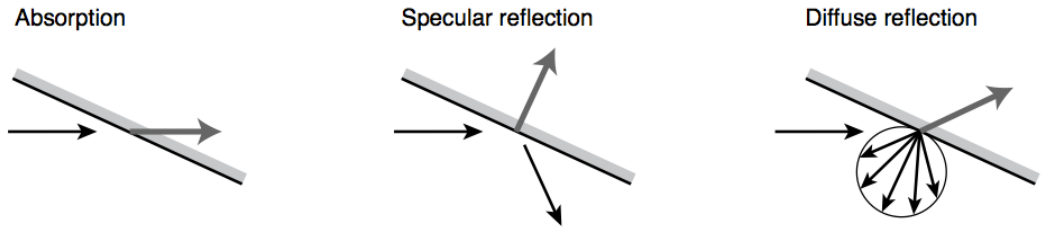

Figure 3.4: Different types of momentum exchange that can occur when a gas particle collides with a spacecraft surface. Extracted from Doornbos, 2011.

3.3 Modelling Techniques and Methods

To study the aerodynamics characteristics of spacecraft there are several methods that can be used. A comparison between these methods can be found on figure 3.5. Note that this methods have then to be paired with models for gas-gas interactions and gas-surface interactions. A small overview of these methods is presented here:

Panel Method

It neglects the intermolecular collisions. The spacecraft is then idealised by discretising it using planar surfaces and a gas-surface interaction model is chosen. Finally the forces on all the panels are computed and the global forces are extracted. This method is the easiest one, and provides a good approximation with minimum amount of time and effort. It is then particularly suited for free-molecular flow.

This method neglects shielding of some surfaces by other parts of the spacecraft and also it does not take into account interaction between panels (i.e. particles reemitted/reflected from one panel colliding with another one). This is the method that has been used in the research presented in this dissertation, as it is suited for free molecular flow, and the geometries analysed are not particularly complex.

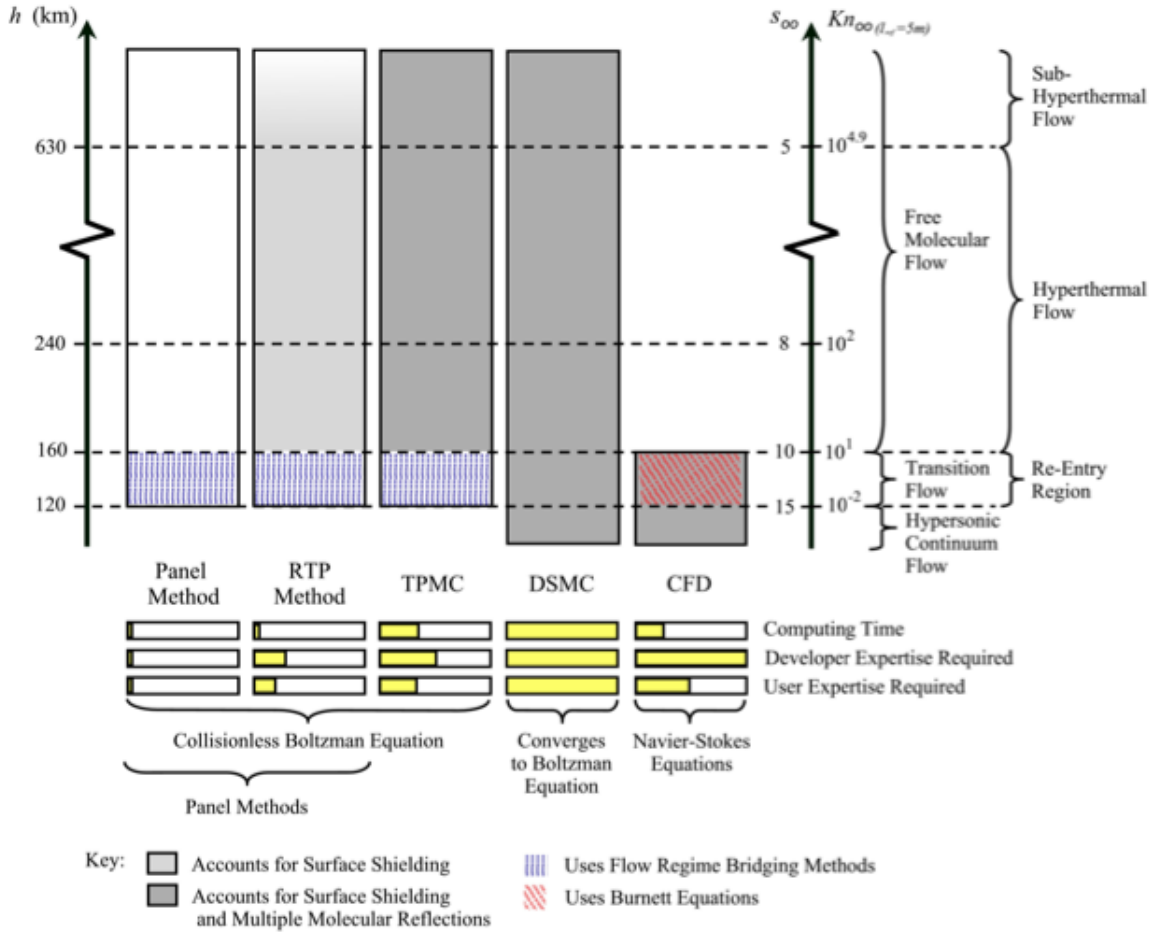

Figure 3.5: Comparison of existing techniques/methods to tackle spacecraft aerodynamics. Extracted from Graziano, 2007.

RTP Method

The Ray-Tracing Panel (RTP) method improves form the panel method as it allows interference of the different panels to be accounted for. The method is borrowed from graphic rendering applications, and it basically assumes that a particle behaves as a beam of light, that when encounters a surface it can be reflected, reemitted or absorbed. After the interaction, the reflected particle can be traced to account for the interaction between panels. Usually a finite number of interactions are allowed.

This method provides the same level of accuracy as the panel method but it allows to analyse more complex geometries.

TPMC Method

In the Test Particle Monte Carlo (TPMC) method, fluid particles (representing thousands of real gas particles) are fired sequentially (with representative flow conditions). The particles can reflect off the surfaces of the model, but do not interact with each other. Hence, TPMC can be used to model multiple reflections.

This method is an intermediate step between the RTP and the DSMC.

DSMC

The Direct Simulation Monte Carlo has become the de-facto method to study rarified-gas aerodynamics. In a nutshell, the method simulates thousands of fluid particles (each of them aggregating several real gas particles) in the simulation domain. These particles can interact with each other (gas-gas interactions) and with the surface (gas-surface interactions). This method has proved to converge to the Boltzmann equation, and hence it can be used to simulate continuum flows up to free molecular flows.

The downside of it is the computing time and its complexity. If K_n is big enough the gas-gas interactions can be turned off and simulate a collision-less flow.

3.4 Gas-Surface Interaction Models

The aerodynamic forces in free molecular flow are dominated by the Gas-Surface Interactions (GSI) as the collisions between gas particles are rare. There exist several GSI models, each of them having different starting assumptions. A comprehensive description of the models used in spacecraft aerodynamics can be found in Moe and Moe, 2010. The most popular GSI models are the Sentman model (Sentman, 1961) and the Schamberg model (Schamberg, 1959). Both of them have been derived making certain assumptions on how the gas particles interact with the surface. Also, in both cases, the calculation of the forces depend on several surface and gas dependant parameters not known *a priori* and that have to be determined experimentally.

In this study, the Sentman model will be used as it is de de-facto standard to compute spacecraft aerodynamic coefficients at low altitudes (Moe and Moe, 2005, 2010).

3.4.1 The Sentman Model

This model assumes that all the incident particles that collide with a surface are adsorbed to be later diffusely reemitted. In the LEO range this seems to be true from the limited available orbital data (Gregory and Peters, 1987; Moe et al., 1998). The particles are then reemitted with partial thermal equilibrium with the surface. How well the thermal equilibrium is accomplished is represented by the energy accommodation coefficient. This energy accommodation coefficient is defined in Eq. 3.7.

$$\sigma_a = \frac{\Delta E_i - \Delta E_r}{\Delta E_i - \Delta E_w} \tag{3.7}$$

where ΔE_i and ΔE_r represent the energy fluxes associated with the incident and reemitted particles. ΔE_w represents the energy flux that would be generated if all particles were reemitted in thermal equilibrium with the surface. In this model, the C_d and C_l can be written, following Sutton notation (Sutton, 2009), as in Eqs. 3.8 and 3.9.

$$dC_d = \left[\frac{P}{\sqrt{\pi}} + \gamma Q Z + \frac{\gamma}{2}\frac{v_r}{v_\infty}\left(\gamma\sqrt{\pi}Z + P\right)\right]\frac{dA}{A_{ref}} \tag{3.8}$$

$$dC_l = \left[lGZ + \frac{l}{2}\frac{v_r}{v_\infty}\left(\gamma\sqrt{\pi}Z + P\right)\right]\frac{dA}{A_{ref}} \tag{3.9}$$

where,

$$\gamma = \cos(\theta) \tag{3.10}$$

$$l = \sin(\theta) \tag{3.11}$$

$$G = \frac{1}{s_\infty^2} \tag{3.12}$$

$$P = \frac{1}{s_\infty} e^{-\gamma^2 s_\infty^2} \tag{3.13}$$

$$Q = 1 + G \tag{3.14}$$

$$Z = 1 + erf(\gamma s_\infty) \tag{3.15}$$

and where,

θ is the angle between the flow and the local normal vector (0^{o} when the surface is normal to the flow and 90^{o} when it is parallel).

v_r is the most probable velocity of the reemitted gas particles.

v_∞ is the relative bulk velocity between the spacecraft and the incident gas particles.

A_{ref} is an arbitrary reference area (usually the cross section area of the spacecraft).

s is the ratio between v_r and the thermal velocity of the gas v_{th}. Hence $s = \frac{v_r}{v_{th}}$.

According to Koppenwallner (Koppenwallner, 2009) the v_r/v_∞ ratio can be written as in Eq. 3.16.

$$\frac{v_r}{v_\infty} = \sqrt{\frac{1}{2}\left[1 + \sigma_a\left(\frac{4RT_w}{v_\infty^2} - 1\right)\right]} \tag{3.16}$$

with,

σ_a being the energy accommodation coefficient.

R being the gas constant.

T_w being the temperature of the surface (wall).

In the lower regions of the LEO range, the atomic oxygen concentration is high. This atomic oxygen gets adsorbed into the spacecraft surfaces masking the original surface properties. Having a surface covered with atomic oxygen rises the accommodation coefficient to very close to one (Moe and Moe, 2005). As in this research project, the flight dynamics at low altitudes are the matter of discussion, then an accommodation coefficient of one will be generally used. Getting surfaces where the atomic oxygen does not get adsorbed, or removing the already adsorbed atomic oxygen, is of great interest as it would let the underlying surface properties to play a role in the gas surface interactions. This would allow to control the type and magnitude of the GSI by selecting the surface properties and hence allow some degree of control over the aerodynamic forces.

Figure 3.6 shows the C_d and C_l predicted by this model at different incidence angles. Note that the lift in these regimes is very low. This is because the model assumes no reflection and that the gas particles are reemitted with thermal equilibrium with the wall as $\sigma_a = 1$ (at a relative low temperature). If we change the energy accommodation up to $\sigma_a = 0.95$ (Fig. 3.7) then the lift is significantly increased. This has also a moderate effect on the C_d, especially at low incident angles.

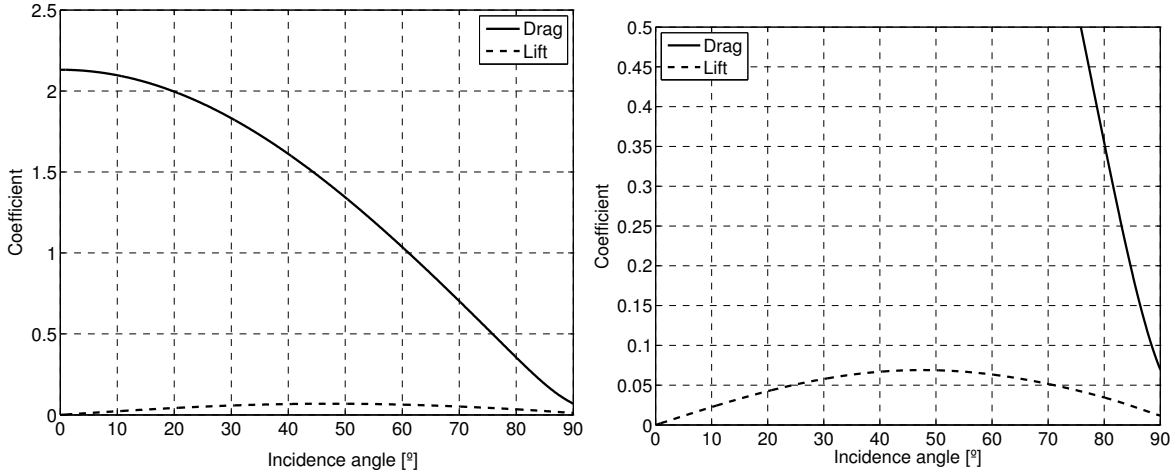

Figure 3.6: Drag and lift coefficients for $\sigma_a = 1$ and $T_w = 300\,K$ at an altitude of $h = 250\,km$. The figure on the right is a magnification showing the detail of the C_l and the C_d at high incidence angles.

Also note that due to the thermal velocity of the gas particles we have drag and lift at $\theta > 90^{\text{o}}$ (Figure 3.8). The drag at these high incidence angles can appear to be small but in slender shapes it can have a significant impact[1] and it must not be ignored.

[1]In the case of a cylinder of radius r and length l the frontal drag will be equal to the lateral drag when $l = r\frac{C_{d,frontak}}{2C_{d,lateral}}$. In the case above that would happen when $l = 15.7r$. But an infinite slender cylinder is more efficient in terms of volume per drag, so in general slender spacecraft are preferred.

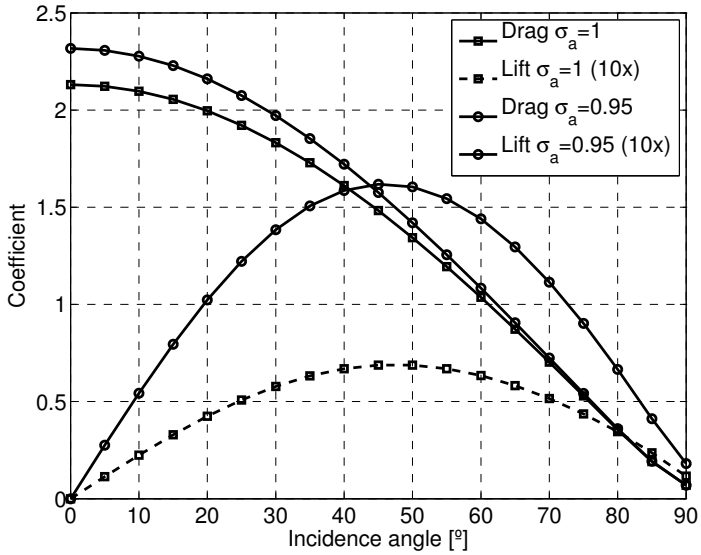

Figure 3.7: Comparison of C_d and C_l for two different energy accommodation coefficients for $T_w = 300\,K$ at an altitude of $h = 250\,km$.

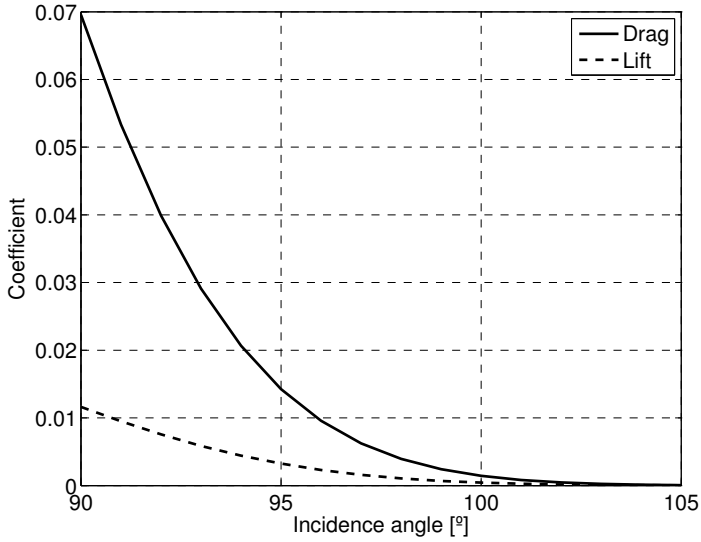

Figure 3.8: C_d and C_l for $\theta > 90^{\text{o}}$ for $\sigma_a = 1$ and $T_w = 300\,K$ at an altitude of $h = 250\,km$.

3.5 Uncertainties in the GSI Models

Moe and Moe (2010) and Mostaza Prieto et al., 2014 have summarised the spacecraft aerodynamics state of the art. The main problem with the models is that all of them are analytically formulated and that the model parameters have then to be adjusted manually depending on several factors (flow and surface composition, surface temperature, flow incident angle, ...). The data required to adjust the coefficients needs to come from orbital experiments as currently there is no ground laboratory capable of recreating the environmental conditions encountered in orbit. As the available data from on orbit experiments is very limited, there is not a complete understanding on

how to adjust the GSI model parameters. Parameters may be set inaccurately, hence leading to inaccurate force estimations.

Also not having a good knowledge of GSI does not allow mission designers to optimise their mission concepts. How to create minimum drag spacecraft? Which surface materials to use on drag-sails to maximise drag?. This lack of understanding goes beyond not knowing how to adjust the parameters in the models. There may be materials where the Sentman model is not applicable (as the gas-particles get specularly reflected for example) and hence these materials could be useful for certain applications.

But coming back to the Sentman model, the parameter that needs to be adjusted in this model is the energy accommodation coefficient σ_a. From the limited orbital data available $\sigma_a \approx 1$, although some empirical models to adjust σ_a do exists (Pilinski et al., 2010). There are also several other publications providing guidance on how to set this parameters based on the limited data available (Moe and Moe, 2005; Bowman and Moe, 2005; Moe and Bowman, 2005; Moe and Moe, 2010). The assumption that $\sigma_a \approx 1$ is due to the adsorption of atomic oxygen present in the thermosphere (see Fig. 2.6a, 2.6b and 2.6). Atomic oxygen gets adsorbed into the spacecraft surfaces hence covering the spacecraft surfaces with atomic oxygen and hence, making them behave very similarly to other spacecraft surfaces (irrespecutful of having different underlaying surface properties).

Unfortunately, not a lot of research exists on how different surface properties or other factors could alter the accommodation coefficient or how the adsorption of atomic oxygen could be mitigated (so that the underlying surface properties could affect the accommodation coefficient). This type of research is essential if methods to minimise or maximise aerodynamic forces are to be used. Also, materials that do not adsorb the atomic oxygen and that could exhibit other type of behaviours (different to adsorption and reemission), as reflection, need to be researched.

3.6 Past Experiments to Determine energy Accommodation Coefficients

There have been efforts in the past to determine the aerodynamic properties of spacecraft and in particular, to understand gas-surface interactions. The first research on gas-surface interactions was performed by Irving Langmuir, that in 1916, demonstrated that surfaces are in general not clean, but that gas and liquid particles get adsorbed in them. Building in Langmuir's work on cleaning surfaces Roberts (1930) performed the first measurements of energy accommodation coefficients on clean surfaces. Roberts also showed that the accommodation coefficients are low on freshly cleaned surfaces but that these coefficients tend to increase over time as the surfaces get contaminated.

After second world war, the research on energy accommodation flourished and Goodman and Trilling, building on earlier work by Baule on static-lattice hard-sphere models, demonstrated that the variation in energy accommodation coefficient with the flow incidence angle could be modelled using Eq. 3.17 (Baule, 1914; Goodman, 1967; Trilling, 1967).

$$\sigma_a = 3.6\frac{\mu}{(1+\mu)^2}\cos\theta \tag{3.17}$$

where μ is the ratio of the molar mass of the gas molecules to that of the surface molecules and θ is the incidence angle . If we assume nitrogen gas particles and an aluminium surface then $\mu \approx 1$. With these conditions, $\sigma_a = 0.9 \cos\theta$ and therefore the energy accommodation coefficient ranges from 0 to 0.9. This equation does not take into account temperature effects and assumes a clean surface, so it is only really useful under laboratory conditions. This great variability of σ_a with the flow incidence angle has been correlated in laboratory experiments by Roberts, 1930, Saltsburg, 1967 and Knechtel and Pitts, 1973, among others. The few on-orbit experiments, as the one conducted by Moe et al., 1995, show that this effect also exists in orbit although the measured effect, has been substantially lower due to atomic oxygen adsorption.

Laboratory experiments clearly show that the energy accommodation coefficient is dependent on the surface properties and that contaminants can mask the underlying surface properties. In LEO, atomic oxygen is the major contaminant and in 1990 Brundle and Broughton already described in detail the mechanism of atomic oxygen adsorption. By that time, and despite the knowledge gained in the laboratory, this knowledge could not be directly applied to spacecraft surfaces due to the presence of atomic oxygen in space. Atomic oxygen adsorbs into most surfaces (Riley and Giese, 1970) and experiments in relevant environments can not be conducted on the ground (lack of appropriate facilities) (Moe and Moe, 2010).

Initial pressure measurements in pressure gauges mounted on sounding rockets and satellites, soon highlighted that atomic oxygen gets adsorbed into nearly all surfaces (Moe and Moe, 1967). Later measurements of the accommodation coefficients on paddlewheel satellites were performed (Karr, 1969; Moe, 1968). Early measurements of accommodation coefficients resulted in high accommodation coefficients $\sim$1 suggesting a strong adsorption of atomic oxygen (not clean surfaces).

Orbital observation of radar calibration spheres made with different materials and with different surface finishes show that the drag coefficient is affected by these parameters (surface material and surface finish). These experiments showed differences on the drag coefficient up to 3% (Moe and Bowman, 2005), suggesting that accommodation coefficients were independent of substrate material (due to atomic oxygen adsorption). But, as only spheres were used the results obtained in those experiments combine the effects of geometry with those of the material (the effect of atomic oxygen adsorption may be different at different incidence angles). Up to this date, there has not been a series of in-orbit experiments that throughly test different surface types (materials and finishes) at different incidence angles. Also, there has been little research in methods that could mitigate atomic oxygen adsorption or cleaning methods that could periodically remove already adsorbed atomic oxygen.

Moe and Moe, 2010 in his recent survey on the GSI experiments that have been conducted in the past, concludes that in-orbit experiments are still required in order to advance the knowledge on GSI and to obtain realistic measures of spacecraft drag coefficients.

Chapter 4

Very Low Earth Orbit (VLEO) for Earth Observation

Lowering the operational altitude of Earth Observation (EO) platforms can potentially make them more competitive. Reducing the operational altitude (hence flying closer to the observation target) of optical payloads, improves the payload radiometric performance, increases its resolution, hence allowing payloads to have greater capabilities (maintaining size, mass, power and cost) or reducing the payload size whilst maintaining the same capability level (reducing mass, power and cost). For radar payloads, reduced antenna areas and power requirements allow a mass and size reduction, potentially reducing the cost of the platform. In addition, lowering the altitude increases the geospatial accuracy of the platform, increases its surveillance footprint and allows more payload mass from the launch vehicles.

The described benefits of a lower operating altitude present an opportunity to make EO platforms more competitive, either by flying more capable platforms at the same cost, or by offering the same capabilities at a reduced cost. But operating at lower altitudes also introduces challenges due to the residual atmosphere (increased drag and atomic oxygen erosion) and reduced communications windows with ground stations.

The potential to increase the competitiveness of EO missions by lowering their operational altitude has raised the interest in platforms operating in Very Low Earth Orbits (VLEO). As these platforms operate through denser parts of the atmosphere this has motivated the research presented in this dissertation. In this chapter, a quick overview of the different aspects and considerations of VLEO is provided.

It has to be noted at this point that the name of VLEO has initially been proposed at Cranfield and that a formal definition of VLEO does not yet exist. The author usually refers to VLEO as those orbits with a mean altitude below 450 km. Generally, at 450 km, the aerodynamic drag is strong enough to make a spacecraft decay in less than 5 years, requiring significant changes in traditional spacecraft designs (which usually come with a 5 year operational lifetime target).

The interaction of spacecraft with the atmosphere is stronger as the altitude decreases due to the increase in atmospheric density. The Low Earth Orbit (LEO) range is commonly defined as those orbits with a mean altitude ranging from 200 km up to 2000 km (hence making VLEO a subset of the LEO range). It is obvious, that in the lower part of LEO, the interaction with the atmosphere (mainly aerodynamic drag) has

an important effect in the flight dynamics, whereas in the upper range, the presence of an atmosphere can be neglected. The approximate effect of the different disturbing accelerations in LEO is shown in Fig. 4.1. Note that the effect of atmospheric drag starts to be significant at an altitude around 500 km and that it dominates above the other perturbations below that altitude (excluding the Earth's gravity field).

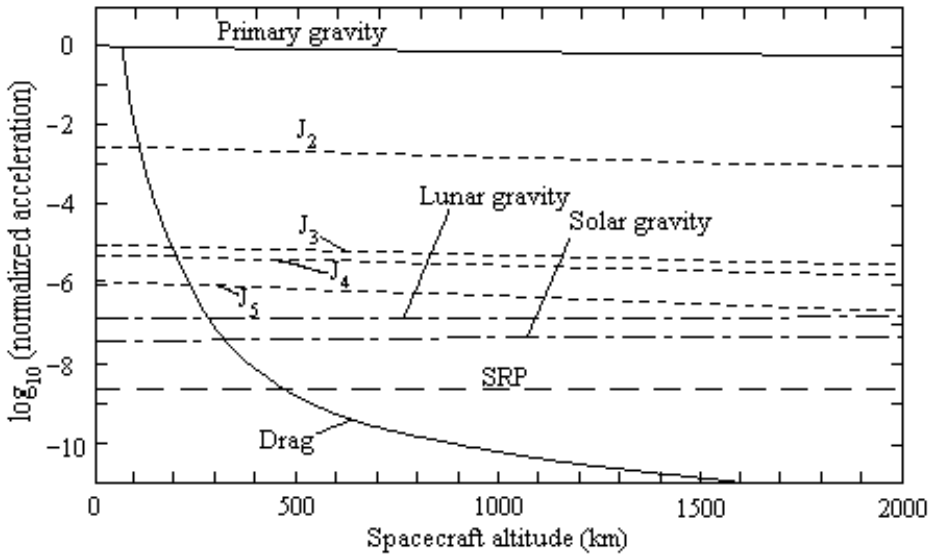

Figure 4.1: Comparison of different disturbing accelerations in LEO. Extracted from Fortescue and Stark, 1995.

4.1 Altitude Windows

The first step for VLEO is to check which are most suitable altitudes to operate for EO missions. Most LEO missions fly at an altitude above 500 km as can be seen from the objects in orbit count shown in Fig. 4.2a. The objects in orbit count roughly correlates with the amount of spacecraft flying in those orbits as it is shown in Fig. 4.2b.

Typical EO missions current preferred orbit is a circular Sun-synchronous orbit with an altitude of 600-1000 km. These orbits are chosen because they can provide consistent illumination conditions on the targets for optical EO missions and near-constant solar power input and thermal environment for non-optical EO missions (this properties are provided by Sun-synchronous aspect of the orbit) and because they can achieve a short revisit time (3 days typically). Another benefit of these high altitude orbits is that their natural decay is very small and hence little propulsion is required to maintain their nominal orbit (propulsion may still be required to compensate for other perturbations).

Three important parameters that need to be considered when selecting an EO mission orbit are: achieve global coverage, the maximum revisit time (the maximum time between consecutive observations of the same ground target) and the ground track repeat period (amount of time for the ground track to repeat itself). For EO missions it is desirable to have global coverage with a low revisit time, and for some EO missions, it is also important to have a repeating ground track (so that targets can be observed

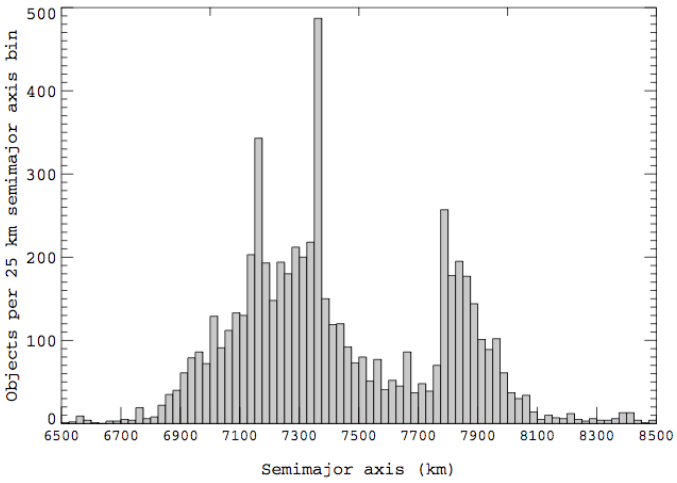

(a)

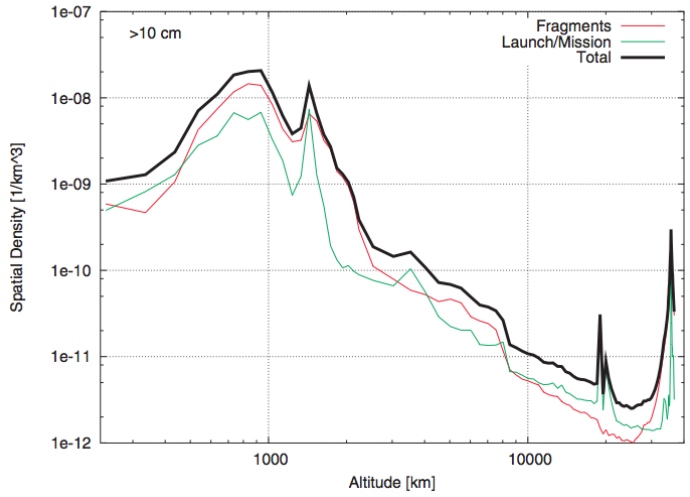

(b)

Figure 4.2: Number of objects in LEO at different orbit altitudes a) with their source detailed in b). Note that radius of the Earth is $R_{Earth} = 6370\,km$. Extracted from Klinkrad, 2006.

periodically with the same spacecraft-target geometry). Long repeating ground track times are acceptable, as with longer repeating times more convenient spacecraft-target geometries are possible for a wider range of target locations. For example, GOCE has a 61 day repeat period giving it the ability to nearly fly overhead any ground target (the target can be a maximum of 20 km away of the ground track).

Figure 4.3 shows the revisit time and Fig. 4.4 shows the discreet altitudes where a ground track repeats itself after a certain time period. From these figures, it is clear that there are certain windows which are preferred. For example around 600-650 km the revisit time is quite short and a wide range of repeat periods can be selected. When going below 500 the revisit time is still acceptable but then, the atmospheric drag start to be a major orbital perturbation source. The aerodynamic drag will make the

spacecraft decay quickly (not achieving a very long lifetime without drag-compensating propulsion). Also, if the mission requires to have a constant altitude, propulsion will potentially be required in the lower altitude orbits. If the mission is flexible in terms of altitude, the spacecraft can be allowed to decay and hence its revisit time and other properties will change over time. If the spacecraft is allowed to decay, the limiting factor will be the lifetime between the upper and lower altitude limits and hence, this will create an upper limit to the spacecraft ballistic coefficient $\beta = \frac{C_d A_{ref}}{m}$. The decay period through certain altitude windows for different ballistic coefficients is shown in Fig. 14.11 on page 171 (the figure is used to show the applicability of the decaying Sun-synchronous orbits with aerodynamic inclination correction).

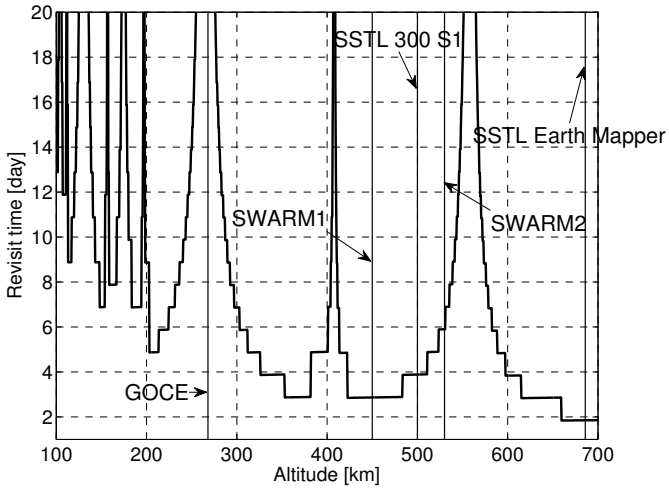

Figure 4.3: Revisit time for a single spacecraft with varying altitudes assuming a Sun-synchronous orbit an off axis looking angle of 45º and a target latitude of 40º. It assumes that observations can only be made during the day (assumes an optical payload).

Note that the revisit time can be improved by having a constellation of spacecraft, or by operating the spacecraft in both day and night conditions, as it is possible with radar missions for example (Fig. 4.3 assumes an optical payload and hence imaging only occurring during the day).

As it can be concluded from this section, there is no obvious restriction to lower the operational altitude of spacecraft when the revisit time and repeat period are considered. Orbits in the VLEO range can offer the same level of performance ,as the traditional high-altitude orbits, although it is true that the windows where this is possible are limited to certain altitude ranges.

4.2 Benefits of VLEO

Flying in a VLEO has some important benefits, specially for EO, that can justify the selection of these orbits. The main benefits are described below with some of them being already identified by Aguttes et al., 2005.

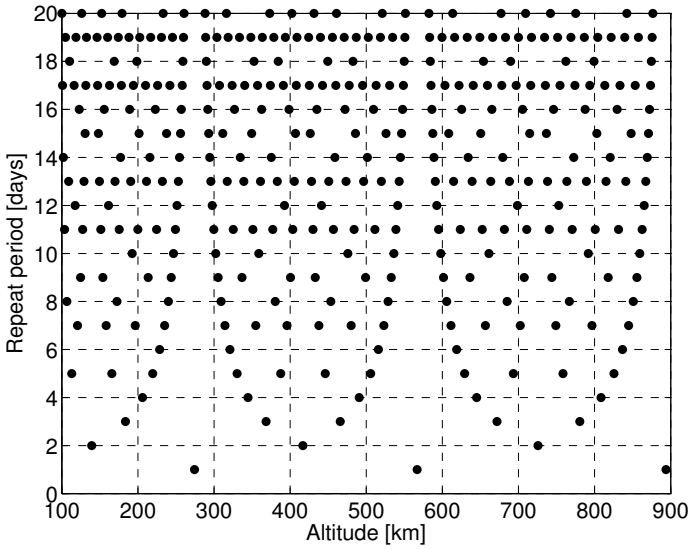

Figure 4.4: Discreet altitudes to achieve repeating ground tracks. The altitudes are approximate as not all gravitational harmonics have been taken into account.

4.2.1 Increased Resolution of Optical Payloads

The angular resolution limit of a telescope is determined by the Rayleigh criterion. This criterion states that the maximum theoretical resolution of an optical system is limited by the diffraction of the light entering the optical system. The resolution of the system can then be determined using Eq. 4.1.

$$\sin\alpha = 1.22\frac{\lambda}{D} \tag{4.1}$$

where α is the angular resolution, λ is the wavelength of the light ($\lambda \approxeq 550\ nm$ for the visible spectrum) and D is the aperture diameter. For EO missions the important metric is the resolution of objects on the ground and hence Eq. 4.1 can be rewritten as Eq. 4.2 for optical payloads (assuming visible spectrum).

$$r = 6.71 \times 10^{-9}\frac{h}{D} \tag{4.2}$$

where r is the ground resolution and h is the spacecraft altitude. Practical considerations (such as optic and sensor quality) can reduce even further the achievable resolution. Therefore, to increase the resolution of a platform, 3 different options exist:

1. Increase the quality of the optics to approach the theoretical limit.

2. Increase the aperture size D.

3. Reduce the flying altitude h.

Increasing the optics quality has a cost implication and can be done up to a certain level as the diffraction limit will always be there. Increasing the optics size has also significant cost implications. Bigger optics also imply a bigger and heavier spacecraft,

more expensive to develop and to launch (note that optics cost grows exponentially with quality and size, as can be easily noted on consumer cameras optics).

By reducing the flying altitude the resolution is automatically increased (without modifying the optics). For example, by halving the flying altitude (from 650 km to 325 km) the resolution would be immediately doubled without any modification to the optical system (only adjusting the sensor to operate in the new altitude). For example, the SSTL-300 platform could achieve a panchromatic nadir ground sampling distance of 1.25 m, instead of the current 2.5 m.

4.2.2 Increased Radiometric Performance

Another benefit of flying closer to the imaging target is that the radiometric performance is improved, as the distance to the target is reduced (that means more signal to noise ratio). The power density of a signal P is proportional to the inverse square distance r from its source as shown in Eq. 4.3.

$$P \propto \frac{1}{r^2} \tag{4.3}$$

Hence reducing the operating altitude (reduces the distance from the source) improves the amount of signals that gets into the receiver. That being an advantage for optical payloads as well as for radars, or passive SIGINT antennas among others. This allows for less sensitive instruments (lower cost) to achieve the same results as more sensitive instruments.

Although not completely equivalent to increased radiometric performance, flying closer to the target may also boost the signal that wants to be measured. This is the case of GOCE (Drinkwater et al., 2007) that operates at such low altitude <300 km (and in extension all gravity surveying missions; Rummel et al., 2002). Flying so low allows GOCE to measure the gravity field with a very high accuracy.

4.2.3 Increased Payload Mass (from Launcher)

As a general rule, the mass that a launcher is capable of injecting into a circular orbit decreases exponentially as the orbit altitude increases. Comparing typical EO orbits at 600 and 300 km the payload capability is increased up to 13% in the VEGA (Arianespace, 2006) launcher and it doubles in the Dnepr launch vehicle (Kosmotras, 2001).

This is clearly beneficial for VLEO missions as it can lower the launcher cost if smaller launchers are selected or increase the spacecraft mass at no additional cost. This can also be used to launch constellations in a single launcher (using the extra mass). Also, having more up-mass available from the launcher, increases the number of launch vehicles that are able to lift the mission, potentially reducing the launch delays risks associated when depending only in one launcher.

Increasing the available mass from the launchers can shift the limiting factor from the launch mass to the available volume on the launcher fairing. Hence, VLEO missions have to ensure that they can fit in the launcher fairing.

4.2.4 No De-Orbit Required

The orbit lifetime at 600-700 km is between 15 and 78 years (depending on the spacecraft ballistic coefficient and solar activity). ESA guidelines state that inactive spacecraft should be de-orbited within 25 years. Therefore, the vast majority of spacecraft operating in the current high altitude orbits will require some sort of de-orbiting device (for example, a de-orbit burn or a drag-sail).

In a 400 km orbit the lifetime is not higher than 3 years and hence the drag becomes an asset at the end of life.

4.2.5 Increased Geospatial Position Accuracy

A shorter path length to the target also increases the geospatial accuracy of the imagery. The spacecraft position and attitude uncertainties have a smaller arm length to propagate and hence the images taken can be geolocated with a greater accuracy (or less capable and less expensive attitude determination systems used to achieve the same performance).

4.2.6 Increase of the Effective Surveillance Footprint Size

If a minimum useful resolution is required for the platform, then the lower the spacecraft flies the bigger will be the area that complies with this requirement. That is due to the shorter path length to the target. This effect causes the timeliness of revisit to also improve.

4.2.7 Lower Risk of Collision with Space Debris

Flying at a lower altitude orbit where the density is higher means that the debris will also decay at a higher rate and hence the orbit will clear itself from debris much faster than higher orbits. Current predictions of space debris population in LEO (see Fig. 4.5), suggest that the VLEO range will remain clean for many years to come and hence it represent an alternative to traditional orbits, if these ones become too crowded or polluted. The VLEO range can then be considered resilient to space debris build ups (so dangerous in higher altitude orbits).

If high altitude orbits experience a significant increase of debris population (due to the Kessler syndrome (Klinkrad, 2006) for example), VLEO may be then a good alternative orbit. Also, due to its inherent resilience to debris build-up, VLEO may be particularly suited for defence missions that would need to be maintained operational even after potential sudden debris build up in traditional orbits.

4.3 Challenges

But flying in a VLEO orbit also has some challenges with the main ones being:

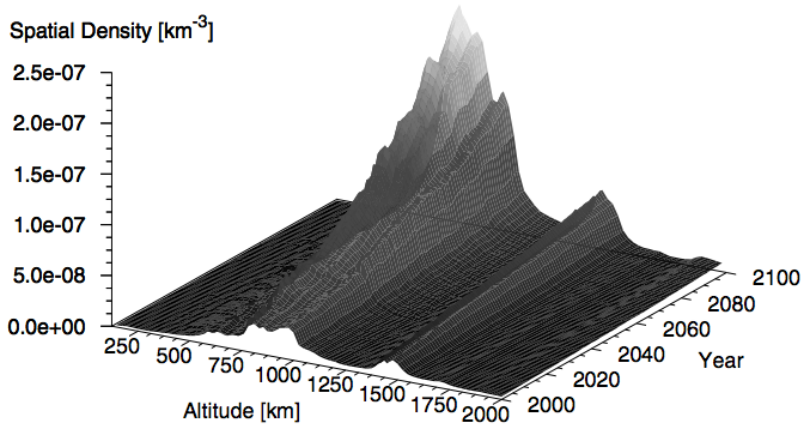

Figure 4.5: Evolution of spatial density altitude profiles in LEO for objects with d > 10 cm, for a business-as-usual scenario, during a 100-year prediction timespan. Extracted from Klinkrad, 2006.

4.3.1 Aerodynamic Forces

Flying through a denser part of the atmosphere increases the aerodynamic forces. Drag is the main aerodynamic force and it mainly makes the spacecraft's orbit decay, hence reducing its lifetime. This is, in general, considered an undesirable effect that needs to be potentially compensated by propulsion to maintain the altitude and hence increase the lifetime.

In order to reduce the propulsion requirements (or completely eliminate them in some cases) the drag has to be reduced. This imposes significant changes to the spacecraft design (slender shapes aligned with the relative velocity are preferred as they have lower drag). Adopting low drag configurations may limit the ability of the spacecraft to change its attitude, as it would loose their lower drag. Also, the aerodynamic torques may also pose a challenge to attitude control orbits. Shaping appropriately the spacecraft can reduce these torques or even use them to stabilise the attitude. Essentially, the aerodynamic forces may introduce significant changes in the spacecraft design. Therefore having a good knowledge of spacecraft aerodynamics is critical to produce good and optimised designs.

As mentioned before, the aerodynamic forces can become an asset at the end of life by passively de-orbiting the spacecraft well within the 25 year guideline and also the aerodynamic forces can be exploited to benefit the mission. The potential to use the aerodynamic forces to benefit the mission is discussed in parts II and III.

4.3.2 Reduced Communication Windows

Operating at a lower altitude reduces the communications windows over a certain ground station (reduces the pass duration; Larson and Wertz, 2005). This means that the ability to downlink data to the ground during the passes over the ground stations is reduced as the altitude decreases. This can become a major design driver for missions that generate a lot of data and may drive VLEO missions to use higher bandwidth com-

munications subsystems. Another alternative is to transmit to a communication relay spacecraft in the geosynchronous belt (commercial service already offered by Inmarsat) in order to increase the communications time (and hence reduced the required bandwidth) and completely eliminate the need of ground stations (bypassing the reduced communications windows limitation).

The stress on communication links is already a reality on current EO missions (given the increasing amount of data being generated) and hence the alternative of transmitting to geosynchronous orbit (GSO) spacecraft relays is already being consider for all types of EO missions. This challenge can be considered that affects all EO missions and that flying in VLEO only makes it worst. Therefore, there is already pressure to solve this challenge.

4.3.3 Atomic Oxygen Erosion

Atomic oxygen is a highly reactive species. Being one of the main atmospheric constituents in the thermosphere can cause concerns on which will be its impact on sensitive surfaces. Atomic oxygen can interact with optical/thermal coatings and sensor surfaces degrading their performance. Special care has then to be taken to account for this degraded performance over time or to select materials that are resistant to atomic oxygen. This can cause some design changes.

4.4 Concepts

At Cranfield University several VLEO mission concepts have been studied during recent years by the students of the MSc of Astronautics and Space Engineering. These studies have been used to identify the benefits and the challenges of the VLEO. Here there is a brief explanation of these projects.

4.4.1 THOR

The THermospheric Orbital Reconnaissance (THOR) (Jové et al., 2012) mission study aimed to demonstrate the commercial viability of a VLEO very high resolution (15cm) ground imaging spacecraft. The mission was required to have a 5 year operational lifetime which was achieved through a slender shaped spacecraft (to minimise drag) and drag-compensating propulsion. To achieve the very high resolution, a TMA on-axis telescope was used. To point to ground targets the telescope was able to rotate inside the spacecraft in the pitch direction, while the spacecraft roll would also roll the telescope. This set-up maintained the spacecraft in minimum drag attitude all the time (the spacecraft had no need to pitch or yaw). The selected orbit was a Sun-synchronous 227 km altitude circular orbit. THOR had electric propulsion to compensate the drag and maintain the altitude. The main challenges of the concept were:

- Drag minimisation and the need of propulsion drove the external configuration.
- Use of a high resolution imaging payload that needs to be shielded from the atomic oxygen. The spacecraft bus acts as a shroud and the imaging payload can move independently inside it, in order to point in the desired direction.

- Communications. The high resolution payload generated massive amounts of data that needed to be downloaded to the ground. In a VLEO orbit the communication windows to the ground are reduced, so a traditional approach required several ground stations to downlink all the data. It was found that a more cost-effective solution was first to transmit to a GSO spacecraft to be later downlinked to the ground (using the GSO spacecraft as a relay).

To help control the attitude of the spacecraft the centre of pressure was behind the centre of mass (aerostability) and also aerodynamics flaps where used. The estimated mission total cost is estimated at 1165.5 M€ including a 22% margin.

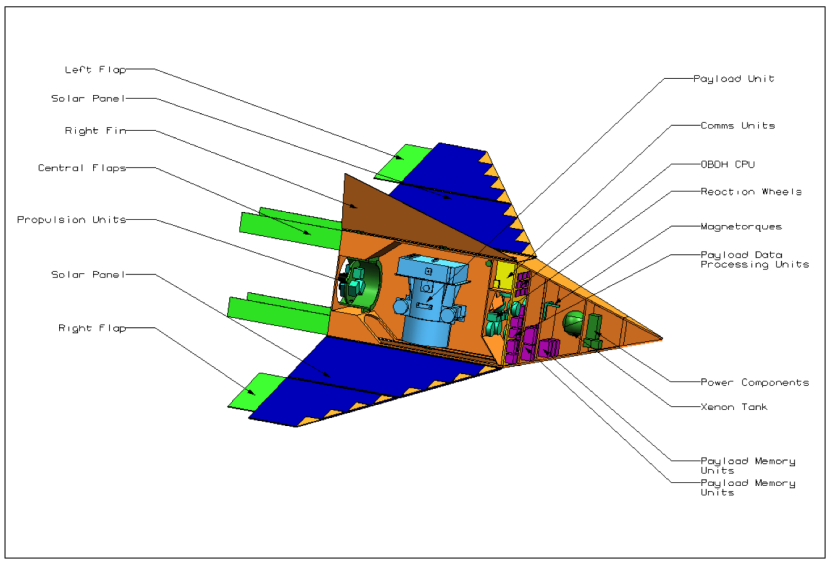

Figure 4.6: Configuration of THOR. Extracted from Jové et al., 2012.

This first mission study showed a possible architecture of a spacecraft if VLEO benefits were exploited to provide very high resolution imagery whilst maintaining a traditional systems engineering approach (monolithic, single spacecraft, 5 year lifetime). Due to the very high resolution it was estimated that the mission would be commercially profitable (although estimation of selling prices of 15 cm imagery was rather a guesswork).

The THOR concept uses the VLEO benefits to increase the capabilities of the mission to a level that would be prohibitory expensive to achieve in traditional high altitude orbits (very wide aperture optics would required). Although it was estimated that this mission would be profitable, it is very difficult that such a concept is to be adopted in the near future.

When the study was finished it was decided that a better route to implement VLEO would be to do it incrementally and not as a step change (as the THOR mission required). Therefore the next study that was perform focused on a concept that could be implemented in the near future and that could be used as a first step into VLEO.

4.4.2 DMC-HD

DMC-HD (Subias et al., 2013) aimed to be a low-cost high-resolution Earth Observation (EO) mission with a near-term implementation (different approach than THOR). While

the typical altitude of current EO missions is 600-700 km, the approach taken in the DMC-HD project was to adapt a commercial platform to fly in VLEO – 300-500 km – but maintaining the same payload, thus increasing its resolution. The chosen platform was the SSTL 300 S1, with a resolution of 1 m in the DMC3 traditional orbit (Davies et al., 2011). The purpose was then to obtain similar data products to GeoEye-1 (0.41 m resolution in panchromatic) using the SSTL 300 S1 platform (doubling its resolution), but at a lower implementation cost to maximise the Return On Investment (ROI). The extra resolution was only a byproduct of lowering the operational altitude. Another goal of the study was to identify the technologies that will enable current spacecraft designs to operate at lower altitudes. The project studied at different altitudes which would be the modifications required and which would be the benefits.

The main challenges when adapting the platform where:

- Propulsion. At the lower altitudes propulsion was required in order to maintain the 5 year target lifetime.
- Flying Configuration. In order to minimise the drag and allocate the propulsion system the flying configuration and operations were modified. Also, some sensors were relocated to cope with the modified flying configuration.
- Expanded solar arrays. To power the propulsion system the solar cells were expanded with deployable solar arrays.
- AOCS. Additional reaction wheels were required to accommodate the extra manoeuvring required when changing the flying configuration.

Instead of producing a unique solution, the study produced 3 different design solutions that had sufficient merit. The resulting designs, shown in Fig. 4.7 have different operating altitudes (hence different resolutions) and different operating configurations. The design that was estimated to be most commercially profitable was the one that was flying lower (315 km). This design was capable of providing panchromatic imagery with a nadir ground sampling distance of 47 cm, a swath width of 11 km, 3 m geospatial position accuracy and with the capacity to collect more than 25,000 km^2/day. The total cost of a constellation of two spacecraft – including development, launch and insurance – ranges from $95 million to $112 million.

DMC-HD also used a traditional approach (monolithic, single spacecraft, 5 year lifetime) but instead of designing a spacecraft from scratch it tried to modify a current design to provide an incremental solution to implement VLEO spacecraft. Its results show that it is possible to adapt a platform but that there are a number of design changes that need to be done.

4.4.3 VLEO SAR

Synthetic Aperture Radar (SAR) missions can also benefit from lowering their operational altitude as shown in Tomas, 2014. This top level study, conducted at Cranfield University, highlights the benefits and challenges that SAR missions face when operating in VLEO. SAR platforms seem well suited to operate in VLEO as they use rectangular and elongated antennas that need to be oriented in the along-track direction. This results in some SAR mission designs already adopting slender configurations

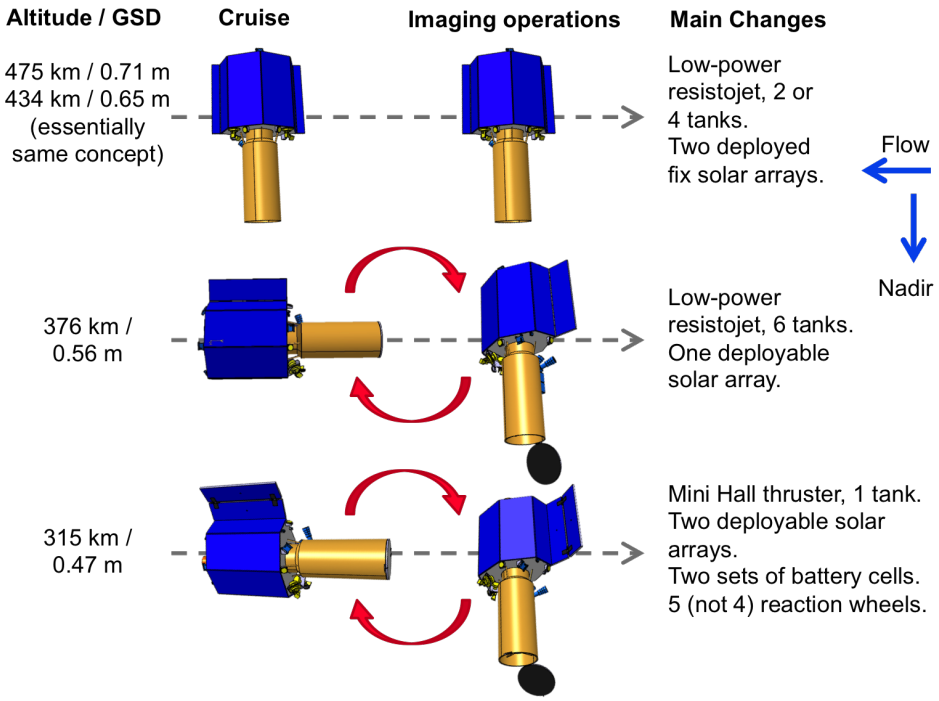

Figure 4.7: Different design adaptations for DMC-HD depending on the altitude. Extracted from Subias et al., 2013.

(such as TerraSAR-X, Tandem-X, Paz and NovaSAR shown in Fig. 4.8) and operating with their long axis aligned with the velocity vector. This seems ideal for VLEO, as this type of configurations already exhibits low drag (due to their low cross-section area) and have an obvious location where to locate any drag compensating propulsion that may be required. Therefore, adapting SAR platforms to operate in VLEO seems a lot simpler than adapting platforms with optical instruments (which have elongated optical systems that need to be pointed towards nadir).

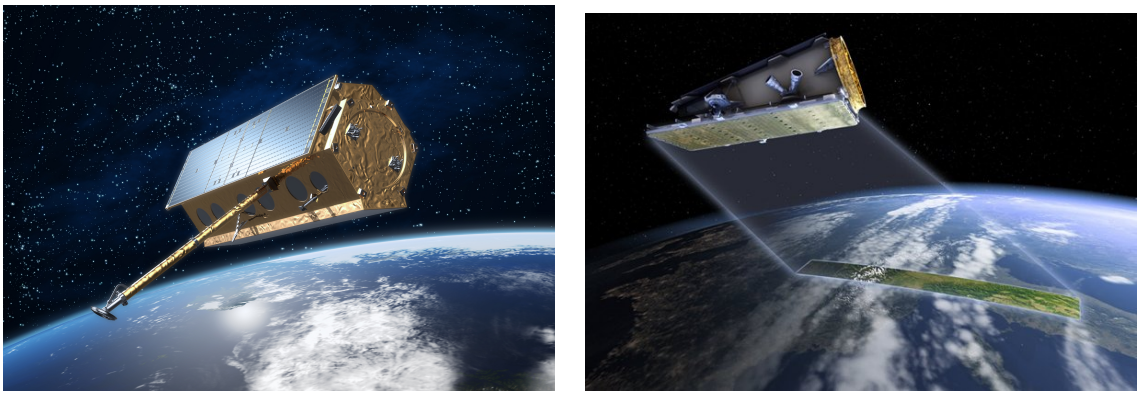

(a) (b)

Figure 4.8: a) TerraSAR-X, Tandem-X and Paz (based on the same platform) and b) NovaSar.

The benefits of lowering the operational altitude of SAR instrument are mainly a

reduction of the antenna area or a reduction of its power (or a combination of both).

The SAR antenna is one of the design drivers of SAR platforms (Aguttes, 2001) and its minimum area is driven by the ambiguity constrains imposed by the minimum and maximum pulse repetition frequency to produce non-ambiguous results. When all the other parameters are maintained constant (operating frequency and signal incidence angle), lowering the operational altitude directly reduces the minimum antenna area that complies with the pulse repetition frequency constrains. The reduction of the minimum antenna area with altitude at different incidence angles is shown in Fig. 4.9.

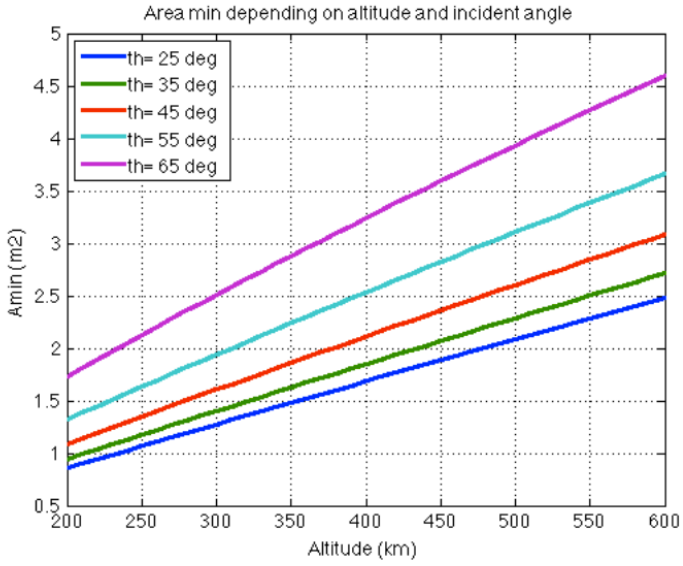

Figure 4.9: Minimum SAR antenna area to produce non-ambiguous results as a function of the altitude and for different incidence angles. Extracted from Tomas, 2014.

The power requirements and cross track resolution can also be improved if the operational altitude is lowered. If the antenna dimensions are maintained constant, then, the power required to achieve a certain cross track resolution can be lowered, or if the power is maintained, then, the resolution can be increased. Also, if the power and resolution are maintained constant, then, the antenna area can be reduced. This trade space is shown in Fig. 4.10. Is then the task of the mission designer to set where in this trade space the design will sit, but it is clear than a reduction of antenna area and power is possible by lowering the operational altitude.

Having a smaller antenna and a lower power requirement can led to smaller, lighter and hence lower cost platforms. The challenges that VLEO SAR platforms face are: increased drag and reduction of the communication windows. Therefore, drag compensating propulsion may be required, as well as extra ground stations. The top level study concludes that VLEO SAR platforms have the potential to be more cost-effective given the identified benefits and challenges. The next step is then to produce a reference design to quantify this competitive advantage.

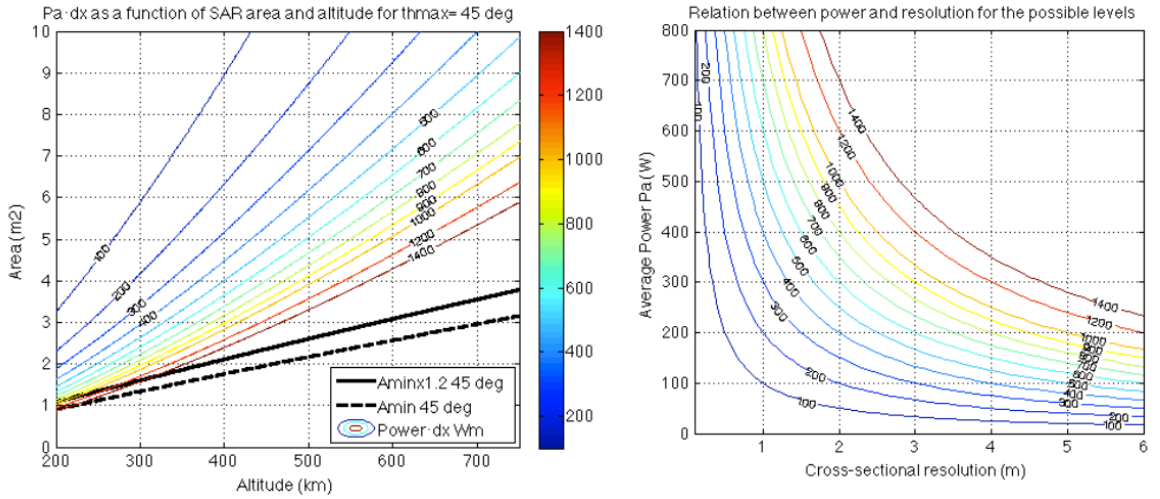

Figure 4.10: The graph in the left shows $Pa \cdot dx$ (where Pa is the power and dx the cross-track resolution) as a function of the antenna area and altitude. Note that the minimum required area A_{min} and area 20% higher than the minimum are also shown. In the right, the relation between the power Pa and resolution dx for the different $Pa \cdot dx$ levels is shown. Extracted from Tomas, 2014.

4.4.4 Responsive Architecture

All the VLEO concepts studied so far use the traditional system engineering approach of using monolithic, single spacecraft and with the usual 5 year operational lifetime target. This results in the drag and the short lifetimes associated with drag being perceived as a negative consequence of VLEO. There is another approach that in VLEO may be more suitable. The approach presented here embraces responsiveness to potentially produce more cost-effective EO systems. This novel approach has not been studied in detail and that is left for future work.

The traditional approach of deploying space systems has been using monolithic spacecraft that host multiple or very large payloads. EO space systems have been no exception. Having a requirements-centred spacecraft design paradigm in conjunction with a minimum-cost acquisition mindset has led system architects and decision-makers to reach the conclusion that the answer to increase cost-effectiveness is greater capability and/or increased lifetimes (Saleh, 2008; Brown and Eremenko, 2006). This has promoted the use of multi-payload, multi-functional and longer lifetime monolithic spacecraft. This in its turn has increased the requirements imposed on the system, increasing the complexity and the size of the spacecraft. The development time, difficulty of integration, testing and launch also increase accordingly (this can be seen in the THOR design). As a consequence of this approach, the cost of the spacecraft increases (cost-complexity death spiral) and its responsiveness decreases defeating any cost saving derived from the longer lifetime or greater capability.

ENVISAT (Dubock et al., 2001) is good example of this monolithic spacecraft approach. ENVISAT carried 9 different instruments, had a launch mass of more than 8 tons, had a total cost of 2.3 billion Euros and its development lasted more than 10 years.

Monolithic architectures are vulnerable to technological changes (not upgradable), launch failure (loss of mission if launch vehicle fails), to demand volatility, and requirements and funding uncertainty (difficult to scale their capabilities up or down during design or during operations).

Fractionated architectures emerge in response to the pitfalls and limitations of the monolithic approach. In fractionated system several smaller and simpler spacecraft deliver the same capability as a big and complex monolithic spacecraft. Fractionated systems have the ability to be more responsive and hence more cost-effective. In addition, given the distributed nature of the system they can offer unique advantages to EO systems.

In a fractionated architecture, each spacecraft can carry only one sensor (single payload), and there can be several spacecraft with the same payload and also other spacecraft with different payloads (heterogenous composition). Flying each type of payload on different spacecraft avoids imposing the most stringent requirements of all the payloads to the whole spacecraft (making it simpler to deal with requirement uncertainty).

These spacecraft can then operate in a number of different physical configurations that provide different advantages. Constellations can be used to increase the coverage and reduce revisit times although some degree of orbit control is required. Swarms goal is to achieve the same but without any orbit control, hence requiring a higher number of spacecraft. Clusters are spacecraft flying together without their relative positions being controlled. Spacecraft in clusters observe the same area and hence can be used for multi-payload (multi-spacecraft) observations of the same target. Formations are clusters where the relative positions are tightly controlled.

Sufficiently populated swarms and constellations can significantly increase the amount of instantaneous coverage provided by the system. Global coverage can be achieved when constellations are in excess of $\sim$30 (at 600 km) (Beste, 1978). At lower altitudes the number of spacecraft grow significantly and if more restrictions (i.e. no more than 20^{o} off looking angle) are applied, the number of spacecraft required can easily raise up to the thousands (Bouwmeester et al., 2011).

Clusters and formations of homogenous spacecraft can be used to augment the capabilities of the payloads (e.g. combining the images of a cluster of optical telescopes, digital elevation maps can be immediately generated or image noise can be drastically reduced). Tight formation flight can enable multiple spacecraft act as a single sensor by producing a synthetic aperture (a SAR could be envisioned where one of the spacecraft emits a radar pulse and several others receive the pulse in different locations, thus creating a synthetic aperture much larger than their individual ones for example). Feasibly synthesising apertures has only been done for radar in space. Combining constellation/swarms of cluster/formations the benefits of both configurations types can be obtained.

Fractionated architecture responsiveness is also major asset of this approach. Systems can be deployed incrementally both in spacecraft numbers (mitigating the risk associated with launch vehicle failure) and in capability (smaller capability set at the start). This allows the system to scale up and down and cope with demand and funding fluctuations.

The incremental deployment approach also allows to replace failed spacecraft (note

that graceful degradation is another benefit of fractionated systems), or just launch more capable versions (with updated technology) or spacecraft with different payload types (offering a wider capability range). This replace and upgrade mindset requires a much shorter spacecraft operational lifetime compared to monolithic spacecraft, hence lifting some of the requirements associated with assured performance over a long lifetime (e.g. redundancy, rad-hard components, etc). Manufacturing a bigger number of spacecraft can also produce savings, due to economies of scale. Financial stress during development can also be reduced as delivering the capability incrementally does not require a long initial development period (revenues are generated sooner).

For all the described benefits, fractionated architectures have the potential to revolutionise EO space systems. There are already some proposals such as TechSat21 (Martin et al., 2001) that use fractionated architectures for EO (see Fig. 4.11). Also the recently launched PlanetLabs Inc. constellation of imaging CubeSat uses most of the fractionated architecture concepts.

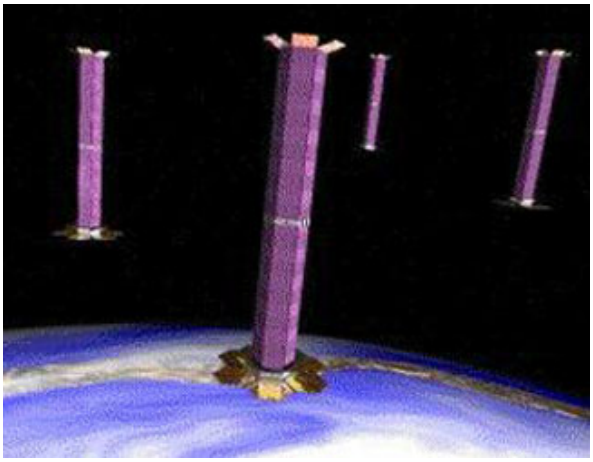

Figure 4.11: TechSat21 artist render.

Flying in VLEO can round-up the benefits of responsive systems. First, the benefits to EO that VLEO provides mean that smaller spacecraft can be flown which have the same capabilities of bigger spacecraft that fly at a higher altitude.

The increased drag at VLEO can also be used to intentionally limit their lifetime. Inherently short lifetimes (enforced by the atmospheric drag) reduce the number of potential debris. So there will be no problem if hundreds or thousands of spacecraft are launched in VLEO, they will all decay in a short time. The short lifetime can be seen as an opportunity to reduce the risk averse attitude (increase innovation) and also to replace the spacecraft more frequently, hence having and incremental approach when building capability (launching first a minimum viable spacecraft and then incrementally increase the capabilities of their replacements) and fixing problems found in previous spacecraft generations (fixing faults). Forcing to replace spacecraft frequently also drives the production numbers up, lowering the production costs (economies of scale) and development cost per unit.

Aerodynamic drag can also be used to control the spacecraft's orbit and hence maintain constellations and clusters.

Although the technical benefits of fractionated architectures using responsive VLEO

systems are clear, the benefits for different Earth Observation usage domains (such as land monitoring, atmospheric measurements, water quality, maritime surveillance, emergency management, security) have still to be quantified. Also, mission concepts that can achieve these benefits still need to be proposed and some technological challenges addressed before these missions can take place. The main technological challenges that need to be addressed are: constellation/swarm/cluster/formation control using aerodynamic forces, precision pointing, inter-satellite links, synchronisation between spacecraft, high-speed downlink, ground station networks, command and control for such large number of spacecraft and data processing of large quantities of distributed space based data.

Finally, the economic viability of these concepts has also to be proven, given current EO demand forecasts, legal framework and launch opportunity prospects.

4.5 Conclusions and Future Work

The benefits and challenges of VLEO spacecraft have been identified. Initial analysis suggest that these missions can provide significant benefits with only modest modification of current platforms. There is still some unsolved challenges that need to be addressed before these missions can be implemented by commercial operators. The issues to be resolved are:

- Quantify the impact of the identified benefits to different Earth Observation usage domains (such as land monitoring, atmospheric measurements, water quality, maritime surveillance, emergency management, security). There are EO domains where VLEO platforms will be more suitable than others. Identifying those can provide reference mission applications that can prove useful when developing future concepts.

- Increase the knowledge of drag modelling to design spacecraft with lower drag. Increasing the drag modelling capabilities can also let to more accurate drag predictions that can remove unnecessary margins. Drag is one of the biggest design drivers in VLEO missions, understanding drag (and how to reduced it) will directly translate in more competitive spacecraft.

- Develop and test aerostability systems to understand their dynamics and to make them more effective and efficient. Aerostability is a property that VLEO spacecraft must have. Not having an aerostable spacecraft means that the attitude control system will be always fighting against the aerodynamic torques, hence increasing the mass, power and cost of these attitude control systems. Also in the event of loss of attitude control, an aerostable spacecraft can maintain an attitude with low drag (like flying aligned with the flow in a slenderly shaped spacecraft). If the spacecraft is not aerostable and it starts tumbling the drag and the decay rate can increase significantly, potentially making it re-enter or reducing the altitude considerably hence wasting the fuel required to rise the altitude afterwards (if the altitude reduction is severe the electrical propulsion system may not be able to rise the spacecraft altitude).

- Develop and test drag compensation systems to ensure that the spacecraft can maintain its altitude successfully. This includes drag estimation techniques and electric propulsion systems. If a fixed altitude need to be maintained then drag-compensation would be required. Maintaining the altitude within a certain range is not equivalent to a drag-free control system. This altitude control systems are expected to be much easier to develop and implement than drag-free control systems (such as the one in GOCE).

- Test the compatibility of the imaging operations with the drag compensation operations. The need to maintain a low drag can limit the attitude range of a VLEO spacecraft. The aerodynamic torques that appear when moving from a nominal attitude (neutral attitude of an aerostable spacecraft) can also present operational challenges. The need of sensors and instruments to be pointed to their targets clashes with the need to maintain a fixed attitude to minimise aerodynamic drag and torques. Operational procedures, spacecraft shapes and attitude control systems need to be design so they can operate in a VLEO environment as part of the same coherent system.

- Develop business cases that prove that the VLEO platforms are economically viable. The benefits of VLEO can produce more cost-effective EO systems. But this has yet to be proved.

Part II

ΔDsat, a QB50 CubeSat Mission to Study Rarefied-Gas Drag Modelling.

Chapter 5

Introduction

The initial research into VLEO concepts (see section 4.4 on page 53) soon led to the conclusion that the aerodynamic forces are a major design driver in these type of missions. Trying to reduce the drag forces experienced by the spacecraft can be accomplished by having a low cross section area (which lets to slender shapes). Also, drag-compensating propulsion can help mitigate the negative effects of drag. In addition, the literature review on spacecraft aerodynamics (see chapter 3) revealed that not a lot is known on rarefied-gas aerodynamics and that more on-orbit experiments are required in order to advance the knowledge in the field (Moe and Moe, 2010). The insights that drag is major design driver for VLEO and that there is a lack of knowledge on rarefied-gas aerodynamics, led to the design of a space mission that would study rarefied-gas aerodynamics in order to produce data that could be useful when designing new VLEO missions. This mission became known as ΔDsat.

At the time that this mission concept was being created, the QB50 mission was also starting and it was looking for participating teams. QB50 is a collaborative mission (50 CubeSats) with the science objective to study the thermosphere (Muylaert et al., 2009). This objective goes very well with the goal of studying spacecraft aerodynamics, and it soon was explored how ΔDsat could benefit from being part of QB50. It was quickly realised, that the benefits provided by the study of the thermosphere could be very useful when studying spacecraft aerodynamics (useful synergies). Therefore, a ΔDsat concept, adapted to be part of QB50, was proposed and later accepted into the QB50 mission. Flying ΔDsat as part of QB50 was done with the goal to exploit the synergies that appear when studying the thermosphere and rarefied-gas aerodynamics together. Being part of QB50 imposed several requirements to the ΔDsat mission, with the most prominent ones being that ΔDsat was to adopt the CubeSat form factor and that ΔDsat would host a QB50 payload.

As the design of the mission progressed it became clear that the ΔDsat design capabilities gave the opportunity to perform other scientific and technology demonstration experiments (as opportunistic science). So the scope of ΔDsat mission objectives was quickly broadened to accommodate: demonstration of aerostability, demonstration of aerodynamic orbit control and measuring thermospheric wind.

This part contains a detailed description of ΔDsat and its scientific objectives.

In this chapter, the final mission statement and objectives of the mission are presented. Also a structure of this part follows later. It is important to note at this point

that ΔDsat is a live project and hence the information contained here will become out of date almost immediately after the publication of this dissertation. Hence, the information here contained is a snapshot of the status of the project as of September 2014, and more up to date information can be requested to the Principal Investigator of the mission Dr. Peter Roberts or the author of this dissertation.

The author has been deeply involved in the development of the ΔDsat mission. The author has developed the science case and has analysed the mission's performance in terms of science capabilities and output. In addition, the author has also helped supervise (role shared with the principal investigator) and contributed (role shared with MSc students) into the development of the CubeSat platform.

5.1 Mission Statement

The final mission statement of the ΔDsat CubeSat mission is:

ΔDsat is a QB50 CubeSat dedicated to study rarefied-gas aerodynamics, to measure thermosphere wind and to demonstrate aerodynamic attitude and orbit control.

5.2 Objectives

The final science (SO - Science objectives) and technology demonstrations (TD - Technology Demonstration) of the ΔDsat CubeSat mission are:

SO-0 Support the hosted QB50 payload. This science objective is included for completeness and the requirements imposed by this science objective and its success criteria are defined by the QB50 consortium. The QB50 hosted payload will perform in-situ measurements of some properties of the thermosphere.

SO-1 Perform differential aerodynamic coefficient measurements of different surface materials/treatments at different incidence angles.

- **SO-1.1** Perform differential drag coefficient measurements of test surfaces, with different surface properties and at different incidence angles with an error lower than 5% (with 90% confidence) at 350 km altitude or lower. Success criteria: Performing at least 25 differential drag measurements, which include measurements of different surface properties at the same incidence angle at the same and at different altitudes, and measurements with the same material at different incidence angles and at the same and at different altitudes.

SO-2 Measure thermospheric wind.

- **SO-2.1** Measure thermosphere wind at different locations and altitudes with an error of less than 15 m/s (3σ) with sufficient spatial frequency to capture the spatial structure of the thermosphere wind. Success criteria: Performing at

least continuous wind measurements during 20 consecutive orbits (to provide global coverage).

TD-1 Demonstrate the ability to control the attitude using aerodynamic torques.

TD-1.1 ΔDsat shall be able to detumble into a flow pointing attitude making use of its aerodynamic properties only. Success criteria: ΔDsat shall be able to recover from tip-off rates of up to 10°/sec within 2 days at a maximum altitude of 380 km[1].

TD-1.2 - Demonstrate aerostability. ΔDsat attitude can be stabilised using aerodynamic torques with or without the help from a damping system. Success criteria: During the aerostability demonstration period, the pitch and yaw of ΔDsat should be less than $\pm 10^\circ$ (3σ) with respect to the inertial velocity. ΔDsat should demonstrate aerostability for at least two consecutive orbits.

TD-2 Demonstrate the ability to control the orbit using aerodynamic forces.

TD-2.1 Make the CubeSat re-enter (with the re-entry considered to occur at 100 km altitude) over a pre-specified circular area centred around a pre-specified location (Cranfield Ground Station) with a 300 km radius 3σ. Success criteria: Getting confirmation that the spacecraft re-enters over the allowed area. This confirmation can come from the spacecraft transmitting its position prior to re-entry (that is why the re-entry are is centred around the Cranfield Ground Station).

Note that the success criteria are set in order to define when a scientific objective has been achieved. As most of these objectives are performed as opportunistic science, the success criteria are defined based on conservative estimates of what the mission can actually achieve. Changes in the design can alter the capabilities of the spacecraft and hence the scientific objectives and technology demonstrations need to be continuously revisited, to ensure that they can be met. If they are not met then the design needs to change and if the design changes are too complex or impractical then the missions objectives need to be modified or dropped to accommodate the CubeSat capabilities.

5.3 Structure of this Part

This part provides a description of the ΔDsat mission and the methods used to achieve its objectives. To cover this content, this part structure follows the order that was followed to define the mission. In the first chapter of this part (chapter 6), the QB50 mission is covered providing an overview of its science objective and the requirements that this objective impose on ΔDsat. Then, in chapter 7, a description of the study of rarefied-gas aerodynamics that ΔDsat performs follows. At this stage the main

[1]This technology demonstrator is included for completeness although the author has not been involved in its development and hence it is outside the scope of this dissertation. The Cranfield PhD student Zhou Hao has been tasked to develop the methods to achieve this technology demonstration.

properties of the mission have been laid out and therefore, the other opportunistic science and technology demonstrations follow (except TD-1.1 see foot note 1).

The presentation of these other objectives starts with aerostability (chapter 8), which is a direct requirement of the method used to accomplish rarefied-gas aerodynamics objective. The wind measurement, which is a scientific objective enabled by the CubeSat's aerostability properties is presented in chapter 9. Then, the orbit control is outlined in chapter 10 as the main description of this method is extensively discussed in chapter 15 in part III.

This part then concludes with a brief description of the CubeSat design in chapter 11 and with conclusions and recommendation for future work in chapter 12.

Chapter 6

QB50

QB50 has the scientific objective to study the lower thermosphere (90-350 km) by taking in-situ measurements of a number of key constituents and atmospheric parameters. These measurements will be taken by a network of 40 double CubeSats, separated by a few hundred kilometres and carrying identical sensors, giving, spatial and temporal resolution to their measurements. The multi-point, in-situ measurements of QB50 will be complementary to the remote-sensing observations by the instruments on Earth observation satellites and the remote-sensing observations from the ground with lidars and radars. All atmospheric models, and ultimately thousands of users of these models, will benefit from the measurements obtained by QB50 in the lower thermosphere. QB50 will also host 10 extra triple technology demonstration CubeSats. Hence raising the total number of CubeSats to 50 (thus the name QB50).

QB50 is partially funded by the European Commission through the FP7 programme. To make the mission financially viable, university teams are encouraged to take part of the project by developing one of the QB50 CubeSats. The teams will have to carry the cost of developing their CubeSat and make a launch contribution of 20k€ (for the double CubeSats). QB50 will provide the custom-designed dispenser system, the standardised sensors for atmospheric research, the launch services and interfaces to the launch vehicle authorities, environmental testing (if requested), and transport of the 50 CubeSats to the launch site.

Although the final orbit has not been officially confirmed, all CubeSats will be launched into a circular orbit at about 380 km altitude, 96º inclination, by a Ukrainian Cyclon 4 (Alcantara Cyclone Space Binational Company, 2010) from Alcântara in Brazil. Due to atmospheric drag, the orbits of the CubeSats will decay and progressively lower and lower layers of the thermosphere will be explored, without the need for on-board propulsion. The CubeSats will operate until re-entry occurs at around 90 km. The low initial orbital altitude reduces the mission lifetime of the individual CubeSats which will be about 3-7 months (depending on the CubeSat ballistic coefficient). The launch is expected to be on the 1Q of 2016 (although delays can be expected).

The standard form factor of QB50 spacecraft is a 2 unit CubeSat with the standard sensors taking nearly half a CubeSat unit (the science unit). The remaining space left will be dedicated to the bus (functional unit). Participating CubeSat teams are free to use any space left in the 'functional' unit of the double CubeSat for a technology package or a sensor of their own choice. The teams are expected to supply the required

documentation in a timely manner, participate in the major project reviews, support the environmental test campaign (but not the launch campaign), operate their CubeSat when in orbit and provide their science data and limited housekeeping data to the QB50 Data Processing and Archiving Centre.

QB50 is lead by the Von Karman Institute in Belgium, and more official and up to date information can be found on https://www.qb50.eu/.

6.1 Why Study the Thermosphere?

The lower thermosphere is a complex region that represents the transition between the well-mixed lower atmosphere and the heterogeneous upper thermosphere. It is also the region where Space Weather effects couple to the meteorology of the middle and lower atmosphere. At auroral latitudes, the lower thermosphere (via the E-region ionosphere) is also the region where the strongest coupling between the neutral atmosphere and the charged ionosphere (linked to the magnetosphere) occurs. The transport, chemistry and photochemistry occurring in the lower thermosphere can affect the middle atmosphere, especially its chemistry. For example, the nitric oxide formed in the lower thermosphere can be transported downwards and equatorwards into the middle atmosphere where it destroys ozone (Dobbin et al., 2006). However, the lower thermosphere is poorly observed since it is too high for balloons or lidar, but too low for satellites (Muylaert et al., 2009). In situ rocket measurements are few and last only minutes. Radar measurements using incoherent scatter radars (such as EISCAT) give limited spatial coverage, and radars track ion trails only between 90-120 km altitude (Mitchell et al., 2002). The TIMED and UARS satellites have provided remote sounding measurements for low- and mid-latitudes over several years of temperatures and wind between 60-250 km altitude (Zhang and Paxton, 2011; Shepherd et al., 2012). These satellites have provided valuable climatology data used by Global Circulation Models (GCMs) to study large-scale features such as tidal forcing (McLandress et al., 1994). The QB50 mission will provide the first ever multi-site in situ measurements of the lower thermosphere which could revolutionise model simulations.

6.2 Sensor Sets

QB50 shortlisted 3 sensor sets (Smith, 2012) to be flown in QB50 and has let the teams decide which of the three sensor sets they want to fly. The three sensors sets are briefly described here. More detailed information on the sensor sets, their operations and their requirements can be found in their Interface Control Documents (Chaudery, 2013; Roßmans, 2014; Bekkeng, 2013).

6.2.1 INMS - Ion and Neutral Mass Spectrometer (Chosen set)

The INMS is a miniaturised analyser designed for sampling low mass ionised and neutral particles in the spacecraft ram direction with the instrument resolution optimised for resolving the major constituents in the lower thermosphere, i.e., O, O2, N2. It therefore provides measurements of the atmosphere density and composition.

The key sensor components (shown in Fig. 6.1) consist of a collimator/ion filter, an ioniser and a charged particle spectrometer. Particles enter the aperture into the ion filter region where charged particles can be rejected. This is followed by a series of baffles for collimation and further charged particle suppression. Collimated neutral particles are subsequently ionised in the ionizer by a 50 eV electron beam followed by mass selection in the analyser. With an energy resolution of 3%, the analyser will provide clean separation of the major constituents. The spectrometer can be operated in different modes, optimised for ions (not activating the ion filter or the ionizer) or for neutral particle analysis. Its mechanical interface is shown in Fig. 6.2.

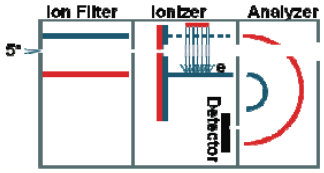

Figure 6.1: Schematic of key INMS sensor components. Extracted from Smith, 2012.

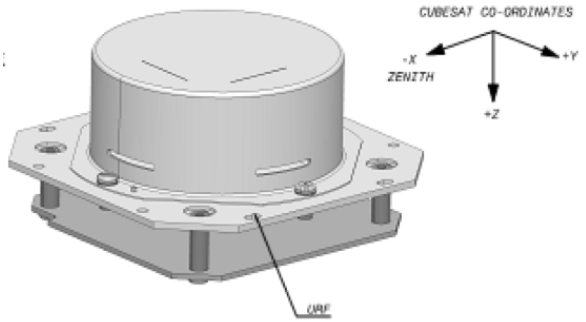

(a)

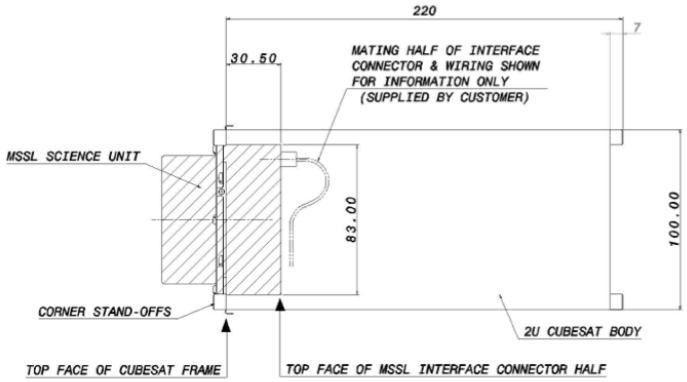

(b)

Figure 6.2: Mechanical design of the INMS a) and its location in the CubeSat b). Extracted from Chaudery, 2013.

In addition to the INMS, 4 thermistor are housed in the CubeSat in order to measure

the temperatures of the side panels of the spacecraft. The INMS is developed by the Mullard Space Science Laboratory from University College London in the UK.

It is worth mentioning at this point that the INMS is the instrument selected for ΔDsat. The density and composition measurements provided by this instruments can greatly benefit the rarefied-gas aerodynamic experiments. More information on the benefits provided by the INMS to the rarefied-gas aerodynamics can be found in chapter 7 on page 75.

6.2.2 FIPEx - Flux-Φ-Probe-Experiment

FIPEx is able to distinguish and measure the time-resolved behaviour of atomic and molecular oxygen as a key parameter of the lower thermosphere. Atomic oxygen is the dominant species in the thermosphere region (see chapter 2 on page 19) and therefore, its measurement is crucial in the validation of atmosphere models. Moreover, erosion of spacecraft surfaces due to interaction with atomic oxygen is a serious concern and merits in-situ study in its own right. The measurement is based on solid oxide electrolyte micro-sensors. The working principle of the developed oxygen sensors as shown in Fig. 6.3 is based on the ion conductivity of ceramic materials (Hammer et al., 2009). Figure 6.3 also shows the engineering model of the sensor. The FIPEx is develop by TU Dresden in Germany.

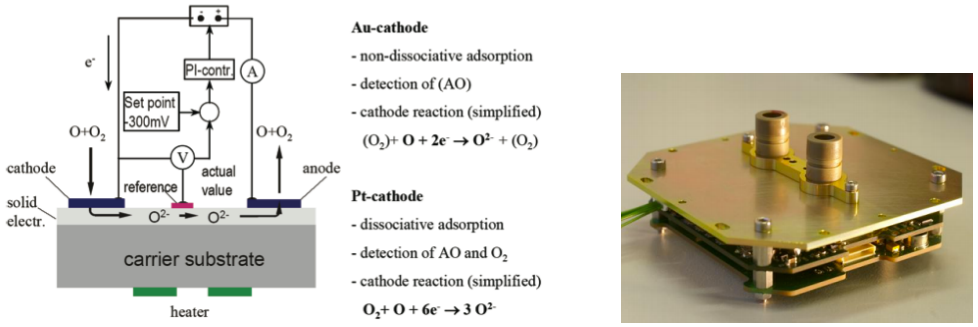

(a) (b)

Figure 6.3: FIPEX schematics(Smith, 2012) a) and FIPEX engineering model b). Extracted from Roßmans, 2014 and Smith, 2012.

6.2.3 mNLP - Multi-Needle Langmuir Probe

The mNLP can provide absolute electron density measurements at ∼1 m spatial resolution for a 320 km orbit, and thereby map regions of F-region plasma turbulence of particular relevance for communication and GNSS signals in polar and equatorial regions. A Langmuir probe will also provide an absolute measurement of plasma density and so provide a means of cross-calibration for the Ion and Neutral Mass Spectrometer (INMS). Figure 6.4 shows the instrument mechanical configuration. The mNLP is developed by the University of Oslo in Norway.

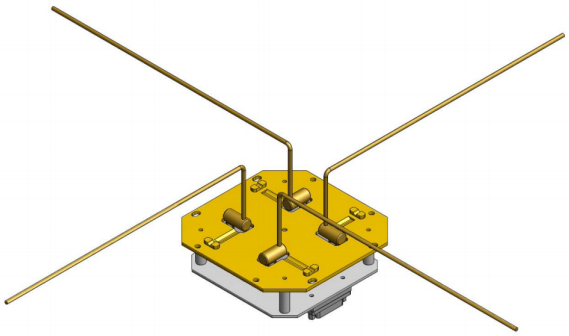

Figure 6.4: mNLP mechanical configuration (Smith, 2012).

6.3 Driving Requirements

As ΔDsat is a QB50 CubeSat, it has to be compliant with the QB50 requirements. The requirements are split into the generic ones (Masutti, 2014) and instrument specific (Chaudery, 2013) (in this case the ones imposed by INMS). Here the generic and INMS specific driving requirements are highlighted:

- Mass limit of 2 kg. The total mass of the CubeSat is limited to 2kg and that does not leave nearly any spare mass for any additional payloads. Reference designs from CubeSat subsystem vendors such as GomSpace (GomSpace, 2012) and ISIS (ISIS, 2012), already surpass this limit only supporting the QB50 science payload. ΔDsat uses COTS components whenever possible and needs to support an additional payload in order to achieve its specific scientific objectives. A waiver was obtained during Critical Design Review to increase the maximum allowable mass of ΔDsat CubeSat to 2.4 kg.

- 9mm extended volumes. The distance between the sides of the CubeSat and the dispenser walls is of only 9 mm. This gap is the only volume available for deployables (stowed). ΔDsat's payload used to support its specific scientific objectives is a deployable and hence it had to fit into this extended volume when stowed. This requirement was a design driver for ΔDsat's payload.

- Attitude knowledge of $\pm 2^{o}$ and attitude control $\pm 10^{o}$. The INMS requires the CubeSat to point to the flow and also have a quite accurate attitude knowledge (for CubeSat standards). At the beginning, this was quite a design driver, specially the attitude knowledge if low cost COTS equipment was to be used. This requirement was later superseded with a more stringent one from the wind measurement method that required the use of more accurate and considerably more expensive attitude determination sensors.

Another driving aspect imposed by QB50 is that the initial orbit inclination is not completely Sun-synchronous, hence the Mean Local Time of the Ascending Node (MLTAN) will drift during the duration of the mission. In addition, the launch MLTAN is still uncertain. This imposed the requirement to the CubeSat to be able to operate at a wide range of MLTAN, which drove the design of the configuration (location of solar cells, GPS antenna and sun sensors for example).

Chapter 7

Studying Rarefied-Gas Aerodynamics

Being able to accurately predict drag and to understand its principles is important for different space applications. In missions that fly at the edge of the atmosphere, such as GOCE (Drinkwater et al., 2007), the drag generated has to be compensated or the spacecraft will re-enter within a fraction of their operational lifetime. In this type of mission it is important to be able to accurately predict drag, as this will lower the propulsion subsystem margins (more optimised design). At the same time, a good understanding of how drag is created can help to design minimum drag spacecraft, and hence lower the propulsion requirements, or allow flight at even lower altitudes.

Another application where a good understanding of drag is critical is in drag-enhancing devices for end-of-life de-orbit. In the case of drag-sails for example, the sizing of the sail can be reduced if the drag per unit of surface is maximised or if more accurate drag prediction techniques are available (as unnecessary margins will be removed). This again, can lead to more cost-efficient and competitive drag-sails.

In the LEO regime the Knudsen number ($K_n = \frac{\lambda}{l_{ref}}$), which is the ratio between the gas particles mean free path and a spacecraft representative length is usually much greater than 1 (see Fig. 3.1 on page 35). From this, it can be assumed that the interactions between gas particles (collisions) are very rare, and hence they can be ignored. When this condition is met, the flow is considered to be a free molecular flow (Bird, 1994), and then the aerodynamic forces are dominated by the gas-surface interactions (GSI).

There exist several GSI models, with the most popular being the Sentman model (Sentman, 1961) and the Schamberg model (Schamberg, 1959). Both of them have been derived making certain assumptions on how the gas particles interact with the surface. Also, in both cases, the calculation of the forces depend on several surface and gas dependant parameters not known *a priori* and that have to be determined experimentally. For example, in the Sentman model an energy accommodation coefficient σ_a is introduced. This coefficient captures the amount of energy transferred from the gas particle to the surface when the gas particle collides with the surface. When $\sigma_a = 1$ the particles transfer all their energy to the surface and they are reemitted in thermal equilibrium with the surface, and when $\sigma_a = 0$ the particles do not transfer any energy to the surface and hence they behave as if being reflected.

These model parameters, far from being constant, are found to be dependant on (Moe et al., 1998): surface roughness, surface molecular composition and lattice con-

figuration, surface cleanliness (atomic oxygen adsorption), surface temperature and incident gas particles molecular composition, velocity and angle. Some of these parameters are given by the environment (as the incident gas particles composition and velocity), but the others can be engineered to reduce/increase the drag (to engineer the aerodynamic properties of the spacecraft).

Setting the values of the model parameters is currently based on data from past in-orbit missions, as ground facilities are unable to recreate the orbital environment (Moe and Moe, 2005). Unfortunately, there has not been any mission specifically designed to study GSI. Therefore, the parameters are set using the very limited set of missions that have been able to provide some limited insight on how the different parameters change with the different environment or surface properties. Little is known, for example, on how the flow incidence angle, the surface material or the surface roughness affects drag. More background information on spacecraft aerodynamics can be found in chapter 3 on page 33.

ΔDsat is a QB50 CubeSat mission dedicated to study rarefied-gas drag modelling. The mission has been designed from the ground up to study GSI and will provide experimental data that will help to quantify the models experimental parameters and will provide insights on how aerodynamic forces are generated. Being part of the QB50 constellation offers the possibility to fly an atmospheric sensor suite that will take in-situ measurements of several atmospheric properties (Muylaert et al., 2009). This information, combined with the data of the other QB50 CubeSats and the planned remote-sensing observations by the instruments on Earth observation satellites and the in-situ measurements by ground based instruments (such as radars and lidars), will provide unprecedented information of the atmospheric environment the spacecraft is flying through.

ΔDsat is designed to study, specifically, how the flow incidence angle, the surface material or the surface roughness affects drag. This will provide useful information that can help to minimise or maximise drag. For example, knowing how the incidence angle affects drag will help designing minimum drag geometries. Also, knowing which materials or surface treatments produce more/less drag, will help to design more effective drag sails or reduce even further the drag on spacecraft that operate at very low altitudes.

The CubeSat is named ΔDsat because the mission extracts its results by measuring the differential (Δ) drag (D) produced when different surfaces with different properties are exposed to the flow. This differential procedure compares the drag coefficients of these different surfaces, with different surface properties, through the ratios of drag coefficients $\frac{C_{d1}}{C_{d2}}$. Therefore, the results will be how much more/less drag a certain combination of surface properties and incidence angle produces with respect to another combination. A differential approach is used in order to minimise any biases or systematic errors in the measurement chain.

7.1 Scientific Objective

ΔDsat scientific objective SO-1 of studying rarefied-gas aerodynamics has been stated in section 5.2. The aim is to provide high fidelity data to validate current GSI models, but also to improve in the understanding of the mechanisms that create drag. If the

differential approach is taken into account, this primary scientific objectives for the mission can be also rephrased as:

- To measure drag coefficient ratios $\frac{C_{d1}}{C_{d2}}$ with a uncertainty level below 5% given a 90% confidence.

This capability will then be used to:

- Determine the effect of the flow incidence angle on the drag coefficient.
- Determine the effect of the surface roughness on the drag coefficient.
- Determine the effect of the surface material on the drag coefficient.

The resolution of 5% on the drag coefficient ratio is based on the expected differences that flow incidence angle and surface roughness and material can produce (Moe and Moe, 2010).

Note that the experiment focuses on drag instead of lift. As can be seen in Fig. 3.6 on page 41, drag is much easier to create than lift and hence it is also easier to measure. Studying the mechanisms that create drag and how different parameters influence it, will have also benefits when estimating drag, as the creation mechanisms (adsorption, energy transfer, reemission) are the same from both forces. Also, it can be argued that drag is a more predominant force and that is a driver for VLEO designs (see chapter 4 on page 45), whereas lift is not.

7.2 Methodology

Being part of QB50 means that ΔDsat is a 2 unit CubeSat with roughly half a unit carrying the QB50 sensor suite. The sensor provided by QB50 is an Ion and Neutral Mass Spectrometer (INMS) that is capable of measuring the total atmospheric density and the atmospheric composition (Smith, 2012). This sensor requires the CubeSat to fly aligned with the local flow direction, with the unit containing the sensor unit facing forward. Then, to achieve ΔDsat's specific objectives, the CubeSat is equipped with a set of 4 Steerable Fins that deploy at the beginning of the mission. The Steerable Fins consist of 4 foldable fins, each one deploying from each long side of the CubeSat. Once deployed the fins are located towards the rear of the CubeSat and stay parallel to the flow, as can be seen in Fig. 7.1a. This configuration is known as the minimum drag configuration.

The Steerable Fins have the ability to rotate (around their long axis) independently from each other and hence expose their surfaces to the flow at different incidence angles (that is why they are called steerable). To avoid creating undesirable aerodynamic torques, 2 fins are rotated at a time (i.e. the upper and lower fins). The two fins that rotate together have the option of co-rotating (rotating both in the same direction) or counter-rotation (rotating in opposite directions). If the fins co-rotate, the fins will produce lift, causing a torque (in pitch or yaw) and making ΔDsat fly at an angle with respect to the flow. The definition of the rotation angles is the same than in aircraft and it is shown in Fig. 7.1b. If the panels counter-rotate the same lift will create a roll

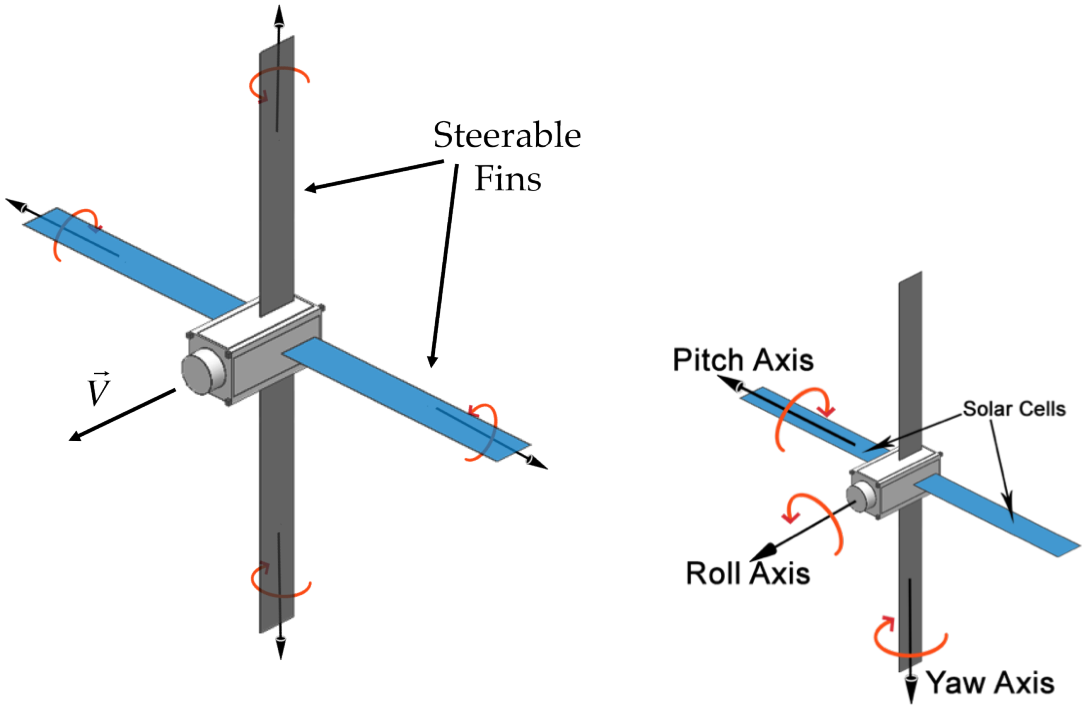

(a) (b)

Figure 7.1: ΔDsat schematic configuration showing the Steerable Fins deployed in the minimum drag configuration. The fins rotation axes are also shown in a) and the CubeSat general rotation axis in b).

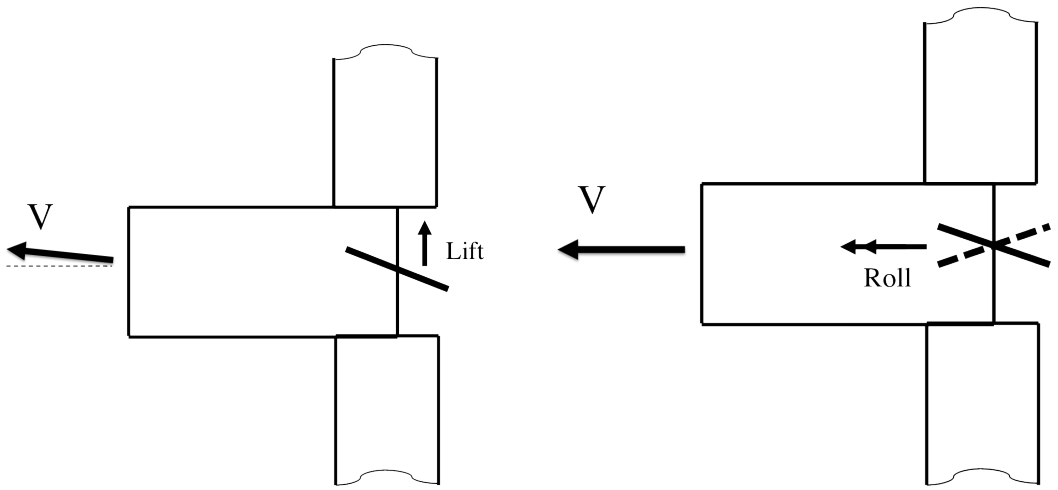

(a) (b)

Figure 7.2: ΔDsat Steerable Fins rotating options and effects. a) Co-rotating Steerable Fins makes ΔDsat fly at an angle. b) Counter-rotating Steerable Fins creates a roll torque.

torque that will make ΔDsat spin (roll). Figure 7.2 shows, schematically, these two options and their effects.

Flying at an angle with respect to the flow (caused by co-rotation) represents an uncertainty in the measurement, as the influence of the flow incidence angle on the drag wants to be studied. Flying at an angle represents an uncertainty because this angle cannot be measured and because this angle is dependant on the aerodynamic properties of the fins, that are unknown (this is what is tried to be measured). Therefore the option selected has been to counter-rotate the fins. The spinning torque can be compensated by on-board actuators (such as magnetic torquers) in order to maintain a stable attitude. Also, roll does not affect the flow incidence angle on the fins (see Fig. 7.1b) and thus it has no impact on the measurements.

From the minimum drag configuration, the Steerable Fins can rotate in either direction (clockwise and counter-clockwise), hence providing 4 different surface types to be exposed (assumes that two opposite fins rotate at a time). The front and rear faces of the vertical fins and the front and rear faces from the horizontal panels.

One side of two fins is covered with solar cells, as shown in Fig. 7.1b, and hence one of the surface types that will be tested is a solar panel like surface. Testing a solar panel like surface is very relevant as all Earth bound satellites have solar panels. Therefore, characterising the solar panels aerodynamic properties seems very relevant. The other surface materials and surface treatments have still to be decided.

Careful consideration has to be given to what surface materials/finishes are to be included. There are two routes that could be followed. The first option consists in characterising materials usually found on current spacecraft surfaces (like Kapton). This route will help to accurately predict drag for future missions that use traditional surface materials. As the past experiment shows, the materials traditionally used in spacecraft adsorb atomic oxygen and thus, their aerodynamic properties do not differ too much (Moe and Moe, 2010). So it seems a rather useless exercise to fly these surface types. The other route consists of including materials and treatments that are suspected to have low atomic oxygen adsorption, or surface types where the atomic oxygen could be easily removed (heating the surface, illuminating them with UV radiation, ...). This route seems to have the potential to produce more interesting results that could be used in the next generation of VLEO missions but, it is more complex, as research has to be done to select promising candidate materials and cleaning methods (and implement these cleaning methods in the CubeSat design). The selection of the surface materials and treatments has been left outside the scope of this dissertation. The focus has been to develop a mission that can characterise the aerodynamic properties of its fins, whatever they are made of. Also, this mission can be seen as the first one of a programme so that more than 4 surface types can be tested.

As it has been already mentioned, the method consists of characterising the aerodynamic properties (the drag coefficient C_d) of two surface types and compare them (differential approach). To get those drag coefficient ratios $\frac{C_{d1}}{C_{d2}}$ the mission first estimates C_{d1} and C_{d2} separately. These individual drag coefficients are estimated through what is known as a test run. These test runs consist of rotating two fins, exposing their surfaces to the flow, during a certain period of time (typically one orbit), exposing with a particular incidence angle one of the 4 surface types. Exposing the fins to the flow increases the drag generated by the CubeSat, and this has an impact on the CubeSat trajectory (the orbit is modified). The spacecraft position and velocity during this period is recorded using an on-board GPS. With an adapted LSQ orbit determination

algorithm (Vallado, 2001) and making use of the density measurements provided by the QB50 mission and the GPS measurements, the drag coefficient of the CubeSat can be estimated. The density measurements form QB50 include the measurements form ΔDsat's own INMS sensor, but also the measurements from all the other CubeSats on the constellation and all the data from the dedicated campaigns (when available). To estimate the accuracy of the method only the measurements coming from the ΔDsat INMS sensor will be considered.

This test run procedure can be summarised as follows:

1. Adjust the Steerable Fins to achieve a desired angle of the fins to the flow. Opposite Steerable Fins (the 2 vertical or 2 horizontal) will rotate simultaneously (to keep the symmetry) and counter-rotate to avoid any aerodynamic torques that causes a misalignment of the CubeSat with respect to the flow. Magnetic torquers will keep the CubeSat from spinning.

2. Over a measurement run of around one orbit period, the Steerable Fins will create aerodynamic forces as in Eq. 7.1 and an on-board GPS will record the trajectory followed by the CubeSat. Also, the INMS will take in situ measurements of the atmospheric density ρ and its composition. In this case the aerodynamic forces (mainly along track) are very insensitive to the wind velocity and hence the inertial velocity (provided by the GPS) can be used without incurring into any significant error (the dynamic pressure increase from atmospheric wind is small, so wind can be safely ignored).

$$\vec{F}_{aero} = \frac{1}{2}\rho \left\| \vec{V}^2 \right\| A_{ref} \vec{C}_F \tag{7.1}$$

3. Post-process the trajectory information to extract the forces that shaped the orbit (using orbit determination algorithms). If all the forces except drag can be modelled (gravity and SRP) the aerodynamic forces can be extracted.

4. With the density measurements from the INMS, and the drag forces, the aerodynamic properties $\vec{C}_F$, mainly C_d, at that particularly configuration can be computed[1].

5. This procedure is then repeated at another configuration to obtain the C_{d1} and C_{d2} pair.

This procedure is shown in Fig. 7.3.

This drag coefficient estimation is for the whole CubeSat and not exclusively for the difference that the fins produce when they rotate. The CubeSat body contribution will be the same on both test runs (up to first order), and hence the difference in the C_d will be due to the drag difference produced by the rotation of the fins. The contribution of the CubeSat body is in fact an inherent limitation of this method specially when computing the drag coefficient ratio $\frac{C_{d1}}{C_{d2}}$. The contribution of the CubeSat body can be easily measured as it is the drag coefficient of the ΔDsat in the minimum drag

[1]In reality step 3 and 4 are combined. The orbit determination algorithm can perform both steps simultaneously. The orbit determination algorithm used is detailed in section 7.6)

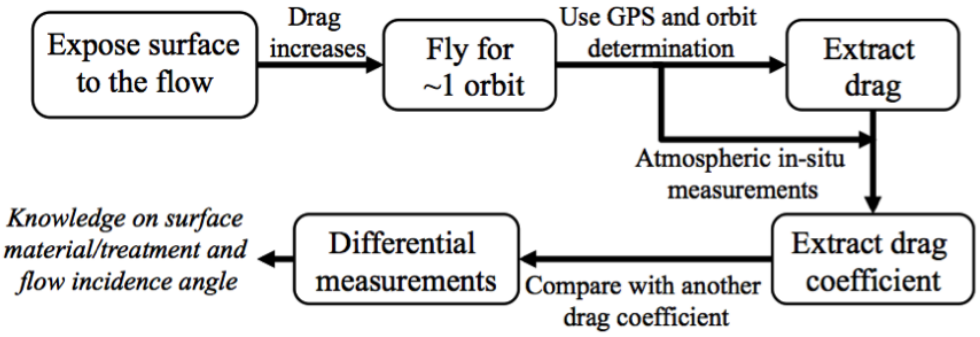

Figure 7.3: Schematic of the steps followed to obtain the differential measurements.

configuration (see Fig. 7.1a). As the drag of the CubeSat body limits the sensitivity of the measurements of the fins drag, the drag of the fins has to be maximised compared to the drag of the CubeSat. This has been done by maximising the area of the Steerable Fins. If this is done, in most of the configurations (rotation angles of the fins) the drag produced by the fins will be much larger than the one produced by the CubeSat body. Finally, if the CubeSat body drag can be estimated in orbit, the information contained in the C_{d1}, C_{d2} their difference and their ratio $\frac{C_{d1}}{C_{d2}}$ can be correctly interpreted.

We can represent the estimated drag coefficient (with the hat) that each test run produces as shown in Eq. 7.2.

$$\hat{C}_d = kC_d + \epsilon \tag{7.2}$$

where k can be assumed as a constant (bias) and ϵ is normally distributed error (noise). We can rearrange $\epsilon = k\epsilon_k$ and dividing different estimations for different surface properties or incidence angle we obtain Eq. 7.3.

$$\frac{\hat{C}_{d1}}{\hat{C}_{d2}} = \frac{C_{d1} + \epsilon_{k1}}{C_{d2} + \epsilon_{k2}} \tag{7.3}$$

This last expression shows how the first order bias in drag estimation is eliminated in the differential approach. This procedure shows that, not only density measurement biases are eliminated, but that all other biases in the measurement chain are eliminated as well.

The remaining problem left is to compute the statistics of the $\hat{C}_{d1}/\hat{C}_{d2}$ ratio. If we assume that $\hat{C}_d$ is a normal distributed variable with mean $\mu = kC_d$ and standard deviation $\sigma = \sigma(\epsilon) = k\sigma(\epsilon_k)$ then $\hat{C}_{d1}/\hat{C}_{d2}$ follows a ratio distribution. Hinkley (Hinkley, 1969) found a form for this distribution, where $Z = X/Y$, $X = N(\mu_x, \sigma_x^2)$, $Y = N(\mu_y, \sigma_y^2)$ and in the absence of correlation the probability density function can be written as in Eqs. 7.4-7.8.

$$p_Z(z) = \frac{b(z)c(z)}{a^3(z)} \frac{1}{\sqrt{2\pi}\sigma_x\sigma_y} \left[2\Phi\left(\frac{b(z)}{a(z)}\right) - 1 \right] + \frac{1}{a^2(z)\pi\sigma_x\sigma_y} e^{-\frac{1}{2}\left(\frac{\mu_x^2}{\sigma_x^2} + \frac{\mu_y^2}{\sigma_y^2}\right)} \tag{7.4}$$

$$a(z) = \sqrt{\frac{1}{\sigma_x^2} z^2 + \frac{1}{\sigma_y^2}} \tag{7.5}$$

$$b(z) = \frac{\mu_x}{\sigma_x^2} z + \frac{\mu_y}{\sigma_y^2} \tag{7.6}$$

$$c(z) = e^{\frac{1}{2}\frac{b^2(z)}{a^2(z)} - \frac{1}{2}\left(\frac{\mu_x^2}{\sigma_x^2} + \frac{\mu_y^2}{\sigma_y^2}\right)} \tag{7.7}$$

$$\Phi(\phi) = \int_{-\infty}^{\phi} \frac{1}{\sqrt{2\pi}} e^{-\frac{1}{2}u^2} du = \frac{1}{2}\left(erf\left(\frac{\phi}{\sqrt{2}}\right) + 1\right) \tag{7.8}$$

The cumulative distribution function can be obtained by integration (numerical) of the probability density function $p_Z(z)$. This distribution is useful to assess how much uncertainty (σ) the mission can tolerate until the objectives are not met. For example, if the drag coefficients of two different configurations are estimated and the real ratio is $\frac{C_{d1}}{C_{d2}} = 1.1$, then the $\hat{C}_d$ uncertainty must be below 2.1% to guarantee that $\frac{\hat{C}_{d1}}{\hat{C}_{d2}}$ lies within a $\pm 5\%$ of the real ratio with a 90% confidence (which is the science objective). It is worth noting at this point that this level of uncertainty is independent of the $\frac{C_{d1}}{C_{d2}}$ value.

This method for determining the result accuracy requires the mean and standard deviation of the single drag coefficients measurements. These two values can be estimated through simulation and be later confirmed whilst in orbit. Note also that this method is only valid when one measurement of C_{d1} and C_{d2} are available. Increased accuracy can be obtained if averages of several measurements are used. In that case the standard deviation of this new set of normal distributed variables ($\hat{C}_d$ average) will be reduced and the precision increased.

For example if a set of 5 measurements is used the standard deviation lowers from $\sigma_{n=1} = 2.1\%$ to $\sigma_{n=5} = 0.94\%$. The more generic equation $\sigma_n = \frac{\sigma_1}{\sqrt{n}}$ can be derived using the following properties $\sigma(cX) = |c|\,\sigma(X)$, $\sigma(X+Y) = \sqrt{\sigma^2(X) + \sigma^2(Y) + 2\sigma(X,Y)}$.

By using a differential approach, biases and systematic errors are automatically removed. The decision to go for a differential approach is based on the fact that current atmospheric models have significant biases (Bowman and Storz, 2003), and at the inception of this concept atmospheric models were to be used to estimate the atmospheric uncertainties. As the same atmospheric model was to be used when estimating both drag coefficients, it could be assumed that even if the atmospheric model provided a wrong absolute density estimation, the atmospheric model could model correctly the change in density. Therefore the method presented here would be able to provide accurate results.

Now that the INMS is present the single drag coefficients could potentially be used on their own (although special care has to be taken to not include any measurement bias). Also, the differential approach is still useful as the QB50 sensor suit is currently in development with final expected accuracy figures have yet to be released and calibration procedures for this type of sensor still to be tested.

7.3 Error Sources and Mitigation

ΔDsat's approach of providing differential measurements instead of absolute ones minimises the errors caused by biases in the measurements. These differential measurements will provide insights that can help design low altitude flying spacecraft or drag-

enhancing de-orbiting devices. But these measurements will not be free from uncertainties.

The uncertainties on ΔDsat's attitude can introduce errors when comparing different incidence angles. Also, the tests of the two different configurations do not happen simultaneously and hence the environment when these two tests are carried out will differ (affecting the comparison). Atmospheric wind, affecting the dynamic pressure and the angle of attack, and the altitude decay can increase these differences. To maximise the accuracy of the results the two configurations to be compared are going to be tested one immediately after the other and the QB50 sensor suite is to be used to characterise the environment and correct these differences (or at least account for them). Although performing the two test runs consecutively will be the standard procedure, comparison at different times is also possible and can provide complimentary information. These comparisons can give information on how drag coefficient change with the environment, with the variability on the environment being due to weather (solar and geomagnetic activity) or due to a change in the altitude (decay).

The main environment related sources of errors identified have been the attitude uncertainty and the presence of atmospheric wind.

7.3.1 Attitude Uncertainty

As with an aircraft, the drag coefficient of a spacecraft is a function of its attitude with respect to the flow. If a body axis system, analogous to the ones applied to aircraft, is used for ΔDsat the CubeSat drag coefficient becomes a function of the pitch and yaw angles (see Fig. 7.1b). The symmetry that ΔDsat presents in roll makes the drag coefficient constant with respect to roll.

For this reason, it is important for the mission to know its relative attitude with respect to the flow. Unfortunately, this is rather difficult, as the atmosphere co-rotation and the atmospheric wind cause the incident flow not to be aligned with the orbital velocity vector. Also, there is no known sensor that is capable of measuring the attitude of the spacecraft with respect to the incident flow.

To mitigate this error ΔDsat is designed to be aerostable. The Steerable Fins act as the fins in an aircraft and provide a restoring torque that ensures that the spacecraft will turn towards the local flow direction, regardless of the atmospheric conditions. This enables the CubeSat to operate aligned with the instantaneous flow direction (or at least close to it), and thus it can be assumed that by rotating the fins, the incidence angle of the flow with respect to the fins can be controlled. Now it is more clear why co-rotating the fins, hence inducing lift that would make ΔDsat to fly at an angle, is not desirable (the angle difference can not be measured).

Here, a brief introduction about the CubeSat aerostability will be provided and a more in depth description of aerostability is included in the following chapter 8 on page 99.

In an aerostable spacecraft there is a particular orientation with respect to the flow where no aerodynamic torques appear (equilibrium attitude). As soon as this special attitude is lost, aerodynamic torques that try to restore that original orientation appear. For ΔDsat, this equilibrium attitude is when the CubeSat is aligned with the relative flow. The torque provided by the Steerable Fins around this equilibrium point

can the be approximated, in a one-dimensional case, by Eq. 7.9.

$$T_a \approx -qk \sin\theta \tag{7.9}$$

where q is the dynamic pressure ($q = 1/2\rho V^2$), k is a constant (will be known as the aerodynamic stiffness) and θ is the perturbation angle from the equilibrium point. From Eq. 7.9 is clear that when ΔDsat departs from the equilibrium point, aerodynamic torques appear that want to restore the attitude of the spacecraft towards the equilibrium orientation (restoring torque).

As it can also be noted in Eq. 7.9, this system will behave as a friction-less pendulum. It is also analogous to a spring-mass system, when small angles are considered, but with attitude instead of position and inertia instead of mass. This means that, when perturbed, the system will oscillate indefinitely around the equilibrium point. Generally the aerodynamic torque does not vary in a perfect sinusoidal fashion as the Eq. 7.9 suggests. This torque is a function of the angle and the spacecraft's angular velocity, as shown in Eq. 7.10. Although the contribution related to the angular velocity is almost negligible (Eq. 7.11), as the velocity of the spacecraft surfaces induced by the spacecraft angular velocity is negligible compared to the bulk velocity of the gas particles (orbital velocity).

$$T_a = f(\theta) + f\left(\dot{\theta}\right) \tag{7.10}$$

$$f(\theta) \gg f\left(\dot{\theta}\right) \Rightarrow T_a \cong f(\theta) \tag{7.11}$$

If the torque is only a function of the perturbation angle and is of the form shown in Eq. 7.9, the system will then be marginally/statically stable (it will oscillate around the equilibrium point when perturbed). To achieve dynamic stability, with the attitude converging to the equilibrium point, damping is required. Damping torques can be expressed using Eq. 7.12.

$$T_d = -c\dot{\theta} \tag{7.12}$$

where c is what is known in a damped harmonic systems as the damping coefficient and is expressed in $Nm/(rad/s)$. The damping torque is a torque proportional and in the opposite direction than the angular velocity $\dot{\theta}$.

The aerodynamic torque can be further simplified, for small perturbation angles, to Eq. 7.13, as it usually done for pendulums where the expected oscillation is small (hopefully ΔDsat will not deviate too much from its equilibrium orientation as well). Note that in Eq. 7.13, qk is equivalent to the stiffness of a spring. The source of this analogous stiffness can be traced to a contribution from the dynamic pressure q and a contribution that is inherent to the CubeSat aerodynamic properties k. This k is then nothing more than $k \approx A_{ref} l_{ref} C_T/\theta$ (see Eq. 3.2 on page 33) and it will be referred from here onwards as the aerodynamic stiffness.

$$T_a \approx -qk\theta \tag{7.13}$$

Under this approximation, and adding the damping, the system takes the standard formulation of a damped harmonic oscillator, which can written as in Eq. 7.14.

$$I\ddot{\theta} + c\dot{\theta} + qk\theta = 0 \tag{7.14}$$

where I is the system inertia. The objective of the aerostability system is then to converge to the equilibrium attitude as fast as possible, and this is achieved through critical damping c_c. The critical damping coefficient value can be computed using Eq. 7.15.

$$c_c = 2\sqrt{Iqk} \tag{7.15}$$

As k is an aerodynamic property it depends on the aerodynamic properties of the CubeSat, and hence it is inherently unknown. To have an estimation of its value, the Sentman model has been used (Sentman, 1961) to estimate the aerodynamic properties of the CubeSat. Figure 7.4 shows how the critical damping coefficient, for the minimum drag configuration, changes when the altitude changes. It has to be noted that as k is an aerodynamic property its value will also change when the steerable fins rotate (change in the spacecraft geometry and also in its inertia). It is also important to note that the required damping will be higher at lower altitudes as the density, and hence the dynamic pressure q, increase.

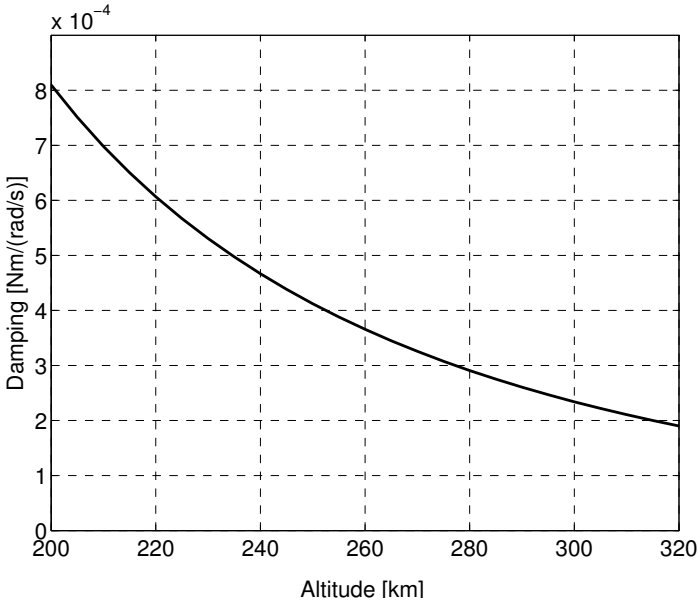

Figure 7.4: Critical damping c_c value for a minimum drag configuration. Assuming moderate solar activity (ISO 14222, 2013), $I = 0.0083\ kg\ m^2$, $\sigma_a = 1$, and $T_w = 300\ K$.

This information is then used to design the damping subsystem. In the current design the damping function will be performed by magnetic torquers. These actuators will produce a torque against the angular rates sensed by the on-board MEMS gyros. The magnetic torquers response will be adjusted depending on the panels deflection and the flying altitude to achieve optimum performance (critical damping) at all times. As the damping coefficient increases when the altitude is reduced, the magnetic torquers may saturate at low altitudes and, under this conditions, the system will

become underdamped and will overshoot (although it will settle anyway, but it will take longer).

In reality, the aerodynamic torque is not perfectly linear nor it does vary sinusoidally. Figure 7.5 shows the estimated restoring torque ($A_{ref}l_{ref}C_T$ shown) created when ΔDsat it is under yaw (or pitch). The restoring torque changes with the panels deflection angle and ΔDsat becomes more stable as the panels are deflected. Note that close to the equilibrium point $\theta = 0$ the restoring torque is quasi linear (validating the approximation made in Eq. 7.13).

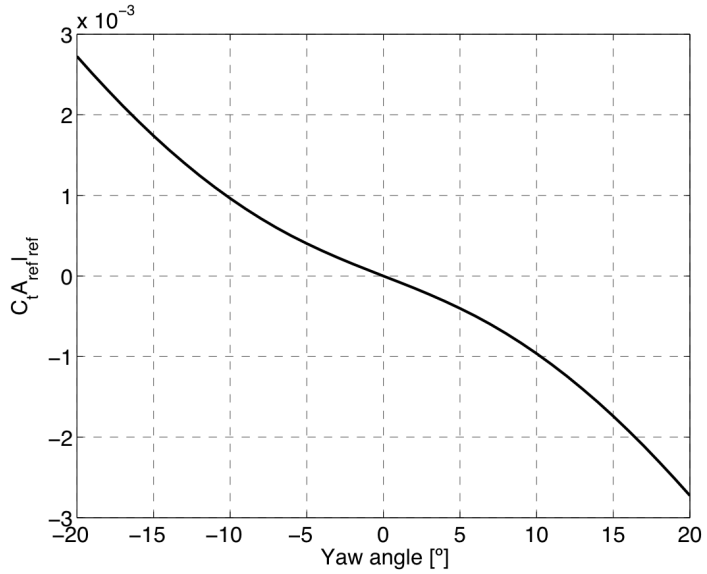

Figure 7.5: Torque produced by ΔDsat under yaw with a minimum drag configuration (Fig. 7.1a). Torque defined as $T = \frac{1}{2}\rho V^2 C_t A_{ref} l_{ref}$. Assumes a fin area of $A_p = 408\ cm^2$ and uses the Sentman model with $\sigma_a = 1$, $T_w = 300\ K$, velocity as the orbital velocity of a circular orbit at an altitude $h = 250\ km$ and atmospheric properties at that altitude assuming medium solar activity (ISO 14222, 2013).

Figure 7.6 shows how the CubeSat aerodynamic stiffness changes as the panels deflect. The aerodynamic stiffness is defined as the restoring torque produced when the spacecraft rotates one degree and is expressed in $m^3/º$ (or if the dynamic pressure is included in $Nm/º$). This parameter can be computed as the slope of the restoring torque (Fig. 7.5) when $\theta = 0$.

Being aerostable ensures that ΔDsat points to the flow during all times (or at lease it will try to follow the changes in direction) and hence the extracted drag coefficient estimations can be matched to the fins deflection angles. Obviously, the flow pointing attitude will not be perfect, as other attitude perturbation sources exists (being Solar Radiation Pressure the most significant) and in addition, ΔDsat will still have to go through the transient periods caused by atmospheric wind (and other perturbations such as when entering and coming out of eclipse).

7.3.2 Atmospheric Wind

The drag coefficient can be defined in its usual form as in Eq. 7.16.

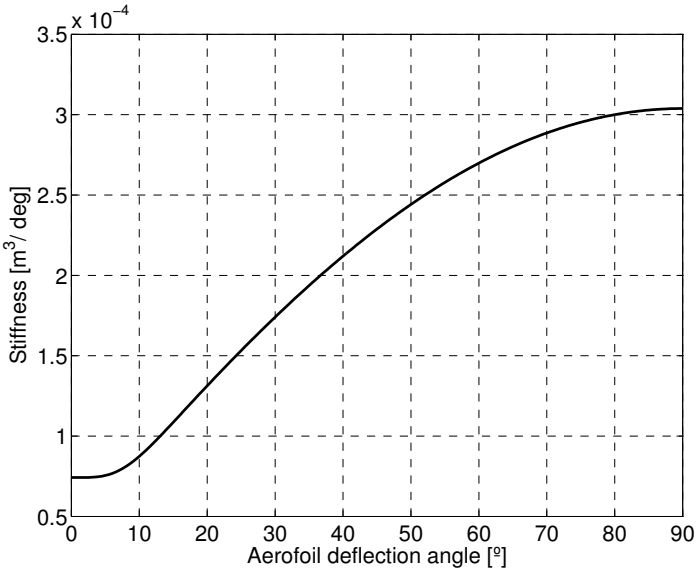

Figure 7.6: CubeSat aerodynamic stiffness at different panel deflection angles (assumes counter-rotation). Assumes a fin area of $A_p = 408\ cm^2$ and uses the Sentman model with $\sigma_a = 1$, $T_w = 300\ K$, velocity as the orbital velocity of a circular orbit at an altitude $h = 250\ km$ and atmospheric properties at that altitude assuming medium solar activity (ISO 14222, 2013).

$$C_d = \frac{D}{\frac{1}{2}\rho V_{rel}^2 A_{ref}} \tag{7.16}$$

where ρ is the density, V_{rel} is the relative velocity with respect to the local flow and A_{ref} as an arbitrary reference area. Then it is clear that atmospheric winds will affect the drag coefficient measurements (as they change the relative velocity V_{rel}). Assuming that ΔDsat is aligned with the flow then an increase in V_{rel} by the wind is equivalent to an increase of the dynamic pressure. ΔDsat carries an Ion and Neutral Mass Spectrometer (INMS) that is a miniaturised analyser designed for sampling low mass ionised and neutral particles in the spacecraft ram direction (Smith, 2012). The INMS is still under development and it is uncertain if the sensor will be able to resolve these changes in flow velocity or weather they will appear as an apparent density change (more mass flow). As a reference Fig. 7.7 shows the apparent density to real density ratio on a typical orbit. If the INMS can resolve these differences (either change in velocity or change in the apparent density) then this effect can be corrected, and if it cannot be resolved, then it will be mixed with the sensor uncertainty. As wind intensity (max of $\sim$400 m/s) is low compared to the inertial velocity, the uncertainty derived from the wind is acceptable.

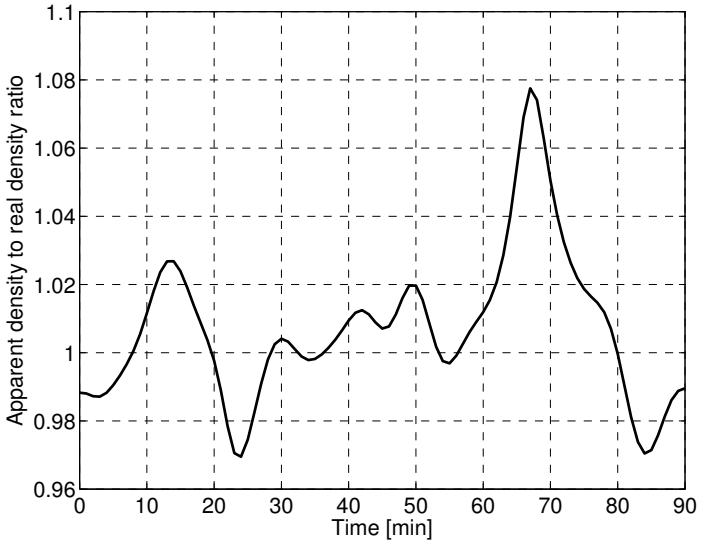

Figure 7.7: Apparent density to real density ratio of on typical orbit. Circular $h = 250\ km$, $i = 79^{\text{o}}$ orbit. Winds computed using the HWM93 (Hedin et al., 1996) model and the density using the NRMLSISE-00 (Picone et al., 2002) assuming medium solar activity (ISO 14222, 2013).

7.4 Simulator

To understand how all these different effects work together, a mission simulator (high precision 6DoF orbit propagator) has been developed in order to assess ΔDsat's expected accuracy. The simulator uses the NRLMSISE-00 model (Picone et al., 2002) to model the atmospheric density and the HWM93 model (Hedin et al., 1996) to model the atmospheric wind. The simulator uses the EGM96 (Lemoine, 1998) gravity field model of the Earth. It also includes the gravity fields of the Sun and the Moon and realistic rotation of the Earth using the ITRF93 model (Boucher et al., 1994) (celestial bodies ephemeris extracted using the SPICE toolkit).

The aerodynamic forces and torques are estimated using the Sentman model using a realistic geometrical model of the CubeSat and with an energy accommodation coefficient of $\sigma_a = 1$. Both the aerodynamic forces and the torques are dependant on the CubeSat attitude with respect to the flow.

The magnetic damping system has also been included, with the damping coefficient set to achieve critical damping at all times. The magnetic torquer rods are modelled to have an actuation level of $0.2\,Am^2$ and have the ability to saturate (magnetic field modelled using the IGRF-11 Earth magnetic field model). The magnetic torquers actuation also suffers from errors derived from the on-board magnetometer resolution of 7×10^{-7} T, the 256 levels magnetic torquer quantisation (command limitation) and a bias of 2.5% 3σ. The gyro that feeds the angular rate that is used to apply the damping has a sensitivity of 0.018^{o}/s.

The simulator includes the perturbation of solar radiation pressure both on the forces and on the torques. It assumes a reflectivity coefficient of $r = 0.9$ with a 10% 1σ uncertainty on the spacecraft reflectivity. The gravity gradient torques have also been included. Finally, the uncertainty of the centre of mass has been set to 1 cm 1σ,

which is then used to generate the uncertainty in inertia, and the uncertainty of the Steerable Fins rotation has been set to 0.5 deg. 1σ.

Summarising, the simulator includes a realistic representation of the CubeSat dynamics, including uncertainties on its physical parameters, so that the results that it gives and the information that is known about the simulated CubeSat can be equivalent to the data and information that will be known during the CubeSat operations. The propagator has been validated comparing its results to the ones provided by STK. The simulator has been later used on different occasions for the research presented in this dissertation and the propagator also used for MSc student projects.

For the measurement chain it has been assumed that the time between GPS and density measurement is 1 minute. The GPS measurements performance is based on an actual commercial unit, offering $10\,m$ 2σ in position and $25\,cm/s$ 2σ in velocity (this GPS unit is to be flown on ΔDsat).

The measured density has been considered to be the apparent density (as if the relative velocity was the orbital velocity and any discrepancies were sensed as a change in the measured density). This observed apparent density is modelled as $\rho_{obs} = \frac{\rho_{real} V_{rel}^2}{V_{obs}^2}$ where the observed relative velocity does not contain the winds (is the orbital velocity). On top of that a bias and a random error is added following $\hat{\rho} = k_\rho \rho_{obs} + \epsilon_\rho$, where $\hat{\rho}$ is the measurement that comes out of the sensor, k_ρ represents any possible bias in the measurement and ϵ_ρ is a normal distributed error with a 1σ gaussian error of 10% of ρ_{obs} (noise).

7.5 Results

With all this simulated data (position, velocity and densities) the C_d is extracted using a least square based orbit determination algorithm (Vallado, 2001, pp. 672-762) (the orbit determination technique is detailed in section 7.6). The drag model used in the fitting is characterised through only a single parameter: a constant drag coefficient. It also does not take into account the attitude dynamics or the solar radiation perturbations (this effects then result in errors in the estimation).

Figure 7.8 shows how the pitch and yaw angles evolve in a typical orbit. As it can be seen in Fig. 7.8, ΔDsat remains stable and the misalignment with the flow is small. Even if the altitude is increased up to the maximum of QB50 ($h = 380\ km$) the misalignment is not higher than 10^{o} with the minimum drag configuration, and not higher than 1^{o} with two panels deflected 90^{o}.

When the panels co-rotate, ΔDsat no longer flies aligned with the flow but flies at an angle. This new equilibrium angle is roughly independent of the altitude and is shown in Fig. 7.9. This new equilibrium angle depends on the lift to drag ratio and its value is unknown (Fig. 7.9 is only an estimate). Therefore, an error is incurred when estimating the C_d if this new equilibrium angle is neglected. This error is shown in Fig. 7.10.

The other option available, counter-rotating the panels, does not produce any of these errors, but then, the roll torque created has to be compensated. With the current configuration and panel sizes, a commercial off the shelf magnetic torquer can easily offset this torque, and hence this is currently the implemented option. Due to the

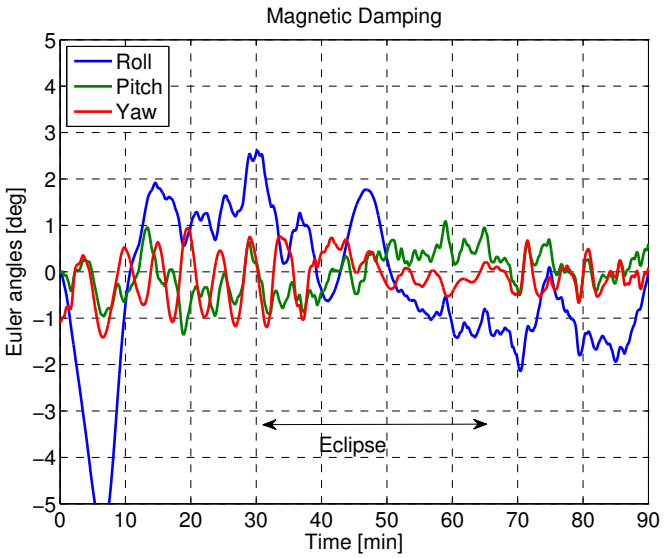

Figure 7.8: Pitch and yaw angles in a typical ΔDsat's orbit with a minimum drag configuration. Circular $h = 250\ km$, $i = 96^{\text{o}}$ orbit.

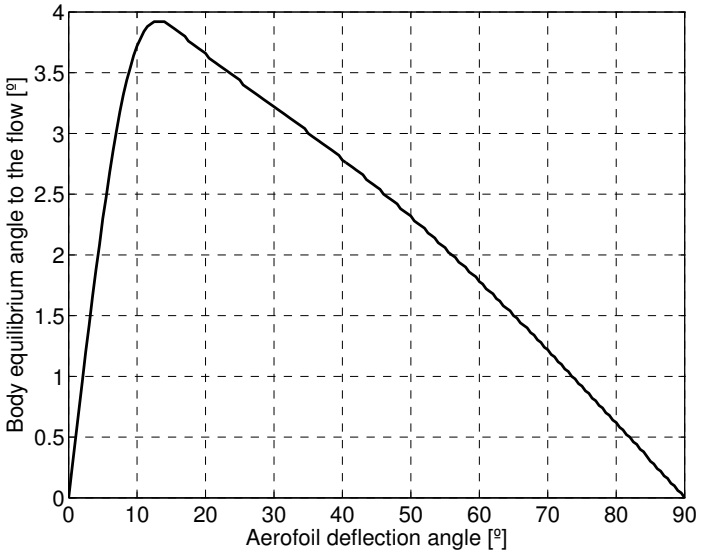

Figure 7.9: Offset angle caused by co-rotating the Steerable Fins. Assumes a panel area of $A_p = 408\ cm^2$ and uses the Sentman model with $\sigma_a = 1$, $T_w = 300\ K$, velocity as the orbital velocity of a circular orbit at an altitude $h = 250\ km$ and atmospheric properties at that altitude assuming moderate solar activity (ISO 14222, 2013).

variability of the magnetic field through the orbit, the magnetic torquer will not always be able to compensate the aerodynamic roll torque and hence the roll will fluctuate by a small amount (does not have an impact in the aerodynamic measurements).

A Monte Carlo method has then been used in order to obtain confidence figures on the estimated drag coefficient. The process, shown in Fig. 7.11, starts by simulating a test with a given configuration. Errors are then introduced to the state vector and to the density results, simulating the uncertainties of the GPS and the INMS. With this,

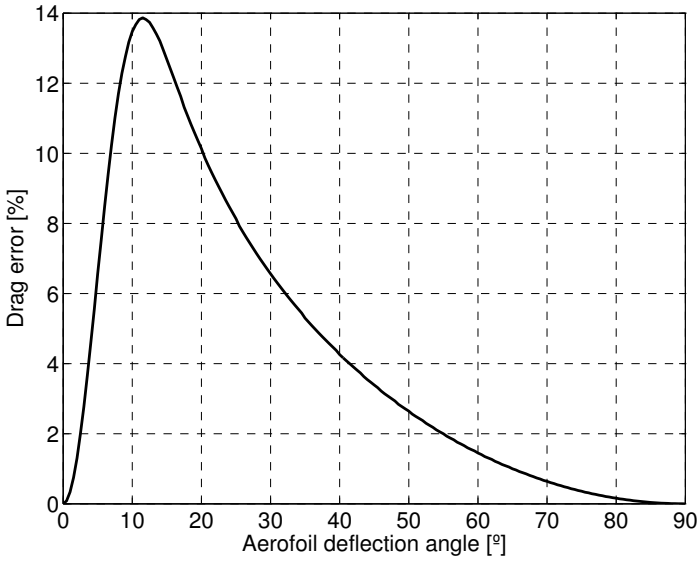

Figure 7.10: Error produced when ignoring the offset angle caused by co-rotating the panels. Error estimated assumes a panel area of $A_p = 408\ cm^2$ and uses the Sentman model with $\sigma_a = 1$, $T_w = 300\ K$, velocity as the orbital velocity of a circular orbit at an altitude $h = 250\ km$ and atmospheric properties at that altitude assuming moderate solar activity (ISO 14222, 2013).

an LSQ method using simplified dynamic models determines the drag coefficient.

Figure 7.12 shows the estimated accuracy obtained when estimating C_d if $k_\rho = 1$ (no bias on the uncertainty associated with the density) for a test duration of 1 orbit. Note that including density bias k_ρ only includes an offset in the results that will be eliminated in the differential comparison of $\frac{\hat{C}_{d1}}{\hat{C}_{d2}}$, hence this has not been included in the figure for clarity.

As expected, the uncertainty decays as the fins are deflected or if the operating altitude is lowered. Deflecting the fins or lowering the altitude increases the total drag and hence the drag effect on the trajectory increases, making the orbit determination algorithm less sensitive to errors (bigger signal to noise). The same effect takes place when the test duration is increased. But this uncertainty reduction does not occur indefinitely as the GPS and density noise act as an accuracy floor. In Fig. 7.12 this floor appears to be reached for low altitudes and high fins deflections (most of the uncertainties converge for 250km altitude), suggesting that in these cases, shorter test duration could be carried without affecting the final accuracy figures. Following the same argument, the accuracy for high altitude and low deflection angles can be increased by increasing the test duration.

It is also worth noting that the confidence intervals in this result are quite large. That is the reason why results for fins deflections above 60^{o} have been omitted in Fig. 7.12 as they are very similar to the 60^{o} case and the confidence intervals overlap (hence not adding much more information). This relatively large confidence intervals are because only 40 samples of each case have been simulated in the Monte Carlo simulation. As the difference between the real and the computed C_d behave as a normal distributed variable, the standard deviation then behaves as a Chi-squared

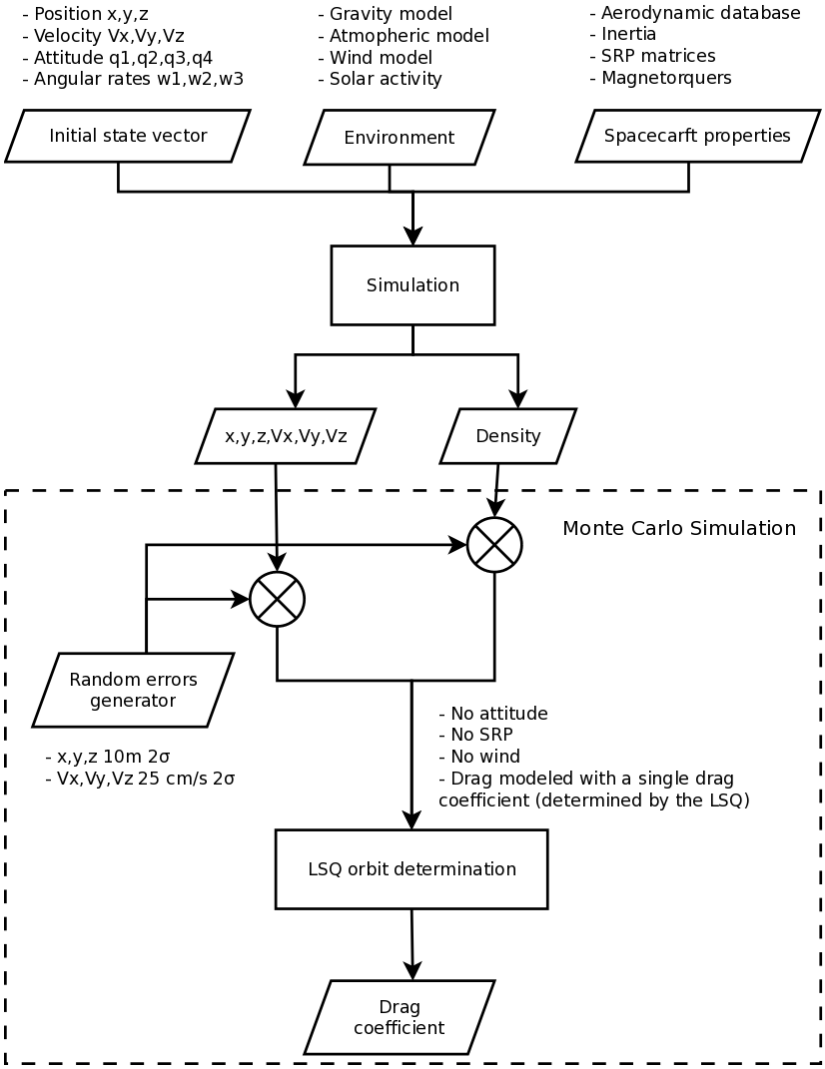

Figure 7.11: Diagram showing the process used to obtain the accuracy figures of ΔDsat's mission.

distribution. With this distribution is then possible to compute the confidence intervals of the results and it can be also shown, that to significantly reduce these intervals the number of simulations required become prohibitive in terms of computing time.

In Fig. 7.12 is shown that below 380 km (max altitude of QB50) the uncertainty upper bound in the C_d estimation is below 2% for deflections greater than 40^{o}. This means that in this altitude and deflection range, the $\frac{\hat{C}_{d1}}{\hat{C}_{d2}}$ ratio has a >5% accuracy (with a 90% confidence) in the drag coefficient ratio and hence it meets the mission objectives. Low deflection angles are not able to meet the objectives during all altitudes and hence a lower accuracy on this cases will be obtained until the spacecraft has decayed to sufficiently low altitudes.

For a 10^{o} deflection the required accuracy on the estimation of the drag coefficient is not achieved even at the lowest altitudes for a 1 orbit test period. In order to reduce the uncertainty in this case bigger fins or longer test runs could be conducted. The actual panel size is already in the limit of what can fit into a CubeSat (limited by

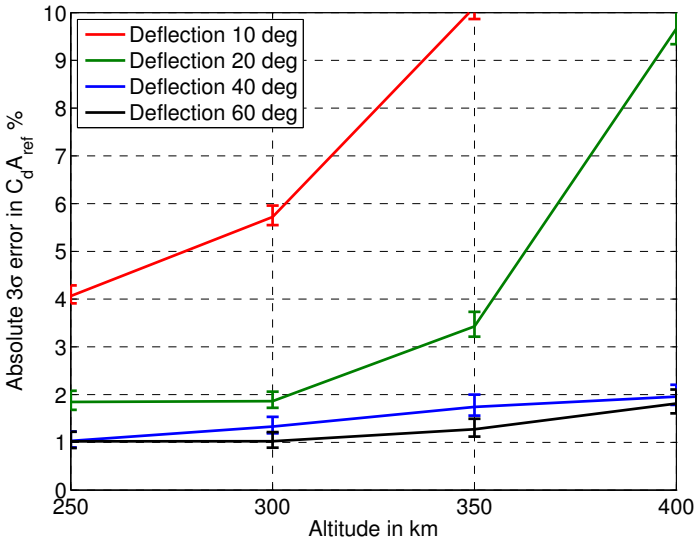

Figure 7.12: Estimated C_d accuracy for different panel deflection angles (θ) at different altitudes. Uncertainty represented as the standard deviation of the difference between the real and the computed C_d. Error bars represent the 95% confidence intervals on those values. This figures have been computed using a 40 sample Monte Carlo simulation assuming a fin area of $A_p = 408\ cm^2$, using the Sentman model with $\sigma_a = 1$, $T_w = 300\ K$, and atmospheric properties at that altitude assuming moderate solar activity (ISO 14222, 2013).

the dispenser available volume). Longer tests are then the only option to bring down the uncertainty. Increasing the test time has also its disadvantages. Mainly, changing atmospheric conditions over longer timescales can make the comparison between different configurations be in not so similar atmospheric conditions. Also. longer tests increase the amount of data generated by the experiment and CubeSat has a limited downlink capability.

At low altitudes and high deflection angles the uncertainty of the C_d estimation drops below 1%, and therefore the confidence of the results having an error below 5% will grow up to the 99.98% and the confidence of the error being below 2.5% will rise up to 93.4%.

Another aspect that could be improved to reduce the uncertainty is to take into account the attitude information in the orbit determination algorithm. The results showed before are computed assuming that the spacecraft is aligned with the flow but this is not very accurate for small deflections at high orbits. Assuming that the C_d grows linearly with small attitude offsets $C_d = C_{d0} + k\theta$, and then, adding the measured attitude in the orbit determination algorithm could yield significant improvements in the estimation accuracies. This has been left for future work.

7.6 Orbit Determination Algorithm

A key step in the method is determining the drag properties by observing the trajectory of the spacecraft and measuring the atmospheric density. To do this, an orbit determ-

ination technique can be used. In this section the technique used in the simulations will be briefly described. The technique is derived from the least squares (LSQ) orbit determination techniques presented in Vallado 2001, pp. 673-762.

The on-board GPS provides time stamped state vectors $\boldsymbol{x}_t$ of the spacecraft in an inertial reference frame at regular intervals (shown in Eq. 7.17). This sate vectors will be referred as waypoints. At the same time, the mass spectrometer provides in-situ measurements of the atmospheric density ρ_t.

$$\boldsymbol{x}_t = [x, y, z, v_x, v_y, v_z] \tag{7.17}$$

A collection of state vectors and densities is therefore available ($\boldsymbol{x}_{t0}, \boldsymbol{x}_{t1}, \ldots, \boldsymbol{x}_{tn}$ and $\rho_{t1}, \rho_{t2}, \ldots, \rho_{tn}$). A high fidelity propagator can then be used to propagate the initial state vector $\boldsymbol{x}_{t0}$. A simplified version of the propagator presented in section 7.4 has been used here. Using a simplified version allows to simulate the inaccuracies of the physicals models used (gravity field and ephemerides). This simplified propagator computes the aerodynamic forces using the measured densities and a constant drag coefficient $\hat{C}_d$ that is initially guessed (not a function of the attitude). Also, an estimate of other perturbation forces (SRP and third body), using estimate models (spacecraft geometry and reflectivity, planet ephemerides) can be included to increase the accuracy of the results. With this propagator, propagated state vectors at the waypoints can then be obtained $\tilde{\boldsymbol{x}}_{t1}, \ldots, \tilde{\boldsymbol{x}}_{tn}$. The propagated and measured state vectors will, in general, not match, as there are errors in the measurements (state vector and density measurements), because the drag coefficient $\hat{C}_d$ is constant (remember that changes in attitude change the drag coefficient), because the drag coefficient $\hat{C}_d$ has been guessed, and because the perturbation forces models are inaccurate (mainly uncertainties in SRP and the other parameters).

When the propagated state vectors at the waypoint $\tilde{\boldsymbol{x}}_{t1}, \ldots, \tilde{\boldsymbol{x}}_{tn}$ have been obtained, the difference between the propagated and the measured state vectors at the waypoints can be computed. The LSQ algorithm will then iteratively modify the initial state (annotated as $\hat{\boldsymbol{x}}_{t0}$) and the guessed drag coefficient $\hat{C}_d$ in order to minimise the errors between the propagated and measured state vectors. Then, the drag coefficient that minimises these differences will be the best estimate of the average drag coefficient of the spacecraft during the considered time interval.

This minimisation is done iteratively adjusting the initial state vector and the guessed drag coefficient by small increments ($\Delta\hat{\boldsymbol{x}}_{t0}$ (6×1) and $\Delta\hat{C}_d$ (1×1)) until they converge. Equation7.18 is used to compute these small incremental updates.

$$\begin{bmatrix} \Delta\hat{\boldsymbol{x}}_{t1} \\ \Delta\hat{C}_d \end{bmatrix} = \left(A^T W A\right)^{-1} A^T W \Delta b \tag{7.18}$$

A is a partial-derivative matrix that is related to the sensitivity of the $\tilde{\boldsymbol{x}}_t$ with respect to changes in the initial state vector $\hat{\boldsymbol{x}}_{t0}$ and the guessed drag coefficient $\hat{C}_d$. Its elements can be computed numerically propagating the initial state vector with small deltas (in both the initial state vector and drag coefficient) and then computing the sensitivities as the difference produced in the propagated state vectors at the waypoints divided by the deltas (difference per unit of initial state vector or drag coefficient change).

An example of this is shown in Eq. 7.19, where the sensitivity of x (at a certain waypoint) with respect to small change in y of the initial state vector is computed. If this is repeated for all the elements of the considered propagated state vector waypoint $\tilde{\boldsymbol{x}}_t$ Eq. 7.20 is obtained. If this is then repeated for all the elements of the initial state vector $\hat{\boldsymbol{x}}_{t0}$ and drag coefficient $\hat{C}_d$, and for all waypoints, then the matrix A can be computed as shown in Eq. 7.21. The A matrix dimensions will then be $6n \times 7$.

$$\frac{\partial \tilde{x}_t}{\partial \hat{x}_{t0}} = \frac{\tilde{x}_{t\delta} - \tilde{x}_{t0}}{\delta \hat{x}_{t0}} \tag{7.19}$$

$$\frac{\partial \tilde{\boldsymbol{x}}_t}{\partial \hat{x}_{t0}} = \begin{bmatrix} \frac{\partial \tilde{x}_t}{\partial \hat{y}_{t1}} & \frac{\partial \tilde{y}_t}{\partial \hat{y}_{t1}} & \frac{\partial \tilde{z}_t}{\partial \hat{y}_{t1}} & \frac{\partial \tilde{v}_{xt}}{\partial \hat{y}_{t1}} & \frac{\partial \tilde{v}_{yt}}{\partial \hat{y}_{t1}} & \frac{\partial \tilde{v}_{zt}}{\partial \hat{y}_{t1}} \end{bmatrix}^T \tag{7.20}$$

$$A = \begin{bmatrix} \frac{\partial \tilde{\boldsymbol{x}}_t}{\partial \hat{\boldsymbol{x}}_{t0}} & \frac{\partial \tilde{\boldsymbol{x}}_t}{\partial \hat{C}_d} \end{bmatrix} = \begin{bmatrix} \frac{\partial \tilde{\boldsymbol{x}}_{t1}}{\partial \hat{x}_{t0}} & \frac{\partial \tilde{\boldsymbol{x}}_{t1}}{\partial \hat{y}_{t0}} & \frac{\partial \tilde{\boldsymbol{x}}_{t1}}{\partial \hat{z}_{t0}} & \frac{\partial \tilde{\boldsymbol{x}}_{t1}}{\partial \hat{v}_{xt0}} & \frac{\partial \tilde{\boldsymbol{x}}_{t1}}{\partial \hat{v}_{yt0}} & \frac{\partial \tilde{\boldsymbol{x}}_{t1}}{\partial \hat{v}_{zt0}} & \frac{\partial \tilde{\boldsymbol{x}}_{t1}}{\partial \hat{C}_d} \\ \frac{\partial \tilde{\boldsymbol{x}}_{t2}}{\partial \hat{x}_{t0}} & \frac{\partial \tilde{\boldsymbol{x}}_{t2}}{\partial \hat{y}_{t0}} & \frac{\partial \tilde{\boldsymbol{x}}_{t2}}{\partial \hat{z}_{t0}} & \frac{\partial \tilde{\boldsymbol{x}}_{t2}}{\partial \hat{v}_{xt0}} & \frac{\partial \tilde{\boldsymbol{x}}_{t2}}{\partial \hat{v}_{yt0}} & \frac{\partial \tilde{\boldsymbol{x}}_{t2}}{\partial \hat{v}_{zt0}} & \frac{\partial \tilde{\boldsymbol{x}}_{t2}}{\partial \hat{C}_d} \\ \vdots & \vdots & \vdots & \vdots & \vdots & \vdots & \vdots \\ \frac{\partial \tilde{\boldsymbol{x}}_{tn}}{\partial \hat{x}_{t0}} & \frac{\partial \tilde{\boldsymbol{x}}_{tn}}{\partial \hat{y}_{t0}} & \frac{\partial \tilde{\boldsymbol{x}}_{tn}}{\partial \hat{z}_{t0}} & \frac{\partial \tilde{\boldsymbol{x}}_{tn}}{\partial \hat{v}_{xt0}} & \frac{\partial \tilde{\boldsymbol{x}}_{tn}}{\partial \hat{v}_{yt0}} & \frac{\partial \tilde{\boldsymbol{x}}_{tn}}{\partial \hat{v}_{zt0}} & \frac{\partial \tilde{\boldsymbol{x}}_{tn}}{\partial \hat{C}_d} \end{bmatrix} \tag{7.21}$$

W is a weighting matrix used to normalise the state vector. Usually position magnitudes are much larger than velocities (if meters and meters per seconds are used) and if no weighting was introduced, the algorithm would only try to correct the position of the spacecraft through the waypoints and not the velocity (as the error in position would be much larger than the error in velocity, so the error in velocity would be considered irrelevant). The weighting helps to correct this difference in magnitude between positions and velocities. The weighting can also help prioritise the correction of errors on certain waypoints (adding more weight to those), but in this case, all waypoints have all the same weight. The weighting applied in this case, uses the deltas δ defined to compute partial-derivative matrix A which have been 0.1 m for positions and 1 mm/s for velocities (ensuring that position and velocities errors are treated equally). The W matrix dimension will then be $6n \times 6n$.

$$W = \text{diag} \begin{bmatrix} W_{t1} & W_{t2} & \dots & W_{tn} \end{bmatrix} \tag{7.22}$$

$$W_t = \text{diag} \begin{bmatrix} \frac{1}{\delta x^2} & \frac{1}{\delta y^2} & \frac{1}{\delta z^2} & \frac{1}{\delta v_x^2} & \frac{1}{\delta v_y^2} & \frac{1}{\delta v_z^2} \end{bmatrix} \tag{7.23}$$

Finally, Δb is the residuals vector that can be computed using Eq. 7.24. Δb dimensions are $6n \times 1$.

$$\Delta b = \begin{bmatrix} \boldsymbol{x}_{t1} - \hat{\boldsymbol{x}}_{t1} \\ \boldsymbol{x}_{t2} - \hat{\boldsymbol{x}}_{t2} \\ \vdots \\ \boldsymbol{x}_{tn} - \hat{\boldsymbol{x}}_{tn} \end{bmatrix} \tag{7.24}$$

Iteratively, the initial state vector $\hat{\boldsymbol{x}}_{t0}$ and drag coefficient $\hat{C}_d$ are adjusted until they converge (until the change between iterations is below a predefined threshold) and the $\hat{C}_d$ estimate is therefore obtained. It is worth noting that this processing is done on the ground an not on the CubeSat.

A measure of the fit between the propagated and the measured state vectors can be obtained by the covariance matrix P, which can be computed using Eq. 7.25.

$$P = \left(A^T W A\right)^{-1} \tag{7.25}$$

7.7 Conclusions

The simulations performed demonstrate that this mission concept meets the scientific objectives. ΔDsat can provide differential drag coefficients measurements with at least a 5% accuracy in all flight conditions and with most panel configurations.

The accuracy of the differential measurements is limited by the uncertainty in the GPS and density measurements. The panels size and the test run duration have also an impact on the mission accuracy. In general, increasing the panels size or the test duration increases the accuracy, at least up to the level where the uncertainties on the GPS and density measurements are dominant. With the current configuration of 408 cm^2 panels (deemed the maximum size that could be realistically fitted in the CubeSat) and tests of 1 orbit, this limit has already been reached for most of the cases, so increasing the panel size or the test duration will not translate into increased accuracies. On the cases where more accuracy is required longer test runs are then recommended (special care to monitor the atmospheric changes is then specially relevant).

There are still several lines of action that could increase the accuracy of the mission. The most obvious one is to reduce the uncertainty on the GPS and density measurements. On the GPS side, a better unit can be purchased and post-processing on the ground can be performed to increase the accuracy on the estimated positions and velocities. On the density side, little can be done, as there are no realistic alternatives to the INMS.

The knowledge of the density is likely to be much better during the QB50 mission than the direct measurements that the on-board INMS portray (as there will be a network of 50 CubeSats monitoring the atmosphere). As the post-processing is done on the ground and can be done after the mission is finished, combining the measurements from all the sensors on-board QB50 CubeSats (task performed by the QB50 consortium) will augment the accuracy of the density measurements of the ΔDsat CubeSat (so better results are then to be expected).

Another strategy that needs to explored is to improve the orbit determination algorithms. There is room to include more complex methods, that take into account the attitude and the aerostable properties of the CubeSat. This could be done by including the attitude when estimating of the aerodynamic forces of the CubeSat (assuming that the C_d changes linearly with the attitude misalignments for example) or/and by adding the attitude into the state vector and estimate a measure of the CubeSat aerostability (i.e. the aerodynamic stiffness) in the orbit determination algorithm. This would reduce the errors derived from the attitude oscillations.

The work performed shows that ΔDsat can provide good quality data and hence, it has sufficient merit to be flown into space. Significant amount of extra work is required before flight. Specifically selecting the materials, providing and experiment plan, and refining the test duration and algorithms in order to maximise the science return. The estimated accuracies need to be updated as the design of the spacecraft gets refined (with more up-to date uncertainties) and the final post-processing software tools also need to be created prior to flight.

The concept and methodology described here are a tool to study rarefied-gas aerodynamics that with minor adaptation could also be applied to other spacecraft design. Also, if the ΔDsat mission successfully demonstrates this method, more mission could follow, starting a more systematic study of rarefied-gas aerodynamics.

Chapter 8

Aerostability in ΔDsat

Aerostability is understood as the capability of a spacecraft to achieve a stable attitude with respect to the incident flow, mainly using aerodynamic forces, and achieving it if possible, with any active system (completely passive). This capability can be very useful for very low altitude flying spacecraft. At a very low altitudes (<450 km), the aerodynamic drag can be quite large and maintaining a minimum drag orientation can be costly if aerostability is not implemented. If aerostability is not implemented then the attitude control system will have to compensate the aerodynamic torques, which in certain orientations could be quite large. Aerostability harness these aerodynamic torques so that they can be used to stabilise the spacecraft. Therefore, aerostability have the potential of saving mass, power and cost.

In addition, in a case of loss of attitude control, a non-aerostable spacecraft will lose this minimum drag attitude (as it will start tumbling) hence increasing its drag and risking a premature re-entry. An aerostable spacecraft would continue to hold this minimum drag attitude, minimising any loss of altitude and maximising the chance of recovery. An example of a spacecraft using aerostability in this context is the ESA mission GOCE (Drinkwater et al., 2007).

Achieving aerostability can also be very beneficial in some science missions where some properties of the atmosphere need to be measured and the spacecraft needs to maintain a certain attitude with respect to the flow. As the flow velocity and the inertial velocity differ (due to atmospheric co-rotation and wind), an aerostable spacecraft can provide this extra level of alignment that would not be otherwise possible/detectable. This is certainly the case of ΔDsat. The accuracy of the INMS and the rarefied-gas measurements are dependant on its alignment with respect to the flow; hence it makes sense for ΔDsat to be aerostable.

In this chapter the aerostability principles are laid out and the aerostability properties of ΔDsat estimated and analysed. It has to be noted that the aerostability properties of ΔDsat have not been left to chance and the CubeSat has been carefully engineered in order to obtain these aerostability properties.

8.1 Aerodynamics

To analyse the aerodynamic properties of the CubeSat the Sentman model (Sentman, 1961) has been used with an energy accommodation coefficient of σ_a=1, as suggested

by Moe and Moe, 2005. To achieve static aerostability the CubeSat needs to provide a restoring torque when the spacecraft is out of alignment with respect its equilibrium attitude.

For ΔDsat, the nominal and equilibrium attitude will be to fly aligned with the flow. In this attitude, there will not be any aerodynamic torque but when the CubeSat deviates from this attitude, an aerodynamic restoring torque will appear, and this torque will then push the CubeSat back towards its equilibrium attitude. The misalignments will be in pitch and yaw only. A rotation in roll will not produce any restoring torque (ΔDsat is not aerostable in roll) because the aerodynamic properties of the CubeSat are independent of the roll rotation (see Fig. 7.1b on page 78 for the rotation axis defination). Roll will then be controlled independently to minimise the Sun angle with respect to the solar panels and avoid the Sun in the exclusion zones of other sensors.

When modelled with the Sentman model the aerodynamic torques are, as shown in Eq. 8.1, a function of the misalignment angle θ (pitch or yaw) and proportional to the dynamic pressure $q = \frac{1}{2}\rho V^2$ (with ρ being the density and V the spacecraft velocity with respect to the unperturbed flow). For aerostability to be possible, the torque needs to be restoring and hence act in the opposite direction of the misalignment, Also, in general, the function $f(\theta)$ will not be linear and in the case of ΔDsat this function can be seen in Fig. 7.5. When the angles are small a linear response of the restoring torque can be assumed (this eases the analysis).

Then, if it is assumed that the torque response is restoring and linear, this aerodynamic torque can be written as in Eq. 8.2. The proportionality constant k can be defined as the aerodynamic stiffness (as it is analogous to the stiffness of a spring). The aerodynamic stiffness gives a sense of how aerostable the spacecraft geometry is (the higher the stiffness the more aerostable will be the spacecraft). The aerodynamic stiffness can also be understood as the amount of restoring torque ($A_{ref} l_{ref} C_T$) produced by a degree of misalignment $m^3/^{\circ}$ (or $mN/^{\circ}$ when the dynamic pressure is taken into account as in qk). Note that the aerodynamic stiffness, as defined here, does not contain the dynamic pressure and hence it is a property of the spacecraft (can be used to compare different spacecraft designs).

$$T_{aero} = q \cdot f(\theta) \tag{8.1}$$

$$T_{aero} \approx -qk\theta \tag{8.2}$$

ΔDsat has been designed so that the Steerable Fins provide this roughly proportional restoring torque. Figure 7.5 shows a representative shape of the $f(\theta)$ for ΔDsat. Then, k can be interpreted as the slope of that curve at $\theta = 0$.

With a surface area of 408 cm^2 each, the ΔDsat fins provide quite a strong restoring torque, significantly larger than the other perturbation torques experienced by ΔDsat, such as Solar Radiation Pressure (SRP) torques and gravity gradient torques. And, as the fins can be rotated from 0° (parallel to the flow as seen in Fig. 7.1a) to 90° (perpendicular to the flow), the slope of the curve can be changed significantly, as it shown in Fig. 8.1 (qk shown). Therefore, it is possible for ΔDsat to change its aerodynamic stiffness by deflecting its fins. The higher the deflection the higher the aerodynamic stiffness and the more aerostable the spacecraft is. Also, as shown in Fig.

8.1, ΔDsat becomes more aerostable as the spacecraft decays (higher density means higher torques).

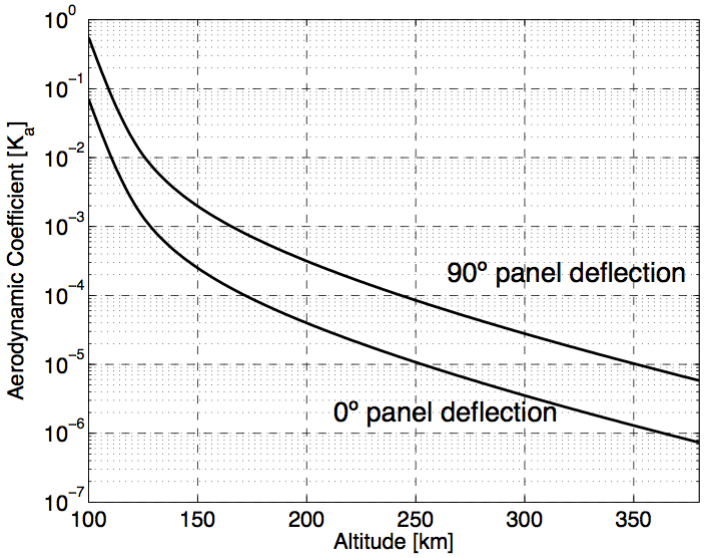

Figure 8.1: qk of ΔDsat at different Steerable Fins panels rotation (all 4 fins rotating together). Uses the NRLMSIS-00 (Picone et al., 2002) model with moderate solar activity to model the atmospheric density (ISO 14222, 2013).

8.2 Dynamics and Oscillations

It can be safely assumed, that the aerodynamic torques on a spacecraft in a free-molecular flow do not depend on the angular velocity, as the velocity of the gas particles is much bigger than the velocity of the of the spacecraft surfaces induced by its rotation. If this assumption is accepted then these aerodynamic torques are conservative. If the aerodynamic torques are restoring torques then, this means that ΔDsat will oscillate around the equilibrium point and it will have a similar behaviour than an harmonic oscillator. The system that derives from Eq. 8.2 is analogous to a spring-mass system and hence it behaves as an harmonic oscillator (as the torque is not completely linear with the misalignment, then the behaviour will not be exactly that of an harmonic oscillator but it will very similar, specially if small angles are considered).

The amplitude of the oscillations will depend on qk (higher qk means smaller oscillations) and on the initial conditions (or perturbations). The frequency response can be approximated by Eq. 8.3 where ω_0 is the angular velocity of the oscillation and I is the spacecraft's inertia (the more linear the curve in Fig. 8.1 the better this approximation). The natural frequency of ΔDsat is shown in Fig. 8.2. Note that the frequency ranges from one oscillation every 10 minutes at high altitudes to more than 10 oscillations per minute at low altitudes (the oscillations are considerably faster than the orbital period ∼90 minutes). Although small, there is the possibility that the aerodynamic oscillations resonate with some perturbations or with the attitude control loops.

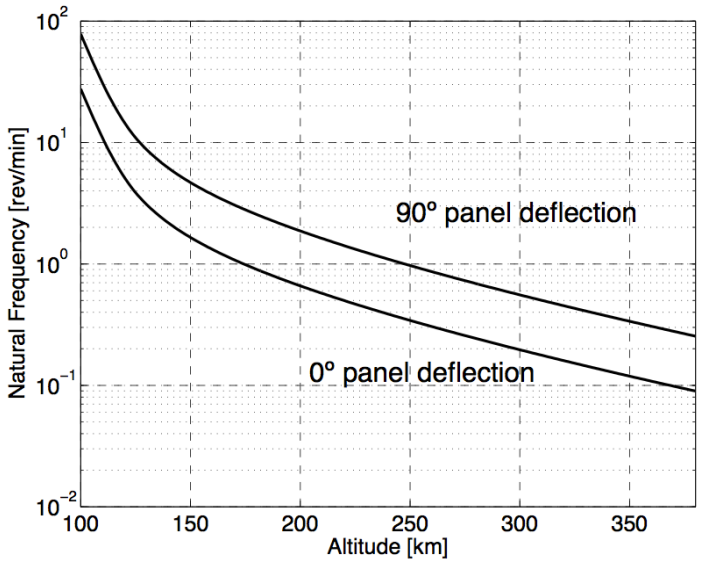

Figure 8.2: Natural frequency of ΔDsat at different Steerable Fins panels rotation (all 4 fins rotating together). Uses the NRLMSIS-00 (Picone et al., 2002) model with moderate solar activity to model the atmospheric density (ISO 14222, 2013).

$$\omega_0 = \sqrt{qk/I} \tag{8.3}$$

8.3 Damping

The system described before will oscillate indefinitely. Adding damping can avoid this indefinite oscillation and settle the system in its equilibrium point. The damping torque can be written as in Eq. 8.4 where c is the damping coefficient.

$$T_{damp} = -c\dot{\theta} \tag{8.4}$$

The approximation to an harmonic oscillator is also helpful here to compute the response of a damped system. An important parameter of a damped harmonic oscillator is the damping ratio ξ which can be compute in Eq. 8.5.

$$\zeta = \frac{c}{2\sqrt{Iqk}} \tag{8.5}$$

The damping ratio defines the different types of response under a step change. This is shown in Fig. 8.3 where a unitary step is applied to a damped harmonic system with different damping ratios. If $\zeta = 0$ there is no damping $c = 0$ (undamped) and then the system oscillates indefinitely. If $0 < \zeta < 1$ the system is underdamped and oscillates a few times before settling (the oscillations amplitude decreases until is settles). If $\zeta = 1$ the system is critically damp and it does not overshoot. This case (critical damping) is the case where settling is achieved in a shorter amount of time (fastest to settle). Finally, if $\zeta > 1$ then the system is overdamped and the system does not overshoot but it returns to its equilibrium position very slowly.

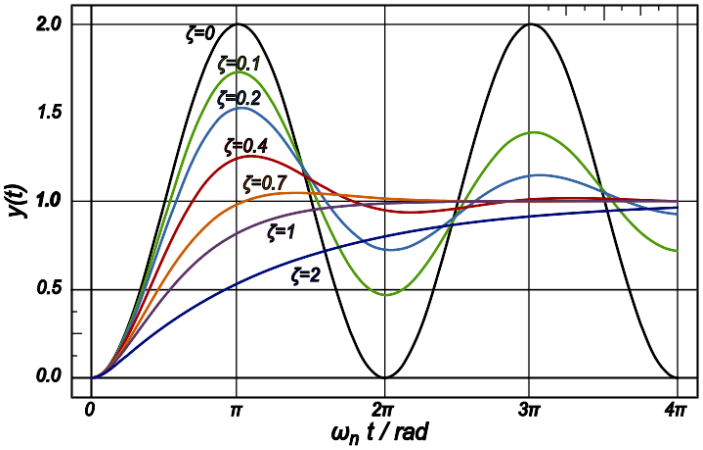

Figure 8.3: Different types of response depending on the damping ratio ζ under a step response $y = 1$ for $t > 0$.

It is clear that the case that would provide more benefits to an aerostable spacecraft is the critically damped case. Therefore the system will be engineered to be critically damped. Achieving a critical damping ensures that the system quickly damps the oscillations (as fast as possible) and that the spacecraft attitude follows the changes in flow direction as best as possible. Equation 8.6 shows how to compute this critical damping coefficient c_c.

$$c_c = 2\sqrt{Iqk} \tag{8.6}$$

Although any type of damping would be suitable to settle the oscillations the critical damping is the one that settles the oscillations faster. Also, in the presence of winds a system that is critically damped will be the one that better follows the variation of flow direction (therefore is the preferred one).

Figure 8.4 shows the evolution of the damping coefficient for ΔDsat at different altitudes and for different Steerable Fins configurations. As the damping torque required increases as the altitude decreases, it might be too high to be achieved (actuators saturation) at the final stages of the mission (when the orbit has decayed to low altitudes). In those cases a lower than optimum damping coefficient may be applied resulting in longer damping periods (let the actuators saturate if the required torque is too big). ΔDsat can achieve this damping using two different methods: 1) with its on-board magnetic torquers and 2) rotating the Steerable Fins (active aerodynamic damping).

As the two damping methods considered, involve active components, ΔDsat aerostability is not completely passive. In a loss of power event, ΔDsat will be statically stable only, and will oscillate around the equilibrium point. This behaviour although not useful for science (it does not really matter if there is no power) it is able to roughly preserve a minimum drag attitude and hence, is useful to minimise the altitude loss in such events.

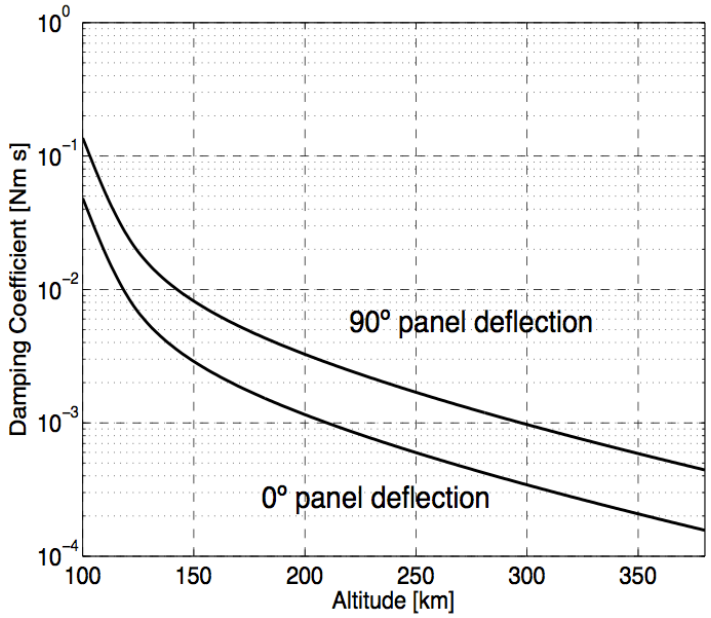

Figure 8.4: Damping coefficient required for ΔDsat to achieve critical damping at different Steerable Fins panels rotation (all 4 fins rotating together). Uses the NRLMSIS-00 (Picone et al., 2002) model with moderate solar activity to model the atmospheric density (ISO 14222, 2013).

8.4 Simulation Results

Using a 6 DoF propagator that uses realistic environment models (EGM96 (Lemoine, 1998) for the gravity, NRLMSISI-00 (Picone et al., 2002) for the atmospheric density. HWM93 (Hedin et al., 1996) for the wind and the IGRF-11 for the magnetic field) and forces and torques models (gravity, gravity gradient, SRP forces and torques, and aerodynamic forces and torques) the attitude evolution of ΔDsat can be simulated. The errors and uncertainties of the CubeSat are also included in the simulation. This includes the error on the measurement of the angular rate, the uncertainties in the CubeSat inertia, mass (in a lesser degree) and SRP coefficients (reflectivity), the misalignment of the Steerable Fins and the errors/uncertainties in the magnetometer and magnetic torquers (magnetometer error, command quantisation, actuation level uncertainty and bias). For the simulation, moderate solar activity has been used. More details about the simulator and the uncertainty levels can be found in section 7.4.

Figure 7.8 on page 90 shows the ΔDsat attitude evolution with a minimum drag configuration on a 250 km altitude typical orbit (a small initial misalignment is introduced as a perturbation) when the magnetic damping is active and Fig. 8.5 shows the attitude evolution under the same conditions but without magnetic (or any) damping.

Note that without damping, the spacecraft oscillates around the equilibrium point. When the magnetic damping is active the spacecraft does not oscillate that much but its attitude is noisier. This is because the torque requirements for the magnetic torquers are not entirely compatible with what it is achievable given the magnetic field direction at that moment and this produces undesired torques (cross coupling between axes).

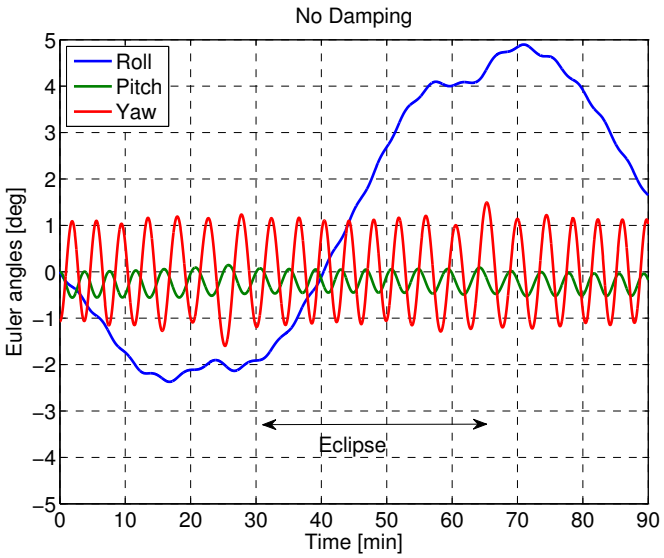

Figure 8.5: Attitude evolution with respect to the flow on a typical orbit at 250 km altitude without damping with the Steerable Fins parallel to the flow.

The magnetic torquers are only capable of producing torques that are normal to the local magnetic field direction. Therefore the torques produced by the magnetic torquers will, in general, not be completely aligned with the required damping torques (even in some areas no damping torques could be produced as the magnetic field and the required damping torques are aligned). This misalignments on the damping torques introduce noise into the system (hence not achieving complete stabilisation). It has to be mentioned that when using the magnetic damping the roll has also been controlled with the magnetic torquers to keep it close to 0° (so introducing even more disturbances). In both cases, the CubeSat stays well aligned with the flow (flow includes atmospheric co-rotation and winds) and well bellow the ±10° requirement imposed by QB50.

It has to be noted that if another method that could produce torques in arbitrary directions was used to produce the damping torques (such as reaction wheels), the performance would be much better, as it would not introduce perturbations and would be always available. Unfortunately, for practicality issues, none of these other actuators can be included in the ΔDsat design.

Figure 8.6 shows the attitude evolution when active aerodynamic damping is used (a small initial misalignment is introduced as a perturbation). The strategy used in this case consists of switching between the nominal deflection (in this case 45°) and a higher and lower deflection (in this case ±15° from the nominal 45° one) of the Steerable Fins. The switch is done when the angular velocities go above or below certain thresholds (hence introducing hysteresis and therefore damping). In this case the magnetic torquers are only used to control the roll. Note that in this case the aerodynamic active damping is capable of partially damping the initial oscillation. A perfect damping is not achieved due to the angular velocity threshold provided. This threshold represents the maximum sensitivity of the on-board MEMS gyros (ΔDsat also carries a 6-40 arcsec star tracker that could be used to reduce this threshold when

the star tracker is available). Also note that the equilibrium point in this case is not 0°. This is because the nominal fins deflection in this method is 45°, with opposite fins rotating in the same direction (co-rotating) and hence creating constant pitch and yaw torques that create this bias (see Fig. 7.9). This particular example with co-rotation has been chosen for its simplicity. If the Steerable Fins were counter-rotated a roll torque will appear that it may be to big for the magnetic torques to compensate. Then, a more complex active aerodynamic control strategy can be implemented to control the roll as well. This all active aerodynamic aerostability is possible although due to its complexity it still needs to be thoroughly tested.

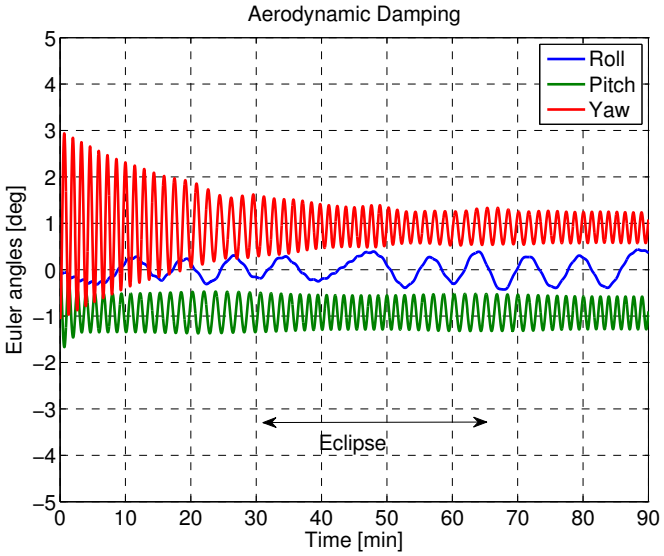

Figure 8.6: Attitude evolution with respect to the flow on a typical orbit at 250 km altitude and using active aerodynamic damping with the Steerable Fins co-rotated 45°.

Active aerodynamic damping could achieve complete attitude control only using aerodynamic forces and although not completely developed, the initial results presented here show that it is promising.

8.5 Conclusions

Aerostability is a very desirable property for VLEO missions. It exploits the natural occurring aerodynamic torques and provides a passive (or close to passive) method to stabilise the spacecraft in a certain attitude with respect to the incident flow. Maintaining the spacecraft with a certain attitude with respect to the flow can be useful to minimise the drag or because the mission requires a flow pointing attitude (as it is the case in ΔDsat). Aerostability can also be used to achieve a simple attitude control method. The only thing required to achieve it is to have the spacecraft shaped appropriately and a damping system. Aerostability can save power and mass compared to traditional attitude control systems. In addition, in the case of spacecraft failure, aerostability ensures that the spacecraft will passively point to a certain direction (even if the damping is not working and the spacecraft oscillates around the equilibrium point),

so making the spacecraft more resilient to failure (aerostability can also be used as a backup system).

This chapter has shown the aerostability properties that have been designed into the ΔDsat CubeSat. The properties of ΔDsat's aerostability have been estimated and what left now is to demonstrate them in orbit. There is obviously a lot of research left before aerostability systems are deployed in VLEO missions but some of the foundations of these systems can be studied using the results that will be delivered byΔDsat on-orbit experiments.

The experiments performed in orbit are still to be detailed but will mainly try to confirm the estimated performance of the system computed on the ground.

Chapter 9

Measuring Thermospheric Wind

The general reasons why studying the thermosphere is relevant have been described in section 6.1 on page 70. Cranfield's ΔDsat will carry one of the standard QB50 payloads, the Ion Neutral Mass Spectrometer (INMS), which will provide in-situ measurements of atmospheric density and chemical composition of the lower thermosphere. In addition, Cranfield has developed a technique that allows ΔDsat to measure the neutral wind with high precision (error < 10 m/s) using the aerostability properties of the CubeSat.

The neutral wind and ion/neutral chemical composition can be used to calculate several important atmospheric parameters, such as the ion-neutral collision frequency, which determines the conductivity of the atmosphere and the strength of the coupling between the ionosphere with the neutral gas, and hence, they have scientific merit. Direct measurements of the neutral wind is difficult since the particles are not charged. Incoherent Scatter Radars (ISR) are able to produce height profiles of ion velocities, but neutral wind must be determined either indirectly from the collisions of neutral particles with ions, or directly from the Doppler shifts of airglow emissions. The indirect method relies on assumptions of the collision frequency, while the latter relies on the presence of emissions at different altitudes. There are only two dominant airglow emission, the red line at 250 km and the green line, which can occur at three different altitudes depending on latitude and geomagnetic activity (90, 120, 150 km). Fabry-Perot Interferometers (FPI) are used to make direct measurements of neutral wind from measuring the Doppler shifts of airglow. There are fewer than 20 FPIs over the globe. There are fewer than 10 incoherent scatter radars over the globe. So continuos measurements from spacecraft (as ΔDsat measurements) can provide unprecedented global coverage of lower thermosphere wind to complement the FPI and ISR measurements. An alternative method to determine thermosphere wind from spacecraft uses very sensitive on-board accelerometers to measure the aerodynamic acceleration vector with respect to the inertial velocity from which the cross-track wind can be inferred. This method assumes the aerodynamic properties of the spacecraft to determine the wind direction and velocity (aerodynamic properties must be known). This method was recently used by CHAMP, GRACE and GOCE (Doornbos, 2011) but at significantly greater economic cost than the proposed method (as use multi million spacecraft instead of a 2.4 kg CubeSat) and without the complementary data set provided by the INMS.

There are many benefits from obtaining continuous and global in situ measure-

ments of the density, atmospheric composition and cross-track wind velocity of the lower thermosphere. Cranfield's ΔDsat, designed, built, tested and operated by Cranfield University, will obtain these data. The density and composition measurements will be taken by the INMS provided by Mullard Space Science Laboratory, and the wind velocity will be indirectly measured using 4 Steerable Fins (developed at Cranfield University) mounted on the spacecraft. To measure the wind the aerodynamic properties of the Steerable Fins will be characterised in orbit using a novel methodology developed by Cranfield (see chapter 7 on page 75), and with the help of the INMS.

9.1 General Wind Measurement Method

The method exploits the sensitivity exhibited by aerostable spacecraft to attitude changes with respect to the relative flow direction to extract wind information. The wind and atmospheric co-rotation change the flow direction with respect to the inertial velocity (measured by the GPS). This difference can be measured, as it is the difference between the equilibrium point of the aerostable spacecraft and the inertial velocity vector. Atmospheric co-rotation can be taken into account (as it is known) and the thermosphere wind therefore measured.

This method assumes a spacecraft where an attitude determination system is present and is providing attitude measurements $\vec{\theta}$. Then, differentiating these measurements or using an angular rate sensor, the angular velocity of the spacecraft $\vec{\omega}$ can be also known. Differentiating the angular velocity measurements the angular acceleration $\vec{\alpha}$ can then be known as well. With these three magnitudes and the inertia of the spacecraft (estimated or measured before launch), the torques acting on the spacecraft can be extracted using Eq. 9.1 by observing the spacecraft attitude evolution.

$$\sum \vec{T} = I\vec{\alpha} + \vec{\omega} \wedge (I\vec{\omega}) \tag{9.1}$$

The sum of torques contains torques from different sources. Equation 9.2 specifies which are these main torques. These include the aerodynamic torque, gravity gradient torque, Solar Radiation Pressure (SRP torque) and magnetic torque (from a residual internal dipole or the magnetic actuators). The torques emerging from unknown sources are included in $\vec{T}_{others}$.

$$\sum \vec{T} = \vec{T}_{aero} + \vec{T}_{grav} + \vec{T}_{SRP} + \vec{T}_{mag} + \vec{T}_{others} \tag{9.2}$$

The method then proceeds to extract the aerodynamic torque. If $\vec{T}_{aero}$ has to be computed, the other torques must be known or at least estimated. An estimation of the the other torques is possible if the geometry, inertia properties, reflectivity, residual dipole and actuator commands are known. It is worth notting, that these estimates will contain errors and hence making $T_{aero} \ggg T_{grav,SRP,mag,others}$ reduces the errors on the computed $\vec{T}_{aero}$.

The aerodynamic torques are a function of the spacecraft attitude with respect to the incident flow as shown in Eq. 9.3 and are proportional to the dynamic pressure $q = \frac{1}{2}\rho V^2$.

$$\vec{T}_{aero} = qf\left(\vec{\theta}_{flow}\right) \tag{9.3}$$

If the function $f\left(\vec{\theta}_{flow}\right)$ is known a priori (via modelling or on-orbit characterisation) then $\vec{\theta}_{flow}$ can be computed. If the inertial velocity is known (via an onboard GPS for example), the difference between the attitude with respect to the inertial velocity $\vec{\theta}_{Vinertial}$ and $\vec{\theta}_{flow}$ is only due to the presence of atmospheric co-rotation and wind. The atmospheric co-rotation velocity can be easily computed and hence the wind can be estimated. The atmospheric co-rotation can be computed using Eq. 14.22 on page 161.

The foundations of the method have been already laid out and what is left now is to derive the properties, limitations and the practical implementation of the method.

As mentioned before, a spacecraft that produce high $\vec{T}_{aero}$ and that its other torques are small in comparison is highly desirable. To avoid creating unnecessary uncertainties it would be also better to avoid any torques created by the spacecraft actuators. Hence, letting the spacecraft free fly and observe its attitude evolution which would be completely dominated by $\vec{T}_{aero}$ is desirable. Aerostable spacecraft are particularly suited for this scenario.

An aerostable spacecraft has an an attitude with respect to the flow where there are no aerodynamic torques and when there is a misalignment with respect to this attitude a restoring aerodynamic torque appears. In, general the restoring torque will not be proportional to the misalignment (not a linear relationship).

To illustrate the method and make it simpler to understand a linear restoring torque will be assumed (as it is the case for small angles in ΔDsat). Also, it will be assumed that the aerodynamic torques in the three different rotation axis (roll, pitch and yaw) are independent (that a rotation in yaw does not affect the torque in pitch). These are good assumptions if the misalignments are small (only a few degrees) and will serve the purpose to illustrate the case. When applying this method in a real mission non-simplified aerodynamic models need to be used.

Under these assumptions, the aerodynamic torque (in one rotation direction) can be then written as in Eq. 9.4. In the absence of any other torques, the spacecraft then behaves as an harmonic oscillator with an angular velocity computed using Eq. 8.3. The assumption that behaves as an harmonic oscillator only holds if the period of the oscillation is much smaller than the timescales at which the other torques (gravity gradient, SRP and residual magnetic dipole) change. That can be easily achieved with respect to the SRP and residual magnetic dipole torques. Gravity gradient changes are directly linked with the rotation of the spacecraft with respect to the Earth and hence it will change at the same frequency as the aerodynamic torques (only in pitch and roll). But as mentioned before it is assumed that gravity gradient torques will be small in comparison and hence will not dominate the dynamics and hence the harmonic oscillator assumption can still be considered valid (at least to derive the properties of the method).

$$T_{aero} = -qk\theta_{flow} \tag{9.4}$$

As it behaves as an harmonic oscillator without damping and as it can be considered that the wind fluctuations are exciting the system, then the gain of the system can be

computed using Eq. 9.5, where ω_w is the angular frequency of the driving perturbation (the wind in this case). Figure 9.1 shows this gain G.

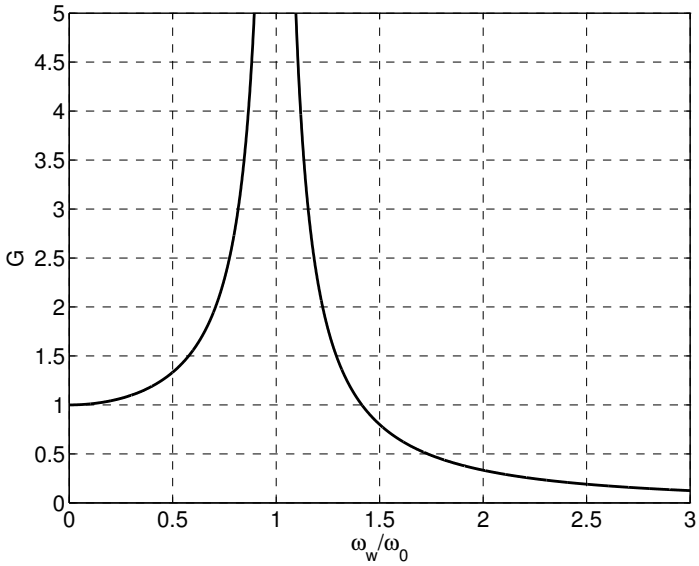

Figure 9.1: Gain of an harmonic oscillator without damping.

$$G = \frac{1}{|\omega_0^2 - \omega_w^2|} \tag{9.5}$$

This gain is useful to compute the spatial resolution of the wind measurements. As the spacecraft is flying around the Earth it flies through regions with different wind environments. This is experienced by the spacecraft as if the wind was changing through time. As the spacecraft is not sensitive to changes in very high frequencies (drop in the gain) that means that the spatial resolution is limited (changes in wind in small spatial scales will not be sensed). The minimum gain where the system is able to measure the winds is related to how accurate the spacecraft can measure its attitude dynamics (as the gain is essentially provides the magnitude of the changes in attitude derived from the perturbing aerodynamic torques at different frequencies). More accurate attitude determination and higher aerostabiliy (higher aerodynamic stiffness of lower altitude so produce higher torques) lowers the minimum gain required to measure the wind.

When the cut-off gain has been established, the other relevant parameter is the period of the harmonic oscillator. The lower the period (high angular velocity) the better. Increasing the frequency (and hence the spatial resolution) can be achieved by (see Eq. 8.3): lowering the inertia, increasing the aerodynamic stiffness (increasing k) or increasing the dynamic pressure q (by flying lower where the density is higher or by having a high eccentricity orbit to achieve high speeds during perigee).

These two parameters (gain threshold and harmonic oscillator period) determine the cut-off frequency and hence the spatial resolution of the system. The relation between the cut-off frequency ω_{co} and spatial resolution can be easily establish if the orbital velocity is taken into account. The expression is shown in Eq. 9.6, where r is the spatial resolution of the measurements. To achieve the described spatial resolution

the sampling should be at least twice as frequent than the cut-off frequency (to comply with the Nyquist criteria).

$$r = \frac{2\pi}{\omega_{co}} V_{inertial} \tag{9.6}$$

Note that it has been pointed out that having extra torques can decrease the accuracy of the method, and that is why aerostable spacecraft are the ones that are most suited for this method. Not having any actuator also means avoiding damping. In addition of producing extra torques, having damping significantly reduces the gain G of the system as shown in Fig. 9.2. This makes the effects of the wind less observable and hence is not desirable. With damping the gain G can be expressed with Eq. 9.7.

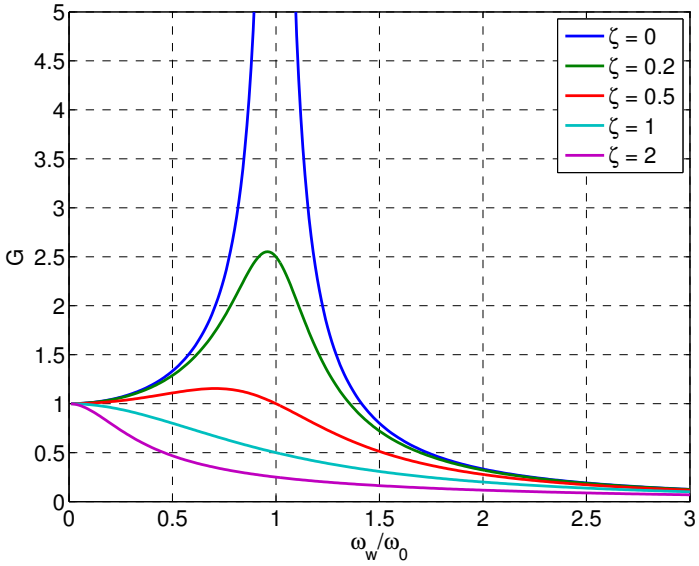

Figure 9.2: Gain of an harmonic oscillator with different levels of damping ratios ζ.

$$G = \frac{1}{\omega_w \sqrt{\left(2\omega_0\zeta\right)^2 + \frac{1}{\omega_w^2}\left(\omega_0^2 - \omega_w^2\right)^2}} \tag{9.7}$$

Damping may still to to be used to control that the amplitude of the oscillations do not grow indefinitely. Damping can be activated when the oscillations magnitude are above a certain threshold (stopping the wind measurement) and when the oscillations have decreased to a lower level stop the damping (and resume the wind measurements).

9.2 Cross-Track and Along-Track Wind Measurement

It is also worth noting that aerostability is not applicable to roll. A rotation in roll does not change the geometry of the spacecraft with respect to the flow and hence, it does not change the torque in the roll direction. Therefore, the method described here, which exploits aerostability, can be used to determine the cross-track wind but not the along-track wind.

A spacecraft geometry that produces a torque in roll will be required to measure the along-track wind. Such geometries are possible but high roll torques are difficult as they rely on aerodynamic lift, which is very small when compared to drag (see chapter 3). The amount of torque in roll changes as the relative velocity changes due to the wind (through the change of dynamic pressure). This change is small and hence it is difficult to detect. If we assume a 100 m/s wind and an orbital velocity of 7.6 km/s, the roll torque would only increase a 2.6% due to the wind. Increasing the base torque in roll makes the relative difference easier to observe (as the relative increment is applied into a bigger initial torque).

Adding a torque in roll, also makes the spacecraft spin and hence adds gyroscopic stiffness (reducing the spatial resolution of the cross-track wind measurements). Making the roll torque reverse direction frequently to avoid spin build-up may be a way around this issue. In general the along-track wind is much harder to measure.

Therefore the measurement of along-track and cross-track winds is done through separate mechanisms. Cross-track wind is measured due to changes in the pitch and yaw torque when the spacecraft attitude is not in the equilibrium point and along-track wind is measured through the change of the roll torque due to the increased dynamic pressure.

Note, that an estimate of the dynamic pressure is required when computing the cross-track winds. An iterative method where the dynamic pressure includes the cross-track wind measured (but not the along-track) is possible and will only incur into minor errors (a 100 m/s along-track wind creates only a 2.6% error in the dynamic pressure estimate).

9.3 Modelling the Uncertainties

A quick assessment of the accuracy of the final results can be easily computed propagating the uncertainties of the measurements (using the generic Eqs. 9.8 and 9.9) through the simplified formulas presented in the previous sections. This is useful to get an idea of the required accuracy on the sensors and on other estimated parameters.

$$x = f\left(a, b, c\right) \tag{9.8}$$

$$\sigma_x^2 = \left(\frac{\partial f}{\partial a}\sigma_a\right)^2 + \left(\frac{\partial f}{\partial b}\sigma_b\right)^2 + \left(\frac{\partial f}{\partial c}\sigma_c\right)^2 \tag{9.9}$$

To compute this expected accuracy a typical scenario must be selected in order to populate the uncertainties in the measurements and also the values of certain parameters. Here, the case of ΔDsat will be used. In this case:

- Wind velocity $V_w = 50$ m/s.
- Oscillation amplitude of 5 degrees.
- Orbital velocity $V_i = 7.8$ km/s with a GPS measurement uncertainty of $\sigma_{V_i} = 20$ cm/s. Corresponding to a 250 km altitude circular orbit.

- Density of $\rho = 10^{-10}$ kg/m^3 with the INMS measurement uncertainty of $\sigma_\rho = 3.3 \cdot 10^{-12}$ (10% 3σ).
- Aerodynamic stiffness of $k = 0.17$ Nm/rad with an uncertainty of $\sigma_k = 0.0057$ Nm/rad (10% 3σ).
- The rest of the torques are ten times smaller than the aerodynamic ones $T_o = \frac{T_a}{10}$ and the uncertainty is 10% 3σ.
- Inertia of $I = 0.0318$ kg/m^2 with an uncertainty of $\sigma_I = 5.3 \cdot 10^{-4}$ kg/m^2(5% 3σ).
- Attitude accuracy of $\sigma_{\theta_{inertial}} = 40$ arcsec 1σ. With filters an angular acceleration accuracy $\sigma_\alpha = 2$ arcsec 1σ can be obtained.

With this scenario, and using Eqs. 9.10-9.21, the accuracy on the resulting wind measurement can be estimated.

$$\sum T = I\alpha \tag{9.10}$$

$$\sigma^2_{\sum T} = (I\sigma_\alpha)^2 + (\alpha\sigma_I)^2 \tag{9.11}$$

$$T_a = \sum T - T_o \tag{9.12}$$

$$\sigma^2_{T_a} = \sigma^2_{\sum T} + \sigma^2_{T_o} \tag{9.13}$$

$$q = \frac{1}{2}\rho V_i^2 \tag{9.14}$$

$$\sigma_q^2 = \left(\frac{1}{2}V_i^2\sigma_\rho\right)^2 + (V_i\rho\sigma_{V_i})^2 \tag{9.15}$$

$$\theta_{flow} = \frac{T_a}{qk} \tag{9.16}$$

$$\sigma^2_{\theta_{flow}} = \left(\frac{\sigma_{Ta}}{qk}\right)^2 + \left(-\frac{Ta}{q^2k}\sigma_q\right)^2 + \left(-\frac{Ta}{qk^2}\sigma_k\right)^2 \tag{9.17}$$

$$\theta_{dif} = \theta_{inertial} - \theta_{flow} \tag{9.18}$$

$$\sigma^2_{\theta_{dif}} = \sigma^2_{\theta_{inertial}} + \sigma^2_{\theta_{flow}} \tag{9.19}$$

$$V_w = \tan\theta_{dif} V_i \tag{9.20}$$

$$\sigma^2_{Vw} = (\tan\theta_{dif}\sigma_{Vi})^2 + \left(V_i\left(1 + \tan^2\theta_{dif}\right)\sigma_{\theta_{dif}}\right)^2 \tag{9.21}$$

This method of computing the accuracy of the results only provides an estimate but is also very useful to crudely assess the sensitivity of the method to the different parameters. When a little bit of analysis is done (playing around with the different parameters) it can be concluded that (for the above scenario):

- The dominant uncertainties are the angular acceleration and in a minor degree the attitude ones.
- Better accuracies are obtained close to $\theta_{flow} = 0$ as in this point the aerodynamic torque is small and hence the uncertainties in the density and in the aerodynamic characterisation have a smaller impact. Also in this point, the angular acceleration is also small hence minimising the effect of the inertia uncertainty.
- The wind magnitude has little impact on the final uncertainty.

This sensitivity analysis can also be used to decide where to invest the effort or the funds to improve the accuracy (what is more cost effective, buy a more expensive and accurate star tracker or invest in a better inertia estimation?).

In the scenario presented the uncertainty in the wind estimation would be 4.8 m/s 1σ when the attitude with respect to the flow is $\theta_{flow} = 0$. When the θ_{flow} grows to 5 degrees then the uncertainty also grows to 26 m/s 1σ with half of the uncertainty due to the density measurement inaccuracies. This uncertainty (in the wind measurement) can be reduced by measuring close to the $\theta_{flow} = 0$ and by filtering the wind measurements (as we have assumed a cut-off frequency the winds can be oversampled and filtered to improve the accuracy).

The uncertainty of the angular acceleration α is derived from its underlying estimation method. As the most accurate attitude sensors (star trackers) do not provide directly angular velocity or angular acceleration, a good technique to obtain a good accuracy is to over sample the attitude (it can be assumed that the torque is nearly constant between samples if the sample frequency is sufficiently high) and use a Kalman filter to estimate the angular velocity and angular acceleration. To achieve a good accuracy on the angular acceleration using the filters, the attitude sensor must be able to provide measurements at much higher rate than what is required for the angular acceleration (above the cut-off frequency), so that when applying the filters the results can be averaged and still have enough samples.

Note that on the estimation of the method uncertainties, it has been assumed that $\sum T = I\alpha$, which is only true in a one dimension case. In a multidimensional case the errors associated when estimating the angular velocities of the spacecraft will also have an impact in the final accuracy (and will contaminate the measurements on the other axis).

9.4 Simulation with ΔDsat

The whole measurement chain has been simulated for the case of ΔDsat, without simplifying the dynamics or the aerodynamic models and including Kalman filters in the attitude estimation and wind output. Then, a realistic estimation of the wind measurement uncertainty can be achieved. Measuring the wind requires quite accurate attitude estimation sensors and hence that was the driving requirement to include a star tracker into the CubeSat (form more information into the CubeSat hardware please see chapter 11). The uncertainties on the parameters are derived from the sensors in the CubeSat design and the aerodynamic characterisation has been assumed to have a 5% uncertainty 3σ (reasonable if the results on chapter 7 are taken into account).

It is also worth mentioning at this point, that the ΔDsat ability to produce a torque in roll is not big enough in order to measure along-track winds and hence the CubeSat will only measure cross-track wind using its aerostable properties.

The first thing to determine is the spatial resolution. In this case the natural frequency of the system has been selected as a cut-off frequency (the natural frequency is shown in Fig. on page 102). This allows to measure close to $\theta_{flow} = 0$ (twice per cycle) and hence obtain good accuracies. The spatial resolution of ΔDsat's wind measurement is shown in Fig. 9.3. Note how altering the fins configuration can change the natural frequency of the system and hence alter the spatial resolution. As seen in the chapter 8 deflecting the fins create extra restoring torque, hence increasing the aerostability of the CubeSat and therefore increasing its spatial resolution. Note also, how the increased density at low altitudes also increases the aerodynamic torques and hence, also increases the aerostability and therefore the spatial resolution.

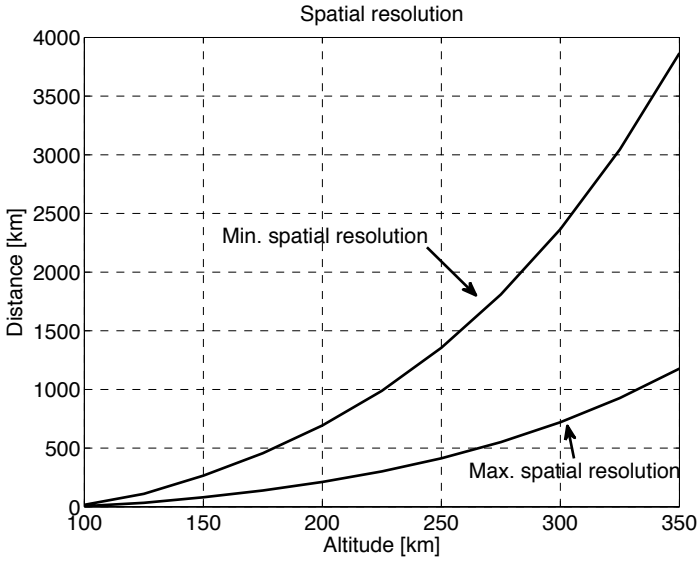

Figure 9.3: Spatial resolution of the wind measurement using ΔDsat.

Selecting a Steerable Fins configuration is a matter of scientific output and operational concerns. Significantly deflecting the fins increases the drag, making the spacecraft's orbit to decay faster and hence reducing the total number of measurements. Otherwise not deflecting the panels extends the lifetime but reduces the spatial resolution.

The simulation also includes the HWM93 (Hedin et al., 1996) wind model and the algorithm is capable of recovering the cross-track winds as shown in Fig. 9.4. Note that the HWM93 is a model of the atmospheric wind and hence may not output all the fine structure of the wind (there might be finer spatial and temporal variations in the wind that the ones suggested by the model).

A Monte Carlo simulation has been performed so that the uncertainty on the measurements can be accurately estimated. The results of this Monte Carlo simulation are shown in Fig. 9.5. It is interesting to note that the uncertainty is constant and does not decrease with the altitude. This is because the limiting factor is determined by the accuracy in the dynamic pressure, which is entirely dominated by the INMS dens-

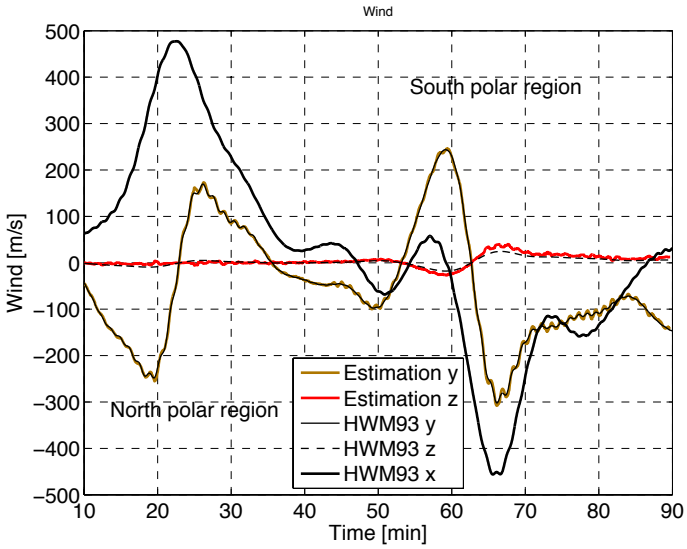

Figure 9.4: Measured winds compared to the HWM93 model for a typical 250 km ΔDsat orbit.

ity accuracy. As the INMS uncertainty has been modelled as relative to the density (10% 3σ), and it does not change with altitude, the wind measurement uncertainty is maintained nearly constant across the whole altitude range.

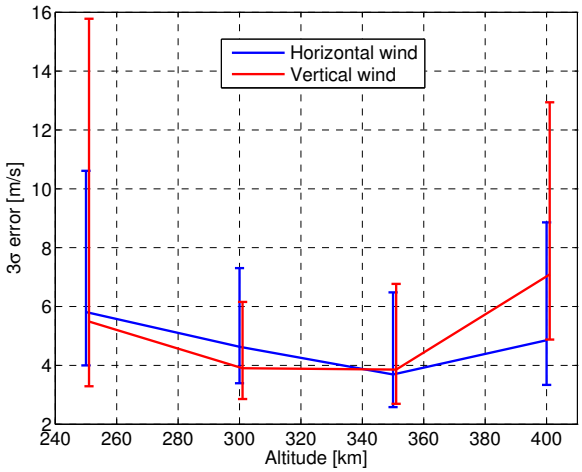

Figure 9.5: 3 σ uncertainties of the wind measurement estimation with a 90% confidence interval.

9.5 Conclusions

This novel method to measure thermospheric wind exploiting the aerostability properties of a purpose build spacecraft has been analysed. The analysis shows that it is feasible to measure cross-track wind, only requiring readily available attitude sensors and density sensors (not COTS, but available as science instruments). This method

can even be used in CubeSats, as it has been shown with the ΔDsat case. In this case, the spatial resolution is acceptable (although higher resolution would add more scientific value) and offers a wind measurement accuracy that is comparable to other wind measurement techniques, as the GOCE accelerometer based or EISCAT radar based, but at a fraction of the cost.

To improve the accuracy, better density sensors need to be developed as this seems to be the limiting factor in ΔDsat. More work has also to be done in the data processing to increase the accuracy of the method as no analysis has been done as to which type of filtering could provide the maximum benefits.

Also, considerations regarding the operations of the method have also been left outside the scope of this study, but they also deserve more work. More work is required to be able to determine where is the optimum point between platform (increase aerostability, sensor selection) and operational cost (lifetime, areas to survey) with respect to scientific value. For the case of ΔDsat, measuring the wind has been an opportunistic scientific objective and the CubeSat was not intentionally designed from scratch to achieve it. Therefore this method needs to be generalised and a mission that could, cost-effectively exploit this method to its full extend, proposed in conjunction with the science community (which may be similar to ΔDsat).

Chapter 10

Active Aerodynamic Orbit Control in ΔDsat

Using the Steerable Fins, the ΔDsat CubeSat is capable of changing its ballistic coefficient by deflecting its fins. This capability can be used to control the amount of drag that the spacecraft is experiencing. The drag of the spacecraft when in maximum drag configuration is 7 times bigger than it is when the CubeSat is in minimum drag configuration. Lift can also be created by the spacecraft but lift is very difficult to crate (see chapter 3) and hence lift forces are very small in the ΔDsat case. As a result, lift has not been considered when thinking about aerodynamic orbit control for ΔDsat (this does not mean that lift can not be useful in other situations, as demonstrated in chapter 14 on page 155).

Also, the stepper motors used, allow for 15^{o} degrees rotation resolution of the fins, hence allowing 28 different drag levels (assuming opposite panels counter-rotate). By rotating the panels, the ballistic coefficient changes, which is linked to the drag by the dynamic pressure ($q = 1/2\rho V^2$). The INMS measuring the atmospheric density and the on-board GPS measuring the inertial velocity help bridge the gap between controlling the ballistic coefficient and controlling the drag force. ΔDsat is therefore, a unique mission as it can control its drag force.

Having this amount of control authority and resolution over the drag created by the ΔDsat can be used to control the CubeSat's trajectory. This capability could then be used to demonstrate several novel aerodynamic orbit control techniques that only require control over the drag such as:

- Rendezvous with an imaginary target in a coplanar orbit.
- Collision avoidance with an imaginary debris object.
- Cluster formation flight with an imaginary cluster
- Re-entering over a predefined area.

It is clear that not all of them could be demonstrated as that involved sacrificing on the other experiments (limited effort to develop the experiments to a flight ready state and limited operational lifetime to accommodate all experiments), so the most novel and less intrusive demonstration was selected. The experiment to re-enterer over a

predefined area controlling the decay using drag was then selected. This method has been generalised and it is covered in detail in chapter 15.

This novel technique guides the spacecraft to a predefined point of atmospheric interface re-entry by adjusting the aerodynamic drag of a spacecraft in a circular orbit. If this method is employed at a sufficiently high starting altitude, any ground track point accessible by the orbit can be targeted. This method can be broken up into two different parts. The first part, consists of finding the decay profile that achieves the desired re-entry location. The second part, consists of keeping the spacecraft within this nominal decay trajectory, given the atmospheric uncertainty and other perturbations. The two parts of this method are presented in detail in chapter 15. For ΔDsat a re-entry point can be targeted with a 3σ error of less than 200 km, if the current set of sensors and actuators on-board the CubeSat are used to assess the method's accuracy.

Chapter 11

The CubeSat

In this chapter, a brief overview of the ΔDsat CubeSat hardware is provided for completeness. Having an overview of the technical design of the CubeSat is useful to understand that the method presented in this dissertation had to deal with the practical implementation issued and the limitations imposed by a real mission. Also, this overview can also help understand the challenges that have been faced, which have, in turn, shaped the science and technology demonstration objectives.

Since the project inception, the author has been deeply involved with the design of the CubeSats. Although the bulk of the development of the CubeSat has been done by MSc students, the author has done major contributions to its design. As ΔDsat is part of QB50, the team had to meet deadlines and the author helped to fill the gaps that could not be covered by MSc students. Also the author helped supervise the development effort and coordinated the production of the reviews documentation.

The design of the CubeSat has been done with contributions from (in chronological order):

- Laura Subias (MSc student) - Systems.
- Zhou (Daniel) Hao (PhD student) - Aerodynamic Attitude Control technology demonstration and attitude control.
- Adithya Kothandhapani (MSc student) - Systems.
- Vanessa Da silva (MSc student) - Steerable Fins.
- David Canales (Visiting student) - Steerable Fins.
- George Diamitriadis (MSc student) - Attitude Determination.
- Nathan Hara (MSc student) - Targeted Re-entry.
- Guillaume Lengline (MSc student) - Vibration testing.
- David de la Torre (Visiting student) - Wind determination.
- Anees Ahmad (MSc student) - Systems.
- Timinere Mackintosh (MSc student) - Thermal.

- Natalia Muñoz (MSc student) - Systems.
- Jack Longley (MSc student) - Interstage.
- Thomas Auriel (MSc student) - On-Board Data Handling.
- Alex Boulch (MSc student) - Attitude determination & Electrical.
- David Dupuy (MSc student) - Structures.
- Natalie Hunneman (MSc student) - Systems.
- Dheeraj Kodiyath (MSc student) - Thermal.
- Kaalidas Krishnan (MSc student) - Assembly Integration and Testing, Solar Cells Integration and Steerable Fins Materials selection.
- Laura Nicolas (MSc student) - Electronics.
- Vishal Pandya (MSc student) - Steerable Fins Mechanical and Manufacture.
- Bhavdeep Pancholie (MSc student) - Steerable Fins Structure.
- Shefali Sharma (MSc student) - Operations.

The advise from the Dr. John Hobbs, Dr. Stephen Hobbs, Dr. Jennifer Kingston and Dr. Peter Roberts is also acknowledged. As ΔDsat is a live project, the information contained in this chapter is probably out of date and more up-to-date information can be requested to the mission Principal Investigator Dr. Peter Roberts.

11.1 Configuration

The external and internal configuration are shown in Fig. 11.1 and 11.2.

11.2 Subsystems

The approach for ΔDsat has been to use COTS components whenever possible. Hence this approach has led to use COTS components in all the subsystems except in the Cranfield's own payload. The subsystems used with their main properties (extracted from their data-sheets) are the following:

- 2U ISIS structure with a mass 324g. Shown in Fig. 11.3a.
- Blue Canyon Technologies Thin Slice Tracker. Has a bore-sight accuracy of 6 arcsec and roll axis accuracy of 40 arcsec 1σ with an update rate of 5 Hz. Total mass 350g and $<$ 1W peak power consumption. It has a 90 deg Sun exclusion angle and a 54 deg glint free exclusion angle (Earth exclusion). Shown in Fig. 11.3b. The star tracker is required to support the wind measurement science objective and is the only adaptation done to accommodate this science objective. Note how the update rate is much higher than the required rate to support the spatial resolution of the wind measurement.

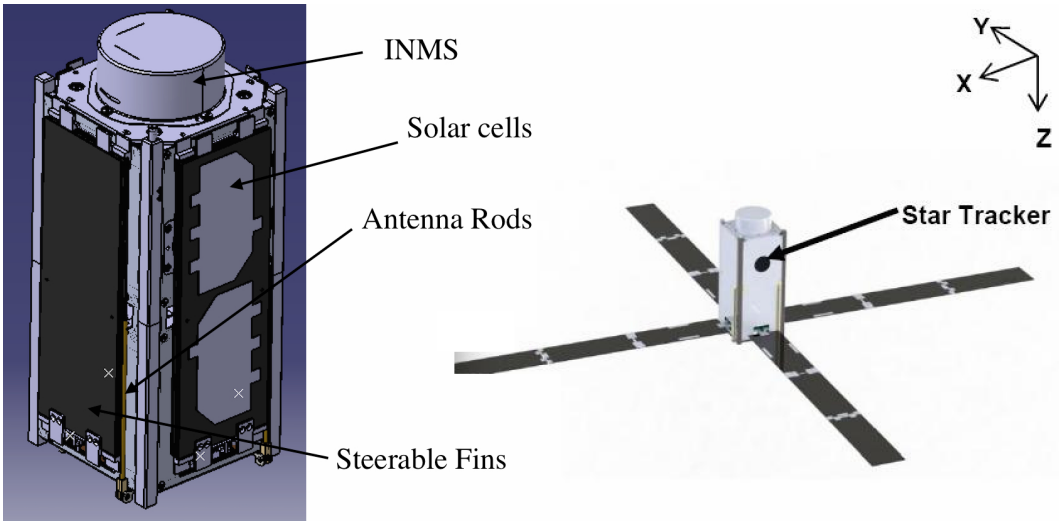

Figure 11.1: External configuration (with the Steerable Fins stowed and Deployed) of ΔDsat produced by Kaalidas Krishnan et al.

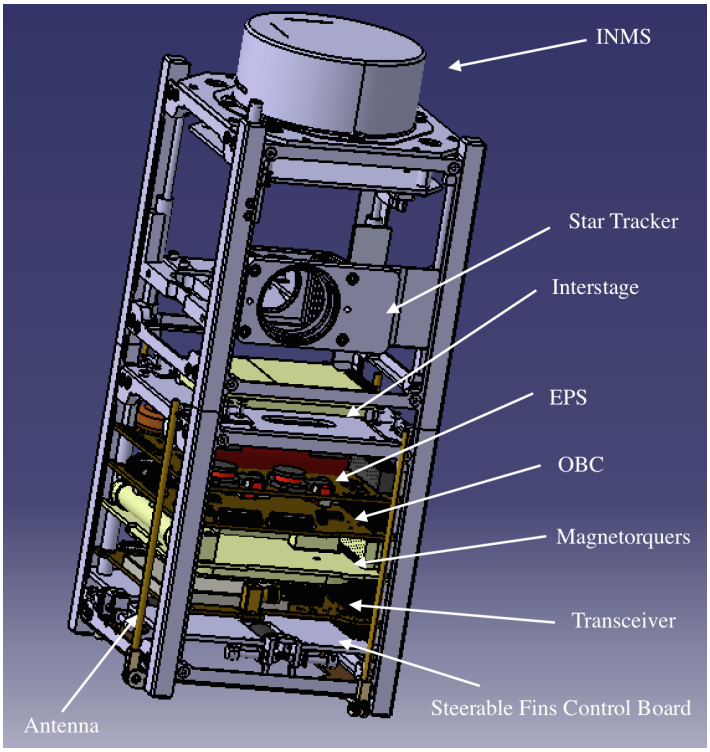

Figure 11.2: Internal configuration of ΔDsat produced by Kaalidas Krishnan et al.

- Three ADIS16260 single axis MEMS gyroscopes with a sensitivity of 0.018^{o}/s and an angular random walk of $2^{\circ}/\sqrt{\text{hour}}$. Shown in 11.3c. The gyroscope is used to measure the angular rates and used to apply the damping (for aerostability) when the star tracker is not available.

- ISIS MagneTorQuer iMTQ 3 axis magnetic torquer. Has a total mass of 195g and 0.2 $Am^2$with a specific power consumption of 1 W/Am^2 in the metal core

torquers and 2 W/Am^2 in the air core torquer. Shown in Fig. 11.3d. This is the only attitude actuator on the CubeSat (apart from the Steerable Fins).

- GOMspace NanoPower P31u power subsystem. Has a total mass of 225g and the lithium ion battery pack has a total capacity of 2600 mAh, which is over 34.6 kJ (assuming a 50% DoD), and can provide a maximum power of 14.8 W. It has 3 photovoltaic inputs capable of converting up to 30W. Shown in Fig. 11.3e.
- 12 TJ Solar Cell Assemblies 3G28A. Each assembly is ready for integration (they include the cover glass, interconnectors and a protection diode) and has an area of 30 cm^2 and an efficiency of 28%. Shown in Fig. 11.3f.
- GOMspace NanoMind A712D (shown in Fig. 11.3g) which is the CubeSat on-board computer and which has the following features:
  - Total mass of 58.85g and peak power of 340 mW.
  - 32-bit ARM7 RISC CPU.
  - Onboard temperature sensors.
  - 3-axis magnetoresistive sensor (10 milli gauss resolution) - Magnetometer.
  - 3 PWM bidirectional outputs 3.3–5V/±3A - To drive the magnetic torquers.
  - Interface to 6 analogue inputs (e.g. to photodiodes).
  - 12 SPI interfaces (e.g. to gyroscopes, extra microSD card).
  - Support for I2C, USART and CAN bus interfaces.
  - 2GB microSD card support.
  - 8-40MHz clock-speed.
- GOMSpace NanoCom U482C UHF half duplex transceiver with a GOMspace ANT430 deployable Turnstile omnidirectional UHF antenna which constitutes the communications subsystem. The total combined mass of the transceiver and the antenna is of 105g and the transceiver can transmit up to 34dBm and has a -126 dBm sensitivity. The transceiver is shown in Fig. 11.3h and the antenna integrated with the structure is shown in Fig. 11.3i. The antenna is deployed using the same hold and release mechanism used for the Steerable Fins.
- NovAtel OEM615 GPS receiver and and Maxtena-104 L1 Passive Patch Antenna. The receiver has 1.2 m, 0.3 m/s and 20 ns position, velocity and time RMS accuracy with a measurement frequency up to 50 Hz. The total mass is 24g and the peak power is below 1W. The GPS receiver is shown in Fig. 11.3j.

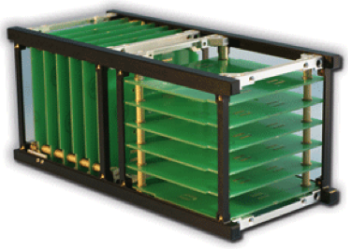

(a) 2U ISIS structure.

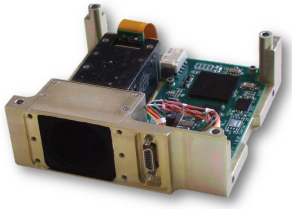

(b) BCT Thin Slice Tracker.

(c) ADIS16260 single axis MEMS gyroscope in an evaluation board.

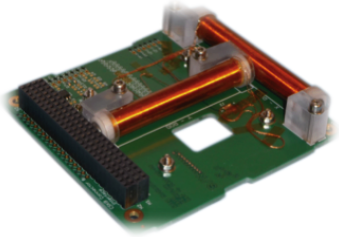

(d) ISIS MagneTorQuer iMTQ.

(e) GOMspace NanoPower P31u.

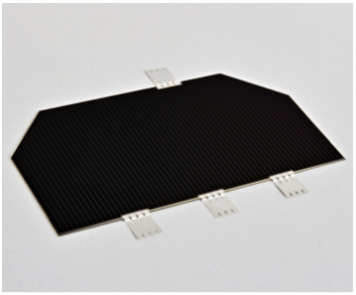

(f) AzurSpace TJ Solar Cell Assembly 3G28A.

(g) GOMspace NanoMind A712D.

(h) GOMSpace NanoCom U482C UHF half duplex transceiver.

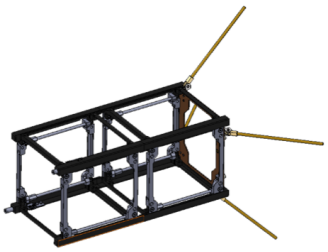

(i) GOMspace ANT430 deployable Turnstile omnidirectional UHF antenna in its deployed configuration.

(j) NovAtel OEM615 GPS receiver.

Figure 11.3: ΔDSat subsystems. Images provided by the vendors.

11.3 Steerable Fins

The Steerable Fins are one of the ΔDsat's payloads and are being developed by Cranfield University. They will enable the science and technology demonstrations specific to ΔDsat (see section 5.2). The main function of the Steerable Fins is to expose different surfaces to the flow at different incident angles. To achieve this, the Steerable Fins are composed of 4 fins that are deployed from the lateral sides of the CubeSat after ejection from the dispenser. These fins can be rotated independently along their long axis (that is why they are called steerable). This and other general characteristics of the Steerable Fins are shown in Fig. 11.4.

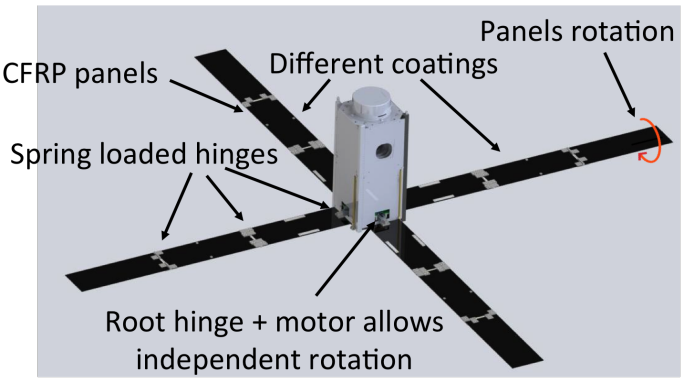

Figure 11.4: Genral view of the Steerable Fins components. Figured prepared by Adithya Kothandhapani and annotated by the author

In addition to its function as enabler of ΔDsat's scientific objectives and technology demonstrations, the Steerable Fins are used for other purposes. The Steerable Fins (the ones facing to the zenith) host the solar cells that raise the electrical power for the spacecraft (shown in Fig. 11.5).

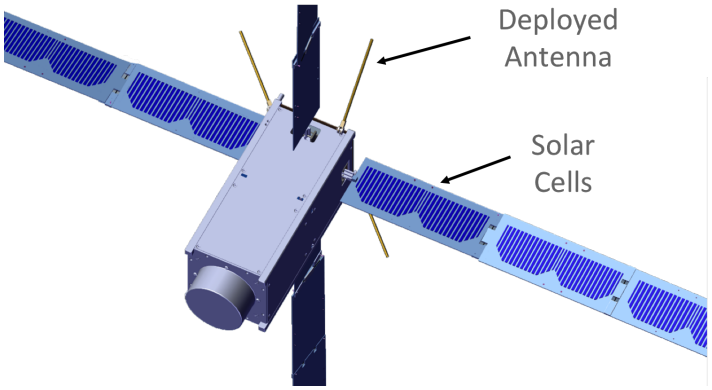

Figure 11.5: Solar cells integrated into 2 Steerable Fins. Figured prepared by Kothandhapani and annotated by the author.

As the Steerable Fins have a high surface area, this arrangement is sufficient to provide all the power required for the CubeSat and is a far superior solution than a body mounted solar cells arrangement. The aerodynamic properties of the Steerable

Fins also provide aerodynamic torques that help the CubeSat maintain its nominal attitude with its long axis pointing towards the flow direction. In technical terms the Steerable Fins provide static aerostability (see sec. 8). These aerodynamic properties of the Steerable Fins help reduce the requirements of the attitude control subsystem.

The Steerable Fins are stowed during launch and then deployed after the CubeSat is ejected from the dispenser. Each Steerable Fin is composed of three panels that are folded in a concertina fashion in order to be stowed along the long sides of the CubeSat. When stowed the Steerable Fins make use of the extended volumes available in the dispenser. Therefore, the thickness of each Steerable Fin when folded (stack of 3 panels) must be less than 9 mm. The inter-panel hinges on the Steerable Fins are spring loaded and hence the Steerable Fins will automatically deploy after they are released. The deployment sequence is shown in Fig. 11.6.

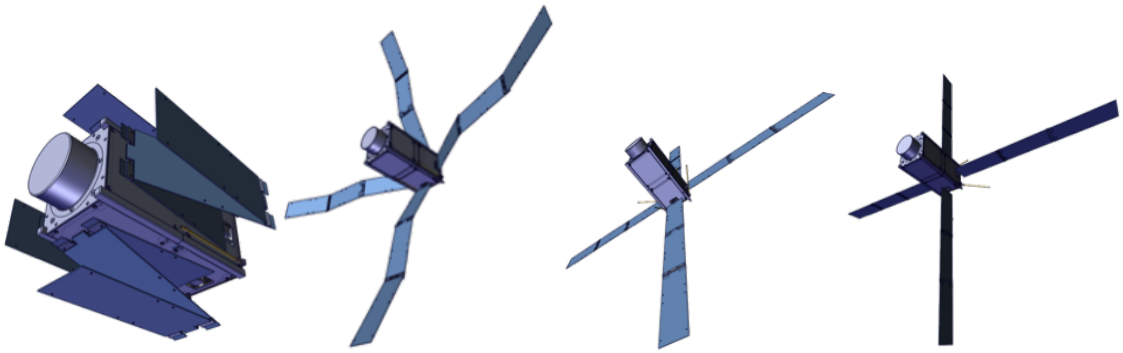

Figure 11.6: Steerable fins deployment sequence. Figure prepared by Kothandhapani.

The inter-panel hinges are designed so that the springs continue to apply torque even when the Steerable Fins have been completely deployed. The hinges include small flaps that physically limit the deployment of the panels and therefore, the residual spring torque is used to ensure that the Steerable Fins are kept deployed and properly aligned for the entire duration of the mission (to keep them in place and aligned even if the spacecraft is tumbling). The inter-panel hinges are made of aerospace grade aluminium with steel fixings and steel torsion springs.

As the inter-panel hinges are spring loaded, the Steerable Fins have a natural tendency to deploy and hence they must be restrained whilst the CubeSat is inside the dispenser. This is achieved through the Hold & Release subsystem. This system consists of a single 0.2 mm UHMWPE wire that is tied around the CubeSat in order to hold the Steerable Fins and also the ANT430 UHF deployable antenna system. When the spacecraft is ejected, a thermal cutter consisting of 0.315 mm Nichrome wire, which when subject to resistive heating, acts as a thermal knife and cuts the UHMWPE wire, releasing the Steerable Fins and the antennas (there are multiple redundant thermal cutters).

When stowed, the Steerable Fins need to survive the launch loads. To achieve this whilst maintaining an overall low profile (less than the 9 mm allowed by the deployer), the Steerable Fins panels are made of 1 mm thick CFRP and the panels assembly is preloaded by the UHMWPE wire. With these two measures, the rattle between the panels is avoided and the natural frequency of the assembly is raised to ∼330 Hz (above the 90 Hz requirement imposed by the launch vehicle). To achieve

the preloading, spacers are located between the different panels to give assembly the appropriate shape. Figure 11.7 schematically shows this preloading and the disposition of the spacers.

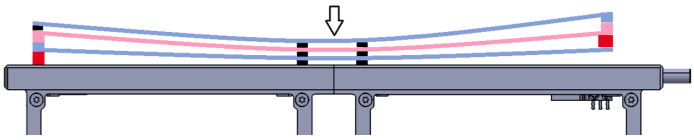

Figure 11.7: Steerable Fins pre-tensioning to increase the natural frequency. Picture prepared by Vanessa da Silva.

Being able to independently rotate each Steerable Fin is a very important design feature. This rotation is achieved through a micro stepper motor that is linked to the panels via the root hinge. This hinge, which also secures each Steerable Fin to the CubeSat structure, is able to support 2 independent rotations: the rotation associated with the fin deployment and also the rotation of the whole fin (when deployed) along its long axis. In addition, the board that will hold the stepper motors, will also hold the stepper motor drivers and the electronics to interface with the rest of the CubeSat and these drivers. This electronics board is currently being designed but will interface with the rest of the CubeSat using an I2C data bus and will be powered with the 5V bus.

11.4 Budgets

The mass and power budget of the CubeSat are shown in Fig. 11.8 and 11.9. Note that the mass goes over the maximum of 2kg allowed by QB50. A waiver was obtained to increase the maximum mass to 2.4 kg and the design is currently compliant (by a small margin).

The power budget shows the power demand during the 2 main operational modes. In Standby mode the CubeSat is just waiting in aerostability (uses its aerostability properties to maintain its attitude with respect to the flow and the star tracker measures the attitude) and charging its batteries. This mode has some equipment switched off and hence, it acts as a power saving/raising mode. The Science mode also uses aerostability, but it assumes that science experiments are taking place and hence the INMS and the GPS boards are active, therefore it is a more power hungry mode.

As the insertion LTAN is not fixed (expected from 8 am and 2 pm) and the inclination is not completely Sun-synchronous, producing a 4hr LTAN drift during the entire mission, the potential range of LTANs experienced by the CubeSat can be from 8 am to 6 pm. This wide range of LTANs combined with the roll restrictions imposed by the Star tracker (has Sun and Earth exclusion constrains), results in a significant difference between the energy that can be raised at different LTANs. The energy raised on these different scenarios is shown in Fig. 11.10. Due to the symmetry in Sun-Earth geometry between am and pm LTANs the energy raised is also symmetrical. An important aspect is that when ΔDsat's LTAN drifts across noon (towards pm LTANs) then the spacecraft will need to roll 180^{o} (flip) to reorient its star tracker to the most favourable direction and also rotate 180^{o} the fins with the solar panels (so that they

ΔDsat Mass Budget

System	Component	Quantity × Unit Mass	Total (g)	System Total (g)
Structure	ISIS 2U Structure	1 × 324	324	361.68
	Long Spacers	8 × 0.6	4.8	
	Margin	*10%*		
ADCS	BCT Nano Star Tracker (+20% margin)	1 × 200	200	484.9
	ISIS IMTQ	1 × 195	195	
	NovAtel GPS	1 × 24	24	
	L1 Patch Antenna (+10% margin)	1 × 4.4	4.4	
	Sun Sensors (+20% margin)	12 × 0.6	60	
	ADIS16265 Gyro	3 × 0.5	1.5	
EPS	NanoPower P31u	1 × 225	225	325.80
	Azur Space Solar Panel (+20% margin)	12 × 7	100.8	
Comms	NanoCom U482C	1 × 75	75	105.00
	NanoCom ANT430	1 × 30	30	
OBC	NanoMind A712D	1 × 55	55	62.70
	microSD card	2 × 3.85	7.7	
QB50 Payload	INMS Unit (+30% margin)	1 × 300	300	300.00
Steerable Fins	Panels and inter-panel hinges	4 × 75.185	300.74	490.392
	Springs and Fasteners	unknown	unknown	
	Root hinge and motor	4 × 15.48	61.92	
	Motor mountings	4 × 1	4	
	Control Board	1 × 42	42	
	Margin	*20%*		
Interstage	Interstage Board	1 x 24	24	91.902
	Corner Stops	4 x 0.6463	2.5852	
	Springs	4 × 1.75	7	
	Bolts, Nuts and Screws	1 x 5	5	
	GPS Fixing Bolts	4 × 2	8	
	Other (Thermal Cutters, MOSFETS, connectors and uC)	1 × 30	30	
	Margin	*20%*		
Misc.	Harnessing	1 × 106	106	127.2
	Margin	*20%*		
		Total Mass		**2349.574**
		Maximum mass allowable		**2400.00**
		Mass Remaining		**50.426**

Figure 11.8: ΔDsat mass budget. Prepared by Natalie Hunneman.

keep facing towards the zenith direction). If this is not done ,the roll margin (to meet star tracker constrains) is reduced and the energy raised is also severely reduced. This scenario is shown in the 1pm no flip case in Fig. 11.10.

As it can be noted from Fig. 11.10, the CubeSat does not raise sufficient power to satisfy the energy needs during science operations (is that under certain conditions as LTANs close to noon) and hence energy raising orbits (without science and in Standby mode) will be required in those scenarios to replenish the batteries.

ΔDsat Power & Energy Budget

System	Component	Average Power (mW)	Peak Power Demand (mW)	Science Mode		Standby Mode	
				Duty Cycle (%)	Duty Cycle Power (mW)	Duty Cycle (%)	Duty Cycle Power (mW)
ADCS	BCT Nano Star Tracker	700	1000	100	700	100	700
	ISIS iMTQ	800	800	20	160	20	160
	NovAtel GPS	1000	1000	100	1000	0	0
EPS	NanoPower P31u	125	125	100	125	100	125
	AS Solar Cells	0	0	100	0	100	0
Comms	NanoCom U482C	5500	5500	10	550	10	550
	GS Antenna	0	0	100	0	100	0
	L1 Patch Antenna	0	0	100	0	100	0
OBC	NanoMind A712D	150	340	100	150	100	150
Payload	INMS Unit	646.8	951.6	100	646.8	0	0
	Aerofoil Control Board	2000	2000	10	200	0	0
Misc.	Interstage Board	100	100	50	50	50	50
	Harness	0	0	100	0	100	0
	ISIS 2U Structure	0	0	100	0	100	0
Margin		*20%*			*0%*		*0%*
Total Average Power		13226.16					
		Total Power during Science Mode			3581.8		
				Total Power during Standby			1735.0

Figure 11.9: ΔDsat power budget. Prepared by Natalie Hunneman.

ΔDsat Energy in different LTAN's (12 solar cells)

LTAN	Average Energy Raised per orbit [kJ]	% Sunlight period of the orbit	% Unused Average Energy per orbit, Science Mode	% Unused Energy per orbit, Standby
8 am / 4 pm	32.85	63.58	41.37	71.60
9 am / 3 pm	27.56	59.61	30.18	66.18
10 am / 2 pm	23.42	57.86	17.88	60.22
11 am / 1 pm	20.01	55.39	3.85	53.43
12 pm	17.53	49.94	-9.75	46.84
1 pm (no flip)	15.70	47.81	-22.67	40.58
5 pm	45.14	76.80	56.87	79.11
6 pm	55.34	100	65.24	83.16

Figure 11.10: Energy raised by the CubeSat at different LTANs and energy margin at different operational modes. Prepared by Natalie Hunneman.

11.5 Project History and Current Status

The inception of the ΔDsat mission took place in late 2011 and in November 2011 a letter of intend was sent to VKI to express Cranfield's interest in participating into the QB50 mission. During 2012 the science case regarding the study of rarefied-gas aerodynamics was developed (with some financial support from the UK Space Agency through a CubeSat Mission Concept Study grant). After the initial assessment of the science case scientific merit, during the summer of 2012, an initial feasibility study of the CubeSat design was done by an MSc student in collaboration with the author. That study outcome demonstrated the technical feasibility of the concept. By the end of the summer of 2012 the initial science case was also finished (rarefied-gas study paper (Virgili and Roberts, 2013) submitted in December 2012). The first bids to secure funding were also submitted a few months later. The first to the Natural Environment Research Council (NERC) bid was submitted during December 2012.

During the 2012-2013 academic year the work on the CubeSat design ramped up,

adding 4 Cranfield MSc students to the task (with their extended thesis related to the ΔDsat CubeSat). Preliminary Design Review was passed in March 2013 with the UKSA in the reviewing panel. After the PDR, a few more MSc students doing Individual Research Projects related to ΔDsat joined the project. At that point, the additional opportunistic science objectives and technology demonstrators were included into the project scope.

At the end of the 2012-2013 academic year, Zhou Hao, who had been working on the project as an MSc student, started his PhD at Cranfield and took over the aerodynamic attitude control technology demonstration and also was put in charge the supervision of the development of the ΔDsat's ADCS subsystem. During the summer of 2013, Cranfield was notified that the NERC bid had been rejected (the science case for ΔDsat was not solid enough by the time the bid was submitted).

At the beginning of the academic year 2013-2014 the team submitted the documentation for the Critical Design Review (November 2013) with the review itself taking place a few weeks later. The UKSA and MSSL joined the CDR review panel. During CDR, waivers for the mass and downlink framing requirements were requested. The CDR was closed in mid 2014 with the waivers granted.

In the 2013-2014 academic year more MSc students joined (doing either extended thesis, Group Design Project or Individual Research Projects) and the team was kept with approximately 10 team members throughout the year. The NERC bid was resubmitted in January 2015. It was refocused to portray the wind measurement as the mission main scientific objective. The bid included the collaboration of UCL for the wind measurement analysis (to engage with the atmospheric modelling user community).

During summer 2014 (during the time of writing) the NERC bid was also rejected given the tight timeline of the project (high risk), although its scientific case scored very high. Given the lack of funds and that the Assembly Integration and Testing Review was coming in October 2014 (and that by then all hardware bits should have been at Cranfield ready for integration), the continuity of ΔDsat as a QB50 mission is currently in question. Other sources of funding that could still add ΔDsat into the QB50 launch manifest are currently being explored. Given the reduced time margin to receive the required funding, the most probable option is to re-align ΔDsat to fly on future flight opportunities. This is the scenario that it is currently being evaluated and pursued.

During this development time important progress has been achieved which will be extremely useful when the next launch opportunity arises. The main milestones achieved are: solid science case, a design that has passed CDR (hence showing understanding and capability to design spacecraft) and functional prototypes of the Steerable Fins (working towards an Engineering Qualification Model). It is expected that only minor modification into the CDR design would be required to fly ΔDsat on other flight opportunities.

Chapter 12

Conclusions and Future Work

This part contained an overview of the ΔDsat mission with details of its scientific objectives and the methods used to achieve them.

The mission original aim was to provide a platform where experiments on spacecraft aerodynamics (rarefied-gas aerodynamics) could be performed. The aim of these experiments is to provide useful data that can advance the knowledge on which are the mechanisms that create aerodynamic forces (on gas-surface interactions). This knowledge, will then lead to better spacecraft designs (with minimum drag in VLEO or maximum drag in drag-sails for example). Having a better understanding of spacecraft aerodynamics has also a positive impact on several other spaceflight related fields such as: more precise orbit propagation and more accurate debris evolution models.

For these experiments to provide meaningful and accurate data across a wide range of incidence angles and altitudes, a completely novel method has been envisioned and a mission (ΔDsat) has been developed to support it. The particular implementation of the method on ΔDsat has been analysed, and it can be safely asserted, that the missions, if flown, is capable of providing meaningful and accurate data. It can determine ratios of drag coefficients of 4 different surface types, at different incidence angles with an accuracy better than 5% 3σ when operating at low altitudes (<380 km). To achieve it, the mission carries a mass spectrometer (to determine the atmospheric density) and a set of Steerable Fins (payload developed at Cranfield) that expose the different test surfaces to the flow.

For this mission concept not be left at the mission concept stage, ΔDsat has been proposed for flying in the QB50 constellation and a design that has cleared out CDR has been produced. ΔDsat has been designed to be part of QB50, as this will provide the mission with a free mass spectrometer and access to the in-situ atmospheric measurements of the other 50 QB50 CubeSats.

Being part of a real mission, with tight schedules and with design reviews, meant that the mission and the method, have had to face a reality check which has helped refine both. Unfortunately, due to funding issues, ΔDsat will probably not fly in QB50. The work done until now has put this mission concept in a very privileged position when the next flight opportunity arises.

The method to provide spacecraft aerodynamic data, although it has only been analysed for the ΔDsat case, can be easily adapted for other missions or scenarios. The main design drivers have been identified. These are: need of a GPS, an atmo-

spheric density sensor and having the test surface areas to create much more drag than the rest of the CubeSat (to achieve a good signal to noise ratio). So, if other flight opportunities arise, where the ΔDsat design can not be recycled, the analysis done so far should be enough to produce a strong science case and develop a technically sound mission concept very quickly. This is then, another area where future work could focus. Generalise the method and come with mission concepts that would exploit the method and be competitive (against other science missions).

One thing that has been left out of the scope of this dissertation is the surface type selection. As important as the method to characterise the aerodynamic properties of the test surfaces is selecting interesting test surfaces to characterise. This is a complete different topic and requires a skill set and a background knowledge substantially different from the ones required to develop the method presented in this part. Understanding which surfaces have the potential to not adsorb atomic oxygen, or envisioning methods to remove this atomic oxygen, requires a deep understanding of surface chemistry. The author acknowledges the urgent need to have an initial assessment of which would be the most interesting test surfaces to fly (when practical considerations are included). This would round-off the science case.

A requirement of the method is for the spacecraft to be aerostable. ΔDsat has then been engineered to be aerostable, and it exhibits a significant degree of aerostability (sufficient to be considered its primary attitude control mode). Aerostability is not something new, but that it has not been studied in great detail in the past. Increasing interest in VLEO has rekindled the interest in aerostability. ΔDsat then, presents the opportunity to demonstrate aerostability, test its performance (measure its properties with different Steerable Fins and damping configurations) and push it to a flight ready state. Also, given the Steerable Fins ability to rotate, ΔDsat is capable of demonstrating active aerodynamic damping. This damping method is completely novel. In general, aerostability is a property that could be very useful for VLEO spacecraft and any effort made to increase its matureness is beneficial for VLEO concepts.

In aerostability not a lot of extra work is required. The aerodynamic properties have been estimated, the control algorithms (damping) implemented and the whole system simulated. The only activities left to do are: to design the experiments (and the test plan) to measure its performance and fit them into the CubeSat operations plan.

An area where more work is required is in active aerodynamic damping. In this area, only the concept has been envisioned an a simple damping method has been simulated in order to demonstrate its feasibility. More work is required to optimise active aerodynamic damping (which is the optimum Steerable Fins configuration and rotations?) and then, a test plan need to be developed.

Thanks to the aerostability properties, a novel technique to measure thermospheric wind has been envisioned and initially analysed. This method has attracted the interest of several researchers in the atmospheric science field (as Dr. Anasuya Aruliah from UCL). Apparently this novel method can provide similar performance (resolution and accuracy) that current ground-based and space-based methods but at a fraction of the cost. This method has been only briefly studied, as it was one of the later opportunistic science that was explored. This novel method deserves a lot more effort, mainly to properly characterise its performance and optimise the data processing chain (specially

how to extract the angular velocity and filter the wind results). In addition, this method can be generalised and potentially, more effective and competitive mission concepts can be proposed.

The ΔDsat CubeSat design, although in an advance stage, has still a lot work left. Specially critical are the operations, an area that should deserve more attention in the future. ΔDsat has an inherently short lifetime as it being deployed in a 380 km altitude. This lifetime is further shortened by the rarefied-gas experiments, which create extra drag. Therefore, the number of experiments that can be done is limited and not all combinations of materials and incidence angles can be tested in a wide range of altitudes. There needs to be a certain degree of planing in order to maximise the science output (considering also all the missions science and technology demonstration objectives) of the mission. Summarising, the following questions need to be answered: When are the experiments to be conducted?, In which order? and What is the impact on the rest of the CubeSat derived from these science operations (in terms of power and data generations)?.

For its capabilities and cost-effectiveness, ΔDsat is a mission that is worth pursuing in the near future. ΔDsat can deliver world-class science outputs, and it does so using a tiny spacecraft and at a fraction of the cost of traditional science missions (delivers great value). In addition, this mission can be entirely developed by a university and hence it can also have an important educational impact (as it has had in Cranfield University during its development until now).

Part III

Aerodynamic Orbit and Attitude Control in the VLEO range

Introduction

Lowering the operational altitude of spacecraft below 450 km can provide significant benefits, specially for Earth Observation (EO) missions when compared to traditional high altitude ∼600 km orbits (Aguttes et al., 2005). The main benefits that Very Low Earth Orbit (VLEO) provide are: increased resolution on optical payloads, increased radiometric performance, increased geospatial accuracy, higher mass available from the launcher, increased surveillance footprint, no de-orbit required (aerodynamic drag becomes an asset at the end of life) and lower debris flux (see chapter 4 on page 45). Some examples of missions that fly or have recently flown in these orbits are: CHAMP (German mission that performed atmospheric and ionospheric research), GRACE (NASA mission that studied the Earth's gravity field), GOCE (ESA mission that studied the Earth gravity field), SWARM (ESA mission that is studying the Earth's magnetic field), and ADM-Aeolus (planned ESA mission capable of performing global wind-component-profile observations). The ISS also flies in this range for some of the benefits mentioned above (mainly increased available payload mass from resupply vehicles). There is a growing interest in flying more EO missions in the VLEO range in order to exploit the described benefits.

Flying this low has also disadvantages, with the main one being aerodynamic drag. Drag makes spacecraft's orbit decay, potentially limiting its operational lifetime. The atmospheric density increases exponentially as the altitude decreases, thus in VLEO the atmospheric density is significant and the aerodynamic forces can be one of the major perturbations in the spacecraft orbit and attitude. The effects of these forces have been traditionally seen as negative and hence the current approach is to avoid them (flying higher) or compensate them (using drag compensating propulsion and the attitude actuators counteracting aerodynamic torques).

But aerodynamic forces can also be used to benefit the mission, hence making these VLEO concepts more attractive. Specifically, aerodynamic forces can be used to control the orbit and the attitude of spacecraft. By using these forces the performance of the orbit and attitude control systems could be increased (providing unique capabilities or saving power, mass or propellant) and their resilience could also be boosted (providing back-up means to control the orbit or attitude when the primary actuators fail).

The idea of exploiting aerodynamic forces is not new. Some research has already been conducted in order to use aerodynamic drag to: perform an aerocapture, control a spacecraft orbit, rendezvous, do formation flight and to do constellation maintenance (Vinh et al., 1986; Leonard et al., 1989; Miele, 1996; Bevilacqua and Romano, 2008; Varma and Kumar, 2012; Putnam and Braun, 2013; Horsley et al., 2013). The use of aerodynamic forces to crudely control the attitude of a spacecraft has also been proposed in the past (Ravindran and Hughes, 1972; Pande and Venkatachalam, 1979; Psiaki, 2004). Although these publications suggest some of the potential applications and outline some of the methods that could be used to exploit them, they only scratch the surface of what it is possible. In addition, the research conducted so far usually simplifies the environmental conditions and do not take into account the issues that arise when implementing these techniques on an operational spacecraft. In this dissertation two new methods that use aerodynamic forces to control the orbit are presented in detail and practical implementation issues discussed.

Before discussing this two new methods a chapter is devoted to generalise the aerostability technique described in chapter 8 for ΔDsat, to the CubeSat form factor in general. In this next chapter 13, different aerodynamic surfaces to be added to the CubeSat body to achieve aerostability are proposed. These geometries are used to determine the effect of the different parameters and define the available design space. Finally, an outline of the different damping methods that could be used is presented.

Then, this part moves on to describe the two new methods that use aerodynamic forces to control the orbit. The first one uses aerodynamic drag and lift to change the inclination of a decaying spacecraft in order to maintain the Sun-synchronous aspect of a decaying orbit (covered in chapter 14). The required lift to drag ratio is in the order of 1.0-1.6, which is not currently achievable with currently characterised surfaces (although it is theoretically possible). This requirement could be bypassed if drag compensating propulsion is used in order to lower the drag to lift ratio requirement to a manageable magnitude.

The second method proposed, controls the atmospheric re-entry interface (the location of the burn-up or the start of significant heating) by modulating the drag and hence controlling the decay rate. This method could be applied to drag-sails carrying big spacecraft that would partially survive re-entry and make them re-entry over unpopulated areas. If this method is applied to ΔDsat it only needs to start modulating its drag at an altitude of 250 km to achieve global coverage and would re-enter within 200 km of its re-entry target location. This method is covered in chapter 15.

Finally a conclusions and future work chapter is added to discuss how this novel line of research could continue in the future.

Chapter 13

Optimising Aerostability on CubeSats

13.1 Introduction

The number of micro- and nano-satellites that are being launched is growing significantly every year. Figure 13.1 shows the track history and current forecasts according to Buchen and DePasquale, 2014, with the vas majority of the growth being driven by CubeSats. This high number of forecasted spacecraft can be a problem if all of them are launched into traditional high altitude orbits (∼600 km). Low decay rates at high altitudes can mean that in coming years the number of spacecraft in these orbits can raise significantly, increasing the risk of collision and increasing the probability for the Kessler syndrome to occur (Klinkrad, 2006).

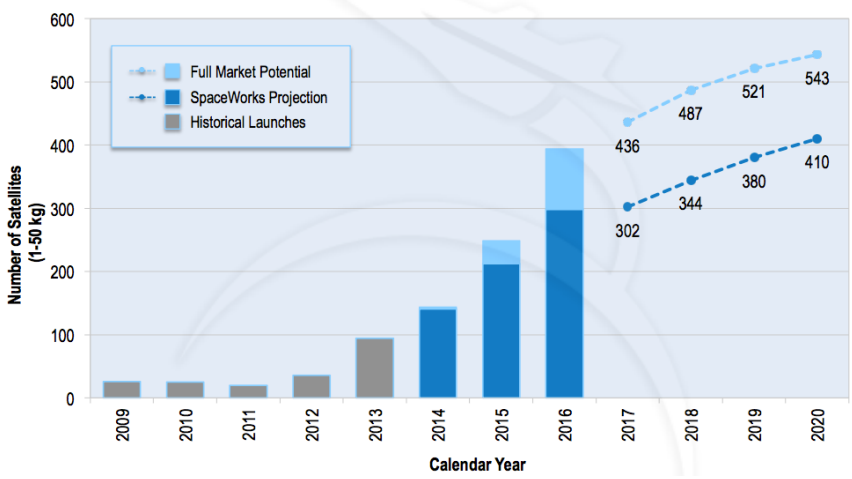

Figure 13.1: Past and forecasted number of spacecraft below 50 kg. Extracted from Buchen and DePasquale, 2014.

An alternative orbit for this growing number of CubeSats can be in Very Low Earth Orbit (see chapter 4 on page 45). The increased atmospheric drag in VLEO ensures that spacecraft will decay quickly and that these orbits will reman clear of debris. In addition, flying in VLEO offers several benefits for Earth observation missions that enable smaller sensors offer the same level of performance than bigger sensors in traditional high altitude orbits. The combination of these two benefits (lower debris build-up

and increased performance of Earth observation sensors) is already being exploited by the Earth observation constellation of CubeSats deployed by PlanetLabs Inc.

In a VLEO, having aerostability can be a great advantage, specially in CubeSats, where current attitude control actuators are bulky and not very capable yet. The design of such aerostability systems for CubeSats is still very open, as no existing CubeSat mission has made use of aerostability. In this chapter a simple way to achieve aerostability is proposed (adding small aerodynamic surfaces). Three different configurations (inspired by the ΔDsat design) are explored and their properties analysed. This chapter shows how CubeSats can be made aerostable, which are the important parameters and how these parameters changes (defines the trade space).

To read this chapter the reader should be familiar with the aerostability concepts that have been presented in chapter 8 on page 99.

13.2 Aerodynamic Properties of a Bare CubeSat Body

With the Sentman model the aerodynamic properties of a bare CubeSat body (without deployables or other aerodynamic surfaces) can be analysed (for more details on the Sentman aerodynamic model see chapter 3). The assumed nominal attitude can be seen in Fig. 13.2. This attitude has the x axis aligned with the flow and the z axis in the direction of the nadir (similar to the ΔDsat nominal attitude).

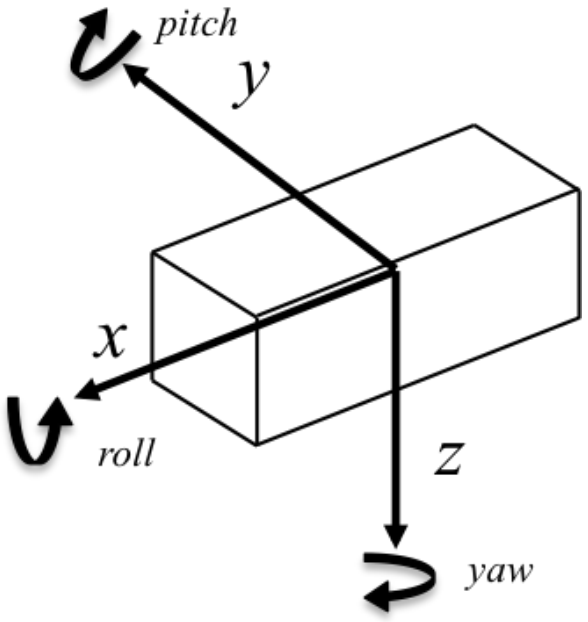

Figure 13.2: Schematic view of a 2U/3U CubeSat with its reference system. x axis aligned with the relative flow and z axis along the nadir direction.

The objective for the aerostability system will be then, to achieve a specific attitude with respect to this nominal frame, specifically to maintain the CubeSat aligned with the relative flow (keep the x axis aligned with the flow). As it is usual with aerostability systems, roll will not exhibit aerostability and other control methods will be required to maintain the desired roll attitude.

From this nominal flow pointing attitude, it can be noted that pitch and yaw are analogous and that rolling does not have any aerodynamic effect. It is also assumed, that the CubeSat mass is uniform and the masses for the different CubeSat standard sizes are: 1 Kg for 1U, 2 Kg for 2U and 3 Kg for 3U. The CubeSat lengths are assumed to be 100 mm, 200 mm and 300 mm for the 1,2,3 U CubeSats.

Surprisingly, for the geometry of a bare CubeSat body, if the centre of mass is located in the geometric centre of the CubeSat, the aerodynamic torques from the frontal face ($+x$) and the torques from the lateral sides ($\pm y$) cancel out, nearly perfectly, under yaw. The top and bottom surfaces ($\pm z$) don't produce any torque under yaw, and if pitch is considered, then the same effect happens but switching the $\pm y$ surfaces for the $\pm z$ ones. Therefore, the CubeSat body is aerodynamically neutral (for all CubeSat sizes), that is, that its attitude will not change due to aerodynamic forces.

It also has to be noted that this is if the centre of mass is in the CubeSat geometric centre. If the centre of mass is in the frontal part the CubeSat will be statically stable, and if it is located at the back the CubeSat will be statically unstable.

13.3 Stabilising Surfaces

An option to achieve statical stability is then to locate the centre of gravity closer to the front side than to the back one. If this is impractical or if higher restoring torque is required then stabilising aerodynamic surfaces can be added to the CubeSat.

Figures 13.3a, 13.3b and 13.3c show three different configurations that include aerodynamic surfaces that provide this added stability. These different configurations are clearly inspired by the ΔDsat designs and other configurations/geometries may be possible (and potentially more efficient). All of these aerodynamic surfaces in the proposed configuration, are located towards the back of the CubeSat (-x face) and will exhibit different aerodynamic properties and may present different advantages and disadvantages (in practical terms and for different missions).

Figure 13.4 shows the torque responses ($A_{ref} l_{ref} C_T$) for the example configurations and for different offset (yaw or pitch) angles. It has been assumed that these extra aerodynamic surfaces have a surface of 10 cm^2. As it can be seen in this figure, all the configurations provide a restoring torque, with configuration 13.3a and 13.3b being the most effective (as have the higher slope).

Another important aspect is the aerodynamic stiffness. This is, the torque slope at zero pitch and yaw ($A_{ref} l_{ref} C_T/^{\circ} = m^3/\,\text{deg}$ or m^3 if radians are used). The aerodynamic stiffness has been also defined in chapter 8 and represented by k. Figure 13.5 shows the aerodynamic stiffness for the different configurations at different altitudes. As it can be seen the aerodynamic stiffness increases slightly with altitude, due to the changes in orbital velocity, atmospheric composition and temperature.

Finally, if the CubeSat is flying sufficiently low, its lifetime can be severely limited by drag. Then, the efficiency of the aerostability system may be another parameter may be of interest. This efficiency can be computed using the ratio of the aerodynamic stiffness to the CubeSat drag coefficient ($k/A_{ref} C_d$). This parameter indicates the efficiency of the CubeSat aerodynamics to create a restoring torque with minimum added drag. This parameter is nearly constant with the altitude but but varies greatly

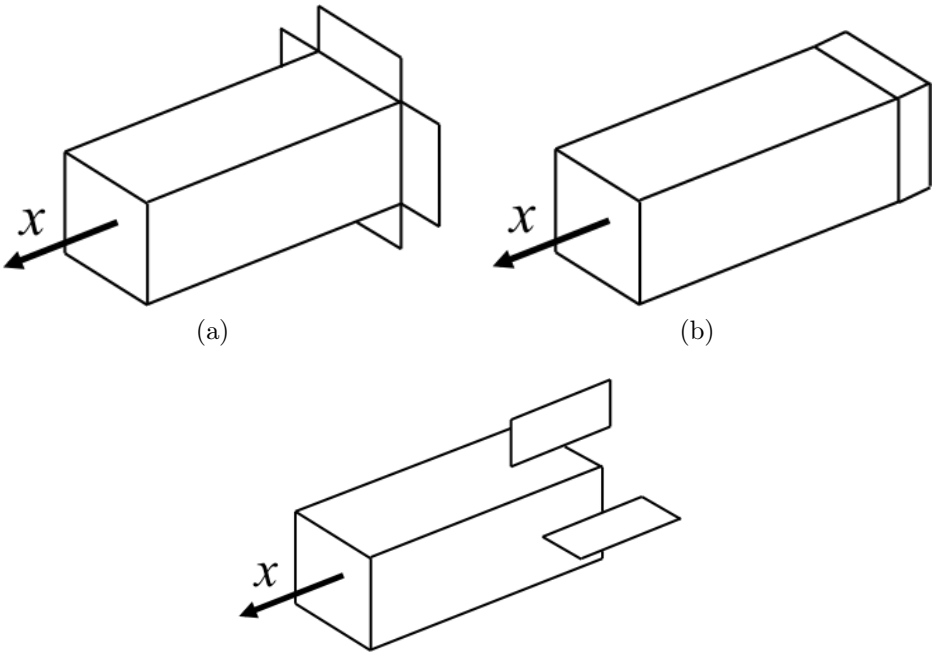

(a) (b) (c)

Figure 13.3: Schematic view of the CubeSat added stability surfaces. a) (top left) has 4 surfaces at the back of the CubeSat that are normal to the CubeSat sides. b) (top right) has 4 extensions of the CubeSat sides. c) (bottom centre) has 4 surfaces that act as fins located also at the back of the CubeSat.

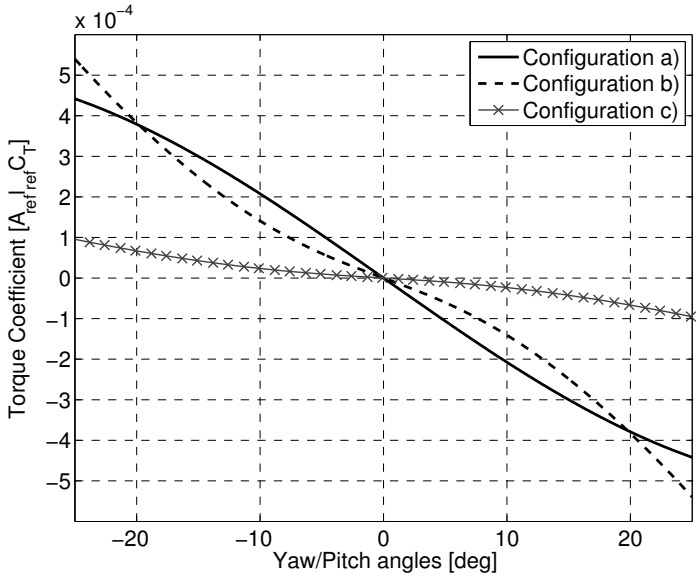

Figure 13.4: Aerodynamic torque $A_{ref} l_{ref} C_T$ provided at different offset angles (pitch/yaw) by a 2U CubeSat with the different example configuration shown in Fig. 13.3. Computed with the Sentman model with $\sigma_a = 1$ at an altitude of 250 km and using the NRLMSISE-00 model (Picone et al., 2002) with moderate solar activity (ISO 14222, 2013).

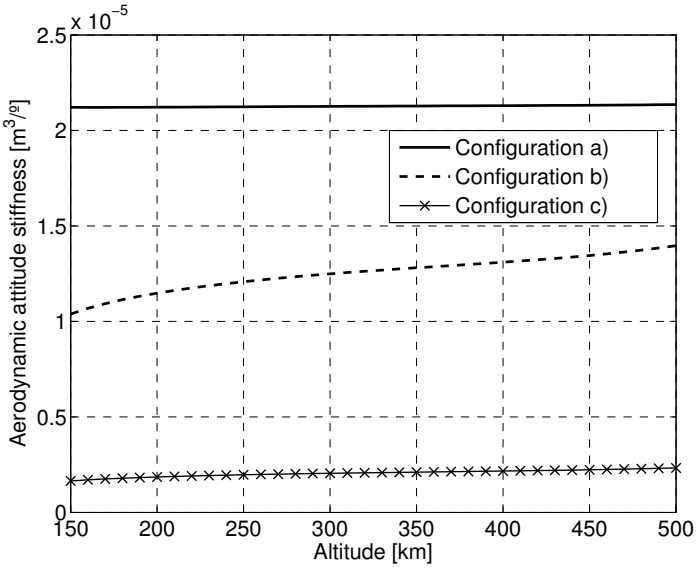

Figure 13.5: Aerodynamic stiffness by a 2U CubeSat with the different example configuration shown in Fig. 13.3. Computed with the Sentman model with $\sigma_a = 1$ at an altitude of 250 km and using the NRLMSISE-00 model (Picone et al., 2002) with moderate solar activity (ISO 14222, 2013).

with the aerodynamic surface area. Figure 13.6 shows this aerostability efficiency for the three configurations and using different panel areas.

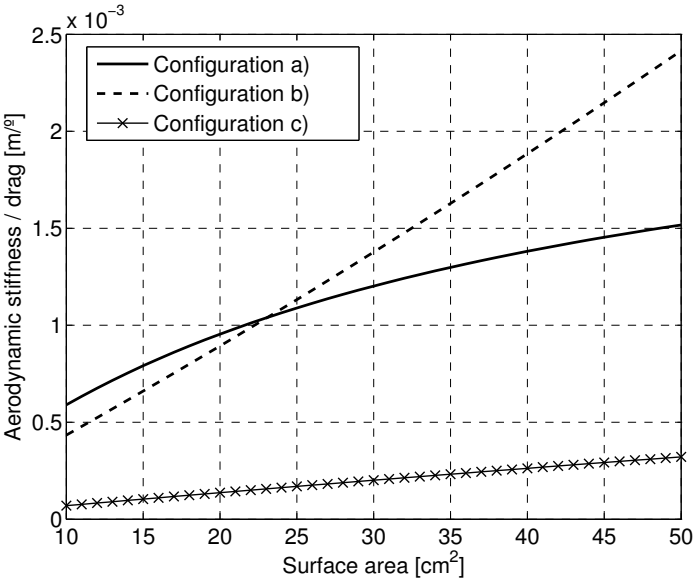

Figure 13.6: Aerodynamic stiffness over drag ($k/A_{ref}C_d$) by a 2U CubeSat with the different example configuration shown in Fig. 13.3. Computed with the Sentman model with $\sigma_a = 1$ at an altitude of 250 km and using the NRLMSISE-00 model (Picone et al., 2002) with moderate solar activity (ISO 14222, 2013).

Again, it is clear that the configurations shown in Fig. 13.3a and 13.3b are the ones that look more promising (the most effective and efficient). The configurations shown

in Fig. 13.3a is the most effective and the most efficient with low surface areas, and is selected for the rest of the analysis (carrying the burden of three different configuration will only make everything more complex without providing any added value).

It is also important to note that the torque provided by these extra aerodynamic surfaces is proportional to the distance to the centre of mass ($T \propto l$). Therefore the same aerodynamic surfaces will provide higher torques for bigger CubeSats. Unfortunately, the effectiveness (how easy is to create angular acceleration $\ddot{\theta}$), is related to the CubeSat inertia $\ddot{\theta} = T/I$, and the inertia of a uniform CubeSat under pitch/yaw can be written as in Eq. 13.1.

$$I = \frac{1}{12} m \left(d_{100}^2 + d_i^2 \right) \tag{13.1}$$

where m is the CubeSat mass (1kg for 1U, 2kg for 2U or 3kg for 3U), d_{100} is 100 mm (equal for 1, 2 or 3U CubeSats) and d_i is 100 mm for 1U, 200 mm for 2U or 300 mm for 3U. The inertias are then $I_{1U} = 0.0017$, $I_{2U} = 0.0083$ and $I_{3U} = 0.0250$ kg m^2.

Therefore the inertia is proportional to the square of the CubeSat length and hence the aerodynamic surfaces will lose effectiveness when the CubeSat gets bigger (as the torque is proportional to the length). To get same level of effectiveness the aerodynamic surfaces will require a surface increase for bigger CubeSats. This parameter can be measured by the aerodynamic stiffness over the inertia (k/I), as can be seen in Fig. 13.7 for the configuration showed in Fig. 13.3a.

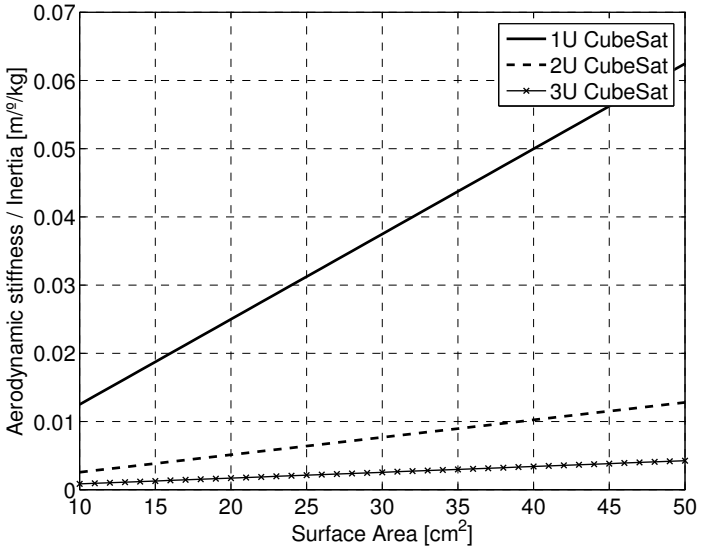

Figure 13.7: Aerodynamic stiffness over CubeSat inertia by different CubeSat sized with the example configuration shown in Fig. 13.3a. Computed with the Sentman model with $\sigma_a = 1$ at an altitude of 250 km and using the NRLMSISE-00 model (Picone et al., 2002) with moderate solar activity (ISO 14222, 2013).

13.4 Dynamics and Damping

Chapter 8 on page 99 contains an explanation of the basic aerostability concepts. As a remainder, aerostable spacecraft behave as simple harmonic oscillators and hence

oscillate indefinitely if no damping is included. When damping is included then the system behaves as a damped harmonic oscillator and settles the attitude of the CubeSat on its equilibrium point (in this case, keeping the CubeSat aligned with the relative flow).

An important parameter of aerostable systems (and harmonic oscillators) is their natural frequency. The natural frequency, is a function of the altitude (through the dynamic pressure q), the aerodynamic stiffness of the CubeSat and the CubeSat inertia. Figure 13.8 shows the natural frequency for a 2U CubeSat at different altitudes and with different surface areas with the Fig. 13.3a configuration. Note that the frequency increase as the altitude decreases (as the higher density of the atmosphere raises the dynamic pressure q) and that increasing the area (which increases the stiffness as seen in Fig. 13.7), also increases this frequency.

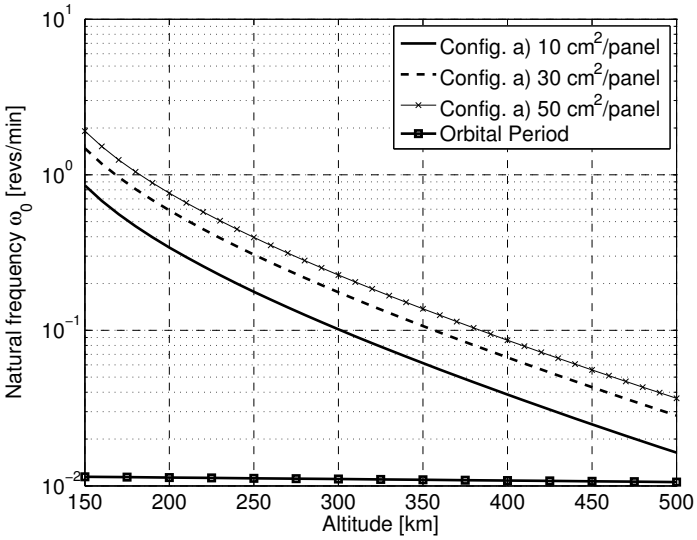

Figure 13.8: Natural frequencies of a 2U CubeSat at different altitudes and surface areas for the configuration shown in Fig. 13.3a. Computed with the Sentman model with $\sigma_a = 1$ at an altitude of 250 km and using the NRLMSISE-00 model (Picone et al., 2002) with moderate solar activity (ISO 14222, 2013).

It is also interesting to point out that the the orbital period frequency is much smaller than the natural frequency of the aerostability system. If this is the case, then attitude dynamics (due to aerostability) occur in much shorter timescales than the potentially induced attitude changes due to the orbit change (SRP, changes in atmosphere, ...) and hence, these longer timescale oscillations will not resonate with the aerostability system. The only coupling could come from the gravity gradient torques (only in pitch) that changes accordingly to the pitch oscillation and hence has the same frequency as the aerostability system. It is then a requirement to produce a spacecraft where its gravity gradient torques are much smaller than the aerostability torques (so that aersotability dominates). This is easy at low altitudes (as the density is small) but it can be challenging at high altitudes (where the density is small and so are the aerodynamic torques, but where the gravity gradient torques magnitude remain nearly constant).

As it has been mentioned before, an aerostable system without damping oscillates

indefinitely. Introducing damping dissipates the energy of the system, settling the spacecraft in its equilibrium attitude. This makes the spacecraft dissipate any perturbations and keep itself aligned with the flow direction. The maximum performance is achieved when the system is critically damped. Figure 13.9 shows the damping coefficient required to achieve critical damping for a 2U CubeSat at different altitudes and with different surface areas with the Fig. 13.3a configuration. It is interesting to point out that increasing the panel area increases the stiffness and hence it also increases the required damping coefficient to achieve critical damping.

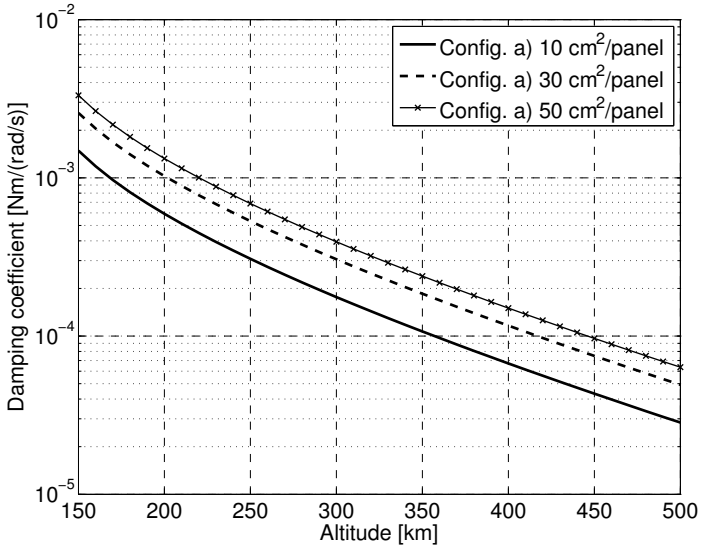

Figure 13.9: Optimum damping (critical damping) of a 2U CubeSat at different altitudes and surface areas for the configuration shown in Fig. 13.3a. Computed with the Sentman model with $\sigma_a = 1$ at an altitude of 250 km and using the NRLMSISE-00 model (Picone et al., 2002) with moderate solar activity (ISO 14222, 2013).

The last important parameter is the maximum torque that is required by the damping system. For a critically damped system that starts at an offset angle θ_0 this maximum damping torque can be easily computed and is shown in Fig. 13.10 for $\theta_0 = 4^{\text{o}}$ (maximum misalignment caused by a 500 m/s wind gust). This figure is useful to size the damping actuators. As the maximum torque increases as the altitude decreases, it may be difficult to find actuators with the sufficient resolution to efficiently damp at high altitudes (where the range of required torques is small) and also that have the sufficient torque range to tackle the required higher torques at low altitudes. If the actuators cannot achieve the required torque and saturate, then the system will overshoot but the system will still settle into the equilibrium altitude (although it may oscillate a bit and will take slightly longer).

13.5 Damping Methods and Techniques

Achieving aerostability requires a geometry which provides restoring aerodynamic torques but also a damping system. This damping system must provide a torque, proportional and in opposite direction of the angular velocity, so that the oscillations can be quickly

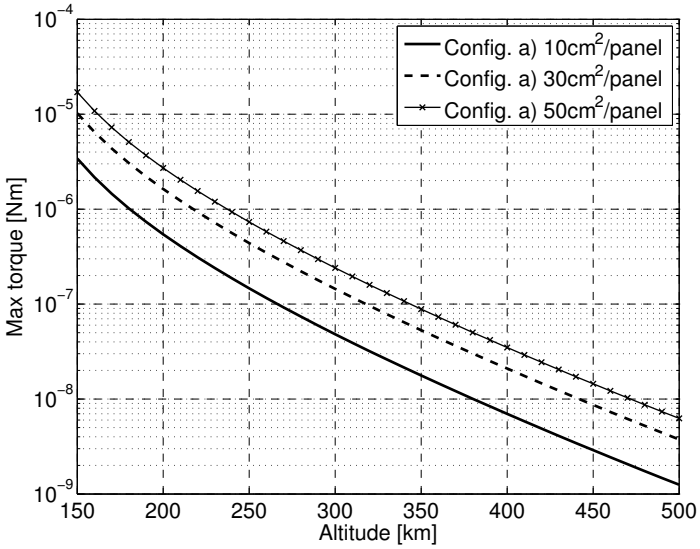

Figure 13.10: Maximum torque on a critically damped 2U CubeSat for and initial perturbation of $\theta = 4^{\circ}$ and using the configuration shown in Fig. 13.3a. Computed with the Sentman model with $\sigma_a = 1$ at an altitude of 250 km and using the NRLMSISE-00 model (Picone et al., 2002) with moderate solar activity (ISO 14222, 2013).

dissipated. This torque can be provided by passive or active systems. The selection of the method and components of this system will depend on the requirements of the CubeSat. In this section a brief description of the envisioned options is provided.

13.5.1 Active Methods

A simple solution to provide the damping torques would be to use the same active attitude actuators and sensors that are already available for CubeSat. This option provides a reliable and simple way to achieve damping, but it requires some power and also some computing cycles (as active attitude actuators and sensors need to be powered and commanded).

To achieve damping, angular velocity sensors and torque actuators are required. As angular velocity sensors, regular gyros, stellar gyros or magnetic field sensors can be used. And the actuators can be magnetic torquers or reaction/momentum wheels. all of these sensors and actuators are currently available for CubeSats (as COTS products) and they exhibit different advantages and shortfalls, so their selection shall be based on the mission requirements and the practical implementation limitations.

The advantage of this type of active system is that the damping coefficient can be changed, while in orbit, to adjust it for the changing environment that the CubeSat can encounter (mainly decaying altitude and solar activity variation).

Some actuators require specific sensors in order to work properly. For example, to produce the torque demanded, a magnetic torquer requires the knowledge of the local magnetic field, which pushes the system to include a magnetometer. As an example, a typical CubeSat magnetic torquer can provide an actuation level of 0.2 Am^2, this can provide a torque up to 6×10^{-6} Nm. This is enough for altitudes above ∼250 km, below that, the system will overshoot. Also, a magnetic torquer cannot provide

a torque in the direction of the magnetic field and hence there will be times where limited torque capability is available. In those cases, the system will oscillate until the torque capability in the desired direction is recovered. Momentum wheels for CubeSat can provide torques up to 1 mNm, more than enough for the damping system (although momentum wheels are generally bulkier than magnetic torquers and need another actuator to de-saturate them).

If the range of the damping coefficient is to big for the damping system, then, the CubeSat may not be critically damped at low altitudes and will overshoot, which increases the time to settle with respect to the optimum. Special attention has to be placed to select angular rate sensors that are capable of sensing the whole range of expected rates (the natural frequency is a function of the altitude and the dynamic pressure).

13.5.2 Passive Methods

Passive damping methods can offer a robust and power free alternative, that combined with the aerodynamic restoring torquers, can achieve a completely passive attitude control system. Two methods of providing passive damping have been identified.

Magnetic Hysteresis Rods

In this case, magnetically permeable rods are placed in the CubeSat. The oscillations of the spacecraft place the rod under a time varying magnetic field. Then, the flux density induced in the rod presents a lag, a phenomenon known as hysteresis. The torque provided by this induced flux in the rod will then make a loop that dissipates energy and hence it produces a damping effect. Figure 13.11 shows a typical hysteresis loop of a magnetic hysteresis rod. This method to provide damping through hysteresis rods has been demonstrated on spacecraft, and on CubeSats in particular, on several occasions (Silani and Lovera, 2005; Santoni and Zelli, 2009; Burton et al., 2012). Hysteresis rods have been traditionally used to de-spin spacecraft or as a damping system of a magnetic oriented attitude system (which also includes permanent magnets).

If hysteresis rods are used, their size and their material will decide the damping properties. Special attention has to be paid that the variability of the magnetic field during the orbit is significantly lower than the variability induced by the attitude oscillations. This could limit the applicability of these method to just damp big oscillations.

Viscous Dampers

Viscous dampers can also be used to damp oscillations. These type of dampers dissipate energy by the friction generated by a moving liquid (or an object summered in a liquid).

A viscous damper could be, for example, a tube half filled with a viscous liquid. As the CubeSat oscillates the liquid will then move from one end of the tube to the other, and the friction of the liquid with the tube wall (and from its own turbulence) will dissipate the oscillation energy as heat. The geometry of the tube can be modified to achieve an optimum performance, but it can not be changed during flight so the system will not be critically damped if it deviates from its design point (as if decays).

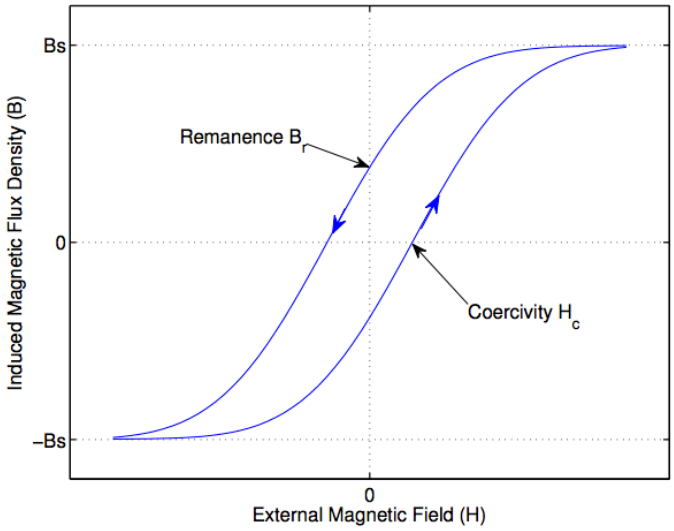

Figure 13.11: Typical hysteresis loop of a magnetically permeable rod. Extracted from Burton et al., 2012.

Other effects as, the movement of a mass in liquid or the mixing of two immiscible different density fluids (exploiting the Rayleigh–Taylor instability), among others, can be also exploited to produce damping. The damping through viscous dampers has also been demonstrated in spacecraft in the past (Davis et al., 1994; Bhuta and Koval, 1966).

Designing a viscous damper seems more complex than including hysteresis rods but it also is independent of the magnetic field and hence it offers greater flexibility. The design of such a damping system, tailored to provide damping in an aerostable system, has never been attempted before and it will represent a major design effort.

13.6 Conclusions

Aerostable attitude control systems can be achieved in CubeSats by the addition of stabilising aerodynamic surfaces and a damping system. The geometry of the aerodynamic surfaces can be diverse, but must produce a restoring torque. This restoring torque will cause the system to be statically stable, and hence oscillate around the equilibrium point. The effectiveness of these surfaces decreases exponentially as the altitude increases (due to the decrease of the dynamic pressure). Hence high altitude flying CubeSats will require bigger surfaces. Alos bigger CubeSat will require bigger surfaces to achieve the same levels of aerostability.

The damping system damps the oscillation by dissipating kinetic energy into heat. Several damping mechanisms can be envisioned, both active and passive. Active systems can be achieved through COTS components, while passive ones are not commercially available although the working principles have already been demonstrated for other missions.

The final attitude control accuracy depends on the combination of the aerodynamics and the damping system properties, and therefore it need to be evaluated on a case

by case basis. An example performance (high performance band) can be seen in the ΔDsat design (see chapter 8). Most CubeSat missions would probably not require such a fine control of their attitude and hence smaller surfaces will be sufficient.

Completely passive aerostability systems (including passive damping methods), although not currently developed, have the potential to provide a completely autonomous and power free method to control the attitude of a CubeSat. More work is still required to produce efficient and small passive damping system designs that could be implemented in CubeSat missions.

Also, the transition between the tumbling state that CubeSats experience after they have been ejected from their dispensers and a flow pointing attitude (required to start the aerostable control), can also be a challenge for a completely passive method. Is there any technique for an aerostable spacecraft equipped with a damping mechanism to detumble directly into aerostable mode, using the aerodynamic properties of the CubeSat? This seems a rather interesting future research topic.

Chapter 14

Descending Sun-synchronous Orbits with Aerodynamic Inclination Correction

Sun-synchronous orbits (SSO) offer near-constant illumination conditions on their ground tracks by keeping the Sun in a near-constant orientation with respect to the orbit plane. The effects of the Earth oblateness are exploited to move the location of the orbit's ascending/descending node so that they precess at the same pace that the Earth revolves around the Sun, hence keeping the Sun in a fixed orientation with respect to the orbit plane, and achieving a SSO. This effect can only be achieved at certain orbit's inclination, which is a function of the orbit's altitude (among other parameters) Vallado (2001, pp. 567-674).

Circular SSO are commonly used in LEO by Earth observation spacecraft that take imagery in the visible or infrared wavelengths because they offer similar illumination conditions over an observation target over different passes. The illumination angles are not completely constant due to the Earth's axial tilt and its eccentric orbit around the Sun, that combined, produce a solar analemma. Imaging missions usually set their SSO Mean Local Time of the Ascending Node (MLTAN) around 10:30 am to achieve optimum illumination conditions. Examples of these type of missions include UK-DMC 2 da Silva Curiel et al. (2005), GeoEye-1 Madden (2009) and the Morning Constellation (which includes Landsat 7 Goward et al. (2001), Terra Salomonson et al. (2000), E0-1 Ungar et al. (2003) and SAC-C Colomb et al. (2004)). Dawn-dusk orbits, where the MLTAN is close to sunrise/sunset, are also widely used for Earth observation missions because flying along the Earth's terminator offers a near constant solar illumination on the spacecraft (terminator orbits also suffer eclipses during certain seasons), which allows to have a constant solar power input and a stable thermal environment. These dawn-dusk orbits have been used by missions such as GOCE Drinkwater et al. (2007), TRACE Handy et al. (1999), TerraSAR-X Werninghaus (2004) and Proba-2 Gantois et al. (2006). As can be seen there is a wide range of Earth Observation missions that use SSO.

Spacecraft that fly in the LEO range are subject to aerodynamic drag, which makes the spacecraft decay. This decay caused by aerodynamic drag does not affect the orbit inclination (decay occurs at constant inclination), therefore a spacecraft that decays

from a SSO will lose the Sun-synchronous aspect of the orbit as the spacecraft loses altitude. The spacecraft inclination will not follow the required SSO inclination as it decays. This negative effect can be avoided if the spacecraft does not decay (either because the spacecraft is in a relatively high altitude orbit or because the aerodynamic drag is compensated with propulsion), or if the spacecraft can correct its inclination whilst decaying. A novel method is presented here where the spacecraft can correct its inclination using aerodynamic lift whilst it is decaying due to aerodynamic drag. This is then used to maintain the Sun-synchronous aspect of the orbit as the spacecraft decays.

The majority of the SSO spacecraft operate at an altitude of around 600 km or above. This is mainly because at these altitudes a short revisit time can be achieved and because the aerodynamic drag is small (not enough to change the orbit's altitude significantly during the spacecraft's operational life). This novel method could allow spacecraft that operate in SSO to lower their operational altitude whilst not requiring any propulsion to compensate the drag or to adjust the inclination. If the total altitude decay caused by aerodynamic drag during the spacecraft's operational lifetime is to great, or if the lift requirements of this method cannot be met, then partially compensating the aerodynamic drag through propulsion could still prove to be useful as the full aerodynamic drag would not need to be compensated (propulsion savings).

The aim of the research presented here is to analyse the feasibility of decaying SSO (allowing operations at lower altitude orbits where the aerodynamic drag is not completely compensated). Lowering the operational altitude of spacecraft can have several benefits for Earth observation missions as detailed in section 4.2 on page 48. There have already been other efforts to increase the range of available SSO Macdonald et al. (2010), demonstrating that a wider variety of SSO is desirable for a broader range of missions.

The method presented here is based on the application of lift in order to change the inclination while the spacecraft decays. The lift acts normal to the orbit plane and changes its inclination. As the decay is caused by aerodynamic drag this method will then require a certain lift to drag ratio on the spacecraft. This requirement can then be modified with on-board propulsion either by partially compensating the drag or by boosting the effect of the lift.

The study first covers the basic dynamics of a descending Sun-synchronous orbit with aerodynamic inclination correction, then, this analysis is expanded to cover the main perturbation sources and then, a validation is provided. After this main section, the study analyses which altitude ranges these orbits could be used in, considering the effect of the decay in the revisit time. To conclude, a brief section covers how the required lift could be achieved, and finally, a discussion on the applicability of this method is presented.

14.1 Simplified Dynamics

In this section the required lift to drag ratio will be derived using simplified dynamics, assuming only first order effects and circular orbits. In this context, Sun-synchronous orbits are achieved when the precession of the ascending/descending node due to the Earth's oblateness matches the orbital rate of the Earth around the Sun, thereby

maintaining a roughly constant angle between the orbit plane and the solar vector. To first order, the change in right ascension of the ascending node due to the Earth's oblateness is given in Eq. (14.1) Vallado (2001, pp. 567-674).

$$\frac{d\Omega}{dt} = -\frac{3nR_{\oplus}^2 J_2}{2p^2}\cos(i) \tag{14.1}$$

where Ω is the right ascension of the ascending node (RAAN), n the mean motion, $R_{\oplus}$ the equatorial radius of the Earth, p the semi-latus rectum, J_2 the Earth's second dynamic form factor and i represents the orbit's inclination. If a circular orbit is assumed, then p is equal to the semi-major axis ($p = a$) and thus the expression can be simplified as in Eq. (14.2).

$$k = \frac{d\Omega}{dt} = -\frac{3nR_{\oplus}^2 J_2}{2a^2}\cos(i) \tag{14.2}$$

where k is the target precession rate, which needs to be equal to the orbital rate of the Earth around the Sun to achieve a Sun-synchronous orbit ($k \approxeq \frac{2\pi}{365.25*24*3600}\ [rad/s]$). If the inclination is isolated, and it is assumed that $n = \sqrt{\frac{\mu}{a^3}}$ (where μ is the gravitational constant of the Earth), the expression can be written as in Eq. (14.3).

$$\cos(i) = -\frac{2ka^{7/2}}{3R_{\oplus}^2 J_2\sqrt{\mu}} \tag{14.3}$$

The SSO inclination with respect to the altitude is shown in Fig. 14.1. Note how it increases with altitude and hence when a spacecraft decays the inclination will need to be reduced.

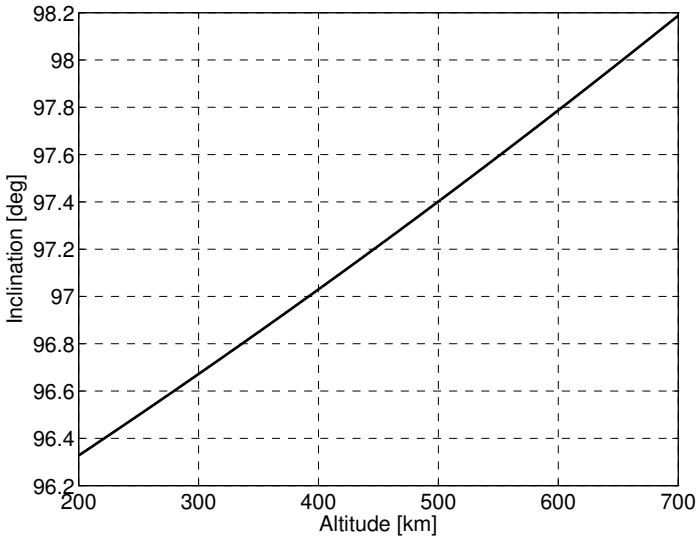

Figure 14.1: Inclination of Sun-Synchronous orbits with respect to the altitude.

Then, differentiating Eq. (14.3) with respect to time, Eq. (14.4) can be obtained.

$$\sin(i)\frac{di}{dt} = \frac{2k}{3R_{\oplus}^2 J_2\sqrt{\mu}}\frac{7}{2}a^{5/2}\frac{da}{dt} \tag{14.4}$$

The expression in Eq. (14.4) relates the change of inclination di with respect to the change of semi-major axis da. It is how much the inclination needs to change as the spacecraft decays (change in semi-major axis).

The effects of the aerodynamic perturbations (drag and lift) on the orbital elements can be computed by using Eqs. 14.5-14.6 (already simplified for circular orbits) Vallado (2001, pp. 567-674).

$$\frac{da}{dt} = -\frac{2}{n}a_D \tag{14.5}$$

$$\frac{di}{dt} = \frac{\cos(u)}{na}a_L \tag{14.6}$$

where a_D is the spacecraft acceleration due to drag, a_L is the acceleration due to lift (normal to the orbit plane) and u represents the argument of latitude (which is the sum of the argument of perigee ω and true anomaly ν, $u = \omega + \nu$). Note that here it is assumed that lift acts perpendicular to the orbit plane, this is an important difference if the reader is used to aircraft aerodynamics where lift is normally used to compensate weight. Equations 14.5 and14.6 show that drag has only a constant effect on the orbit altitude, and that lift has an effect on the orbit inclination but that it depends on the argument of latitude u (following a cosine law with maximum effect at the equator, where u is 0° or 180°, and changing sign every half orbit, where u is 90° or 270°).

Combining Eqs. (14.4), (14.5) and (14.6) an expression, which links the required out of plane lift acceleration a_L to adjust the inclination to the drag acceleration a_D can be obtained. This expression is written in Eq. (14.7).

$$\sin(i)\frac{\cos(u)}{na}a_L = -\frac{2k}{3R_\oplus^2 J_2\sqrt{\mu}}\frac{7}{2}a^{5/2}\frac{2}{n}a_D \tag{14.7}$$

Combining Eq. (14.7) with the Sun-synchronous inclination requirement expressed in Eq. (14.3) the more compact expression in Eq. (14.8) can be obtained.

$$\frac{a_L}{a_D} = \frac{L}{D} = \frac{7}{\cos(u)\tan(i)} \tag{14.8}$$

Equation (14.8) shows the required instantaneous lift to drag ratio (L/D) to maintain a Sun-synchronous inclination in an orbit decaying due to aerodynamic drag. Note that this ratio only depends on the inclination (thus the altitude) and the argument of latitude. Also note that this ratio becomes infinite when u is 90° or 270°. Another peculiarity is that the lift will need to change its acting direction every half orbit as $\cos(u)$ will change sign when the orbit crosses $u = 90°$ and $u = 270°$.

To overcome the infinite ratio required in some parts of the orbit, the spacecraft can have a constant lift to drag ratio that has an equivalent effect. This lift to drag ratio will then be maintained for half an orbit (the ascending part) and then reversed (changing its sign) for the other half (the descending part). Note that the magnitude of the require lift is the same in the ascending and the descending part of the orbit (symmetric).

The mean L/D that has the same effect as the instantaneous L/D can be computed using two different methods. In the first method, it is assumed that the rate of change on a and i (da/dt and di/dt) is constant over the whole averaging period (the orbital

elements are nearly constant during half an orbit), therefore Eq. (14.4) can be re-written for the averaging period as in Eq. (14.9).

$$\sin(i)\Delta i = \frac{2k}{3R_{\oplus}^2 J_2\sqrt{\mu}}\frac{7}{2}a^{5/2}\Delta a \tag{14.9}$$

Using the same assumption as before and using Eqs. (14.5) and (14.6), Δa and Δi can be computed by Eqs. (14.10) and (14.11).

$$\Delta a = \int_{t_0}^{t_f} -\frac{2}{n}a_D \; dt = -\frac{2}{n}a_D \int_{t_0}^{t_f} dt \tag{14.10}$$

$$\Delta i = \int_{t_0}^{t_f} \frac{\cos(u)}{na}a_L dt = \frac{a_L}{na}\int_{t_0}^{t_f} \cos(u) \; dt \tag{14.11}$$

The integration range is $u = [-90°,\ 90°]$ ($u = [90°,\ 270°]$ could also be used due to symmetry exhibited between the ascending and descending parts of the orbit). For circular orbits, the variable transformation shown in Eq. (14.12) to transform dt to du can be used. With this transformation, Eqs. (14.10) and (14.11) can be re-written and integrated as shown in Eqs. (14.13) and (14.14).

$$t = \frac{u}{n} \tag{14.12}$$

$$\Delta a = -\frac{2}{n^2}a_D \int_{-\frac{\pi}{2}}^{\frac{\pi}{2}} du = -\frac{2\pi}{n^2}a_D \tag{14.13}$$

$$\Delta i = \frac{a_L}{n^2 a}\int_{-\frac{\pi}{2}}^{\frac{\pi}{2}} \cos(u) \; du = \frac{2}{n^2 a}a_L \tag{14.14}$$

Finally, rearranging Eqs. (14.13), (14.14) and (14.9) the required mean L/D can be computed as in Eq. (14.15).

$$\left(\frac{L}{D}\right)_{mean} = \left|\frac{a_L}{a_D}\right| = \frac{7\pi}{2\tan(i)} \tag{14.15}$$

This last equation (Eq. 14.15) shows the constant L/D that the spacecraft needs to sustain to maintain the Sun-synchronous inclination while the orbit decays due to the aerodynamic drag. Note that the L/D is only a function of the inclination (thus the altitude). This mean L/D is shown in Fig. 14.8 (labelled as baseline) along with the required mean L/D considering other perturbation sources. The required L/D considering other perturbation sources are computed in the following sections.

Equations (14.5) and (14.6) from Vallado, 2001 are expressed in an orbital reference frame where z points along the radius vector, x is perpendicular to z, in the orbit plane and along the direction of motion and y completes the right hand triad. Therefore, a_D will point in the $-x$ direction as drag acts against the velocity vector. Then, as in Eq. (14.8), $\tan(i) < 0$ for Sun-synchronous orbits (retrograde), it is clear that $a_L < 0$ (points in the $-y$ direction) when $-90° < u < 90°$ (during the ascending part of the orbit) and $a_L > 0$ (points in the $+y$ direction) when $90° < u < 270°$ (during the descending part of the orbit).

It is also interesting to note that lift can also have an effect on the rate at which the RAAN rotates, as it is shown on Eq. (14.16) for circular orbits Vallado (2001, pp. 567-674). However, as the rate of rotation of the RAAN due to lift is proportional to the $\sin(u)$ it cancels out if a constant lift from pole to pole is maintained, as the method described here does. Therefore no secular change in RAAN will be caused when using this method.

$$\frac{d\Omega}{dt} = \frac{\sin(u)}{na\sin(i)} a_L \tag{14.16}$$

The other method to obtain the mean L/D directly integrates the instantaneous L/D in Eq. (14.8) as in Eq. (14.17).

$$\left(\frac{L}{D}\right)_{mean} = \frac{\int_{-\frac{\pi}{2}}^{\frac{\pi}{2}} \frac{7}{\cos(u)\tan(i)} du}{\pi} = \frac{\frac{7}{\tan(i)} \left[\ln\left(\frac{1}{\cos(u)} + \tan(u)\right)\right]_{-\frac{\pi}{2}}^{\frac{\pi}{2}}}{\pi} \tag{14.17}$$

Unfortunately, the integral in Eq. (14.17) is not bounded, and therefore its solution corresponds to $D = 0$ (no drag). Another route to obtain an analytical solution is then to compute the integral of the multiplicative inverse as in Eq. (14.18).

$$\left(\frac{D}{L}\right)_{mean} = \frac{\int_{-\frac{\pi}{2}}^{\frac{\pi}{2}} \frac{\cos(u)\tan(i)}{7} du}{\pi} = \frac{\frac{\tan(i)}{7} \left[\sin(u)\right]_{-\frac{\pi}{2}}^{\frac{\pi}{2}}}{\pi} = \frac{2\tan(i)}{7\pi} \tag{14.18}$$

In this later case, the integral is bounded and its solution recovers what was previously found in Eq. (14.15).

$$\left(\frac{L}{D}\right)_{mean} = \frac{7\pi}{2\tan(i)} \tag{14.19}$$

As this second method to obtain the solution is more straightforward it is used in the rest of the analysis when numerical integration is required (that is when the integrals do not have analytical solutions).

It is also important to note that the averaging method used to get to equations (14.15) and (14.19) is only valid for circular orbits (where the relation of argument of latitude u and time t is constant), for a spherically symmetrical atmosphere (density only changing with altitude) and if the change in altitude during half orbit is small (so that the averaging process can be done at a constant altitude, therefore not valid near re-entry when the altitude loss per orbit is significant).

14.2 Perturbations

The models presented in the preceding section 14.1 assumed simplified dynamics and there are several effects that can change the required nominal L/D presented in section 14.1. In this section these other effects have been analysed.

14.2.1 Atmospheric Co-Rotation

It is generally accepted that the atmosphere co-rotates with the Earth Challinor (1968) thus making the direction of the relative incidence flow differ from the inertial velocity vector. Therefore the aerodynamic drag and lift vectors are no longer aligned with the orbital x and y axes and hence there will be an angle between the inertial velocity (in the orbital x, y, z frame) and the relative incident flow. Figure 14.2 shows a schematic of the disposition of the real aerodynamic drag and lift acceleration vectors a_D and a_L compared to the apparent a'_D and a'_L (the ones aligned with the orbital x, y, z frame used in equations (14.5) and (14.6)). Then, the relation between $a'_{D,L}$ and $a_{D,L}$ can be written as in Eqs. (14.20) and (14.21).

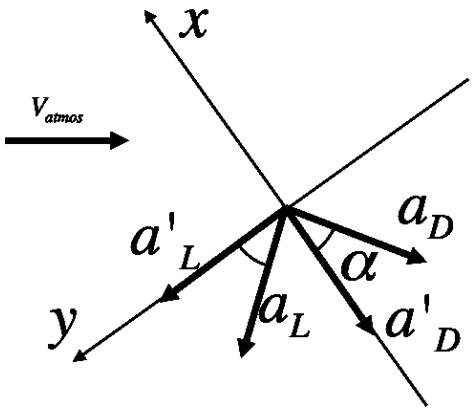

Figure 14.2: Schematic of the disposition of the apparent drag a'_D and lift a'_L accelerations compared to the aerodynamic a_D and a_L.

$$a'_D = a_D \cos(\alpha) + a_L \sin(\alpha) \tag{14.20}$$

$$a'_L = a_L \cos(\alpha) - a_D \sin(\alpha) \tag{14.21}$$

The α angle is not constant and depends on the orientation of the inertial velocity with respect to the atmospheric co-rotation velocity. The magnitude of the atmospheric co-rotation V_{atmos} is related to the Earth's angular velocity $\omega_\oplus$, the spacecraft latitude ϕ and the spacecraft altitude (through the semi-major axis a) by Eq. (14.22).

$$V_{atmos} = \omega_\oplus a \cos(\phi) \tag{14.22}$$

Using spherical trigonometry, the latitude can be easily computed using Eq. (14.23).

$$\sin(\phi) = \sin(u) \sin(i) \tag{14.23}$$

Using spherical trigonometry and a velocity triangle (see Fig. 14.3) the angle between the inertial and the relative velocity can be computed using Eqs. (14.24-14.27).

$$\sin(\alpha) = \frac{V_{atmos}}{V_r} \sin(\gamma) \tag{14.24}$$

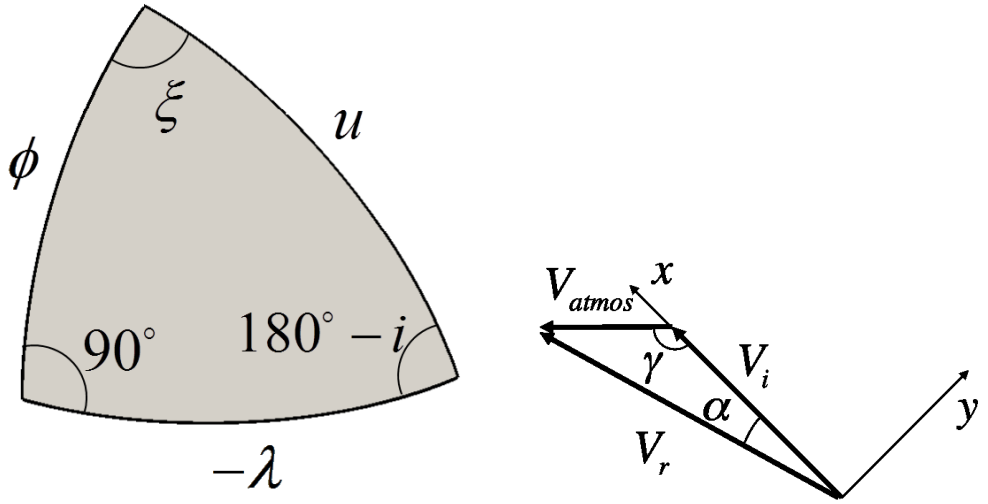

(a) (b)

Figure 14.3: a) Geometric disposition of the orbit (retrograde) with respect to the latitude ϕ and longitude λ. b) Triangle of velocities with the atmospheric co-rotation.

$$V_r^2 = V_i^2 + V_{atmos}^2 - 2V_i V_{atmos}\cos(\gamma) \tag{14.25}$$

$$\gamma = 90^\circ + \xi \tag{14.26}$$

$$\tan(\xi) = \frac{1}{\cos(u)\tan(180^\circ - i)} \tag{14.27}$$

where V_i is the inertial velocity, that in a circular orbit can be expressed as $V_i = \sqrt{\mu/a}$. Note that in Eqs. (14.24) and (14.27) the sign of α and ξ needs to be reversed when $90^\circ < u < 270^\circ$ (descending part of the orbit).

Figure 14.4 shows the evolution of α during an orbit at different altitudes. Note how it follows a cosine curve and how its amplitude slightly increases with the orbit's altitude. Then, the relation between the true aerodynamic a_L/a_D of the spacecraft and the apparent a'_L/a'_D in the orbital reference frame can be written as in Eq. (14.28).

$$\frac{L}{D} = \frac{a_L}{a_D} = \frac{\frac{a'_L}{a'_D}\cos(\alpha) + \sin(\alpha)}{\cos(\alpha) - \frac{a'_L}{a'_D}\sin(\alpha)} \tag{14.28}$$

The apparent a'_L/a'_D is what needs to match the results of the previous section 14.1, and then, a_L/a_D can be computed. This true aerodynamic a_L/a_D will be what the spacecraft will need to be capable of achieving.

Figure 14.4 shows the relative difference between the apparent a'_L/a'_D with respect to the spacecraft aerodynamic a_L/a_D in a 400 km altitude orbit. The figure then shows that atmospheric co-rotation increases the apparent a'_L/a'_D for a given aerodynamic a_L/a_D , having a maximum effect during the ascending and descending nodes.

Then, combining Eq. (14.28) with Eq. (14.8) the required instantaneous true aerodynamic L/D under atmospheric co-rotation can be computed by Eq. (14.29).

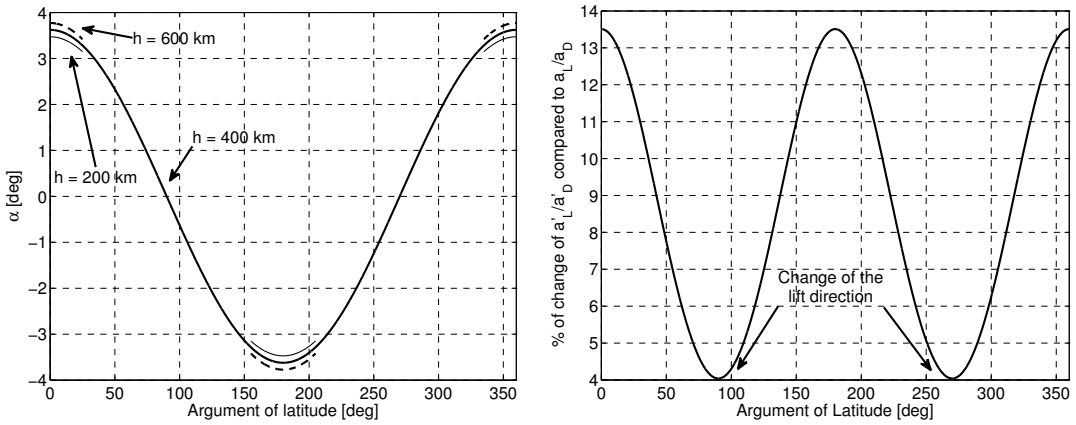

(a) (b)

Figure 14.4: a) α angle evolution at different altitudes. b) Relative difference between the apparent a'_L/a'_D with respect to the aerodynamic a_L/a_D.

$$\frac{L}{D} = \frac{\frac{7}{\cos(u)\tan(i)}\cos(\alpha) + \sin(\alpha)}{\cos(\alpha) - \frac{7}{\cos(u)\tan(i)}\sin(\alpha)} \tag{14.29}$$

Equation (14.29) can then be numerically integrated to obtain the mean aerodynamic L/D required to maintain the Sun-synchronous inclination whilst the orbit decays due to the aerodynamic drag in a co-rotating atmosphere. As Fig. 14.4 shows, the atmosphere co-rotation increases the apparent a'_L/a'_D and thus reduces the required aerodynamic L/D. This happens because the shift in the direction of the drag, due to the atmospheric co-rotation, makes the drag point into the direction of the required lift ($-y$ in the ascending part of the orbit) and hence it contributes to change the inclination. Therefore, to achieve the same effect, the L/D can be reduced.

Figure 14.8 shows the mean aerodynamic L/D required if the atmospheric co-rotation is considered. Note that if the atmospheric co-rotation is considered the required L/D is reduced, and that this reduction slightly increase with altitude as the co-rotation magnitude increase with altitude. This result could be anticipated as it is generally known that the atmospheric co-rotation reduces the inclination of the orbits King-Hele (1987, pp. 140-164).

14.2.2 Atmospheric Wind

Apart form the atmospheric co-rotation, there is also wind in the upper atmosphere. Figure 2.5 shows, as an example, the wind pattern and magnitude at an altitude of 450 km with moderate solar activity ISO 14222 (2013) during the northern hemisphere summer solstice according to the HWM93 model Hedin et al. (1996).

This wind is essentially unpredictable and current models are quite inaccurate and only take into account horizontal wind Drob et al. (2008). In this analysis the HWM93 model Hedin et al. (1996) will be used and only the horizontal wind will be taken into account.

As can be seen in Fig. 2.5 on page 24, the wind is usually stronger in the polar regions than in the equatorial regions, where the lift is less effective to change the inclination, and they generally blow in the opposite direction than the rotation of the Earth, hence partially cancelling the atmospheric co-rotation.

Adding the atmospheric wind into the analysis can be treated in a very similar way than adding the atmospheric co-rotation. In fact, only Eq. (14.26) needs to be updated to reflect that now the atmospheric wind velocity is not only zonal (East-West) but it also includes a meridional (North-South) component. Figure 14.5 (equivalent to Fig. 14.3) and Eq. (14.30) show these changes.

$$\gamma = 90^\circ + \xi + \beta \tag{14.30}$$

Then, in Eq. (14.30), the angle β is the angle of the atmospheric wind velocity with respect to the local East-West direction. This is shown in Fig. 14.5.

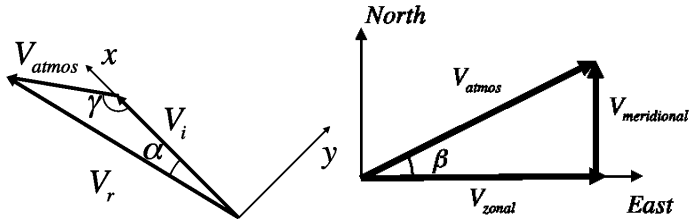

(a) (b)

Figure 14.5: a) Triangle of velocities including atmospheric winds. b) Definition of the β angle caused by the presence of meridional winds.

Taking this small variation into account and following the same procedure as before, the mean aerodynamic L/D to maintain the Sun-synchronous inclination whilst the orbit decays due to the aerodynamic drag in a co-rotating and windy atmosphere can be computed. Note that now, this mean will depend on the particular wind on that particular orbit. Therefore, to maintain a Sun-synchronous orbit the mean L/D will need to be adjusted from orbit to orbit to adjust for the changing wind, or to maintain an average one during several orbits. A comparison between the typical mean aerodynamic L/D required in different scenarios (taking into account, or not, the atmospheric co-rotation and the atmospheric wind) is shown in Fig. 14.8. The mean aerodynamic L/D includes the 1σ uncertainty bar that takes into account the variability in the wind conditions.

As it can be noted in Fig. 14.8, the wind tends to slightly increase the required L/D ratio. This is because the wind tends to blow in the opposite direction of the Earth rotation and hence it partially cancels the effect of the atmospheric co-rotation.

14.2.3 Higher Gravity Harmonics

Up to now only the J_2 effect has been taken into account in order to simplify the derivation of the equations, but the rotation of the RAAN is affected by higher degree harmonics. Using the first six zonal harmonics Eq. (14.31) can be obtained Vallado (2001, pp. 567-674).

$$\frac{d\Omega}{dt} = -\frac{3J_2R_\oplus^2 n\cos(i)}{2a^2} + \frac{3J_2^2R_\oplus^4 n\cos(i)}{32a^4}\left[12-80\sin^2(i)\right] + \frac{15J_4R_\oplus^4 n\cos(i)}{32a^4}\left[8-14\sin^2(i)\right] - \frac{105J_6R_\oplus^6 n\cos(i)}{1024a^6}\left[64-288\sin^2(i)+264\sin^4(i)\right] \quad (14.31)$$

From Eq. (14.31) the Sun-synchronous inclination and also the di/da derivative can be extracted. Then, Eq. (14.32) shows how to compute the instantaneous L/D ratio using the di/da derivative. This equation can be easily derived by using Eqs. (14.5) and (14.6). If equations (14.31) and (14.32) are used and integrated the required mean L/D ratio can be obtained for the higher gravity harmonics case. This is shown in Fig. 14.8, and as it can be seen, it just slightly decreases the required lift to drag ratio.

$$\frac{L}{D} = \frac{di}{da}\frac{-2a}{\cos(u)} \quad (14.32)$$

14.2.4 Density Variations

The Earth atmosphere is not perfeclty spherical and hence it presents density variations across the same altitude and hence across a circular orbit. Therefore, when averaging Eq. (14.8) to get the mean L/D required, more weight has to be given to the orbit areas that have higher density. The most important density variations are caused by the atmospheric oblateness King-Hele (1987, pp. 77-87). Due to this oblateness, circular orbits go through a thinner atmosphere around the poles and a denser atmosphere around the equator. In addition, there is the day-night density variation caused by the solar heating in the illuminated side. If this weighting factor is applied, Eq. (14.18) can be written as in Eq. 14.33, where ρ_r is the relative density with respect to the mean density over the integration range ($\rho_r = \rho/\rho_{mean}$).

$$\left(\frac{D}{L}\right)_{mean} = \frac{\int_{-\frac{\pi}{2}}^{\frac{\pi}{2}} \frac{D}{L}\rho_r du}{\pi} \quad (14.33)$$

In Fig. 14.6 the distribution of ρ_r over a whole orbit and at different orbiting altitudes is shown. No winds or other effects have been considered in this figure and the density has been extracted from the NRLMSISE-00 Picone et al. (2002) model, assuming medium solar activity ISO 14222 (2013) and considering an Earth flattening factor off $f = 1/298.256$ Larson and Wertz (2005). Figure 14.6 shows the averaged results over the different longitudes of the ascending node for noon-midnight orbits. On this figure the effect of the atmospheric oblateness (higher ρ_r over the equator and lower ρ_r over the poles), and the day and night variation (equator ρ_r peak is higher in the day side of the Earth than at the night side) can be clearly seen. Another interesting aspect is that at higher altitudes the day-night variation dominates the ρ_r variation over the atmospheric oblateness.

Figure 14.8 shows the required mean L/D to maintain Sun-synchronous orbit while decaying in an atmosphere with density fluctuations compared to the mean L/D in a

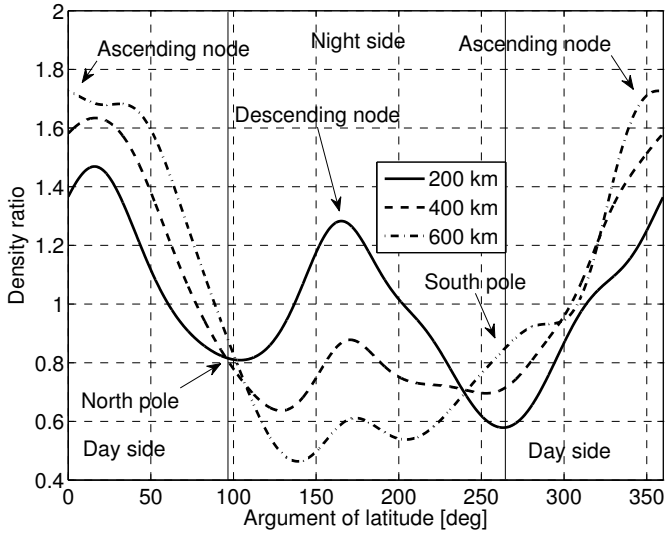

Figure 14.6: Variation of $\rho_r = \rho/\rho_{mean}$ in a typical Sun-synchronous orbit at different orbit altitudes.

spherical atmosphere. Note how the required L/D lowers if a non-spherical atmosphere is taken into account. This is because the atmospheric oblateness reduces the density over the pole areas, therefore reducing the weight, during the averaging, on the higher instantaneous L/D required on those areas, and increasing the weight on the lower instantaneous L/D required on the equatorial areas. It is also interesting to note that the day-night variations have a small effect in the mean L/D. All this can be seen in Fig. 14.7, which shows the difference with respect to the spherical atmosphere assumption of the mean L/D for different scenarios.

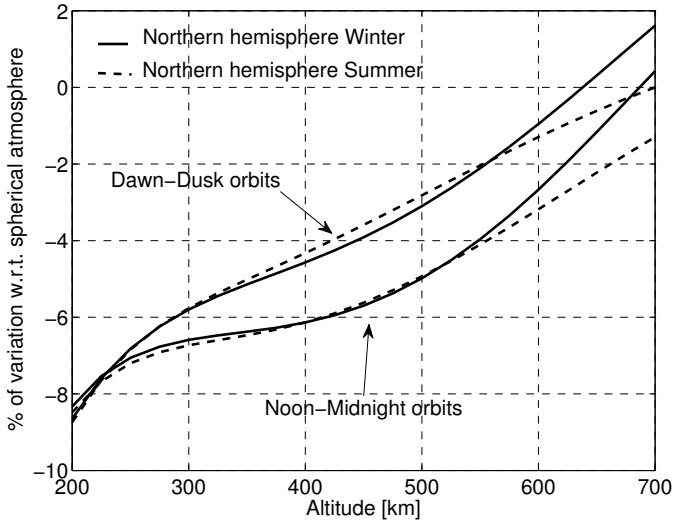

Figure 14.7: Relative change in % from the mean L/D required assuming a spherical atmosphere for several orbits scenarios.

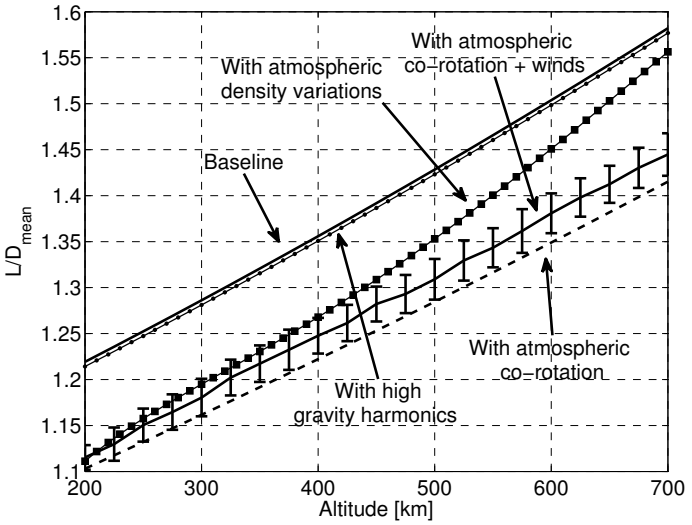

Figure 14.8: Required mean L/D to maintain Sun-synchronous orbit while decaying under different scenarios.

14.2.5 Eccentricity

Another effect that has to be analysed is what happens when the orbit is not completely circular. In that case, equations (14.3), (14.5) and (14.6) have to be replaced for the following expressions Vallado (2001, pp. 567-674) in Eqs. (14.34-14.37).

$$\frac{d\Omega}{dt} = -\frac{3nR_{\oplus}^2 J_2}{2a^2(1-e^2)^2}\cos(i) \tag{14.34}$$

$$\frac{da}{dt} = \frac{2}{n\sqrt{1-e^2}}\left[-e\sin(\nu)\sin(\gamma) - \frac{a(1-e^2)}{r}\cos(\gamma)\right]a_D \tag{14.35}$$

$$\frac{di}{dt} = \frac{r\cos(u)}{na^2\sqrt{1-e^2}}a_L \tag{14.36}$$

$$\frac{de}{dt} = \frac{\sqrt{1-e^2}}{na}\left[-\sin(\nu)\sin(\gamma) - \left(\cos(\nu) + \frac{e+\cos(\nu)}{1+e\cos(\nu)}\right)\cos(\gamma)\right]a_D \tag{14.37}$$

where e is the orbit's eccentricity, ν the true anomaly, r the orbit radius and γ the flight path angle. Then, differentiating Eq. (14.34) and substituting the da/dt, di/dt and de/dt by equations (14.35), (14.36) and (14.37) the required instantaneous L/D can be found. This expression is written in the set of equations (14.38-14.44).

$$\frac{L}{D} = \frac{A\left[BG + CF\right]}{E} \tag{14.38}$$

$$A = \frac{2k\left(1-e^2\right)a^{5/2}}{3\sqrt{\mu}R_{\oplus}^2 J_2\sin(i)} \tag{14.39}$$

$$B = \frac{7}{2}\left(1-e^2\right) \tag{14.40}$$

$$C = -4ae \tag{14.41}$$

$$E = \frac{r\cos(u)}{na^2\sqrt{1-e^2}} \tag{14.42}$$

$$F = \frac{\sqrt{1-e^2}}{na}\left[-\sin(\nu)\sin(\gamma) - \left(\cos(\nu) + \frac{e+\cos(\nu)}{1+e\cos(\nu)}\right)\cos(\gamma)\right] \tag{14.43}$$

$$G = \frac{2}{n\sqrt{1-e^2}}\left[-e\sin(\nu)\sin(\gamma) - \frac{a(1-e^2)}{r}\cos(\gamma)\right] \tag{14.44}$$

To obtain the mean L/D, Eq. (14.38) needs to be integrated with respect to time. Also, in this case, the direction of the lift needs to be reversed when the spacecraft crosses $u = 90°, 270°$, but unlike the other cases the mean L/D required for the ascending and the descending sections will differ (as in general, the average r will be different in those sections due to the eccentricity). Then, the mean L/D with respect to the whole orbit (although it will still change direction) must be found. Also, as the spacecraft will fly at different altitudes in an eccentric orbit, a density weighting parameter needs to be introduced to add more weight in the averaging to the sections of the orbit that travel through denser parts of the atmosphere. Here an exponential atmospheric model as shown in Eq. (14.45) will be used.

$$\rho(h) = \rho_0 e^{-\frac{h-h_o}{H}} \tag{14.45}$$

where, ρ_0 is a reference density at the altitude h_0 and H represents the scale height. Here the values of $h_0 = 350$ km, $\rho_0 = 6.66 \times 10^{-12}$ kg/m^3 and $H = 55$ km will be used (for more accurate predictions more complex atmospheric models need to be used). Figure 14.9 shows the required mean L/D ratio for a perigee altitude of 400 km and for different eccentricities and different arguments of the perigee. Note that the figure only shows the argument of perigee from 0° to 90°, this is because the results are symmetric and hence all the rest of arguments of perigee (from 0° to -90°, from 180° to 270° and from 180° to 90°) will output the same results as shown in Fig. 14.9.

The eccentricity has two effects on the L/D ratio. The first one, is that the density around the perigee section is higher than the density around the apogee section and hence, for small eccentricities the mean L/D tends to move towards the instantaneous L/D required at the perigee. The second effect comes because in an eccentric orbit the average distance to the Earth is higher than the perigee altitude and hence the mean L/D increases (see Fig. 14.8). Those two effects acting together is what can be seen in Fig. 14.9. It is interesting to note that the L/D decreases for small eccentricities and perigees close to the equator.

It is also important to note that in eccentric orbits the argument of the perigee will be drifting due to J_2, the aerodynamic lift and the drag. So the argument of the perigee will also change during the decay.

High eccentric SSO are are not commonly used and during the rest of the analysis circular orbits will be used.

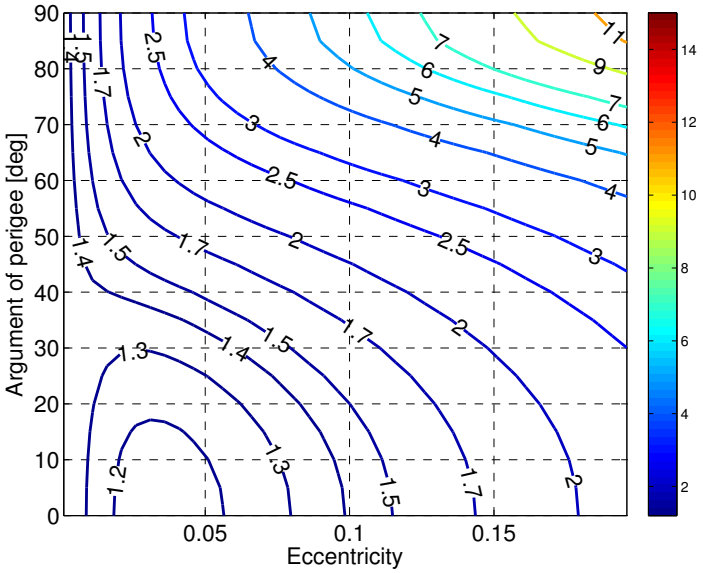

Figure 14.9: Required mean L/D ratio for different eccentricities and different argument of the perigee for a perigee altitude of 400 km.

14.3 Combined Analysis

If all the effects stated in the previous sections are taken into account more realistic estimates can be obtained. Figure 14.10 shows the mean L/D including atmospheric co-rotation, atmospheric winds, atmospheric density variation and higher gravity harmonics. This figure includes the 1σ uncertainty bounds generated taking into account the variability in the density and wind activity (simulated by changing the time of year, local solar time and solar activity). This figure has been generated using a 40 samples Monte Carlo simulation and hence it contains some noise inherent of the Monte Carlo method.

14.4 Usable Altitude Windows

For most Sun-synchronous Earth observation missions a global coverage with frequent revisit times is required Iglseder et al. (1995); Williams et al. (2000). This is normally achieved by tailoring the altitude of the orbit so that the maximum time between observations of the same target is limited to only a few days Sengupta et al. (2010). As in the proposed method, the spacecraft is continuously descending the effect of the decay on the revisit time shall be assessed.

Note that using an orbit with repeating ground tracks can also be beneficial for some applications (specially synthetic aperture radar Rim et al. (2000) and geodesy Rummel et al. (2002)) but, as in this method, the spacecraft is continuously descending, an orbit which maintains a repeating ground track is not achievable, and hence this method may not be suitable for those missions that require repeating ground tracks.

Assuming a circular orbit, a maximum off axis looking angle of 45° and a 40° latitude of interest, the maximum revisit time for each altitude is given in Fig. 4.3 on page 48. This has been calculated by considering the viewable portion of the ground at 40°

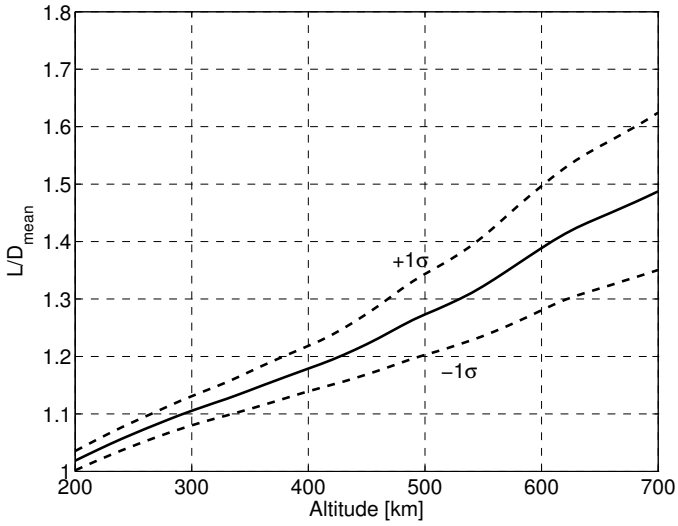

Figure 14.10: Required mean L/D ratio considering atmospheric co-rotation, atmospheric winds, atmospheric density variations and higher gravity harmonics.

latitude per orbit pass. Each pass was then recorded and the time taken to achieve complete global coverage, when all longitudes from 0° to 359° had been seen, could then be inferred. It has been assumed here that the only perturbations are the Earth's rotation and the Earth oblateness. Figure 4.3 on page 48 details how certain altitudes can have very high, and undesirable, repeat periods.

To avoid these large repeat periods a spacecraft that is descending is restricted to operate only within certain altitude windows. The drag force that the spacecraft experiences and hence the time that the spacecraft has within these windows is governed by atmospheric conditions and the properties of the spacecraft, which is defined by its ballistic coefficient B_C in Eq. (14.46) Larson and Wertz (2005, pp. 131-155).

$$B_C = \frac{m}{A_{ref} C_d} = -\frac{\rho V^2}{2a_D} \tag{14.46}$$

where m is the mass of the spacecraft, A_{ref} is an arbitrary reference area, C_d is the coefficient of drag, ρ is the atmospheric density and V is the relative flow velocity. As an example, it can be assumed that the altitude windows with acceptable revisit times are defined as those with repeat periods which stay below 5 days Davies et al. (2011). The altitude windows that meet this criteria (from 4.3 on page 48) are from 414 km to 523 km, from 312 km to 401 km and from 212 km to 221 km. There is also an upper window which extends from 589 km out beyond 700 km. In practice it can be argued that any spacecraft orbiting at an altitude beyond 589 km will not suffer from significant drag, therefore, the orbit decay would be relatively small. However, for these higher altitudes the limiting factor is the maximum altitude allowed by the payload(to achieve a certain performance), in effect creating its own altitude window. As an example, the current SSTL Earthmapper platform is a Sun-synchronous spacecraft with a maximum operating altitude of 686 km SSTL (2011). Therefore, for completeness, a satellite with its own altitude window from 589 km to 686 km with varying B_C has been included in the analysis.

The decay time through this different altitudes windows with varying B_C can then be computed and it is shown in Fig. 14.11. For the decay analysis the mean atmospheric conditions defined in ISO 14222 (2013) have been used.

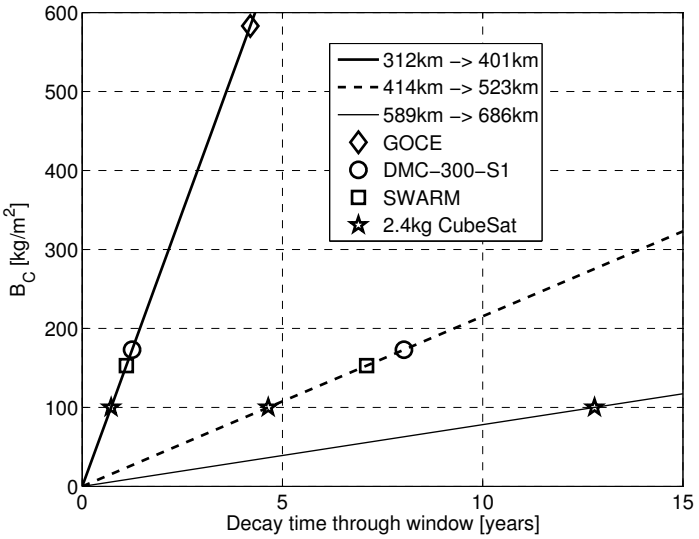

Figure 14.11: Decay time for varying ballistic coefficients.

Current satellite missions are displayed in Fig. 4.3 on page 48 and 14.11 as examples to demonstrate how real missions would behave if these spacecraft decayed within the altitude windows identified, which some currently operate close to or within. For each mission its B_C was estimated using Eq. (14.46) and with a generic C_D of 2.4.

This analysis shows how a spacecraft may need to tune its B_C to provide the necessary lifetime in a specific altitude window. The lowest altitude window (212 - 221 km) may presents a problem as even with a low drag spacecraft, the decay through the altitude window would be extremely quickly (within a few days) as the window is very small and at a very low altitude. The 312 - 401 km window could be feasibly used by a spacecraft with a high ballistic coefficient to achieve an appreciable 5 year lifetime without any drag compensation propulsion, though for higher drag spacecraft compensation would also be necessary in this window. The 414 - 523 km altitude window would allow most spacecraft to operate for over 5 years without any compensation. The final window demonstrates that a satellite limited by the maximum altitude allowed by the payload can also constrict the altitude window, hence inflicting requirements on the satellites required B_C.

14.5 Validation

In the previous sections, analytical expressions have been used to analyse the dynamics of the problem and to extract the required lift to drag ratios. Figure 14.12 shows the required L/D when a high fidelity numerical orbit propagator is used for a noon-midnight orbit. The propagator used (the same than in section 7.4 on page 88), models the Earth's rotation according to the ITRF93 model Boucher et al. (1994), the Earth's gravity field according to the EGM96 model Lemoine (1998), the Earth's

atmospheric density according to the NRLMSISE-00 Picone et al. (2002) model, the atmospheric winds according to the HWM93 Hedin et al. (1996) model and it also takes into account the perturbations caused by the Sun and the Moon gravity and the Solar Radiation Pressure (SRP) acting on the spacecraft. Some of these perturbations introduce osculating changes into the orbital elements, therefore, in Fig. 14.12 the mean orbital elements have been used to compute the required L/D. In addition some of the perturbations are highly variable (winds and atmospheric density) and some others depend on the mission profile and spacecraft properties (SRP and MLTAN). Figure 14.12 shows the averaged required L/D if all these different variability sources are taken into account, but it also shows as an example, how variable the required L/D can be during a descent.

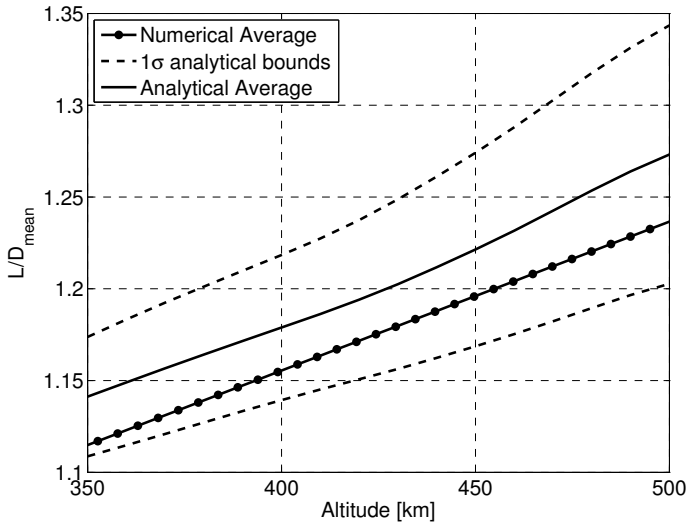

Figure 14.12: Required L/D ratio required to maintain a SSO in a typical decay using a high fidelity numerical propagator.

It has to be noted at this point, that the effects of the Sun, the Moon and the SRP, which have not been taken into account in the analytical study and which can have a secular effect on the orbit's inclination, do not appear to have a significant impact on the required L/D extracted from the high fidelity simulation. The effect of the solar radiation pressure depends on the spacecraft design (area to mass ratio and reflectivity) and hence, each particular mission will require its own analysis with respect to the SRP. Figure 14.12 results show a good level of agreement with the results presented in the previous sections and therefore validates the method presented here. The numerical results show that the numerical average is lower when compared to the analytical one. This is because a noon-midnight orbit has been chosen and these orbits have a lower required L/D (see Fig. 14.7).

14.6 Achievable Lift to Drag Ratios

In order to achieve the required L/D the spacecraft has to be shaped appropriately. To study maximum L/D geometries the aerodynamics of the candidate geometries have to be modelled. Unfortunately drag modelling in a rarefied-gas environment is not

completely understood (see chapter 3 on page 33) as there is a lack of knowledge on how the different surface properties affect the aerodynamic coefficients Moe and Moe (2010). Therefore, it can be difficult to optimise the surface properties in order to maximise the L/D.

Despite these uncertainties a few theoretical models exist which have shown good agreement with the limited set of on-orbit experiments that have been conducted. One of these models is the Sentman Sentman (1961) model which is the one that will be used in this section to analyse the aerodynamic properties. How to compute aerodynamic forces using the Sentman model has already been covered in section 3.4.1. This model, which has been extensively used to model the aerodynamic properties of LEO spacecraft Moe and Moe (2005), assumes that all gas particles that collide with the spacecraft surfaces are adsorbed to be later re-emitted. During the time that the gas particle is attached to the surface, energy is transferred from the particle into the surface bringing the particle into thermal equilibrium with the surface. The level of the thermal equilibrium achieved is measured by the energy accommodation coefficient σ_a. If $\sigma_a = 1$ the particle is re-emitted in complete thermal equilibrium with the surface, and hence it is re-emitted with the surface temperature T_w. If $\sigma_a = 0$ no accommodation has occurred and the particle is re-emitted with its original temperature. In the LEO environment the accommodation coefficient is usually close to one Moe and Moe (2005).

Using the Sentman model the C_l/C_d at different incidence angles for a flat plate, for different accommodation coefficients and wall temperatures can be obtained (shown in Fig. 14.13). The environmental parameters for this figure have been generated assuming a 400 km circular orbit with moderate solar activity ISO 14222 (2013) and using the NRLMSISE-00 atmospheric model Picone et al. (2002). Note how the aerodynamic forces extend beyond $\theta = 90°$ due to the random thermal motion of the gas particles. The C_l/C_d increases very rapidly at high θ angles because of the effect to the gas thermal random motion and because at those angles the drag has been significantly reduced.

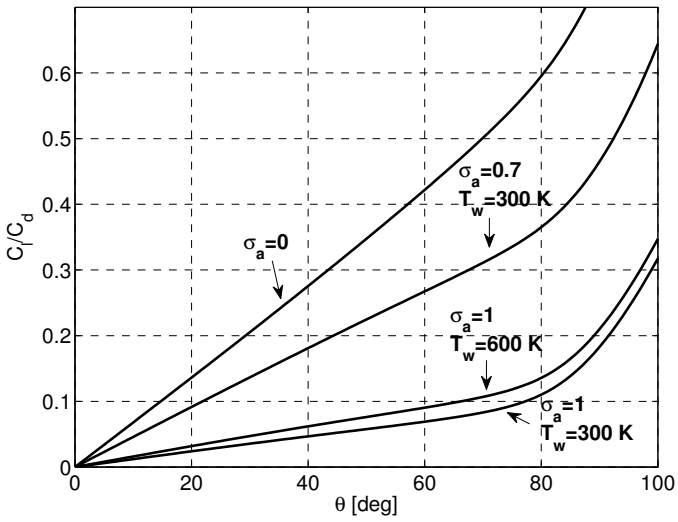

Figure 14.13: C_l/C_d at different incidence angles θ for one sided flat plate and for different accommodation coefficients and wall temperatures.

As seen in Fig. 14.13 the C_l/C_d increases as the incidence angle gets shallower, as the energy accommodation coefficient σ_a decreases and as the surface temperature increases (higher effect at high σ_a). Also, the achievable C_l/C_d is very low, well below 1 and even less if the orbital experiments suggesting that $\sigma_a \approx 1$ are taken into account Moe and Moe (2005). It is then clear that achieving the required L/D is impossible with currently used surface materials due to the high levels of energy accommodation. More advanced surfaces with reduced energy accommodation coefficients could potentially provide in the future the required L/D ratios.

To provide an upper limit of what would be feasible with advanced surface materials, Fig. 14.14 shows the C_l/C_d for a model that assumes ideal reflection (no energy transfer) for both specular or diffuse reflection Bird (1994). Again, the environmental parameters for this figure have been generated assuming a 400 km circular orbit with moderate solar activity ISO 14222 (2013) and using the NRLMSISE-00 atmospheric model Picone et al. (2002)

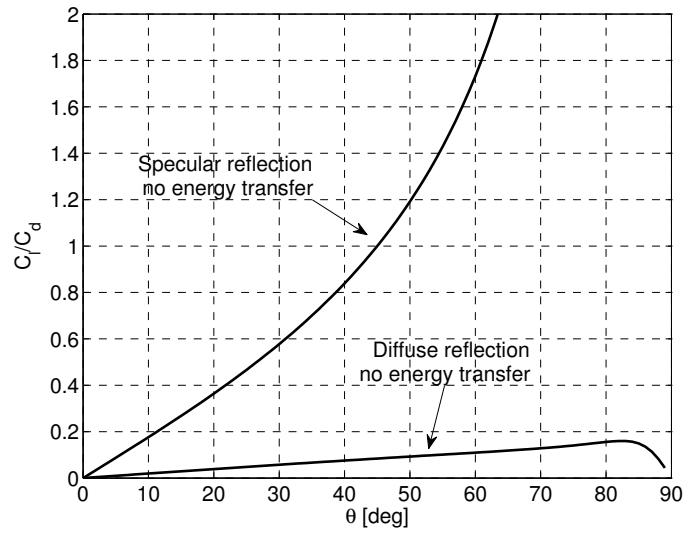

Figure 14.14: C_l/C_d at different incidence angles for a flat plate for ideal specular and diffuse reflection Bird (1994).

In Fig. 14.14 it can be seen that for specular reflection $C_l/C_d > 2$ could be achieved and hence the whole concept of descending Sun-synchronous orbits with aerodynamic inclination correction would become feasible. Identifying surface materials capable of achieving specular reflection requires additional research on the effects that the surface properties have on the aerodynamic coefficients.

14.7 Proposed Spacecraft Geometry and Attitude Control Strategy

In the previous section the maximum achievable L/D of an isolated flat surface exposed to the flow has been analysed and if it is assumed that specular reflection could be achieved in the future, then it is conceivable, that future spacecraft might use the

method presented here to its full extent. In this section a candidate high L/D shape will be presented as an example to discuss how the L/D can be controlled by controlling the spacecraft attitude with respect to the flow. This type of geometry will be first analysed using specular reflection and then with the Sentman model, to provide an overview of what could be possible in the future and at present.

A wedged shaped spacecraft orbiting with its thin edge as its leading edge and with that edge aligned with the radial direction z can provide a high and controllable L/D by just yawing ψ that wedge with respect to the flow. In addition, if the bottom and top flat faces are angled inwards (so that they are shadowed from the incoming flow), then the aerodynamic properties of that wedged shaped spacecraft only depend on the angle of the wedge ξ, its orientation with respect to the flow ψ and would be insensitive to pitch (up to a certain angle). Figure 14.15 shows the geometrical representation of such a spacecraft shape. At this point it has to be noted that the proposed shape has been developed only considering its aerodynamic properties and therefore it could prove impractical for a real spacecraft design.

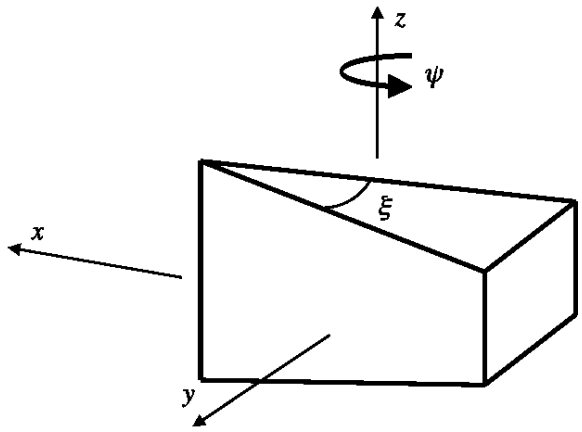

Figure 14.15: Proposed spacecraft shaped only considering its aerodynamic properties.

Figure 14.16 shows the L/D of a wedge spacecraft for different wedge angles ξ and at different yaw angles ψ if specular reflection is assumed. Note how the $L/D = 0$ if the yaw $\psi = 0$ and how positive and negative L/D can then be achieved by yawing the wedge with respect to the flow. Note that the $L/D < 0$ when $-90^\circ < u < 90^\circ$, so during that period the wedge shall maintain a negative yaw (to produce a $a_L < 0$) and that the $L/D > 0$ when $90^\circ < u < 270^\circ$, so during that period the wedge shall maintain a positive yaw (to produce a $a_L > 0$). Therefore, when traveling over the pole areas the spacecraft will need to reverse its yaw angle. It has to be noted that yawing a wedged shaped spacecraft could increase its absolute drag (still maintaining a good L/D) with respect to the drag with no yaw, hence a higher decay rate would be experience when using this method and a compromise would need to be sought.

If it is assumed that a minimum L/D of 1.4 is required to operate at all considered orbits and all considered environmental conditions, then it is clear from Fig. 14.16 that a wedge with an angle of 30° would be enough to generate the required L/D (higher L/D can be generated with shallower wedges) . Figure 14.17 shows the L/D and the

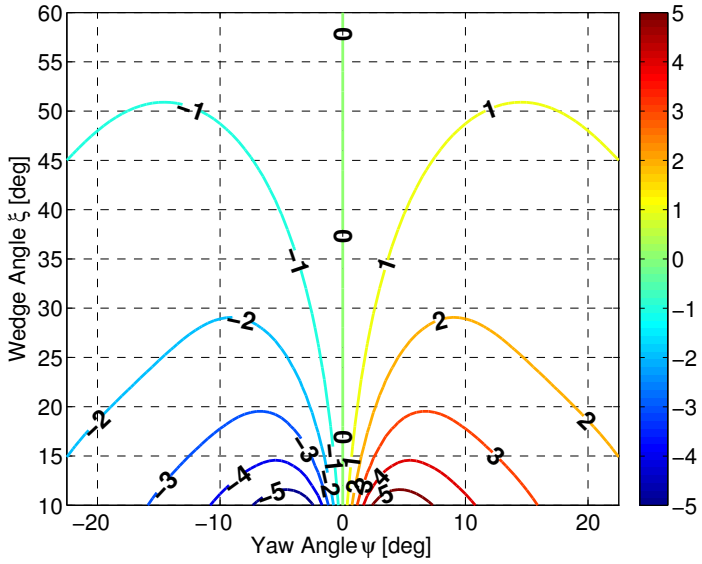

Figure 14.16: L/D of a wedge shaped spacecraft for different wedge angles ξ at different yaw angles ψ with respect to the flow.

drag increase when a 30° wedged spacecraft yaws. Note that that there is a peak in the L/D curve at approximately $\pm 10°$ and hence there are two yaw angles (at each side of the peak) that can provide the required L/D. Also note that beyond the peak the curve is relatively flat, hence requiring less accurate attitude control (less sensitive to yaw). In Fig. 14.17 it can also be seen that the drag increases significantly when the wedged spacecraft yaws. So to reduce the requirements on the attitude control it seems better to chose the yaw option that is located beyond the peak, but to minimise drag it seems better to chose the one that is before the peak. Depending on the mission requirements and constraints there will be a preferable option. The features shown in Fig. 14.17 are shared among all wedged shaped spacecraft.

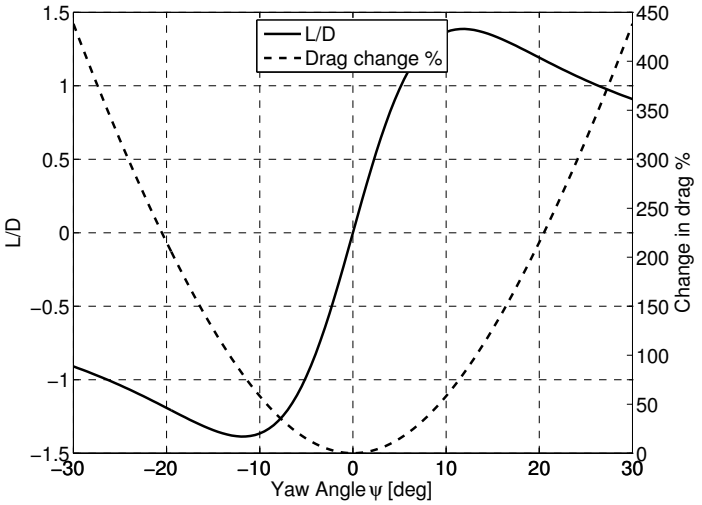

Figure 14.17: L/D and drag increase for varying yaw angles ψ for a 30° wedge shape spacecraft as in Fig. 14.15 assuming specular reflection.

The lateral sides of the wedge do not need to be flat and could be curved to tune the shape of the L/D curve shown in Fig. 14.17, so that the plateau is flatter (less sensitive to yaw) and matches the required L/D range on the mission scenario and also to provide a sharper transition (so reducing the magnitude of the yaw manoeuvres over the poles).

From the results presented in section 14.5 it is clear that a certain attitude would need to be maintained so that an average L/D is generated over several orbits. From the example shown in Fig. 14.17 it does seem feasible that an attitude control system could be designed that achieves this purpose.

If a more realistic aerodynamic model it is assumed, then the achievable L/D are much lower. Figure 14.18 shows the L/D and the drag increase when a 45° wedged spacecraft yaws if the Sentman Sentman (1961) model is assumed with total energy accommodation. Note that the maximum achievable L/D is around 0.1 but also note how the drag does not increase significantly for a wide range of yaw angles. This results opens the door to using the method presented here in combination with drag compensating propulsion.

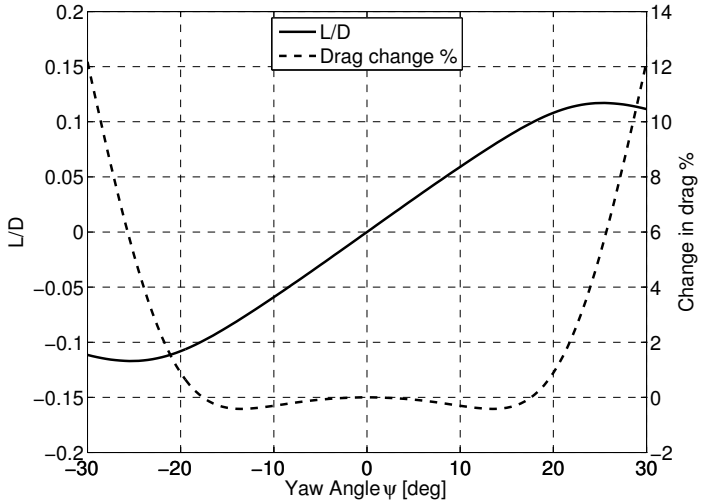

Figure 14.18: L/D and drag increase for varying yaw angles ψ for a 45° wedge shape spacecraft as in Fig. 14.15 assuming the Sentman model with total energy accommodation.

14.8 Discussion

The proposed method presented here has the potential to maintain the Sun-synchronous inclination while a spacecraft decays due to aerodynamic drag. This can potentially allow the operation of Earth observation spacecraft at lower orbit altitudes with minimal drag compensating propulsion. Lowering the operating altitude will result in potentially different data products that the ones that are being collected in the current higher altitude orbits. This difference in the data products will need to be taken into account when planning a mission that exploits this method.

Also, as shown in section 14.6, the L/D that it is currently achievable is not enough to satisfy the $L/D \approx 1.0 - 1.6$ that is required to maintain the Sun-synchronous inclination whilst decaying due to aerodynamic drag. Partially compensating the drag can lower the required L/D. For example, if propulsion is provided to compensate half the drag, the required aerodynamic L/D is then halved. Therefore, this technique could currently be used to save propellant in a Very Low Earth Orbit mission by letting the spacecraft decay at a slow pace and compensating the change of inclination with a small L/D. For example if the required L/D is 1.3 and the spacecraft has an aerodynamic $L/D = 0.1$ (perfectly achievable as shown in section 14.7) the propulsion system would only need to compensate 92% of the drag and hence a 8% ΔV saving would be possible. If the accommodation coefficient can be reduced and the L/D can be raised to 0.5 then the savings would increase to 38%. It is also to be noted that shaping the spacecraft to achieve the required L/D could potentially lead to an increase of the dry mass making the savings in propulsion questionable.

By looking at the available altitude windows that provide short revisit times and the ballistic coefficients required to last more than 5 years in those altitude windows, it can be claimed that these method can already be used to reduce the propulsion requirements of those missions. Instead of having a propulsion system that maintains the altitude, the mission could take advantage of a small aerodynamic lift to lower the propulsion requirements and letting the spacecraft decay through those windows. It also has to be noted that to fully achieve the potential of these orbits better aerodynamics (that could provide 4) are required, and hence more research is necessary in this area.

In addition, as this is essentially a method to aerodynamically control the inclination while the spacecraft decays, the orbit maintenance manoeuvres to maintain the MLTAN could also be integrated into the method. For example if the spacecraft has higher L/D than the one required, the inclination will be reduced more than required when decaying and hence the MLTAN will start to shift to earlier times, also, if the spacecraft has a lower L/D than the one required the inclination will not be reduced as required when decaying, and hence the MLTAN will then shift to later times. Therefore, by controlling the deviation of the L/D with respect to the required one the MLTAN could also be controlled.

14.9 Conclusions

The method proposed of correcting the inclination through aerodynamic lift in descending Sun-synchronous orbits requires an aerodynamic lift to drag ratio of $1.0 - 1.6$. Although it may be currently impossible to achieve the required aerodynamic lift to drag ratio, using currently characterised surface properties, this method can still be used with the help of some drag compensating propulsion. In this case this method can be used to save fuel (currently around a 8% ΔV saving) by letting the spacecraft slightly decay whilst still maintaining the Sun-synchronous aspect of the orbit. If generating the required aerodynamic lift to drag ratios is possible in the future, this method will be fully applicable and hence it will not require any drag compensating propulsion. If that is achieved, a wedged shaped spacecraft could generate the required aerodynamic lift to drag ratio and hence fully exploit the proposed method.

Chapter 15

Atmospheric Interface Re-Entry Point Targeting Using Aerodynamic Drag Control

The aerodynamic forces experienced by spacecraft orbiting in Low Earth Orbit (LEO) are usually considered perturbations that need to be avoided or compensated. Although this is generally the case, these aerodynamic forces can be controlled and used to achieve something useful.

Here a novel method is presented where the aerodynamic drag is used in order to target the re-entry point of a spacecraft. The method presented here has been only applied to circular orbits and its extension to eccentric orbits is left for future studies. The control of the aerodynamic drag is assumed to be achieved trough the control over the ballistic coefficient. How to control the ballistic coefficient of a spacecraft and its practical considerations have been left outside the scope of this study, but it is not difficult to envision simple ways to do so. For example, changing the cross section area of the spacecraft by changing the attitude of the spacecraft or by altering the geometry of a drag sail would be sufficient.

The method presented in this chapter is therefore an orbit control technique that aims to control the spacecraft's decay rate such that the spacecraft re-enters over a predefined location. Such a method could prove useful for drag enhancing de-orbit devices de-orbiting large spacecraft, where some components of the spacecraft are expected to survive re-entry. In this case, this technique could be used to avoid re-entering over populated areas. Also, this method could be applied to provide a passive method for small re-entry capsules to crudely target their landing area (as the method targets the re-entry location and not the landing point).

This chapter starts by providing a statement of the problem that it tries to solve. After that, the methodology to obtain the nominal decay profile to achieve this targeted re-entry is discussed, using simplified dynamics first, and then, some comments are provided to address the differences that appear when using high fidelity models. Next, a simple design of a controller that ensures that the spacecraft follows the prescribed nominal trajectory despite of the uncertainties in the environment is provided. All this theory is then applied for the case of the ΔDsat CubeSat to illustrate its applicability and performance, and finally, some discussion about the potential applications

is provided.

15.1 Problem Statement

The problem consists in making a spacecraft re-enter over a pre-designated ground point by changing its ballistic coefficient. The problem can be considered solved when a time history of the ballistic coefficient that makes the spacecraft satisfy the previous condition is provided.

To find an appropriate solution, the problem can be subdivided into two independent problems that can be tackled independently:

1. Compute a nominal trajectory (decay history) that would make the spacecraft re-enter over the designated point. To compute this trajectory it is assumed that the atmospheric environment is well known and that the spacecraft ballistic coefficient can be perfectly controlled. This essentially delivers the nominal ballistic coefficient time history that the spacecraft needs to follow.

2. Implement a control algorithm to make the spacecraft follow the nominal trajectory in the presence of the variations in the atmospheric environment and the uncertainties of the ballistic coefficient.

It is important to note that here the point that is targeted is the atmospheric interface re-entry point and not the impact/landing point. This is an important difference. As it is difficult to define where the re-entry starts, it is assumed that it starts when the spacecraft start to heat up significantly or start to break-up. For the analysis contained here this will be assumed to happen when the spacecraft decays below 100 km. Although this is somewhat arbitrary and this altitude will need to be adjusted depending on each case, it does not change the approach or the methodology presented here.

15.2 Nominal Trajectory

If a spacecraft maintains a constant ballistic coefficient (C_B) during all its decay it will re-enter over a certain point. This re-entry point then, is a function of the spacecraft's initial position and velocity, its ballistic coefficient, the Earth's gravity field, the atmospheric environment and of other forces (such as solar radiation pressure and third body perturbations). If one of the mentioned parameters changes then the re-entry point will change. Therefore, assuming everything else remains constant, a simple method to change the re-entry point would be to change the spacecraft ballistic coefficient to a different constant value. If this is the case, and the spacecraft can adopt a range of different ballistic coefficients that are to be maintained constant throughout its decay, then the spacecraft can alter its re-entry point but only along a line. Figure 15.1 shows an example of this considering an initial 70 deg. inclination circular orbit decaying from 300 km to 100 km with ballistic coefficients ranging from $C_{B1} = 0.0201$ to $C_{B2} = 0.0200\,m^2/kg$. This line (re-entry point locus) closely resembles the orbit ground track but is not exactly the same.

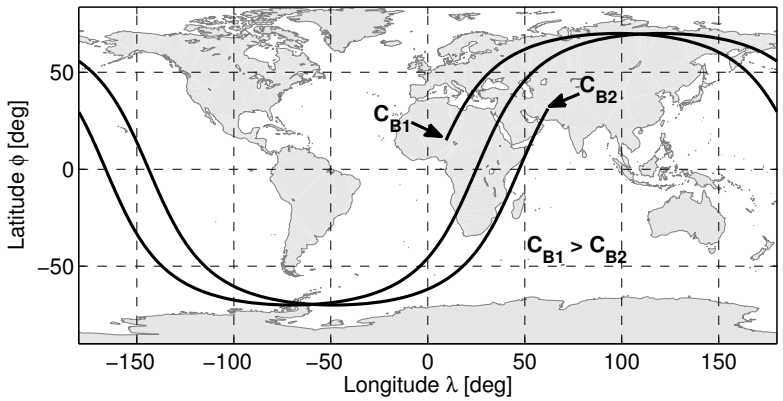

Figure 15.1: Re-entry points (not to be confused with a ground track) applying different constant ballistic coefficients C_B throughout the decay.

This simple strategy can be useful at the final stages of the decay because it allows a point along the re-entry point locus (only along-track) to be targeted. But this simple strategy is not very useful if global coverage is required as it does not provide any cross-track targeting capabilities. This strategy essentially targets the argument of latitude of the re-entry and the time of re-entry is a by-product of this. Therefore, the position of the spacecraft in the orbit plane when it re-enters is specified by the target argument of latitude and the by-product time of re-entry fixes the position of the Earth with respect to the orbit plane. So the argument of latitude fixes the latitude and the time of re-entry the longitude of the re-entry point. To get cross track capabilities these two variables (time of re-entry and argument of latitude at re-entry) need to be controlled independently.

Targeting the re-entry time independently from the argument of latitude can be achieved by changing the ballistic coefficient during the orbital decay $C_B = f(t)$. This alters the decay rate and achieves different decay profiles. Figure 15.2a shows the evolution of the altitude with respect to the orbit count (argument of latitude), and Fig. 15.2b with respect to time, for three different ballistic coefficient profile scenarios that share the same initial conditions and atmosphere. These figures show that different ballistic coefficient profiles can make the spacecraft re-enter at the same argument of latitude (and hence at the same latitude) but at different times (and hence at different longitudes). The re-entry time of these three trajectories can be computed by adding the period of all their orbits and, as their decay profiles are different, their re-entry time will be different (hence re-entering at different longitudes).

The three example trajectories shown in the figure can be classified looking at their relative decay rates. The trajectory with a constant ballistic coefficient throughout the decay $C_B = k$ will serve as a reference. Then, $C_B = f_1(t)$ shows a slower decay at the beginning and a more rapid decay at the end (slow-rapid) and $C_B = f_2(t)$ shows a more rapid decay at the beginning and a slower decay at the end (rapid-slow) when compared to the reference decay $C_B = k$. All of these trajectories re-enter after spending the

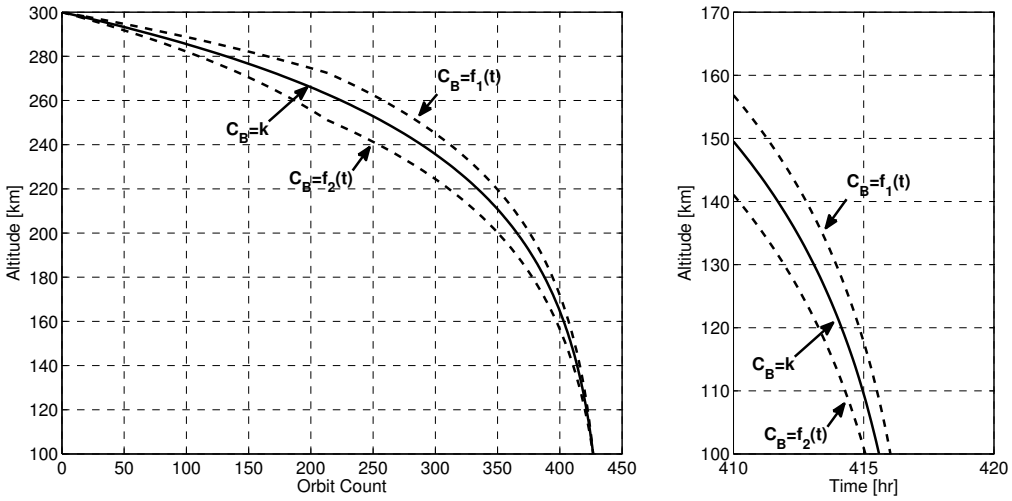

(a) (b)

Figure 15.2: Altitude decay with respect to the orbit count (proportional to the argument of latitude) in a) and detail of the last part of the decay with respect to time in b).

same number of orbits (as they share their final argument og latitude) but they spend these orbits at different altitudes (where the periods are different), hence achieving different re-entry times.

The trajectory with a slow-rapid decay will spend more orbits at a higher altitude (where the orbital period is longer) than the reference trajectory ($C_B = k$) and hence it will re-enter at the same argument of latitude (same latitude) but at a later time (westward longitude). Also, the trajectory with a rapid-slow decay spends more orbits at a lower altitude (where the period is shorter) than the reference trajectory ($C_B = k$) and hence it will re-enter at the same argument of latitude (same latitude) but at an earlier time (eastward longitude).

This technique to target independently the re-entry time and the re-entry argument of latitude can be exploited to target the re-entry point latitude and longitude, thus achieving cross-track targeting capabilities.

A convenient way to explore the dynamics of such a method is to discretize the ballistic coefficient function so that the whole time interval is comprised by segments of constant ballistic coefficient. Figure 15.3 shows the trajectory broken down into these discrete segments. In this scenario, a state transition function can be defined as in Eq. 15.1 so that it outputs the next state vector $\boldsymbol{x}_{n+1}$ from the current state vector $\boldsymbol{x}_n$ assuming that the ballistic coefficient remains constant in that interval. As it it defined in Eq. 15.1 this state transition function outputs the difference between two consecutive state vectors, so that if the current state vector is known $\boldsymbol{x}_n$, the next state vector $\boldsymbol{x}_{n+1}$ can be then computed.

$$\boldsymbol{x}_{n+1} = \Phi_n \left(\boldsymbol{x}_n, C_B \right) + \boldsymbol{x}_n \tag{15.1}$$

If this state transition function could be computed then the effects of an arbitrary ballistic coefficient time function could be evaluated. The construction of such functions

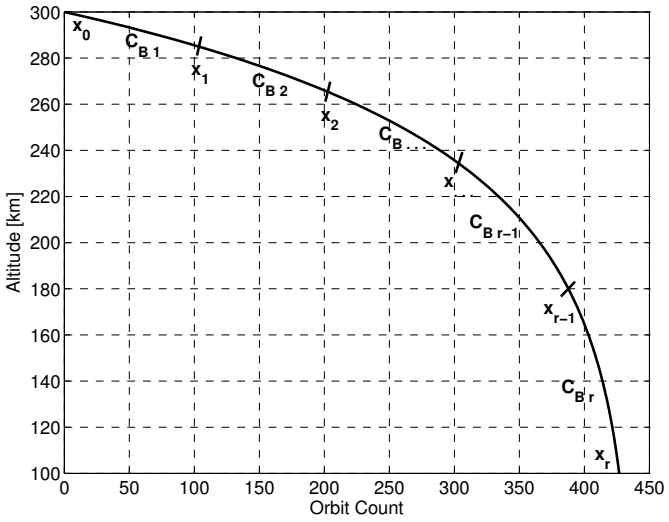

Figure 15.3: Discretization of the ballistic coefficient function.

can be done using numerical propagators but the results lack the insight provided by an analytical approach. If the the dynamics of the problem are sufficiently simplified, analytical expressions of this state transition function can be found, therefore providing an insight into the dynamics of the problem. With the analytical expressions solutions can then be found that can be used as first guesses in the numerical algorithms.

In the sections that follow, a method to construct the nominal trajectory is provided. First, to provide an insight into the problem, the nominal trajectory will be constructed analytically (using simplified dynamic models) and then some comments will be made when using numerical propagators (with accurate dynamic models).

15.2.1 Analytical Approach Using Simplified Dynamic Models

The main simplifications that will be assumed in the simplified dynamics case are that there will be only two forces shaping the orbit. First the gravitational pull of the Earth modelled as a point mass plus a contribution due to the Earth's oblateness (J_2) and the second force being the aerodynamic drag caused by an exponential atmosphere. Under these assumptions the orbit of a spacecraft can be considered Keplerian but with secular variations on its orbital parameters (due to drag). Also, the physical body of the Earth will be modelled as a sphere with a radius of $R_\oplus$ and finally, it will be assumed that the orbits are circular. Under these assumptions a good representation of the state vector can be the orbital parameters describing a circular orbit as shown in Eq. 15.2.

$$\boldsymbol{x} = \left[\; t, \quad u, \quad a, \quad \Omega, \quad i \; \right] \tag{15.2}$$

where t refers to the time, a to the semi-major axis, u to the argument of latitude, Ω to the right ascension of the ascending node (RAAN) and i to he orbit's inclination. At this point, it is pertinent to explicitly state that under the current assumptions, the orbit's altitude h can be related to the orbit's semi-major axis a by $h = a - R_\oplus$,

so their role as state vector variables is interchangeable. Here the semi-major axis is used, but the altitude will appear in the figures to make their interpretation easier.

State Transition Function

In a decaying orbit the state vector parameters will change during the decay. The objective is to get a function that can interrelate these changes to one of the state variables. This will be the state transition function.

Here all the state variables will be written in terms of the semi-major axis as $t, u, \Omega, i = f(a)$. Therefore, the discretization shown in Fig. 15.3 will be defined by the semi-major axis at the segment limits.

This process can start with the inclination, which is the simplest case, as an orbit subject to aerodynamic drag will decay with a constant inclination. This assumption holds when only J_2 and aerodynamic drag effects from a stationary atmosphere are considered King-Hele (1987, pp. 140-164) (these are the assumptions made). Therefore i is a constant during the decay and hence is not a function of a. This can be easily written as Eq. 15.3.

$$i_{n+1} = i_n = i_0 \tag{15.3}$$

The only secular change in the semi-major axis will be produced by the aerodynamic drag (J_2 only produces periodic variations). The semi-major axis change with respect to time when subject to aerodynamic drag in a circular orbit can be written as in Eq. 15.4 Vallado (2001, pp. 567-674) (already simplified for circular orbits).

$$\frac{da}{dt} = -\frac{2}{n} a_D \tag{15.4}$$

where a_D is the acceleration due to drag and $n = \sqrt{\mu/a^3}$ is the mean motion that can be written in terms of the semi-major axis a and the gravitational constant of the Earth μ. Then, the acceleration due to drag can be written as in Eq. 15.5.

$$a_D = qC_B \tag{15.5}$$

$$q = \frac{1}{2}\rho V^2 \tag{15.6}$$

where q (Eq. 15.6)is the dynamic pressure that is a function of the atmospheric density ρ and the relative velocity of the spacecraft with respect to the flow V. Although the atmosphere co-rotates with the Earth Challinor (1968) and there are atmospheric winds Drob et al. (2008) here a stationary atmosphere has been assumed and hence V can be taken as the spacecraft orbital velocity. The ballistic coefficient C_B is defined in Eq. 15.7 and is a function of the spacecraft's reference area A_{ref}, drag coefficient C_D and its mass m Larson and Wertz (2005, pp. 131-155).

$$C_B = \frac{A_{ref} C_D}{m} \tag{15.7}$$

By grouping all the constant terms in the Eq. 15.5 in the constant K_1, the drag acceleration expression can be simplified as shown in Eq. 15.8.

$$a_D = K_1 \rho V^2 \tag{15.8}$$

$$K_1 = \frac{C_B}{2} \tag{15.9}$$

As already mentioned in the assumptions, the density will be modelled using an exponential atmospheric model. Therefore, the atmospheric density can be written as in Eq. 15.10.

$$\rho(a) = \rho_0 e^{-\frac{a-a_o}{H}} \tag{15.10}$$

where ρ_0 is the density at semi-major axis a_0 and where H represents the scale height. Also if we assume that the velocity relative to the flow is the orbital velocity then this velocity can be computed following Eq. 15.11.

$$V = \sqrt{\frac{\mu}{a}} \tag{15.11}$$

Combining equation 15.8 with 15.10 and 15.11 the change in the semi-major axis can be re-written as in Eq. 15.12.

$$\frac{da}{dt} = K_2 \sqrt{a} e^{\frac{-a}{H}} \tag{15.12}$$

where K_2 is a compact representation of the constant terms.

$$K_2 = -2K_1 \sqrt{\mu} \rho_0 e^{\frac{a_0}{H}} = -C_B \sqrt{\mu} \rho_0 e^{\frac{a_0}{H}} \tag{15.13}$$

Making use of the following variable time transformation $t = u/n$, Eq. 15.12 can be written as in Eq. 15.14.

$$\frac{da}{du} = K_3 a^2 e^{\frac{-a}{H}} \tag{15.14}$$

again with the constant terms included in K_3.

$$K_3 = \frac{K_2}{\sqrt{\mu}} = -C_B \rho_0 e^{\frac{a_0}{H}} \tag{15.15}$$

Integrating Eq. 15.12 results in Eq. 15.16 (where erfi is the imaginary error function).

$$t = f_t(a) = \int \frac{1}{K_2 \sqrt{a} e^{\frac{-a}{H}}} da = \frac{\sqrt{\pi}\sqrt{H}\,\mathrm{erfi}\left(\frac{\sqrt{a}}{\sqrt{H}}\right)}{K_2} + const \tag{15.16}$$

Integrating Eq. 15.14 results in Eq. 15.17(where Ei is the exponential integral).

$$u = f_u(a) = \int \frac{1}{K_3 a^2 e^{\frac{-a}{H}}} da = \frac{a\,\mathrm{Ei}\left(\frac{a}{H}\right) - H e^{\frac{a}{H}}}{K_3 H a} + const \tag{15.17}$$

Note how both Eqs. 15.16 and 15.17 can be used to link changes in a to changes in t and u.

A similar expression for the RAAN Ω (Eq. 15.18) can be obtained by looking at the change in RAAN produced by the Earth's oblateness Vallado (2001, pp. 567-674).

$$\frac{d\Omega}{dt} = -\frac{3nR_{\oplus}^2 J_2}{2a^2}\cos(i) = K_4 a^{-7/2} \tag{15.18}$$

$$K_4 = -\frac{3R_{\oplus}^2 J_2 \cos(i)\sqrt{\mu}}{2} \tag{15.19}$$

where J_2 is the Earth's second dynamic form factor. This expression can be written in terms of $d\Omega/da$ if it is combined with Eq. 15.12 as in Eq. 15.20.

$$\frac{d\Omega}{da} = K_5 a^{-4} e^{\frac{a}{H}} \tag{15.20}$$

$$K_5 = \frac{K_4}{K_2} = \frac{3R_{\oplus}^2 J_2 \cos(i)}{2C_B \rho_0 e^{\frac{a_0}{H}}} \tag{15.21}$$

Integrating Eq. 15.20 results in Eq. 15.22.

$$\Omega = f_{\Omega}(a) = \int K_5 a^{-4} e^{\frac{a}{H}} da = \frac{K_5\left(a^3 \mathrm{Ei}\left(\frac{a}{H}\right) - He^{\frac{a}{H}}\left(2H^2 + Ha + a^2\right)\right)}{6H^3 a^3} + const \tag{15.22}$$

Then, functions f_t, f_u, f_{Ω} can be used to compute the state vector at any semi-major axis (altitude) during a decay provided that the ballistic coefficient remains constant. These functions can also be used then to compute the state vector at the different segment limits as shown in Eq. 15.23-15.26.

$$t_n - t_{n-1} = \Delta t_n = f_t\left(a_n, C_{Bn}\right) - f_t\left(a_{n-1}, C_{Bn}\right) \tag{15.23}$$

$$u_n - u_{n-1} = \Delta u_n = f_u\left(a_n, C_{Bn}\right) - f_u\left(a_{n-1}, C_{Bn}\right) \tag{15.24}$$

$$\Omega_n - \Omega_{n-1} = \Delta\Omega_n = f_{\Omega}\left(a_n, C_{Bn}\right) - f_{\Omega}\left(a_{n-1}, C_{Bn}\right) \tag{15.25}$$

$$i_{n+1} - i_n = \Delta i_n = 0 \tag{15.26}$$

The state transition function can then be written as in Eq. 15.27.

$$\Phi_n = \begin{bmatrix} f_t\left(a_n, C_{Bn}\right) - f_t\left(a_{n-1}, C_{Bn}\right) \\ f_u\left(a_n, C_{Bn}\right) - f_u\left(a_{n-1}, C_{Bn}\right) \\ a_n - a_{n-1} \\ f_{\Omega}\left(a_n, C_{Bn}\right) - f_{\Omega}\left(a_{n-1}, C_{Bn}\right) \\ 0 \end{bmatrix} \tag{15.27}$$

Therefore, if an initial set of conditions are set $\boldsymbol{x}_0$ then all the subsequent state vectors up unto re-entry $\boldsymbol{x}_0$, $\boldsymbol{x}_1$, ..., $\boldsymbol{x}_n$, ..., $\boldsymbol{x}_{r-1}$, $\boldsymbol{x}_r$ can be computed using the formulas provided in this section. This can be written in a function format as shown in Eq. 15.28.

$$\boldsymbol{x}_n = \begin{bmatrix} t_n \\ u_n \\ a_n \\ \Omega_n \\ i_n \end{bmatrix} = [\boldsymbol{x}_0 + \Phi_1 + \ldots + \Phi_n] = F_{\boldsymbol{x}n} \begin{pmatrix} \boldsymbol{x}_0 \\ a_0, \ldots, a_n \\ C_{B1}, \ldots, C_{Bn} \end{pmatrix} \tag{15.28}$$

This last function $F_{\boldsymbol{x}n}$ can be used to compute the state vector at any semi-major axis (altitude) during a decay providing that the ballistic coefficient can be discretized as a function of the semi-major axis.

Latitude and Longitude

The state vector is useful but it does not explicitly provide the latitude ϕ and the longitude λ where the spacecraft is over the Earth. The latitude can be computed using spherical trigonometry with the following formula shown in Eq. 15.29.

$$\sin\phi = \sin u \sin i \tag{15.29}$$

The longitude can be computed as shown in the following Eq. 15.30.

$$\lambda = \lambda_{AN\,0} + (\Omega - \Omega_0) + \arcsin(\tan\phi \sin i) - \omega_\oplus t \tag{15.30}$$

where $\lambda_{AN\,0}$ is the initial longitude of the ascending node, Ω_0 the initial RAAN and $\omega_\oplus$ is the Earth's angular velocity. The latitude and longitude can be also related to the orbit state vector (although some of the state variables are not directly relevant to compute ϕ and λ) through a function that is shown in Eq. 15.31.

$$\begin{bmatrix} \phi \\ \lambda \end{bmatrix} = \begin{bmatrix} \arcsin(\sin u \sin i) \\ \lambda_0 + (\Omega - \Omega_0) + \arcsin(\tan\phi \sin i) - \omega_\oplus t \end{bmatrix} = F_{\phi,\lambda}(t, u, a, \Omega, i) \tag{15.31}$$

Therefore, the function G_n defined in equation 15.32 can be used to compute the latitude an longitude at any semi-major axis (altitude) during a decay providing that the ballistic coefficient can be discretized as a function of the semi-major axis.

$$G_n = F_{\phi,\lambda}(F_{\boldsymbol{x}n}) \tag{15.32}$$

With this function G_n the location where a spacecraft re-enter (crosses the 100 km altitude) can be easily computed using only analytical expressions.

System Dynamics

A way to explore the behaviour of this particular system is to compute the Jacobian of G_n that can be defined the following Eq. 15.33.

$$J_{G_n} = J_{F_{\phi,\lambda}} J_{F_{\boldsymbol{x}n}} = \begin{bmatrix} \frac{\partial\phi}{\partial a_0} & \cdots & \frac{\partial\phi}{\partial a_n} & \frac{\partial\phi}{\partial C_{B1}} & \cdots & \frac{\partial\phi}{\partial C_{Bn}} \\ \frac{\partial\lambda}{\partial a_0} & \cdots & \frac{\partial\lambda}{\partial a_n} & \frac{\partial\lambda}{\partial C_{B1}} & \cdots & \frac{\partial\lambda}{\partial C_{Bn}} \end{bmatrix} \tag{15.33}$$

where $J_{F_{\phi,\lambda}}$ and $J_{F_{\boldsymbol{x}}}$ can be defined as in Eq. 15.34-15.35.

$$J_{F_{\phi,\lambda}} = \begin{bmatrix} \frac{\partial \phi}{\partial t} & \frac{\partial \phi}{\partial u} & \frac{\partial \phi}{\partial a} & \frac{\partial \phi}{\partial \Omega} \\ \frac{\partial \lambda}{\partial t} & \frac{\partial \lambda}{\partial u} & \frac{\partial \lambda}{\partial a} & \frac{\partial \lambda}{\partial \Omega} \end{bmatrix} \tag{15.34}$$

$$J_{F_{\boldsymbol{x}n}} = \begin{bmatrix} \frac{\partial F_{\boldsymbol{x}t}}{\partial a_0} & \cdots & \frac{\partial F_{\boldsymbol{x}t}}{\partial a_n} & \frac{\partial F_{\boldsymbol{x}t}}{\partial C_{B1}} & \cdots & \frac{\partial F_{\boldsymbol{x}t}}{\partial C_{Bn}} \\ \frac{\partial F_{\boldsymbol{x}u}}{\partial a_0} & \cdots & \frac{\partial F_{\boldsymbol{x}u}}{\partial a_n} & \frac{\partial F_{\boldsymbol{x}u}}{\partial C_{B1}} & \cdots & \frac{\partial F_{\boldsymbol{x}u}}{\partial C_{Bn}} \\ \frac{\partial F_{\boldsymbol{x}a}}{\partial a_0} & \cdots & \frac{\partial F_{\boldsymbol{x}a}}{\partial a_n} & \frac{\partial F_{\boldsymbol{x}a}}{\partial C_{B1}} & \cdots & \frac{\partial F_{\boldsymbol{x}a}}{\partial C_{Bn}} \\ \frac{\partial F_{\boldsymbol{x}\Omega}}{\partial a_0} & \cdots & \frac{\partial F_{\boldsymbol{x}\Omega}}{\partial a_n} & \frac{\partial F_{\boldsymbol{x}\Omega}}{\partial C_{B1}} & \cdots & \frac{\partial F_{\boldsymbol{x}\Omega}}{\partial C_{Bn}} \end{bmatrix} \tag{15.35}$$

Note that in $J_{F_{\phi,\lambda}}$, $\frac{\partial \phi}{\partial a} = \frac{\partial \lambda}{\partial a} = 0$ and also in $J_{F_{\boldsymbol{x}}}$, $\frac{\partial F_{\boldsymbol{x}a}}{\partial a_n} = \frac{\partial F_{\boldsymbol{x}a}}{\partial C_{Bn}} = 0$ therefore these two Jacobian can be simplified using the following Eq. 15.36-15.37.

$$J_{F_{\phi,\lambda}} = \begin{bmatrix} \frac{\partial \phi}{\partial t} & \frac{\partial \phi}{\partial u} & \frac{\partial \phi}{\partial \Omega} \\ \frac{\partial \lambda}{\partial t} & \frac{\partial \lambda}{\partial u} & \frac{\partial \lambda}{\partial \Omega} \end{bmatrix} \tag{15.36}$$

$$J_{F_{\boldsymbol{x}n}} = \begin{bmatrix} \frac{\partial F_{\boldsymbol{x}t}}{\partial a_0} & \cdots & \frac{\partial F_{\boldsymbol{x}t}}{\partial a_n} & \frac{\partial F_{\boldsymbol{x}t}}{\partial C_{B1}} & \cdots & \frac{\partial F_{\boldsymbol{x}t}}{\partial C_{Bn}} \\ \frac{\partial F_{\boldsymbol{x}u}}{\partial a_0} & \cdots & \frac{\partial F_{\boldsymbol{x}u}}{\partial a_n} & \frac{\partial F_{\boldsymbol{x}u}}{\partial C_{B1}} & \cdots & \frac{\partial F_{\boldsymbol{x}u}}{\partial C_{Bn}} \\ \frac{\partial F_{\boldsymbol{x}\Omega}}{\partial a_0} & \cdots & \frac{\partial F_{\boldsymbol{x}\Omega}}{\partial a_n} & \frac{\partial F_{\boldsymbol{x}\Omega}}{\partial C_{B1}} & \cdots & \frac{\partial F_{\boldsymbol{x}\Omega}}{\partial C_{Bn}} \end{bmatrix} \tag{15.37}$$

All the functions and Jacobians defined up to this point can be written as analytical formulas. In particular the derivates of the $J_{F_{\boldsymbol{x}}}$ can be easily computed referring to equations 15.16, 15.17 and 15.22 as the following Eq. 15.38.

$$\begin{aligned} \frac{\partial F_{\boldsymbol{x}\,t,u,\Omega}}{\partial a_i} &= \frac{\partial f_{t,u,\Omega}(a_i, C_{Bi})}{\partial a_i} - \frac{\partial f_{t,u,\Omega}(a_i, C_{Bi+1})}{\partial a_i} \\ \frac{\partial F_{\boldsymbol{x}\,t,u,\Omega}}{\partial C_{Bi}} &= \frac{\partial f_{t,u,\Omega}(a_i, C_{Bi})}{\partial C_{Bi}} - \frac{\partial f_{t,u,\Omega}(a_{i-1}, C_{Bi})}{\partial C_{Bi}} \end{aligned} \tag{15.38}$$

The Jacobian of G is a function of the initial state vector the semi-major axis limits of the segments and the ballistic coefficients $J_G\left(\boldsymbol{x}_0, a_0, \ldots, a_n, C_{B1}, \ldots, C_{Bn}\right)$.

This Jacobians are very useful when studying the dynamics of the system and also when constructing the numerical algorithms to find solutions or other properties of the systems. The equations presented in this section contain all the required tools to start exploring the potential solutions of the problem.

The Strategy

It is clear that to adjust the latitude and the longitude only 2 degrees of freedom are required.

The strategy envisioned by the author assumes that the spacecraft can alter its ballistic coefficient within a range $[C_{Bmin}, C_{Bmax}]$ where a mean or nominal ballistic coefficient can be defined as $C_{Bmean} = \left(C_{Bmax} + C_{Bmin}\right)/2$. To provide enough degrees of freedom, the spacecraft will maintain an initial ballistic coefficient C_{B1} from its initial altitude a_0 until it reaches a transition altitude a_t where it will transition to a second ballistic coefficient C_{B2} that it will be maintained until re-entry a_r. Assuming that the initial position cannot be chosen and that the re-entry altitude is fixed (100 km), this approach seems to have three degrees of freedom (C_{B1}, C_{B2} and a_t). To reduce this to the only two degrees of freedom required it will be assumed that both ballistic coefficients are equidistant to the the mean ballistic coefficient, but one being

higher and the other being lower ($C_{B1} = C_{Bmean} + \Delta C_B$ and $C_{B2} = C_{Bmean} - \Delta C_B$). Note that ΔC_B can be either positive or negative and that for this strategy to be successful C_{B1} and C_{B2} need to be within the achievable range (and potentially leaving some control authority for the onboard trajectory control). With this strategy, the parameters are reduced to the transition altitude a_t and the ballistic coefficient delta ΔC_B. This arrangement is shown in Fig. 15.4.

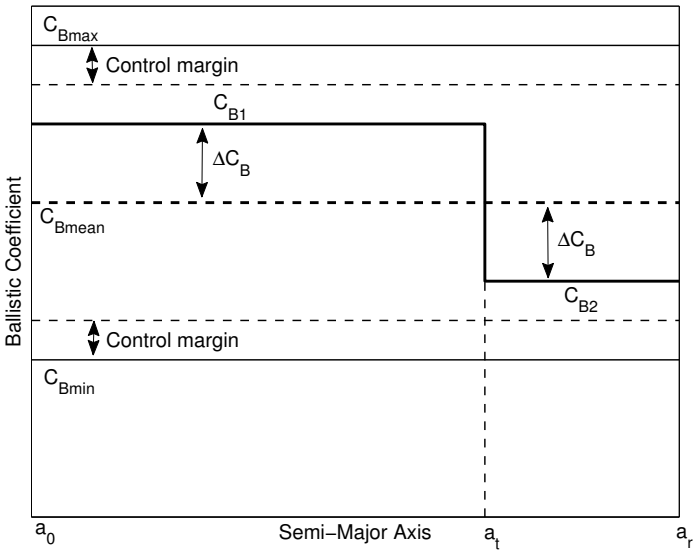

Figure 15.4: Proposed strategy outline. A constant ballistic coefficient C_{B1} is maintained from the initial semi-major axis a_0 to a transition semi-major axis a_t where the ballistic coefficient is changed to C_{B2} until the spacecraft re-enters at a_r.

Then, a way to explore the area that can be targeted is to set ΔC_B to its maximum (so that the ballistic coefficient reach their maximum and minimum) and move the transition semi-major axis a_t from a_0 to a_r. This process will produce two lines (one for positive ΔC_B and another one with negative ΔC_B) that separately, will resemble the one shown in Fig. 15.1, and that when plotted together will enclose the area that the spacecraft is capable to target. An exaggerated example of this is shown in Fig. 15.5. The values used to produce this figure have been: $h_0 = 200\,km$, $h_f = 100\,km$, $C_{Bmax} = 0.0223\,m^2/kg$, $C_{Bmin} = 0.0222\,m^2/kg$, $i = 70^{\text{o}}$, $H = 55\,km$, $\rho_0 = 6.66 \times 10^{-12}\,kg/m^3$, $a_{\rho_0} = 350\,km$ with the longitude difference between the two lines being exaggerated by a factor of 750 (so it can be clearly seen in the figure). The centre line in Fig. 15.5 can be obtained by setting a constant ballistic coefficient throughout the decay and then scanning through all possible ballistic coefficients (so setting the transition altitude to the initial $a_t = a_0$ and going through $-\left(C_{Bmax} - C_{Bmin}\right)/2 < \Delta C_B < \left(C_{Bmax} - C_{Bmin}\right)/2$).

Targeting the points that are enclosed in this area can be achieved by changing the ΔC_B and a_t within the achievable limits. Figure 15.6 shows how these parameters need to change to target any point within the accessible area. The same values as in Fig. 15.5 have been used to generate Fig. 15.6. It is clear that having a positive ΔC_B (so $C_{B1} < C_{B2}$) moves the re-entry point to the east and having a negative ΔC_B (so $C_{B1} < C_{B2}$) moves the re-entry point to the west. Then if $\Delta C_B > 0$ increasing the transition altitude increases the argument of latitude of the re-entry point and if

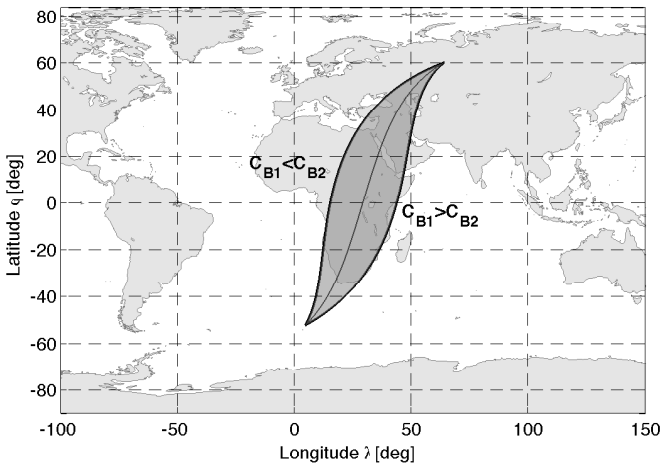

Figure 15.5: Area that can be targeted by changing ΔC_B and the transition altitude a_t. The ballistic coefficients are $C_{B1} = C_{Bmean} + \Delta C_B$ and $C_{B2} = C_{Bmean} - \Delta C_B$. The limits shown by the solid lines correspond to maximum ΔC_B (so that the ballistic coefficients reach their limits C_{Bmax} and C_{Bmin}).

$\Delta C_B > 0$ increasing the transition altitude reduces the argument of latitude of the re-entry point.

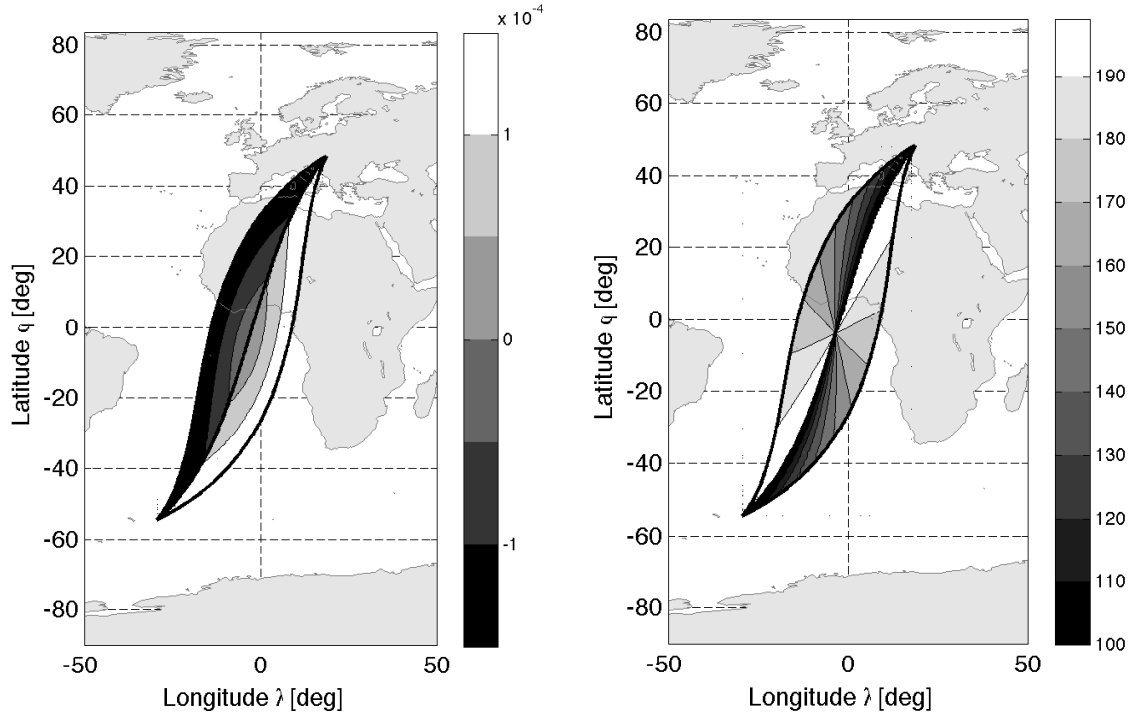

(a) (b)

Figure 15.6: Re-entry point for different ΔC_B and transition altitudes h_t.

The longitude difference between the two exterior lines (maximum and minimum

ΔC_B) at equal argument of latitude (equal latitude) can be used as a proxy for the amount of area that can be targeted. Figure 15.7 shows how this metric evolves when the ΔC_B and the initial altitude h_0 are increased. The values used to produced this figure are the following: $h_0 = 250\,km$, $h_f = 100\,km$, $C_{Bmax} = 0.0223\,m^2/kg$, $C_{Bmin} = 0.0222\,m^2/kg$, $i = 70^{\text{o}}$, $H = 55\,km$, $\rho_0 = 6.66 \times 10^{-12}\,kg/m^3$, $a_{\rho_0} = 350\,km$ and this time the longitude difference has not been exaggerated for clarity. As it could be expected, increasing the ΔC_B increases the longitude difference and therefore the area that can be targeted, also, increasing the initial altitude, also increases the longitude differences and also retards the re-entry argument of latitude (it takes longer to decay).

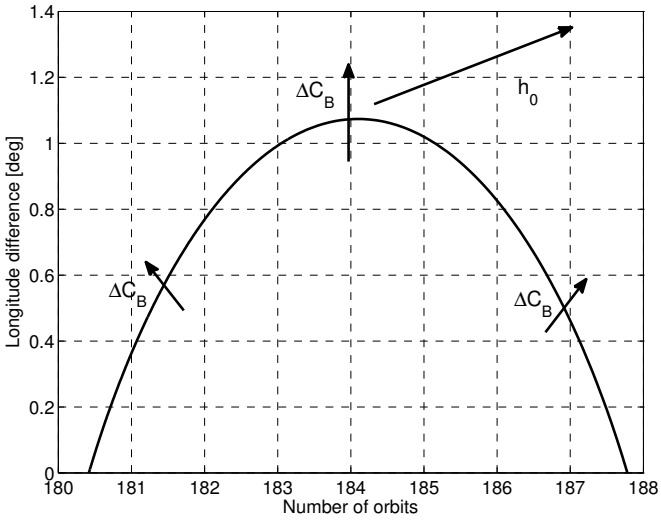

Figure 15.7: Longitude difference between the two exterior lines (maximum and minimum ΔC_B) at equal argument of latitude (equal latitude). The arrows show how increasing different parameters affect this longitude difference.

With this technique, and a spacecraft that has the capability to change its ballistic coefficient, the re-entry point can be targeted. By increasing the initial altitude a_0 or increasing the range of ballistic coefficients available ΔC_B, the spacecraft will eventually achieve global coverage (the accessible latitude is obviously limited by the orbit's inclination). These minimum conditions to achieve global coverage are dependent on the atmospheric density, lower densities (low solar activity periods) increase the decay time hence, reducing the required initial altitude a_0 and range of ballistic coefficients available ΔC_B to achieve the global coverage.

These minimum conditions can be found by increasing a_0 and ΔC_B so that the accessible area covers the whole Earth. Figure 15.8 shows how the minimum required altitude to target any longitude at a particular latitude decreases as the ΔC_B range increases. The example shown assumes a $C_{Bmean} = 0.03\,m^2/kg$, an orbit inclination of 50 deg, a 0 deg target latitude and the minimum altitude is computed in 0.1 km steps.

If when this strategy is implemented the minimum conditions to achieve global coverage are exceeded then it will often occur that when targeting a specific location there will be more than one possible solution (combination of ΔC_B and a_t). An example

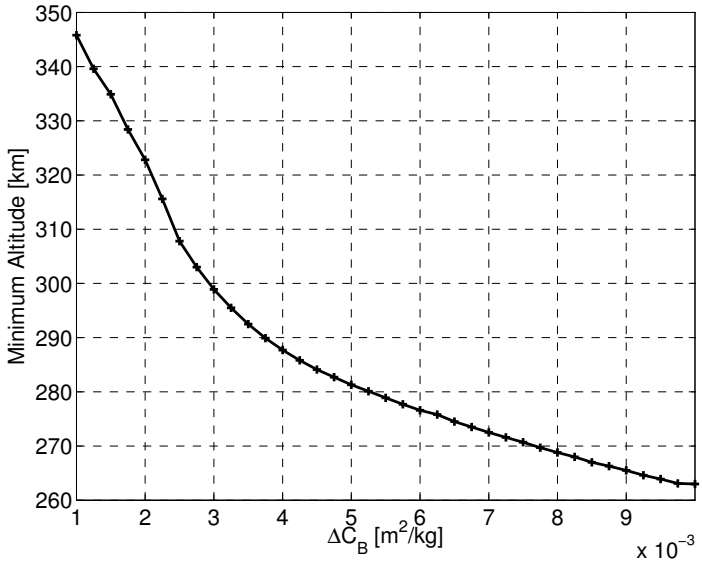

Figure 15.8: Minimum required altitude to target any point with respect to ΔC_B.

is provided in Fig. 15.9. In that case, and ignoring any other constraints that the spacecraft may have, choosing the solution with the lower ΔC_B seems to be a good option as it is the solution that offers more margin of C_B to control the decay and cope with atmospheric uncertainties when executing this option.

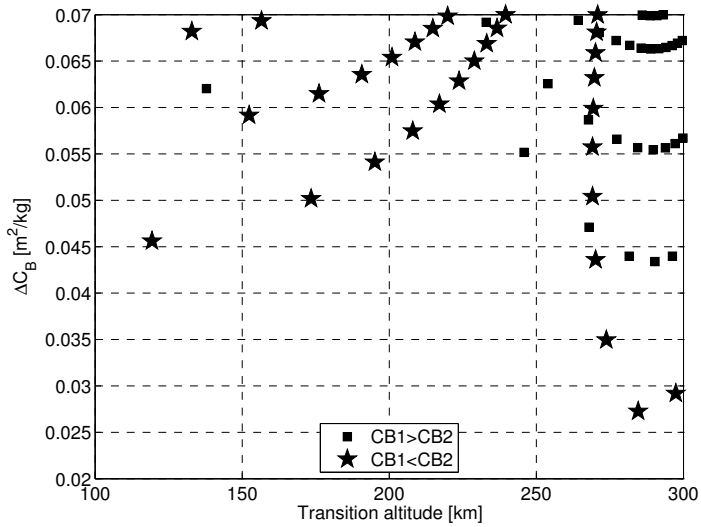

Figure 15.9: Example of the solutions available when targeting a specific location and when the minimum conditions for global coverage have been exceeded.

15.2.2 Numerical Approach

The behaviour when the full dynamics are considered is more complex but very similar. The disadvantage is that the algorithms to identify the solution take much longer as, instead of evaluating analytical expressions, lengthy numerical propagations have to

be performed. The analytical solutions could serve as a first guess for the numerical algorithm. The main challenge to have a good initial first guess is to adjust the exponential atmospheric model to match with more accurate and complex atmospheric models.

In fact, the solutions are quite sensitive to the atmospheric conditions and hence special care has to be taken when setting the parameters of the exponential model. If the exponential atmosphere density profile differs substantially from the atmospheric model used in the numerical approach, then the solutions from the analytical and numerical approach will diverge. A way to solve this issue, and maintain good agreement between the analytical and numerical approach, is to break down the exponential atmosphere into altitude bands and apply different parameters (ρ_0 and H) within these bands. With this technique a density profile that which matches the density profile produced with atmospheric models used in numerical propagators can be generated.

Also, when propagating using full dynamics of the system, the effects of the uncertainty of the parameters not present in the models has to be assessed. The uncertainty in the initial spacecraft position and velocity, in the Solar Radiation Pressure or in the gravity models will produce a re-entry uncertainty footprint. This uncertainty footprint can be partially corrected during the decay by the control but it already uses part of the controller range, which will be no longer available to control other expected errors or uncertainties that may arise during the decay (as changes in atmospheric density). Hence it is important to have accurate information of the spacecraft state vector and also of its properties. A case by case assessment has to be performed in order to assess the impact of these uncertainties.

15.3 Navigation and Control

Once the nominal decay profile has been selected (a_t and ΔC_B) the spacecraft will have to control its decay in order to remain on target. As this nominal decay will have been computed using simplified or inaccurate models, the spacecraft will have the tendency to deviate from the nominal decay path. The uncertainty in the atmospheric environment, mainly in density, is likely to be the main difference between the models used to compute the nominal decay and the real dynamics. Atmospheric models are not perfectly accurate Picone et al. (2002); Bowman and Tobiska (2008); Pardini et al. (2012) and the solar activity is difficult to forecast, hence making predictions of atmospheric densities inaccurate. In order to remain on target with this atmospheric environment uncertainty, the ballistic coefficient can be adjusted to cope with the density uncertainty. In addition, the nominal decay can be updated regularly when more up to date atmospheric information becomes available.

Here a simple control strategy is presented although it is clearly not the only one that could be used and is not probably the most effective although it shows that the system is controllable. More research into this particular area is required in order to come up with more effective strategies.

15.3.1 Strategy

Once the nominal decay trajectory has been computed it is uploaded to the spacecraft. Then to control this decay the following control process can be followed:

- A Δt (time interval) is defined based on the current altitude and the aerodynamic capabilities of the spacecraft.
- The current state of the spacecraft is propagated forward p times the Δt time interval $p\Delta t$. The parameter p, is another parameter defined based on the altitude and the aerodynamic capabilities of the spacecraft.
- The predicted future position is compared with the nominal decay position and velocity at that particular time.
- The C_B at the n different Δt intervals are adjusted so this error is minimised (this can be done using a simple LSQ technique). The error normal to the orbit plane is not controlled as the change of the ballistic coefficient has very little effect on this direction in the short term so if the controller would saturate very easily if this error was to be controlled.
- The new C_B are implemented on the spacecraft.
- The spacecraft orbits (decays) for a period of Δt with the new C_B and then, the process is repeated.

This process can be done on-board the spacecraft using simplified models or can be carried out on the ground with higher accuracy and uplink the results into the spacecraft in time (before the Δt period expires and it is time to implement the updated ballistic coefficients).

The strategy outlined before controls the along-track and vertical differences in positions and velocity to make them track the nominal decay by adjusting the spacecraft C_B. When the current state of the spacecraft is propagated by $p\Delta t$ and the propagation shows that the spacecraft has then re-entered, then, the strategy changes from matching the position and velocity in a future point to matching the time of re-entry. The process is then the following:

- A new Δt is defined based on the current altitude and the aerodynamic capabilities of the spacecraft.
- The current state of the spacecraft is propagated until re-entry.
- The predicted re-entry time is compared to the nominal decay re-entry time.
- The C_B at the different Δt intervals until re-entry are adjusted so this error is minimised.
- The new C_B are implemented on the spacecraft.
- The spacecraft orbits (decays) for a period of Δt with the new C_B and then, the process is repeated until re-entry.

Again, this process can be done on-board of the spacecraft or on the ground and the results uplinked into the spacecraft. If all the control can be performed on the spacecraft (and there is no reason to believe that it can not be implemented on-board the spacecraft) then the control of the trajectory can be done entirely autonomously.

This strategy that only uses the adjustment of the ballistic coefficient can control quite effectively the deviations in the orbit plane (both in position and velocity) but has very limited capabilities in controlling the deviations normal to the orbit plane. Fortunately the main source of error comes from the uncertainty in the density that causes errors mainly in the along track direction (the long term deviations would cause the cross-track re-entry position to drift). Note that the uncertainty in the spacecraft ballistic coefficient behaves as the uncertainty in the density and can in fact be merged as a single uncertainty source (uncertainty in the drag force).

As the atmospheric density decreases exponentially as the altitude increases, the Δt and p parameters have to be defined so that the uncertainty that dominates during the $p\Delta t$ is either the atmospheric or the ballistic coefficient uncertainty. As the altitude increases other errors can become increasingly relevant such as the error in the location and velocity of the spacecraft and the uncertainty in the solar radiation pressure. Trying to correct the solar radiation pressure (which can act in the normal plane direction) or trying to react over the state vector uncertainties (coming from GPS errors) can exhaust the control authority and mask out the deviations caused by the atmospheric and ballistic coefficient uncertainties, which are the ones that cause real errors in the re-entry location in the long run. These others errors can effectively limit the applicability of this method at high altitudes, as these errors will dominate at high altitudes. Increasing the ΔC_B range would be required in order to be able to correct these other errors at lower altitudes by re-computing the nominal decay trajectory.

It is also worth mentioning that if the deviations are very big then the controller will saturate. In this case the ballistic coefficient will be set to its maximum or minimum achievable value. The saturation is more likely to occur during the last stages of the decay when the uncertainties in atmospheric density and ballistic coefficient have a bigger impact and there is left time to correct them. It is therefore important to size the ΔC_B range so that saturation happens as late as possible or that the impact of the saturation in the late stages of the decay is acceptable in terms of the re-entry dispersion footprint.

Nominal decay profiles that use nominal C_B closer to the C_{Bmean} leave more of the ΔC_B range to the control hence minimising the saturation. So when multiple nominal decay solutions are available the one with nominal C_B closer to the C_{Bmean} is recommended.

15.4 Case Study

The case of the ΔDsat CubeSat is studied here in order to show how this method can be used in a real mission. ΔDsat is 2U CubeSat that is scheduled to fly as part of the QB50 network Muylaert et al. (2009). Its main scientific objectives are to study rarefied-gas aerodynamics, to measure thermosphere winds and demonstrate aerostability (more information on the CubeSat can be found in part II). To do so it has 4 deployable panels that can rotate independently from one another as seen in Fig. 7.1a. This

gives the CubeSat the ability to change its cross section area and hence to change its ballistic coefficient from 0.02 to 0.16 m^2/kg. This big range will allow ΔDsat to demonstrate the novel technique proposed here. One secondary objective will then be to make the spacecraft re-enter over Cranfield University (UK) where the main ground station of the mission will be located. Targeting Cranfield would allow the Cranfield, or other neighbouring ground stations, to receive the CubeSat transmissions just before re-entry (the CubeSat will broadcasting its position) and hence assess if the technology demonstration has been successful or not. Targeting Cranfield does not pose any risk to property or population as the CubeSat will completely vaporise during re-entry and no debris are expected to reach the ground.

Based on the latitude of Cranfield of 52º N, the 98º inclination of the orbit and the aerodynamic capabilities of the CubeSat, the minimum required altitude in order for ΔDsat to ensure that is able to target Cranfield is estimated to be between 240 and 250 km depending on the solar activity. Lower solar activity allows a lower starting altitude. Having such a low starting altitude for the re-entry control allows the CubeSat to perform its other science experiments without interference at higher altitudes as it will be deployed in a 380 km circular orbit.

Figure 15.9 shows an example of the solutions when Cranfield is targeted from an initial altitude of 300 km. These solutions would change depending on the local time of the ascending node (initial orbit-Earth geometry) which is still uncertain and will also depend on the solar activity.

Figure 15.10 shows the expected re-entry location dispersion 3σ from the target if the control method described in section 15.3 is applied and if an initial altitude of 250 km and a decay profile with $C_{B1} = 0.0715$ and $C_{B2} = 0.1209\,m^2/kg$ is set. This case is then a realistic one as it simulates a typical decay profile with the segmented decay with two different ballistic coefficients equidistant to $C_{Bmean} = 0.0962\,m^2/kg$.

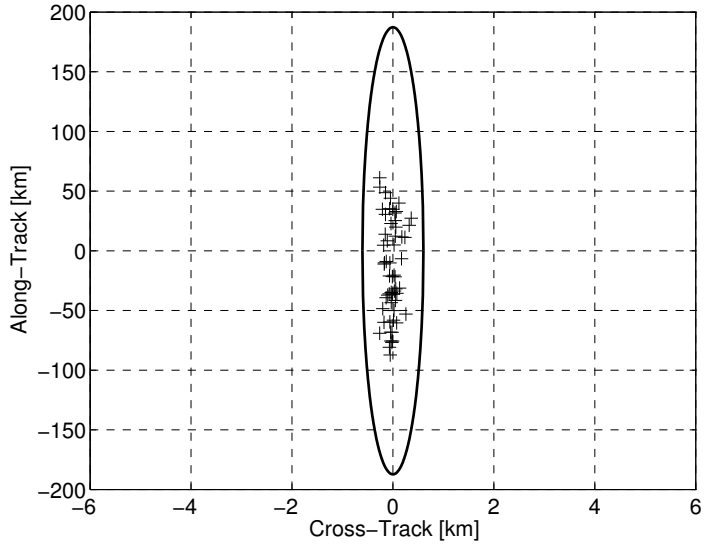

Figure 15.10: Dispersion from the target re-entry location.

To simulate the uncertainty of the atmospheric density and the spacecraft C_B, a gaussian error of 20% 3σ has been introduced on the real C_B (biases of the atmospheric density are corrected by the navigation algorithm just by adjusting the mean C_B to

cope with the bias). In addition the HWM93 wind model has been omitted in the control algorithms but included in the propagator to simulate the uncertainty of the winds. The knowledge of the spacecraft position and velocity contains a 4.5 m and 0.1 m/s 3σ error (based on the GPS unit to be flown) and a 15% uncertainty has been added to the solar radiation pressure forces. No uncertainty has been introduced in the gravity field model. Figure 15.10 shows the result of a 60 sample Monte Carlo simulation.

As can be seen in Fig. 15.10 the main dispersion occurs in the along track direction with a much smaller dispersion in the cross track direction (long term deviations from the predicted decay are unlikely when controlled). The estimated dispersion of the re-entry location for ΔDsat is small enough so that if Cranfield was targeted, the ground station from Cranfield, or other neighbour ground stations could pick up the signals of the spacecraft emitted moments before it burns up.

It is fair to say that the case presented here overestimates the control capability of the CubeSat as some disturbances or delays have not been modelled. For example, it has been assumed that the on-board computer has enough computing power to handle orbit propagations with relatively high fidelity models and that it does them instantly (no delays in applying the control ballistic coefficients). This will not be the case, the on-board propagator will use simplified models and there will be delays in applying the output of the controller. This estimations need to be refined prior to the launch of the mission.

Another interesting point is illustrated by looking at the final C_B applied during the decay. Figure 15.11 shows the 3σ range of C_B applied in this 60 run Monte Carlo simulation. Note how the Δt time interval is shorten as the decay progresses. This keeps the C_B dispersion range constant and well below the limits of the spacecraft. Before the transition in strategy the controller saturates in some of the simulated cases, but after the transition the dispersion on the C_B is reduced, as the Δt time interval is reduced significantly. But as the spacecraft approaches re-entry the dispersion in the applied C_B grows significantly again and it reaches the limits (hence saturating). To reduce this saturation the Δt time interval could be reduced until the practical limit is reached.

The performance of the controller on another case (best case) can also be seen in Fig. 15.12. This figure is very similar to what is shown in Fig. 15.11, but the decay is performed with a constant ballistic coefficient. This would represent a best case scenario as there is the maximum margin for the C_B to change and control the trajectory. This figure shows a similar behaviour as the other case. The Δt time interval is also shorten as the decay progresses (feature of the controller), again keeping the CB dispersion range nearly constant. In this case though the controller did not saturate in any of the cases (as the control margin is higher) prior to the transition to the re-entry time control mode. Again, once the control strategy transitions to control the re-entry time the dispersion is initially reduced (as the Δt time interval is reduced) to increase again as it approaches the end of the decay (saturating just prior re-entry). It is interesting to note though, that the dispersion in the re-entry location is very similar to the more realistic case, indicating that saturation in a small number of cases does not have a major impact on the final re-entry dispersion.

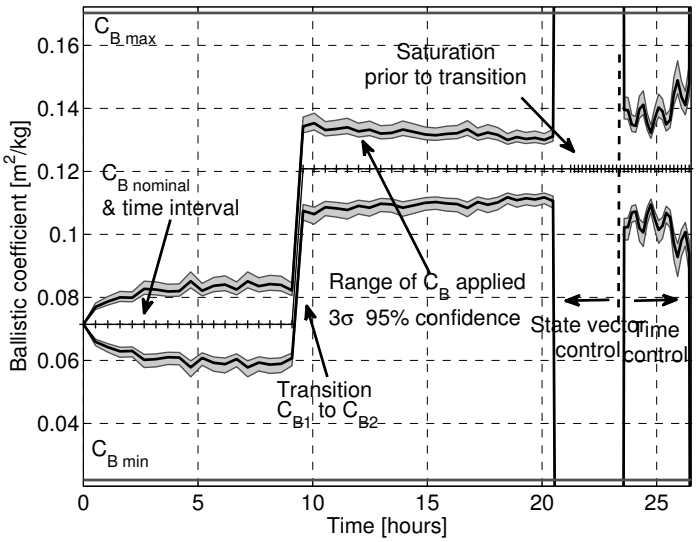

Figure 15.11: C_B applied during the 60 sample Monte Carlo simulation with a decay using 2 different ballistic coefficients.

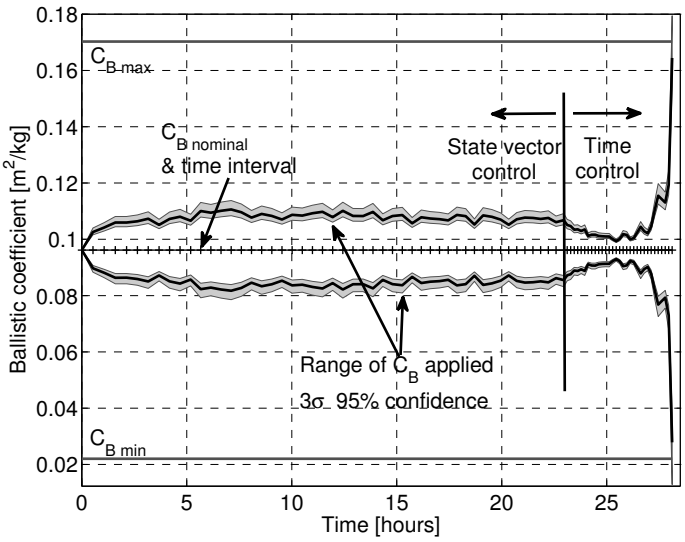

Figure 15.12: C_B applied during the 60 sample Monte Carlo simulation with a decay using the mean ballistic coeffiecnt throught the decay.

15.5 Potential Applications

The novel method presented here has mainly two major potential applications. The first one is in drag enhancing de-orbiting devices. These devices increase the drag on a spacecraft after the end of the spacecraft operational life in order to speed up their decay and to reduce the risk of collision with other operational spacecraft or debris Hobbs et al. (2013). These devices are passive and hence the location of re-entry is not controlled. On spacecraft that have components that will survive re-entry this can be a problem as they pose a risk to the population and property. The method described in this chapter could then be used to engineer a drag-enhancing de-orbit device which

could change the amount drag it creates and hence control its re-entry point. The re-entry point could be selected to target remote areas as the South Pacific. As this safe re-entry area is quite large it requires a relatively low precision and hence a small ΔC_B range, that could potentially be achieved with a drag-sail.

The second potential application is in passive small re-entry capsules with inflatable heat shields Jason Andrews (2011). In this case a small re-entry capsule could be crudely guided by this method using a similar device as the one used in ΔDsat in order to re-enter over a predefined area. The advantage of this method is that it is passive and hence no propulsion is required. This allows for a cost and complexity reduction. Combining this method with an inflatable heat shield as the one envisioned in Jason Andrews (2011), a complete targeted re-entry system could be contained in a very small spacecraft (potentially down to a CubeSat size). This method is not very precise (refer to case study in section 15.4) and hence a large landing area will be expected. Therefore part of the complexity is transferred to the search and recovery of the craft once on the ground.

These two potential applications will need to be studied separately in order to define their requirements and to adapt the method presented here.

15.6 Conclusions

A novel method to control the re-entry location of a spacecraft in a circular orbit by controlling its decay rate has been presented in this chapter. Constructing the nominal decay is fairly simple when simplified dynamics are used. When more complex and realistic dynamics are considered finding the nominal decay trajectory can be very computationally intensive. This can be a challenge when the nominal decay of a spacecraft need to be recomputed between ground passes. Also, when considering full dynamics the impact of the uncertainties in the spacecraft position and dynamic models needs to be taken into account. The case study has shown that the two phase control algorithm has an acceptable performance for the example mission and for other potential applications. The range of ballistic coefficient required is dependent on the mission profile and hence needs to be assessed on a case by case basis. Finally, this chapter is only the first work on this new area and hence further research in determining nominal decay profiles and control techniques could provide increased accuracy and extend this method to other mission scenarios (as eccentric orbits).

Chapter 16

Conclusions, Future Work and Further Research Topics

16.1 Conclusions and Future Work

In this part, three different aerodynamic attitude and orbit control techniques have been presented. Using aerodynamic forces to control the attitude or the orbit of a spacecraft is not entirely new, although it is an area that is still mostly unexplored. The recent increase of interest in VLEO missions has raised again the interest in these methods.

Harnessing the aerodynamic forces to perform something useful can provide several benefits for VLEO missions. Using aerodynamic forces, instead of traditional actuators, saves mass and power. Also, the aerodynamic forces are always available and hence completely passive systems can be designed. Aerodynamic attitude and orbit control methods can be used as primary control methods, as back-up or to boost the performance of traditional systems. Summarising, aerodynamic attitude and orbit control system can make VLEO space systems perform better, be more robust, and, in general, be more competitive.

The first method presented has been aerostability for CubeSats. Aerostability had already been discussed in chapter 8 in the ΔDsat context. The work presented in this chapter 13 proposes aerostable designs (adding aerodynamic surfaces) for CubeSats. These proposed designs are then used to analyse the aerostability properties and check how the different parameters affect the performance of the system. That results in a design trade space. Then, the CubeSat designer needs to define its design depending on the unique requirements of the mission being considered.

With the rapid popularity increase of CubeSats, launching them in the traditional high altitude orbits can pose a risk in the mid to long term (debris build up). Launching CubeSats in VLEO then seems a good alternative. Specially considering that most of these CubeSats are built as technology demonstrations or as educational exercises and their success rate is rather small. Launching CubeSats in VLEO inherently limits their operational lifetime and directly eliminates the risk of debris build-up. This allows for many CubeSats to be launched and not worry too much about their orbital lifetime. In these scenario, where CubeSats are launched in VLEO, having aerostability can be a great advantage (considering the mass, power and volume limitations on

CubeSats). Aerostability can be used to replace traditional attitude control systems on most missions.

The study done falls short of proposing a complete solution to the problem. Different damping systems have been identified, as well as different geometries, but no work has been done to assess which combination or design would be the most beneficial to a wide range of CubeSat missions (considering, common applications, power and attitude requirements, clearance for other deployables, ...). A study that could identify and design a system which could be used for a wide variety of future CubeSat mission would be an excellent continuation of the work done here. The aim should be to develop a COTS unit that could be easily integrated into the CubeSat (an approach commonly used by other COTS subsystem vendors).

A major area that needs more research is in the damping systems. Active magnetic damping using magnetic torquers (used in ΔDsat) is quite mature, as COTS hardware exists and as the dynamics of such a system are easy to model and to understand. Unfortunately, active magnetic damping is an active damping system, and as such, it requires power and a functioning OBDH system that is able to command it. A completely passive damping would be desirable (more reliable and less time consuming during the mission design). This can be achieved through magnetic hysteresis rods or through viscous dampers. The applicability of hysteresis rods is very limited (as it is linked to the local magnetic field). Viscous dampers have a higher potential, but designing, modelling and understanding the behaviour of this type of dampers is much more difficult. Another interesting research area would be then to look at the design of such viscous dampers.

In addition to aerostability in CubeSats, this part also presents two techniques to control the orbit of a spacecraft using aerodynamic forces. The first one, maintains the Sun-synchronous inclination of a decaying orbit by applying lift normal to the orbit plane. This is one of the first proposed uses of lift for orbit control. This method requires quite a high lift to drag ratios, which seem impossible to achieve with currently used surfaces. More research in rarefied-gas aerodynamics could result in surfaces types and spacecraft shapes that could achieve the required lift to drag ratios (as it is theoretically possible if specular reflection is achieved). In this case, the research has been focused on exploring the method and the required lift to drag.

Partially compensating the drag lowers the lift to drag ratio requirement and hence this method can still be used in the near future without any further research in spacecraft aerodynamics. In this case, the technique is then used to lower the propulsion requirements as the propulsion system does no longer need to completely compensate the drag. The spacecraft is allowed to decay and the inclination is corrected. The challenges involved in designing a spacecraft that achieves a certain lift to drag ratio can potentially cancel out any of the advantages obtained when lowering the propulsion requirements. So the advantages of applying this method in the short term are not clear.

One area that deserves more work is the control of the inclination during the decay. This has only been briefly studied in the research presented in this dissertation. Maintaining a constant lift to drag ratio is not sufficient. Perturbations (as winds, and changes in density) change the required lift to drag ratio, hence, this ratio has to be controlled in order to achieve the desired inclination whilst decaying. But the ultimate

goal is to maintain the local time of the ascending/descending node fixed during the decay, thus, a control algorithm that keeps the MLTAN constant (through the change in inclination) needs to de developed and simulated.

Also, the use of lift normal to the plane, in addition of changing the inclination, can also be used to control the RAAN. A change in inclination or a change of RAAN can be used to indirectly or directly control the MLTAN of spacecraft that completely compensates the drag (and experiences no decay). This could potentially be useful for some missions.

The other method that has been studied is controlling the location of the re-entry interface by modulating the drag that the spacecraft creates during its decay. This method proves to be feasible and is capable of obtaining small re-entry location dispersion footprints if the control authority over drag is sufficiently high. Challenges still exist in how to patch the analytical solutions with the numerical ones, and also in how to implement the control algorithms on-board the spacecraft. The impact that the implementation of the control algorithm on an on-board computer would have on the performance of the method has not been assessed. This is an area where the author acknowledges that more work is required. Assessing the impact of the lag and the available computational power (accuracy of the models) is missing from the research presented.

This method to control the re-entry location, has been proved feasible using the ΔDsat as a case study. ΔDsat is a very peculiar platform, which turns out to be very suited for this application, given its mass spectrometer (measuring atmospheric pressure) and its capability to change its ballistic coefficient between a wide range and with a good resolution. The envisioned applications (drag-sails, and small re-entry capsules) will potentially have different requirements that would let to different capabilities and hence different performances and limitations. The author encourages to explore which would be the performance and design requirements for such applications.

Although being a relatively unexplored topic, aerodynamic orbit and attitude control has a clear potential to benefit VLEO missions. The research presented here has analysed three particular methods but there are many more that can be studied. There is still a tremendous amount of work to be done before these aerodynamic attitude and orbit control techniques are implemented into VLEO missions. Missions like ΔDsat can help bridge the gap between theoretical, paper base studies, and demonstrated and flight ready techniques.

16.2 Further Research Topics on Aerodynamic Attitude and Orbit Control

The previous work on aerodynamic orbit and attitude control has barely scratch the surface of what are the applications that could benefit from using aerodynamic forces.

A partial list of novel applications and techniques that could be studied in the future is: use of aerodynamic forces to perform collision avoidance manoeuvres against cooperative and uncooperative targets; use of aerodynamic forces to deploy and maintain very large clusters, swarms and constellations in VLEO; use of aerodynamic lift to control the Local Time of Ascending Node of Sun-synchronous orbits; use of aerodynamic

forces to provide completely passive attitude stabilisation, and use of aerodynamic flaps or attitude offsets to generate torques and control the attitude or desaturate other actuators (active aerodynamic attitude control).

Another interesting aspect that could be studied is how both applications domains (orbit and attitude control) could be linked together. To change the orbit of the spacecraft a change in the drag or lift is required. This drag/lift change can be accomplished by a change of the attitude of the spacecraft with respect to the incident flow. Therefore, changing the attitude can regulate the drag and lift generated and thus control the orbit. Then, methods to change the attitude using aerodynamic forces (or other methods) can be linked to aerodynamic orbit control techniques (e.g. avoid collisions and manage a cluster/swarm/constellation by adjusting the attitude of their spacecraft, hence creating differential drag and lift).

As these methods use the forces generated by the interaction of the atmosphere with the spacecraft, they do not require any power to operate, they are always available, and they do not present saturation (as other momentum storage devices). In addition, the implementation of such methods is very simple as no additional hardware (as thrusters, momentum wheels or magnetic torquers) is required. Therefore, controlling the orbit and attitude with aerodynamic forces can provide a unique set of benefits.

These benefits may not fully justify the use of these methods as the only orbit and specially the only attitude control method. But using aerodynamic forces in conjunction with other traditional actuators can augment the capabilities and increase the performance of the attitude and orbit control systems (making more cost-effective manoeuvres and saving power/fuel). The use of hybrid/mixed actuator attitude control systems is very promising Dennehy (2014). The use of pseudospectral optimal control Ross and Karpenko (2012) which can compute optimal control solutions for hybrid systems could be easily implemented in flight systems to take advantage of the aerodynamic torques already occurring on flying spacecraft. Combining traditional attitude actuators with aerodynamic torques has been recently demonstrated by the so called Zero Propellant Maneuvers Bedrossian et al. (2007) implemented on the ISS to save propellant. Additional research could expand the use of these techniques to cope with other scenarios that include aerodynamic forces and will also determine the modifications that would be required to current and proposed spacecraft to take full advantage of these methods. Case studies could be used to showcase the advantages of using such hybrid control techniques and to demonstrate that they have been develop to a flight-ready state.

The use of aerodynamic forces in conjunction with other traditional actuators can also make the control systems more robust (providing back-up control when the primary actuator fails). A good example of this is the Kepler spacecraft that after loosing two of its reaction wheels (with the control system becoming rank deficient) the science operations were finally resumed by using the solar radiation pressure as an alternative way to control the spacecraft's attitude Putnam and Wiemer (2014). Similar methods could be employed using aerodynamic forces instead. This particular application could be also studied and showcased in case studies.

Another area of interest is which new science missions these techniques could open up. For example, having an aerodynamic attitude control method that accurately aligns the spacecraft to the flow, can be extremely useful when using mass spectrometers to

measure atmospheric density and composition, or to study rarefied-gas aerodynamics as explained in previous sections. Also aerostability opened up the opportunity to develop novel thermosphere wind measurement techniques.

The effects and potential use of aerodynamic forces during proximity operations could be also an area of research. Usually the orbit control during proximity operations is achieved using thrusters Zimpfer et al. (2005). Using aerodynamic forces can provide significant fuel reduction and decrease the detectability (no plume emitted) of the approaching craft. Controlling a spacecraft or other autonomous vehicle with an on-board robotic manipulator can also benefit from aerodynamic torques (e.g. aerodynamic torques can help providing the required torques when moving a massive spacecraft that could saturate traditional attitude actuators and require fuel expenditure).

Finally, bridging the gap between the theoretical research into the actual flight implementation is an area that could be the focus of additional research. Past research used simplified environmental models and ignores practical implementation issues. Therefore, research is required to validate the control algorithms in high fidelity simulations that use realistic environmental models (mainly with respect to the atmosphere and actuators performance) and also use hardware-in-the-loop (HIL) simulations.

The identified benefits of the proposed future research are:

- Benefits to the GN&C community. The proposed research will add new methods and techniques to control the orbit and attitude of a spacecraft. This new knowledge will benefit the broader GN&C community that it could build on these ideas and methods proposed to conduct further research on the same area or apply the conducted research to other GN&C domains.

- Enhancing the spacecraft capabilities. Having additional methods to control the attitude and orbit of spacecraft will increase the capabilities of future spacecraft. It will allow spacecraft to be more robust to hardware failures, more fuel/power efficient and it will open up possibilities that where not possible before. This will help deliver a greater value from space assets.

- Making VLEO mission concepts more attractive. Having methods to control the orbit and attitude using aerodynamic forces is of particular interest to VLEO missions. Making these techniques ready to use will make VLEO concepts more attractive helping them to become a reality and thus exploit the benefits that VLEO provide. This can potentially have an impact on all the Earth Observation domains, including land monitoring, atmospheric measurements, water quality, maritime surveillance, emergency management, security, etc.

- Enhancing the research capabilities. Some of the techniques to control the orbit and the attitude of spacecraft using aerodynamic forces can become enablers of some science missions. In particular, missions that are interested in doing in-situ measurements of the atmosphere they are flying through could greatly benefit from these techniques.

Publications

The publications that have been derived from the work presented in this dissertation are:

Peer Review Journals

[1] Virgili Llop, J., Roberts, P. C. E., Palmer, K., Hobbs, S., and Kingston, J., "*Descending Sun-Synchronous Orbits with Aerodynamic Inclination Correction*," Journal of Guidance, Control, and Dynamics, pp. 1–12, doi:10.2514/1.G000183.

[2] Virgili Llop, J. and Roberts, P. C., "Δ*Dsat, a QB50 CubeSat mission to study rarefied-gas drag modelling*," Acta Astronautica, Vol. 89, 2013, pp. 130 – 138, doi:http://dx.doi.org/10.1016/j.actaastro.2013.04.006.

[3] Kingston, J., Hobbs, S., Roberts, P., Juanes-Vallejo, C., Robinson, F., Sewell, R., Snapir, B., Virgili Llop, J., and Patel, M., "*Use of CYPRES^{TM} cutters with a Kevlar clamp band for hold-down and release of the Icarus De-Orbit Sail payload on TechDemoSat-1*," Acta Astronautica, Vol. 100, 2014, pp. 82–93, doi:http://dx.doi.org/10.1016/j.actaastro.2014.03.014.

A paper dealing with targeted re-entry using aerodynamic drag has been submitted to Journal of Guidance, Control, and Dynamics and it is currently under revision.

Published Conference Proceedings

[1] Virgili Llop, J., Roberts, P. C. E., and Hao, Z., "*Aerodynamic Attitude and Orbit Control Capabilities of the DDSAT CubeSat*," in "Proceedings of the 37th Annual AAS Rocky Mountain Section Guidance and Control Conference held January 31 – February 5, 2014, Breckenridge, Colorado.", AAS 14-063, 2014, pp. 321–333.

[2] Virgili Llop, J., "*Aerostability for low altitude flying CubeSats*," in "Proceedings of the 2nd IAA Conference on University Satellites Missions and Cubesat Workshop," , 2013, pp. IAA–CU–13– 10–03.

References

Aguttes, J. P. (2001). High resolution (metric) SAR microsatellite, based on the CNES MYRIADE bus. In *Geoscience and Remote Sensing Symposium, 2001. IGARSS '01. IEEE 2001 International*, volume 1, pages 224–226 vol.1.

Aguttes, J. P., Fernandez, N., and Foliard, J. (2005). Low altitude flying for high resolution imaging satellite: Comparison of low circular and elliptical orbits. In *Geoscience and Remote Sensing Symposium, 2005. IGARSS '05. Proceedings. 2005 IEEE International*, volume 5, pages 3421–3423. IEEE.

Alcantara Cyclone Space Binational Company (2010). Cyclone-4 launch vehicle user's guide. Technical report, Alcantara Cyclone Space Binational Company, Edificio Corporate Financial Center SCN Qd. 2 Bl. A Cj. 603, Brasilia – DF 70712-900 Federative Republic of Brazil.

Arianespace (2006). Vega user's manual. Technical report, Arianespace.

Barlier, F., Berger, C., Falin, J., Kockarts, G., and Thuillier, G. (1978). A thermospheric model based on satellite drag data. *Annales de Geophysique*, 31(1):9–24.

Baule, A. (1914). Theoretische behandlung der erscheinungen in verdünnten gasen. *Annals of Physics*, 44:145.

Bedrossian, N., Bhatt, S., Lammers, M., Nguyen, L., and Zhang, Y. (2007). First ever flight demonstration of zero propellant maneuver attitute control concept. In *AIAA Guidance, Navigation and Control Conference and Exhibit*. American Institute of Aeronautics and Astronautics. doi:10.2514/6.2007-6734.

Bekkeng, T. A. (2013). QB50 mNLP Science Unit Interface Control Document. Issue 3. Technical report, University of Oslo.

Beste, D. C. (1978). Design of satellite constellations for optimal continuous coverage. *IEEE Transactions on Aerospace and Electronic Systems*, AES-14(3):466–473, doi:10.1109/TAES.1978.308608.

Bevilacqua, R. and Romano, M. (2008). Rendezvous maneuvers of multiple spacecraft using differential drag under J2 perturbation. *Journal of Guidance, Control, and Dynamics*, 31(6):1595–1607, doi:10.2514/1.36362.

Bhuta, P. G. and Koval, L. R. (1966). A viscous ring damper for a freely precessing satellite. *International Journal of Mechanical Sciences*, 8(5):383–395, doi:10.1016/0020-7403(66)90009-9.

Bird, G. A. (1994). *Molecular Gas Dynamics and the Direct Simulation of Gas Flows.* Oxford Science Publications.

Boucher, C., Altamimi, Z., and Duhem, L. (1994). Results and analysis of the ITRF93. *IERS Technical Note*, 18:1–313.

Bouwmeester, J., Gill, E., Sundaramoorthy, P., and Kuiper, H. (2011). Design and verification of a very compact and versatile attitude concept study of a leo constellation of nanosatellites for near real time optical remote sensing. In *62nd International Astronautical Congress 2011. 3-7 October 2011, Cape Town, South Africa.*, volume IAC-11-B1.2.1.

Bowman, B. R. and Moe, K. (2005). Drag coefficient variability at 175-500 km from the orbit decay analyses of spheres. In *AAS/AIAA Astrodynamics Specialists Conference, Lake Tahoe, CA, August 7-11, 2005.*

Bowman, B. R. and Storz, M. F. (2003). High accuracy satellite drag model (HASDM) review. *Advances in the Astronautical Sciences*, 116(3):1943–1952.

Bowman, B. R. and Tobiska, W. K. (2008). A new empirical thermospheric density model JB2008 using new solar and geomagnetic indices. In *Astrodynamics Specialist Conference 18-21 August 2008, Honolulu, Hawaii. AIAA 2008-6438.* AIAA/AAS.

Brown, O. and Eremenko, P. (2006). Fractionated space architectures: A vision for responsive space. In *4th Responsive Space Conference. April 24–27, 2006. Los Angeles, CA.*

Bruinsma, S. (2013). DTM2013 evaluation report. Technical report, CNES.

Brundle, C. R. and Broughton, J. Q. (1990). The initial interaction of oxygen with well-defined transition metal surfaces. *Chem. Physics of Solid Surfaces and Heterogeneous Catalysis, Elsevier, Amsterdam, vol. 3, Part A*, pages 131–388.

Buchen, E. and DePasquale, D. (2014). 2014 nano microsatellite market assessment. Technical report, SpaceWorks Enterprises, Inc.

Burton, R., Starek, J., and Rock, S. M. (2012). A new method for simulating the attitude dynamics of passively magnetically stabilized spacecraft. In *Proceedings of the 22nd AAS/AIAA Space Flight Mechanics Meeting*, Charleston SC. AAS/AIAA, AAS/AIAA.

Challinor, R. (1968). The apparent rotation of the upper atmosphere. *Planetary and Space Science*, 16(5):557–566, doi:10.1016/0032-0633(68)90097-4.

Chaudery, R. A. (2013). QB50 INMS Science Unit Interface Control Document. Issue 7. Technical report, Mullard Space Science Laboratory, UCL.

Colomb, F., Alonso, C., Hofmann, C., and Nollmann, I. (2004). SAC-C mission, an example of international cooperation. *Advances in Space Research*, 34(10):2194–2199, doi:10.1016/j.asr.2003.10.039.

COSPAR (2013). CIRA-2012 models of the Earth's upper atmosphere. Technical report, Committee on Space Research.

da Silva Curiel, A., Boland, L., Cooksley, J., Bekhti, M., Stephens, P., Sun, W., and Sweeting, M. (2005). First results from the disaster monitoring constellation (DMC). *Acta Astronautica*, 56(1):261–271, doi:10.1016/j.actaastro.2004.09.026.

Davies, P., Cawthorne, A., Carter, P., Sills, L., and da Silva Curiel, A. (2011). The DMC-3 1m small satellite constellation. In *8th IAA Symposium on Small Satellites for Earth Observation, 04-08 April 2011. Berlin, Germany.* IAA.

Davis, L. P., Cunningham, D., Bicos, A. S., and Enright, M. (1994). Adaptable passive viscous damper: an adaptable D-Strut. *Proc. SPIE 2193, Smart Structures and Materials 1994: Passive Damping*, 2193:47–58, doi:10.1117/12.174114.

Dennehy, N. (2014). Spacecraft hybrid control at NASA: A historical look back, current initiatives, and some future considerations. In *Proceedings of the 37th Annual AAS Guidance and Control Conference held January 31 – February 5, 2014, Breckenridge, Colorado.*, number AAS 14-101, pages 583–603.

Dobbin, A., Aylward, A. D., and Harris., M. J. (2006). Three-dimensional GCM modelling of nitric oxide in the lower thermosphere. *Journal of Geophysical Research*, (111).

Doornbos, E. (2011). *Thermospheric Density and Wind Determination from Satellite Dynamics*. PhD thesis, Technische Universiteit Delft.

Drinkwater, M. R., Haagmans, R., Muzi, D., Popescu, A., Floberghagen, R., Kern, M., and Fehringer, M. (2007). The GOCE gravity mission: ESA's first core earth explorer. In *Proceedings of the 3rd International GOCE User Workshop, 6-8 November, 2006, Frascati, Italy*, pages 1–8. ESA.

Drob, D. P., Emmert, J. T., Crowley, G., Picone, J. M., Shepherd, G. G., Skinner, W., Hays, P., Niciejewski, R. J., Larsen, M., She, C. Y., Meriwether, J. W., Hernandez, G., Jarvis, M. J., Sipler, D. P., Tepley, C. A., O'Brien, M. S., Bowman, J. R., Wu, Q., Murayama, Y., Kawamura, S., Reid, I. M., and and, R. A. V. (2008). An empirical model of the Earth's horizontal wind fields: HWM07. *Journal of Geophysical Research: Space Physics*, 113(A12304), doi:10.1029/2008JA013668.

Dubock, P., Spoto, F., Simpson, J., Spencer, D., Schutte, E., and Sontag, H. (2001). The Envisat satellite and its integration. *ESA bulletin*, 106:26–45.

ECSS Secretariat (2008). ECSS space engineering - space environment. Technical Report ECSS-E-ST-10-04C, ESA.

Fortescue, P. W. and Stark, J. P. W. (1995). *Spacecraft Systems Engineering, 4th Edition*. Wiley and Sons, Inc.

Fuller-Rowell, T. (1998). The "thermospheric spoon": A mechanism for the semiannual density variation. *Journal of Geophysical Research*, 103(A3):3951–3956.

Gantois, K., Teston, F., Montenbruck, O., Vuilleumier, P., Braembussche, P., and Markgraf, M. (2006). Proba-2 mission and new technologies overview. In *Small Satellite Systems and Services-The 4S Symposium*, pages 25–29.

Ghosh, S. (2002). *The Neutral Upper Atmosphere*, volume 249 of *Astrophysiscs and Space Science Library*. Springer.

GomSpace (2012). Platform recommendation for QB50 missions with gomspace. Technical report, GomSpace.

Goodman, F. (1967). Dimensional hard spheres theory of scattering of gas atoms from a solid surface. *Surface Science*, 7:391– 421.

Goward, S. N., Masek, J. G., Williams, D. L., Irons, J. R., and Thompson, R. (2001). The Landsat 7 mission: Terrestrial research and applications for the 21st century. *Remote Sensing of Environment*, 78(1):3–12, doi:10.1016/S0034-4257(01)00262-0.

Graziano, B. P. (2007). *Computational Modelling of Aerodynamic Disturbances on Spacecraft within a Concurrent Engineering Framework*. PhD thesis, Cranfield University.

Gregory, J. C. and Peters, P. N. (1987). A measurement of the angular distribution of 5 ev atomic oxygen scattered off a solid surface in Earth orbit. In Boffi, V. and Cercignani, C., editors, *Proceedings of the 15th international symposium on rarefied gas dynamics*, volume 1, pages 644–656.

Hammer, F. U., Messerschmid, E., and Rogg, M. (2009). A novel solid electrolyte oxygen sensor system for in-situ measurement and process control. In *AIP Conference Proceedings*, volume 1282, page 69.

Handy, B., Acton, L., Kankelborg, C., Wolfson, C., Akin, D., Bruner, M., Caravalho, R., Catura, R., Chevalier, R., and Duncan, D. (1999). The transition region and coronal explorer. *Solar Physics*, 187(2):229–260.

Hanslmeier, A. (2007). *The Sun and Space Weather*, volume 347 of *Astrophysiscs and Space Science Library*. Springer.

Harris, I. and Priester, W. (1962). Time-dependent structure of the upper atmosphere. *Journal of the Atmospheric Sciences*, 19(4):286–301, doi:10.1175/1520-0469(1962)019<0286:TDSOTU>2.0.CO;2.

Hedin, A. E., Fleming, E. L., Manson, A. H., Schmidlin, F. J., Avery, S. K., Clark, R. R., Franke, S. J., Fraser, G. J., Tsuda, T., Vial, F., and Vincent, R. A. (1996). Empirical wind model for the middle and lower atmosphere. *Journal of Atmospheric and Terrestrial Physics*, 58(13):1421–1447, doi:10.1016/0021-9169(95)00122-0.

Hedin, A. E., Reber, C. A., Newton, G. P., Spencer, N. W., Brinton, H. C., Mayr, H. G., and Potter, W. E. (1977a). A global thermospheric model based on mass spectrometer and incoherent scatter data MSIS, 2. Composition. *Journal of Geophysical Research*, 82(16):2148–2156, doi:10.1029/JA082i016p02148.

Hedin, A. E., Salah, J. E., Evans, J. V., Reber, C. A., Newton, G. P., Spencer, N. W., Kayser, D. C., Alcaydé, D., Bauer, P., Cogger, L., and McClure, J. P. (1977b). A global thermospheric model based on mass spectrometer and incoherent scatter data MSIS, 1. N2 density and temperature. *Journal of Geophysical Research*, 82(16):2139–2147, doi:10.1029/JA082i016p02139.

Hinkley, D. V. (1969). On the ratio of two correlated normal random variables. *Biometrika*, 56(3):635–639.

Hobbs, S., Kingston, J., Roberts, P., Juanes, C., Sewell, R., Snapir, B., Robinson, F., Virgili-Llop, J., Hobbs, J., and Patel, M. (2013). De-orbit sail design for Techdemosat-1. In *Sixth European Conference on Space Debris. Darmstadt, Germany, 22–25 April 2013.* ESA/ESOC.

Horsley, M., Nikolaev, S., and Pertica, A. (2013). Small satellite rendezvous using differential lift and drag. *Journal of Guidance, Control, and Dynamics*, 36(2):445–453, doi:10.2514/1.57327.

Iglseder, H., Arens-Fischer, W., and Wolfsberger, W. (1995). Small satellite constellations for disaster detection and monitoring. *Advances in Space Research*, 15(11):79–85, doi:10.1016/0273-1177(95)00077-R.

ISIS (2012). CubeSatShop.com QB50 platforms recommendations and offerings. Technical report, Innovative Solutions In Space.

ISO 14222 (2013). ISO 14222 space environment (natural and artificial). Earth upper atmosphere. Technical Report ISO 14222:2013, ISO.

Jacchia, L. G. (1971). Thermosphere and exosphere static models with empirical thermal profiles, giving temperature, density and composition as function of height. *Smithsonian Astrophysical Observatory Special Report*, (332).

Jacchia, L. G. (1972). Atmospheric models in the region from 110 to 2000 km. in: CIRA 1972: COSPAR International Reference Atmosphere. *Akademie-Verlag, Berlin*, pages 227–338.

Jason Andrews, Krissa Watry, K. B. (2011). Nanosat deorbit and recovery system to enable new missions. In *Proceedings of the AIAA/USU Conference on Small Satellites, Mission Enabling Technologies II, SSC11-X-3.* AIAA/USU.

Jové, P. G., Fraux, V., Thomas, Varughese, A. M., Moser, C., Payet, D., H.Y.Lam, E., Hamid, F., Lardin, F., Paris, G., Brazier, L., Solyga, M., Micucci, P., Duteïs, P., da Cunha, S. M., and Bertrand, T. (2012). THermospheric Orbital Reconnaissance - Executive Summary. Technical report, GROUP DESIGN PROJECT REPORT - Cranfield University.

Karr, G. R. (1969). A study of effects of the gas-surface interaction on spinning convex bodies with application to satellite experiments. Technical report, Illinois Univ at Urbana Coordinated Science Lab.

King-Hele, D. G. (1987). *Satellite Orbits in an Atmosphere: Theory And Application*. Blackie Academic and Professional.

Klinkrad, H. (2006). *Space Debris – Models and Risk Analysis*. Springer.

Knechtel, E. D. and Pitts, W. C. (1973). Normal and tangential momentum accommodation for Earth satellite conditions. *Astronautica Acta*, 18:171–184.

Koppenwallner, G. (2009). Energy accommodation coefficient and momentum transfer modeling. HTG–TN–08–11, HTG, Katlenburg Lindau.

Kosmotras (2001). Space launch system DNEPR user's guide. Technical report, International Space Company Kosmotras.

Langmuir, I. (1916). The evaporation, condensation and reflection of molecules and the mechanism of adsorption. *Phys. Rev.*, 8:149–176, doi:10.1103/PhysRev.8.149.

Larson, W. J. and Wertz, J. R. (2005). *Space Mission Analysis and Design*. Space Technology Library. Microcosm Press, 3rd.

Lemoine, F. (1998). Geopotential model EGM96. Technical report, NASA, Goddard Space Flight Center.

Leonard, C. L., Hollister, W. M., and Bergmann, E. V. (1989). Orbital formationkeeping with differential drag. *Journal of Guidance, Control, and Dynamics*, 12(1):108–113, doi:10.2514/3.20374.

Macdonald, M., McKay, R., Vasile, M., and De Frescheville, F. B. (2010). Extension of the Sun-synchronous orbit. *Journal of Guidance, Control, and Dynamics*, 33(6):1935–1939, doi:10.2514/1.49011.

Madden, M. (2009). GeoEye-1, the world's highest resolution commercial satellite. In *The Conference on Lasers and Electro Optics*, pages 1–1. IEEE.

Martin, M., Klupar, P., Kilberg, S., and Winter, J. (2001). Techsat21 and revolutionizing space missions using microsatellites. In *Proceedings of the AIAA/USU Conference on Small Satellites. SSC01-1-3*.

Masutti, D. (2014). QB50 System Requirements and Recommendations. Issue 6. Technical report, Von Karman Institue.

McLandress, C., Rochon, Y., Shepherd, G. G., Solheim, B. H., Thuillier, G., and Vial, F. (1994). The meridional wind component of the thermospheric tide observed by WINDII on UARS. *Geophysical Research Letters*, 21(22):2417–2420, doi:10.1029/94GL02367.

Miele, A. (1996). The 1st John V. Breakwell memorial lecture: Recent advances in the optimization and guidance of aeroassisted orbital transfers. *Acta Astronautica*, 38(10):747 – 768, doi:http://dx.doi.org/10.1016/S0094-5765(96)00076-8.

Mitchell, N., Pancheva, D., Middleton, H. R., and Hagan., M. E. (2002). Mean winds and tides in the arctic mesosphere and lower thermosphere. *Journal of Geophysical Research*, (107).

Moe, K. (1968). Recent experimental evidence bearing on satellite drag coefficients. *AIAA Journal*, 6(7):1375–1377, doi:10.2514/3.4754.

Moe, K. and Bowman, B. R. (2005). The effects of surface composition and treatment on drag coefficients of spherical satellites. In *AAS/AIAA Astrodynamics Specialists Conference, Lake Tahoe, CA, August 7-11, 2005*.

Moe, K. and Moe, M. M. (1967). The effect of adsorption on densities measured by orbiting pressure gauges. *Planetary and Space Science*, 15(8):1329–1332, doi:http://dx.doi.org/10.1016/0032-0633(67)90186-9.

Moe, K. and Moe, M. M. (2005). Gas-surface interactions and satellite drag coefficients. *Planetary and Space Science*, 53(8):793–801, doi:10.1016/j.pss.2005.03.005.

Moe, K. and Moe, M. M. (2010). Gas-surface interactions in Low-Earth Orbit. In *27th International Symposium on Rarefied Gas Dynamics, 2010*. American Institute of Physics.

Moe, K., Moe, M. M., and D, S. (1998). Improved satellite drag coefficient calculations from orbital measurements of energy accommodation. *Journal of Spacecraft and Rockets*, 35(3):266–272.

Moe, M. M., Wallace, S. D., and Moe, K. (1995). Recommended drag coefficients for aeronomic satellites. In Johnson, R. and Killeen, T., editors, *The upper Mesosphere and Lower Thermosphere: A Review of Experiment and Theory, Geophysical Monograph Series, Vol. 87*. American Geophysical Union.

Mostaza Prieto, D., Graziano, B. P., and Roberts, P. C. E. (2014). Spacecraft drag modelling. *Progress in Aerospace Sciences*, 64(0):56–65, doi:http://dx.doi.org/10.1016/j.paerosci.2013.09.001.

Muylaert, J.-M., Reinhard, R., Asma, C. O., Buchlin, J.-M., Rambaud, P., and Vetrano, M. R. (2009). QB50, an international network of 50 CubeSats for multipoint, in-situ measurements in the lower thermosphere and re-entry research. In *Atmospheric Science Conference Barcelona, Spain, 7-11 September 2009*.

Paetzold, H. K. and Zschörner, H. (1961). An annual and a semiannual variation of the upper air density. *Pure and Applied Geophysics*, 48(1):85–92.

Pande, K. and Venkatachalam, R. (1979). On optimal aerodynamic attitude control of spacecraft. *Acta Astronautica*, 6(11):1351 – 1359, doi:http://dx.doi.org/10.1016/0094-5765(79)90127-9.

Pardini, C., Moe, K., and Anselmo, L. (2012). Thermospheric density model biases at the 23rd sunspot maximum. *Planetary and Space Science*, 67(1):130 – 146, doi:http://dx.doi.org/10.1016/j.pss.2012.03.004.

Picone, J. M., Hedin, A. E., Drob, D. P., and Aikin, A. C. (2002). NRLMSISE-00 empirical model of the atmosphere: Statistical comparisons and scientific issues. *Journal of Geophysical Research: Space Physics*, 107(A12), doi:10.1029/2002JA009430.

Pilinski, M. D., Argrow, B. M., and Palo, S. E. (2010). Semiempirical model for satellite energy-accommodation coefficients. *Journal of Spacecraft and Rockets*, 47(6):951–956, doi:10.2514/1.49330.

Psiaki, M. L. (2004). Nanosatellite attitude stabilization using passive aerodynamics and active magnetic torquing. *Journal of Guidance, Control, and Dynamics*, 27(3):347–355, doi:10.2514/1.1993.

Putnam, D. and Wiemer, D. (2014). Hybrid control architecture for the kepler spacecraft. In *Proceedings of the 2014 Gudance Navigation and Control Conference January 31 - February 5, 2014 Breckenridge, CO*, number 14-102. AAS.

Putnam, Z. R. and Braun, R. D. (2013). Drag-modulation flight-control system options for planetary aerocapture. *Journal of Spacecraft and Rockets*, 51(1):139–150, doi:10.2514/1.A32589.

Ravindran, R. and Hughes, P. C. (1972). Optimal aerodynamic attitude stabilization of near-earth satellites. *Journal of Spacecraft and Rockets*, 9(7):499–506, doi:10.2514/3.61730.

Riley, J. A. and Giese, C. F. (1970). Interaction of atomic oxygen with various surfaces. *The Journal of Chemical Physics*, 53(146):146–150.

Rim, H. J., Schutz, B. E., Webb, C. E., Demarest, P., and Herman, A. (2000). Repeat orbit characteristics and maneuver strategy for a synthetic aperture radar satellite. *Journal of Spacecraft and Rockets*, 37(5):638–644, doi:10.2514/2.3612.

Roberts, J. K. (1930). The exchange of energy between gas atoms and solid surfaces. iii. the accommodation coefficient of neon. In *Proceedings of the Royal Society of London. Series A*, volume 129, pages 146–161.

Ross, I. M. and Karpenko, M. (2012). A review of pseudospectral optimal control: From theory to flight. *Annual Reviews in Control*, 36(2):182–197, doi:http://dx.doi.org/10.1016/j.arcontrol.2012.09.002.

Roßmans, P. (2014). QB50 FIPEX Science Unit Interface Control Document. Issue 2. Technical report, TU Dresden.

Rummel, R., Balmino, G., Johannessen, J., Visser, P., and Woodworth, P. (2002). Dedicated gravity field missions - principles and aims. *Journal of Geodynamics*, 33(1-2):3–20, doi:10.1016/S0264-3707(01)00050-3.

Saha, K. (2008). *The Earth's Atmosphere: Its Physics and Dynamics*. Springer.

Saleh, J. (2008). Flawed metrics: Satellite cost per transponder and cost per day. *Aerospace and Electronic Systems, IEEE Transactions on*, 44(1):147–156, doi:10.1109/TAES.2008.4516995.

Salomonson, V., Guenther, B., Barnes, W., Therrien, N., and Murphy, R. (2000). Early instrument performance results from the Terra/Moderate Resolution Imaging Spectroradiometer (MODIS). In *Geoscience and Remote Sensing Symposium, 2000. Proceedings. IGARSS 2000. IEEE 2000 International*, volume 3, pages 943–946. IEEE.

Saltsburg, H. (1967). *Fundamentals of Gas-Surface Interactions*. Academic Press.

Santoni, F. and Zelli, M. (2009). Passive magnetic attitude stabilization of the UNISAT-4 microsatellite. *Acta Astronautica*, 65(5–6):792–803, doi:http://dx.doi.org/10.1016/j.actaastro.2009.03.012.

Schamberg, R. (1959). A new analytic representation of surface interaction for hyperthermal free molecular flow. In *Proceeding of Heat Transfer and Fluid Mich Ins. Palo Alto, Stanford Univ. Press*.

Sengupta, P., Vadali, S. R., and Alfriend, K. T. (2010). Satellite orbit design and maintenance for terrestrial coverage. *Journal of Spacecraft and Rockets*, 47(1):177–187, doi:10.2514/1.44120.

Sentman, L. (1961). *Free Molecule Flow Theory and Its Application to the Determination of Aerodynamic Forces*. Lockheed Missile and Space Co.

Shepherd, G. G., Thuillier, G., Cho, Y.-M., Duboin, M.-L., Evans, W. F. J., Gault, W. A., Hersom, C., Kendall, D. J. W., Lathuillère, C., Lowe, R. P., McDade, I. C., Rochon, Y. J., Shepherd, M. G., Solheim, B. H., Wang, D.-Y., and Ward, W. E. (2012). The Wind Imaging Interferometer (WINDII) on the Upper Atmosphere Research Satellite: A 20 year perspective. *Reviews of Geophysics*, 50(2):n/a–n/a, doi:10.1029/2012RG000390.

Silani, E. and Lovera, M. (2005). Magnetic spacecraft attitude control: a survey and some new results. *Control Engineering Practice*, 13(3):357–371, doi:http://dx.doi.org/10.1016/j.conengprac.2003.12.017.

Smith, A. (2012). Sensor selection working group. final report. Technical report, Mullard Space Science Laboratory.

SSTL (2011). Earthmapper datasheet. Technical report, Surrey Satellite Technology Ltd.

Subias, L., Chen, R., Ertekun, E., Evain, H., Jimenez, J., Laurence, J., Marchetaux, G., Nouvellon, S., Palmer, K., Peters, R., Vora, A., Zurdo, P., Virgili, J., and Roberts, P. C. E. (2013). DMC-HD, a very low Earth orbit high resolution small satellite. In *9th IAA Symposium on Small Satellites for Earth Observation, April 8-12, 2013, Berlin, Germany. IAA-B9- 1309P*.

Sutton, E. K. (2009). Normalized force coefficients for satellites with elongated shapes. *Journal of Spacecraft and Rockets*, 46(1):112–116, doi:10.2514/1.40940.

Tomas, L. R. (2014). Very Low Earth Orbit SAR: Feasibility and advantages. Master's thesis, Cranfield University.

Trilling, L. (1967). *Fundamentals of Gas-Surface Interactions*, chapter Theory of Gas-Surface Collisions, pages 392–421. USA: Academic Press.

Ungar, S. G., Pearlman, J. S., Mendenhall, J. A., and Reuter, D. (2003). Overview of the Earth Observing One (EO-1) mission. *IEEE Transactions on Geoscience and Remote Sensing*, 41(6):1149–1159, doi:10.1109/TGRS.2003.815999.

Vallado, D. (2001). *Fundamentals of Astrodynamics and Applications*. Microcosm Press, 2nd edition.

Varma, S. and Kumar, K. D. (2012). Multiple satellite formation flying using differential aerodynamic drag. *Journal of Spacecraft and Rockets*, 49(2):325–336, doi:10.2514/1.52395.

Viereck, R. A., Murad, E., Green, B. D., Joshi, P., Pike, C. P., Hieb, R., and Harbaugh, G. (1991). Origin of the shuttle glow. *Nature*, 354(6348):48–50.

Vinh, N. X., Johannesen, J. R., Mease, K. D., and Hanson, J. M. (1986). Explicit guidance of drag-modulated aeroassisted transfer between elliptical orbits. *Journal of Guidance, Control, and Dynamics*, 9(3):274–280, doi:10.2514/3.20103.

Virgili, J. and Roberts, P. C. (2013). DDsat, a QB50 CubeSat mission to study rarefied-gas drag modelling. *Acta Astronautica*, 89(0):130 – 138, doi:http://dx.doi.org/10.1016/j.actaastro.2013.04.006.

Virgili, J., Roberts, P. C. E., Palmer, K., Hobbs, S., and Kingston, J. (2014). Descending sun-synchronous orbits with aerodynamic inclination correction. *Journal of Guidance, Control, and Dynamics*, pages 1–12, doi:10.2514/1.G000183.

Werninghaus, R. (2004). TerraSAR-X mission. In *Proceedings SAR Image Analysis, Modeling, and Techniques VI*, pages 9–16. International Society for Optics and Photonics.

Williams, E., Crossley, W., and Lang, T. (2000). Average and maximum revisit time trade studies for satellite constellations using a multiobjective genetic algorithm. *The Journal of the Astronautical Sciences*, 49(3):385–400.

Zhang, Y. and Paxton, L. J. (2011). Long-term variation in the thermosphere: TIMED/GUVI observations. *Journal of Geophysical Research*, (116).

Zimpfer, D., Kachmar, P., and Tuohy, S. (2005). *Autonomous Rendezvous, Capture and In-Space Assembly:Past, Present and Future*. American Institute of Aeronautics and Astronautics.

